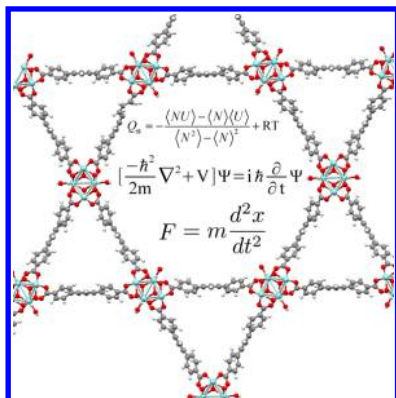


Quantum-Chemical Characterization of the Properties and Reactivities of Metal–Organic Frameworks

Samuel O. Odoh,* Christopher J. Cramer, Donald G. Truhlar, and Laura Gagliardi*

Department of Chemistry, Chemical Theory Center, and Supercomputing Institute, University of Minnesota, Minneapolis, Minnesota 55455-0431, United States



CONTENTS

1. Introduction	B	2.5. Time-Dependent Density Functional Theory (TDDFT)	M
1.1. What Are Metal–Organic Frameworks (MOFs)?	B	2.6. Inclusion of Spin–Orbit Coupling Effects	M
1.2. Current and Potential Uses of MOFs	C	2.7. Performing Electronic Structure Calculations on MOFs	M
1.2.1. Gas Adsorption and Separation	C	2.7.1. Molecular Cluster Calculations	N
1.2.2. Gas Storage and Delivery	D	2.7.2. Periodic DFT and DFT+U Calculations	N
1.2.3. Luminescent MOFs	D	2.7.3. Combined Quantum Mechanical and Molecular Mechanical (QM/MM) Methods	O
1.2.4. Magnetic MOFs	D	3. Properties of Metal–Organic Frameworks	O
1.2.5. Catalysis	D	3.1. Structural, Mechanical, and Electronic Properties of MOFs	O
1.3. Design and Characterization of MOFs	D	3.1.1. MOF-5	P
1.4. Theoretical Studies of MOFs	E	3.1.2. MOF-74	Q
2. Electronic Structure Methods	E	3.2. Framework Flexibility in MOFs and Its Effects on Functional Properties	S
2.1. Hartree–Fock Theory	G	4. Gas Adsorption and Separation	W
2.2. Post-HF Methods	H	4.1. Computing Adsorption Energetics with Electronic Structure Methods	W
2.2.1. Møller–Plesset Second-Order Perturbation Theory	H	4.1.1. Physisorption and Choice of Electronic Structure Method	W
2.2.2. Coupled Cluster Theory	H	4.1.2. Periodic and Truncated Cluster Models	Y
2.3. Beyond HF and Post-HF Methods	H	4.1.3. Gas Separation and Trends in Adsorption Energies	Y
2.3.1. Complete Active Space Self-Consistent Field (CASSCF) Theory	I	4.2. Influence of Electronic Structure on Adsorption Energetics	Z
2.3.2. Complete Active Space Second-Order Perturbation (CASPT2) Theory	I	4.3. Effects of Trace Gases on Gas Adsorption and Separation	AB
2.4. Density Functional Theory (DFT)	I	4.4. Coadsorption and Diffusion of Gases in MOFs	AC
2.4.1. Exchange–Correlation Functionals	J	4.5. Ligand-Assisted Adsorption in MOFs with Open Metal Sites	AE
2.4.2. Gradient Approximation Functionals	J	4.6. Gas Adsorption by Guest Molecules or Functionalizing Reagents	AE
2.4.3. Meta-Gradient Approximation Functionals	K	4.6.1. Amine Ligands at Open Metal Sites	AE
2.4.4. Hybrid Functionals	K	4.6.2. Decorating MOFs with Metal Atoms	AF
2.4.5. DFT+U Approaches	K	4.6.3. Organic Linkers Functionalized with Lithium Atoms	AG
2.4.6. Screened Exchange Functionals	L	5. Catalysis and Reactivity	AH
2.4.7. Dispersion-Corrected Functionals	L	5.1. Oxidation Reactions	AH
2.4.8. Multiconfiguration Pair-Density Functional Theory	M	5.2. Hydrogenation Reactions	AJ
		5.3. Knoevenagel Condensation Reactions	AJ
		5.4. Electronic Structure Effects on Catalysis and Reactivity	AJ

Special Issue: Calculations on Large Systems

Received: October 5, 2014

6. Spectroscopic Properties	AK
6.1. X-ray Absorption Spectroscopy	AK
6.2. Infrared Spectroscopy	AL
6.2.1. Calculation of IR Spectra	AL
6.2.2. IR Spectra of Bare MOFs	AL
6.2.3. IR Spectra of Adsorbed Species in MOFs	AN
6.2.4. Origins of the Shifts in Vibrational Frequencies of Adsorbed Gases	AN
6.3. UV–vis Absorption and Emission Spectroscopy	AO
6.4. Band Gaps	AP
7. First-Principles Force Fields	AR
7.1. Recent Force Fields—Development and Validation	AT
7.2. Applications of First-Principles Force Fields	AV
8. Conclusions and Prospects	AW
8.1. Creation and Large-Scale Screening of a MOF Database	AW
8.2. Electronic Structure Methods and Computing Architectures	AX
8.3. Improving Grand Canonical Monte Carlo (GCMC) Simulations	AX
8.4. Prediction and Scoring of Synthetic Pathways for MOFs	AX
Author Information	AY
Corresponding Authors	AY
Notes	AY
Biographies	AY
Acknowledgments	AZ
Acronyms and Abbreviations	AZ
References	BA

1. INTRODUCTION

The present review is concerned with quantum mechanical electronic structure calculations on metal–organic frameworks (MOFs) to elucidate their properties and functionalities. There are many previous reviews on MOFs. As examples, the Feb 8, 2012 issue of this journal was devoted entirely to MOFs, and Sholl et al. wrote a review of quantal and classical simulations of MOFs in 2009.¹ There is also a recent perspective on the stimuli-responsive behavior of metal–organic frameworks as well as covalent organic frameworks, dense coordination polymers, and molecular frameworks.² The unique aspect of the present review, as compared to previous reviews of MOFs, is that not only does it cover more recent work but also in it we explain the quantum mechanical electronic structure theories that have been applied to MOFs rather than referring to the scattered literature for these explanations. This is done in a coordinated and coherent way in section 2, in contrast to an approach in which these explanations are spread throughout the review. Section 2 is selective in that it explains those aspects of the theoretical methods that are important for treating MOFs, rather than explaining all aspects of these methods. It is also limited to methods of direct relevance to MOFs. The remaining sections are best read with section 2 read first as background. We also envisage that section 2 will come to be seen as a pedagogical tool or repository for training students in performing electronic structure calculations on MOFs.

This review is organized thus as follows: section 1 is an introduction to the world of MOFs, their properties, and potential uses. Section 2 gives background on quantum mechanical electronic structure methods. In section 3, we

review the intrinsic properties of MOFs (without any guest or adsorbed molecules), as revealed by electronic structure calculations. In sections 4–6, we review the functional properties of MOFs in gas adsorption, separation, and storage, catalysis, and chemical reactivity as well as their spectroscopic properties, all probed with electronic structure approaches. In section 7, we discuss the use of quantum mechanical electronic structure calculations to parametrize and validate force fields, which are then used in classical simulations. Section 8 has concluding remarks.

1.1. What Are Metal–Organic Frameworks (MOFs)?

MOFs are a class of nanoporous materials containing three-dimensional (3D) and periodic networks of metals, metal clusters, or metal oxide clusters held together by bridging organic linkers.³ They are also referred to as coordination polymers or coordination networks in the literature. One class of MOFs that is emphasized in the present review is the class of MOFs with open metal sites. An example of such a MOF is illustrated by Figure 1, which shows the building blocks of the

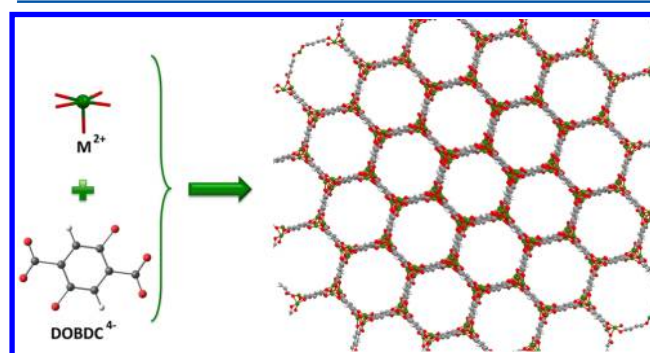


Figure 1. $M_2(\text{DOBDC})$ MOFs (also called $M\text{-MOF-74}$) have interesting CO_2 capture properties. This MOF contains divalent metals cations (M^{2+}) linked together by DOBDC^{4-} (2,5-dioxido-1,4-benzenedicarboxylate) units. M, O, C, and H atoms are represented as green, red, gray, and white spheres, respectively. Notice that the M^{2+} ions are pentacoordinate, with an open site available for coordination.

$M_2(\text{DOBDC})$ MOF, also known as $M\text{-MOF-74}$ or CPO-27-M , where to date $M = \text{Mg, Mn, Fe, Co, Ni, Cu, and Zn}$ have all been described, as have cases involving mixtures of two or more of these metals.⁴ This MOF has a 3D topology containing divalent metal (M^{2+}) sites and the organic DOBDC^{4-} (2,5-dioxido-1,4-benzenedicarboxylate or 2,5-dioxidoterephthalate) linker.

As synthesized,⁴ each M^{2+} site in the $M\text{-MOF-74}$ series is hexacoordinate; five coordination sites are occupied by oxygen atoms from DOBDC^{4-} ligands, and one site is occupied by the solvent. To activate the material for various purposes, the coordinating solvent can be removed, e.g., by heating in a vacuum, thus leaving the M^{2+} ions coordinated to five oxygen atoms in a square pyramidal arrangement. The coordinatively unsaturated metal centers can then, for example, interact with gas molecules using their open sites. In general, MOFs with coordinatively unsaturated metal sites have higher heats of gas adsorption and steeper adsorption isotherms than those that lack such sites (see section 4 for more detail on gas adsorption in MOFs).⁵ There are many other MOFs with open metal sites. Examples include Cu-BTC ,⁶ MOF-76 ,⁷ as well as the various members of the MIL-100 ,⁸ MIL-101 ,⁹ and ZJU-26 ¹⁰ series.

MOFs exhibit important properties from a technology standpoint: they are usually thermally stable, crystalline, and

characterized by high porosities (up to 90% free volume) and also possess record-breaking surface areas (in excess of 6000 m²/g).¹¹ These properties make them good candidates as gas adsorbents. In addition, the chemical functional groups found in their pores as well as the shapes and sizes of those pores can be tuned in a controlled fashion. In Figure 2, we present several

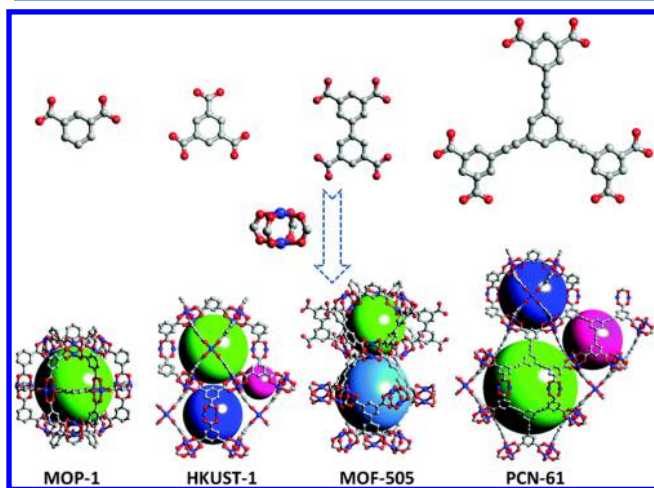


Figure 2. Several MOFs based on the dicopper paddle-wheel $\text{Cu}_2(\text{COO})_4$ SBU. Pore sizes are systematically tuned as the sizes of the *m*-benzenedicarboxylate linkers are systematically increased and their topology varied. HKUST-1 is also known as Cu-BTC or MOF-199. Cu, O, and C atoms are represented as blue, red, gray, and white spheres, respectively. H atoms are omitted to allow for better visibility. Pore channels of the MOFs are represented as large greenish, bluish, or pinkish spheres, respectively. Reprinted with permission from ref 13. Copyright 2014 Royal Society of Chemistry.

MOFs containing a bimetallic paddle-wheel $\text{Cu}_2(\text{RCOO})_4$ structural building unit (SBU). The MOFs' porosities are systematically tuned by increasing the sizes of the organic carboxylate linkers.¹² This potential for a logical design of materials is an intrinsic property of MOFs, as there are large numbers of metals, metal clusters, metal oxides, metal oxide clusters, and organic linkers that can be combined to form MOFs having different topologies. As a result, the rational design, synthesis, and characterization of MOFs having optimal performance for specific applications continue to be the focus of significant scientific interest.

The vast number of possible combinations of metal clusters and organic linkers precludes us from compiling a list of all existing MOFs. A representative list of MOFs is however provided in Table 1. We emphasize that this list is not at all comprehensive. It does not even contain all the MOFs mentioned in this review. The organic linkers in some of the MOFs listed in Table 1 are shown in Figure 3. The members of the MIL-53, MIL-101, MOF-2, and UiO-66 series all have BDC linkers. These MOFs however have different metallic components, which differ not only in their atomic compositions but also in their symmetry as well as the number of available sites for coordination to the organic linker. For these reasons, the resulting MOFs have completely different topologies as well as physical properties. While they are not comprehensive, Table 1 and Figure 3 allow us to illustrate the immense diversity in topology and properties that can be achieved by changing the metallic or organic components of MOFs or both. A few of the MOFs listed in Table 1 are shown in Figure 4. To illustrate, we highlight the fact that Chavan et al. found the total pore volume

Table 1. A Few MOFs (or series of MOFs) and Some Associated Experimental and Theoretical References

MOF	description	empirical work	theoretical work
MIL-53	trivalent metals (e.g., Al, Fe, Cr) and 1,4-benzenedicarboxylate (BDC) linkers	14	15
MIL-101	trivalent metals oxide trimers (e.g., Cr_3O) and BDC linkers	16	17
MOF-2	divalent metals (e.g., Zn, Ni) and 1,4-benzenedicarboxylate (BDC) linkers	18	
MOF-4	divalent metals (e.g., Zn, Ni) and 1,3,5-benzenetricarboxylate (BTC) linkers	19	
MOF-5	Zn_4O clusters and 1,4-benzenedicarboxylate (BDC) linkers	20	21
MOF-74	divalent metals (e.g., Zn, Ni) and dioxido-benzenedicarboxylate (DOBDC) linkers	4	22
NU-1000	octahedral $(\text{Zr}/\text{Hf})_6(\text{O})_4(\text{OH})_4$ nodes linked by 1,3,6,8-tetrakis(<i>p</i> -benzoic acid) pyrene with 4 each coordinating HO and H_2O ligands	23	24
UiO-66	octahedral $\text{Zr}_6(\text{O})_4(\text{OH})_4$ nodes with each Zr node coordinated to 12 1,4-benzenedicarboxylate (BDC) linkers	25	26
UiO-67	octahedral $\text{Zr}_6(\text{O})_4(\text{OH})_4$ nodes with each Zr node coordinated to 12 4,4'-biphenyldicarboxylate (BPDC) linkers	25,27	28
ZIF-7	2-benzimidazolate anions and Zn ions ordered into a sodalite topology	29	30
ZIF-8	2-methylimidazolate anions and Zn ions ordered into a sodalite topology	31	32

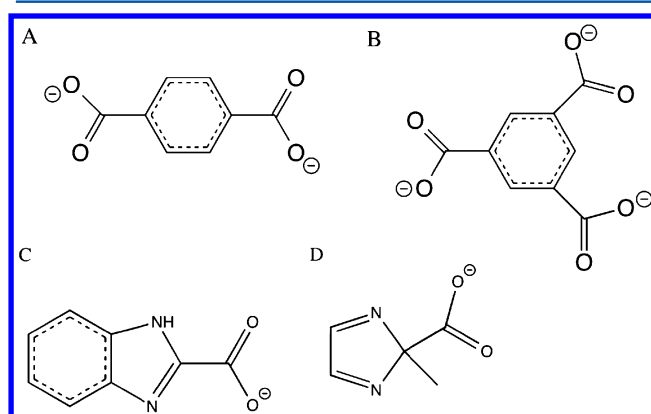


Figure 3. Organic linkers of some of the MOFs listed in Table 1. These are (A) 1,4-benzenedicarboxylate, (B) 1,3,5-benzenetricarboxylate, (C) 2-benzimidazolate, and (D) 2-methylimidazolate.

of UiO-67 to be 0.95 cm³/g, almost double that of UiO-66 (0.52 cm³/g). This change was effected by switching from BDC linkers to longer BPDC linkers, Table 1.²⁸ As another example, although the BDC linker is found in both MIL-53 and UiO-66, the differences in their metallic components and overall topologies result in remarkable differences in their framework flexibilities^{15a,33} as well as mechanical properties.³⁴

1.2. Current and Potential Uses of MOFs

Like other nanoporous materials, such as zeolites, carbon nanotubes, and activated carbon, MOFs have been proposed as excellent candidates for several energy-related applications.³⁵ The potential applications of MOFs are much greater than those that will be reviewed here. The applications to be discussed in this review can be classified into five broad groups.

1.2.1. Gas Adsorption and Separation. As noted above, MOFs are excellent candidates as gas adsorbents due to their high porosity and surface areas. In fact, their unique adsorption

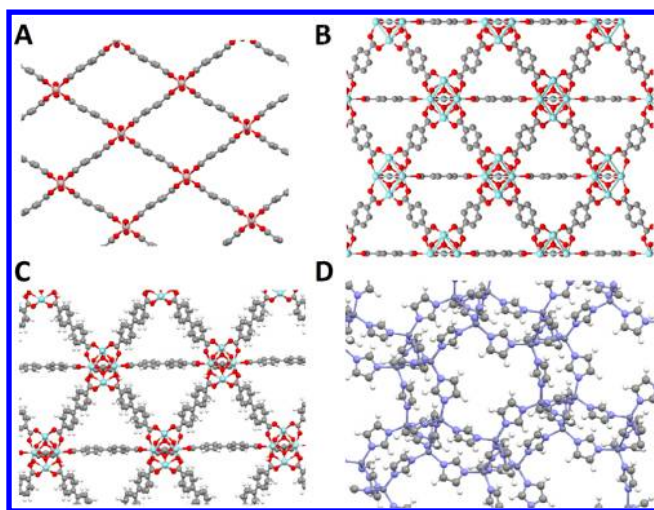


Figure 4. Representations of (top) (A) MIL-53(Al) and (B) UiO-66. The former has Al^{3+} cations that are bound to six oxygen atoms, whereas the latter has Zr_6 nodes coordinated to 24 oxygen atoms from the organic linkers. (Bottom) (C) UiO-67 and (D) ZIF-8. UiO-67 has larger pore sizes than UiO-66 as it has a longer linker (biphenyldicarboxylate).

characteristics were among their earliest promising properties.³⁶ In many instances, their commendable thermal stability also allows for the removal of included guest species through a thermal reactivation process, making them potentially suitable for gas adsorption/capture as well as gas separation and purification.³⁷ Regarding the former, the capture of carbon dioxide, CO_2 , from industrial emissions has been of particular interest owing to its role as a greenhouse gas contributing to global climate change.^{37c,f,i,m,38} Also, regarding the latter, gas separation in MOFs is typically a thermodynamic phenomenon, based on differences in the adsorption energies of different gases in different MOFs, although in some cases it is possible to achieve kinetics-based separations.³⁹

1.2.2. Gas Storage and Delivery. The development of a viable and safe approach for the on-board storage of molecular hydrogen, H_2 , would likely significantly accelerate the widespread commercialization of hydrogen-fueled automobiles. There are several MOFs with very large surface areas (permitting the capture of more gas molecules at high H_2 pressure) as well as high affinity for H_2 , these being key properties required for efficient H_2 storage. Some examples of these are MOF-5, Cu-BTC, and Mg-MOF-74.⁴⁰ MOF-5 has Zn_4O tetrahedral clusters joined by benzenedicarboxylate linkers to form an extended 3D framework with interconnecting pores of 8 Å width and 12 Å diameter, Table 1.²⁰ The structure of Cu-BTC will be described in more detail below. MOFs have also been studied for their abilities to capture, store, and deliver many other gases, including natural gas for vehicle fuel purposes. Some studies are provided in refs 6 and 41.

1.2.3. Luminescent MOFs. Luminescent materials have been widely used in lighting, sensing, display, and optoelectronic devices. Currently, there is substantial interest in developing luminescent MOFs suitable for practical applications.³⁵ The presence of organic linkers and metal ions in MOFs ensures that both can be used as sources of emissive phenomena. Additionally, the close contacts between the metal and the linker can result in unique emissive properties by

altering the rigidity and/or conjugation of the organic linker.^{35,42}

1.2.4. Magnetic MOFs. Magnets have a wide range of important applications. Magnetic properties can be incorporated into MOFs by either embedding in them paramagnetic metal ions (usually 3d transition metals) or using open-shell organic ligands that allow for strong magnetic interactions between centers of spin.^{35,43} Magnetic MOFs made this way fall into the category of molecular magnets. Paramagnetic centers, however, generally tend to be aligned antiferromagnetically or noncooperatively, so that MOFs lack bulk ferromagnetism. The structural flexibility of MOFs makes it quite enticing to pursue ligand and topology designs that maximize strong exchange interactions between metal and/or linker sites to enhance cooperativity, bearing in mind that design possibilities can be limited to some extent by the generally short-range nature of strong magnetic couplings.^{43g,44}

1.2.5. Catalysis. In addition to their thermal stability and high crystallinity, MOFs have high concentrations of metals organized at regular distances and in long arrays. These properties are highly desirable in industrial catalysts. Like other heterogeneous catalysts, MOFs have the advantages over homogeneous catalytic systems of easier separation of products from the reaction mixture and easier recyclability of the catalyst. As compared to other heterogeneous catalysts, they have the advantage of holding the catalytic metal sites apart with no danger of sintering. As such, MOFs have good prospects for better catalyst stability.⁴⁵ There have been many reports in which MOFs containing catalytically active metals have been used to achieve efficient reaction catalysis.⁴⁶ In addition, some potential catalytic applications are based on the size and shape of the pores found in the MOF.³⁵ This topic is addressed in more detail in section 5. A particularly interesting possibility, which we think will be extensively investigated in the future, would be to covalently graft existing catalysts into the pore channels at regular intervals provided by the framework.⁴⁷ Such catalytic sites should maintain their activity while being resistant to sintering due to their separation.

1.3. Design and Characterization of MOFs

There have been many reviews of the synthesis, modification, characterization, and application of MOFs.^{40,42h,45,46k,l,48} An emerging area of interest focuses on the rational design of MOF topologies to have optimal performance for certain applications. To date, there have generally been two approaches for designing these optimally performing MOFs. The first approach is largely experimental and based on crystal design research. MOFs with various polydentate ligands are synthesized in the attempt to incorporate desired functional groups into the framework. The performances of the resulting MOFs in gas adsorption, gas storage, gas separation, optical, and catalysis applications are subsequently characterized. Although this prospecting approach has provided the bulk of our current knowledge of MOFs, it is nevertheless expensive and time consuming.^{3a,20,49}

The second approach predicts the topologies of MOFs that can be formed from various metal/metal oxide clusters and organic linker units. This usually involves creating large libraries of potential materials.^{21b,50} The enumeration of the potential MOF topologies is then followed by screening for specific properties such as higher pore volumes, stability to water vapor, presence of coordinatively unsaturated metal sites, and higher capacity/selectivity for certain gas substrates. Potential MOFs

with desired properties can then be targeted for experimental synthesis and characterization.^{50a} As an example, NU-100 was initially designed and characterized using molecular simulations. Experimental attempts to synthesize this MOF were motivated by the simulations that also predicted that NU-100 would have an ultrahigh Brunauer–Emmett–Teller (BET)⁵¹ surface area. This material was subsequently synthesized and characterized experimentally, with the experimental data and the simulated data being in excellent agreement.⁵

A crucial aspect of this combinatorial approach is the availability of computational models that can be used to predict the specific properties of the potential MOFs. These computational methods generally fall into two groups: electronic structure methods based on the principles of quantum mechanics⁵² and classical simulation methods⁵³ (including molecular dynamics and Monte Carlo simulations) using interatomic potentials that are defined by analytical potential energy functions.

1.4. Theoretical Studies of MOFs

Theoretical calculations on materials generally involve two steps; we will say more about the separation into steps in section 2. However, for this introduction, we note that the first step is usually to obtain a potential energy surface and the second step is dynamics or statistical mechanics or some combination thereof. A potential energy surface is the potential energy for nuclear motion as a function of nuclear coordinates; it is also called a potential energy function. The local minima of a potential energy surface occur at the equilibrium structures, and saddle points of the potential energy surface are conventional transition states. Equilibrium structures and saddle points are collectively called stationary points. Nuclear dynamics (in other words internuclear dynamics, as we are not concerned with motions internal to the nuclei) is governed by the potential energy surface in the sense that the forces acting on the nuclei are given by the negative partial first derivatives of the energy with respect to the nuclear coordinates (the collection of these partial derivatives is encapsulated in the gradient). For this reason the potential energy surface is sometimes referred to as a “force field”, a term that is often used with a more specialized meaning, referring to an analytical representation of the potential energy surface, from which the forces may be calculated analytically. We will use the force field language with that meaning in the present review. Analytical force fields are also called classical force fields or molecular mechanics (MM) force fields. Traditional MM force fields are applicable only in the vicinity of a local minimum or a few local minima connected by low-barrier torsions. Extensions to reactive systems (in other words, systems in which bonds are broken or rearranged) are sometimes called reactive force fields. Examples of these are the ReaxFF force field⁵⁴ and the valence-bond order method.⁵⁵

MM force fields generally contain parameters that describe the interactions between various atoms or groups of atoms. One can broadly divide the method for determining these parameters into two groups. In empirical force fields, the parameters are obtained by fitting experimental structural, thermochemical, and spectroscopic data. In contrast, for first-principles force fields, the parameters are fit to the results of electronic structure calculations.

Sometimes the first step of obtaining a description of the potential energy surface is sufficient. An example would be if one is simply interested in predicting stationary point

geometries and their relative energies. However, for ensemble averaging of complex systems or to compute rate constants as well as other dynamical properties, the second step is needed and may involve molecular dynamics (MD)⁵⁶ or Monte Carlo (MC)⁵⁷ simulations or transition-state theory.⁵⁸ We note that MC simulations provide information about ensemble averages and thermodynamic quantities like free energies,⁵⁹ but they do not provide dynamical information. In contrast, MD simulations can predict real-time dynamics even though they are often used more simply for ensemble averaging, relying on ergodicity to make time averages equal ensemble averages. MD and MC simulations can provide insights into the properties of synthesized or potential MOFs.

Electronic structure calculations are computationally more expensive than analogous computations exploiting classical force fields. For this reason, the former have primarily been used for the prediction of microscopic properties (such as gas adsorption sites and binding energies), while classical force fields in combination with simulations have been widely used for the prediction of macroscopic properties (such as adsorption isotherms, isosteric heat of adsorption, and gas diffusion constants) of MOFs.⁶⁰ On the other hand, as they can be more accurate than insufficiently tuned classical force fields, there is a large and growing number of reports in which electronic structure calculations have been used to study the properties and performances of MOFs. In addition, an increasing number of classical simulations of MOFs have employed force fields derived from targeted electronic structure calculations.^{60a} Although there have been several reviews focusing on classical MD and MC simulations of MOFs,⁶⁰ the literature of electronic structure calculations on MOFs has not yet been as comprehensively and critically reviewed, but that is a goal of the present review.

A key issue in comparing the use of electronic structure methods to classical simulations with force fields is the issue of sampling, that is, when the adsorption site is *a priori* clear (e.g., binding to an open metal site), electronic structure may be applied to the well-defined adsorption site. However, in cases where that binding site is not obvious or no single “site” can be defined at the relevant conditions of temperature or pressure, then classical force fields offer a welcome reduction in cost that allows sampling. Extensive sampling is important for another reason as well, namely, for the calculation of thermally averaged bulk observables such as adsorption isotherms.^{60a,61}

Thus, in this review, we summarize and analyze literature reports on the use of quantum-mechanical (QM) calculations and *ab initio* molecular dynamics simulations as applied to understanding or predicting the properties of MOFs. In section 2, we summarize the state-of-the-art electronic structure methods that have been most widely employed. In sections 3, 4, 5, and 6, we highlight the application of these methods for studying the structural properties of MOFs, gas adsorption and separation by MOFs, catalytic properties of MOFs, and spectroscopic properties of MOFs, respectively.

2. ELECTRONIC STRUCTURE METHODS

Electronic structure calculations on MOFs are generally aimed at calculating their physical and chemical properties while knowing only their atomic compositions and the positions of those atoms in a unit cell. Some of the properties of interest in the present review include ground-state structural properties (e.g., bond distance and valence angles), bulk mechanical properties, magnetism, vibrational frequencies and IR spectra,

X-ray absorption spectra, catalytic activity, reaction and activation energies associated with particular chemical transformations, gas adsorption properties, as well as optical and excited-state properties. Because so many different properties are of interest, a variety of theoretical methods are employed. Even if we restrict our attention to only one type of property, there can be significant diversity. We illustrate this with an example. If we are interested in considering the adsorption of gases at the open metal sites of MOFs, say Fe–MOF-74 as an example, then we need to note that the adsorption of methane in this particular MOF presents different challenges than the adsorption of O₂. This may provide a further appreciation of why so many techniques are used. In what follows we give an introductory review of the techniques that are in our view most relevant to the treatment of MOFs.

Under steady state conditions (i.e., absence of time-dependent external fields), a system for which only the atomic composition and positions are known is described by the many-body time-independent Schrödinger equation, eq 2.1

$$\hat{H}\Psi = E\Psi \quad (2.1)$$

In this equation, E is the total energy of the system, Ψ is the wave function, and a caret denotes a differential operator. The Hamiltonian, \hat{H} , includes the kinetic energies of the nuclei, \hat{T}_n , and the electrons, \hat{T}_e , as well as the Coulomb interactions between nuclei and electrons, V_{ne} , among electrons, V_{ee} , and among nuclei, V_{nn}

$$\hat{H} = \hat{T}_e + \hat{T}_n + V_{ne} + V_{ee} + V_{nn} \quad (2.2)$$

The wave function, Ψ , contains all of the information that can be extracted about the system within the limits set by the Heisenberg uncertainty principle. However, this equation is too complicated to be solved exactly, except for very small systems, which a MOF most definitely is not. For this particular reason, most modern computational approaches adopt a number of simplifying approximations.

The first step in most treatments is the Born–Oppenheimer approximation,⁶² which is valid when all excited electronic states are much higher in energy than the ground state; the ground state is often the one of primary interest. This is generally the case for many closed-shell singlet systems in which all molecular orbitals are doubly occupied (but not for cases involving a near degeneracy, as may frequently occur in open-shell systems containing transition metals). In such a case, it is a good approximation to solve the Schrödinger equation by the following two-step procedure. In the first step, one treats the nuclei as stationary, in which case \hat{T}_n is thus dropped from eq 2.2 and the electronic wave function can then be solved for a set \mathbf{R} of nuclear positions as parameters

$$\hat{H}_{\text{B-O}}(\mathbf{R}_1\mathbf{R}_2\cdots\mathbf{R}_n) = \hat{T}_e + V_{ne} + V_{ee} + V_{nn} \quad (2.3)$$

With this simplification, the eigenvalue of eq 2.1 corresponds to the sum of the electronic energy and the nuclear repulsion; for convenience, this sum is usually just called the electronic energy, and it will be denoted henceforth as V . Then, if we write the wave function Ψ as a product of the just determined electronic wave function Ψ_e and a nuclear wave function Ψ_n , eq 2.2 may be replaced by

$$\hat{H} = \hat{T}_n + V \quad (2.4)$$

and eq 2.1 becomes

$$(\hat{T}_n + V)\Psi_e\Psi_n = E\Psi_e\Psi_n \quad (2.5)$$

The Born–Oppenheimer approximation then replaces $\hat{T}_n\Psi_e\Psi_n$ by $\Psi_e\hat{T}_n\Psi_n$, which can be justified (when there are no low-lying electronic states) by the small ratio of the electronic mass to a nuclear mass, and this reduces eq 2.5 to

$$(\hat{T}_n + V)\Psi_n = E\Psi_n \quad (2.6)$$

In this equation, we can solve for a nuclear wave function with the electronic energy V acting as a potential energy for nuclear motion (which is why we called it V in the first place). A local minimum of V corresponds to an equilibrium structure of the system, and solving eq 2.6 for a nuclear wave function near such geometries gives the vibrational frequencies. However, one may also calculate V along reaction paths, and the saddle points of V correspond to highest energy points on lowest energy paths; these are the classical barrier heights (the quantal barrier heights must also take into account lost zero-point vibrational energy in the reaction coordinate and the variation of vibrational frequencies for motions transverse to the reaction path as the system proceeds along the reaction path).

In summary, in the Born–Oppenheimer approximation, the first step is the calculation of the electronic energy by solving the fixed-nuclei Schrödinger equation, which may be called the electronic Schrödinger equation. This gives the electronic energy V as a function of the nuclear coordinates, and this may be called the potential energy function or the potential energy surface (PES). The local minima of the potential energy surface are the equilibrium structures, and the saddle points are transition structures for chemical transformations (chemical reactions or conformational isomerizations) from one equilibrium structure to another. If desired, the potential energy function may then be used in a second step to calculate vibrational frequencies or the wave function for nuclear motion along a reaction path. If one is willing to calculate the nuclear motion classically instead of by nuclear wave functions (this is often a good approximation except for hydrogen atom and hydrogen ion transfer), the classical motion is governed by the potential function V , so this function is also a starting point for classical MD simulations. In particular, the classical mechanical forces (or simply, force fields) used in classical MD simulations are the negative gradients (negative partial first derivatives) of the potential energy function.

When the Born–Oppenheimer approximation is not valid, for example, in photochemical reactions where a photon excites the system to an excited electronic state, or for systems with low-energy excited electronic states that may be excited thermally, one can use the generalized Born–Oppenheimer approximation.⁶³ In this approximation, one again solves the fixed-nuclei Schrödinger equation but now one solves for more than one eigenvalue. These electronic eigenvalues yield a potential energy surface, V_j , for each electronic state j of the system. In this case, the nuclear motion becomes intrinsically nonclassical, proceeding on an effective potential energy surface due to a coherent mixture of coupled electronic states that changes as a function of nuclear motion. Decoherence then usually reduces this effective potential to one of the generalized Born–Oppenheimer eigenvalues V_j , in which case we say that the system has made a transition to state j . The coupling between potential energy surfaces is caused by the action of the nuclear kinetic energy operator, which we neglected above but which is no longer negligible when one or more excited electronic states are accessible. An interesting case occurs when

the coupled electronic states have different total electron spin quantum numbers (e.g., singlet and triplet or doublet and quartet). For such situations, we must extend the above treatment in one key respect, namely, we must go back to eq 2.2 and include not just the Coulomb interactions but also the interaction of the electrons' spins with electronic orbital angular momentum. In the absence of this spin–orbit term, spin would be a good quantum number and would be conserved. However, the spin–orbit operator can couple states of different spin.

We have seen that the key step in quantum-chemical characterization of the properties and reactivities of MOFs as well as other molecular or solid-state systems is the solution of the electronic Schrödinger equation. There are many approaches to solving this equation while taking advantage of the Born–Oppenheimer or generalized Born–Oppenheimer approximation. These methods may be divided into two general branches. On the one hand, we have wave function theory (WFT) approaches, where one uses variational methods, perturbation theory, or many-body theory to achieve an approximate solution of the Schrödinger equation. On the other hand, we have density functional theory (DFT), where one exploits a one-to-one mapping between the electron density and the wave function.

In both the WFT and the DFT approaches, quantitative accuracy can be achieved only when one includes the energetic effect of the dynamical correlation of the motion of the electrons to reduce their mutual repulsion. In the DFT category, the most widely applied approach at present is Kohn–Sham theory, where dynamical correlation is added by an exchange–correlation functional. In the WFT category, the methods for including dynamic correlation may be divided into two groups, depending on how one obtains a reference wave function to which dynamical correlation is added. If the reference wave function corresponds to a single configuration (which means a set of orbitals that are all doubly or singly occupied), the method is a single-reference method. If however the reference wave function is a superposition of configurations with different sets of orbital occupancies, the method is labeled a multireference method.

The orbitals for single-reference methods are almost always obtained by Hartree–Fock theory, and dynamical correlation is added by post-Hartree–Fock methods such as Møller–Plesset perturbation theory methods (MP n), configuration interaction (CI), or coupled cluster (CC) theory. The reference wave function for multireference methods is obtained by multi-configuration self-consistent-field theory (MCSCF), usually complete active space self-consistent field theory (CASSCF), and dynamical correlation can then be added by various methods. Two examples are the complete active space second-order perturbation method theory (CASPT2) and the multireference configuration interaction (MRCI) approach. Coupled cluster theory and CASPT2 are the prime examples of post-SCF wave function methods that provide, in principle, the most systematically reliable results, at least so long as adequate single-particle basis sets are employed.

In the subsequent subsections, we provide more details of both the WFT and the DFT approaches. In the mean time, we note that when MOFs are treated with periodic boundary conditions (PBC), there is a wide range of sizes of the periodic cells that can be used in the calculations. Additionally, when adsorbates are present, the size of the unit cell required for a realistic treatment may have to be increased. On the other hand, when cluster models that describe specific local portions

of the MOF are used, there is again a wide range of system sizes that can be constructed and used in electronic structure calculations. For this reason, generalizations are difficult in the face of the great diversity of size and complexity of the model systems as well as the disparate electronic structure calculations that have been used by researchers over the years. However, one generalization that is certainly valid is that the most reliable WFT methods, to be introduced in sections 2.2.2 and 2.3.2, can currently be applied only to the smallest cluster models (or to small fragments of systems treated by multilevel fragment methods), whereas the treatment of the largest and most complex model systems is usually limited to the DFT methods employing the exchange–correlation density functionals with a small number of ingredients, which are introduced in sections 2.4.2, 2.4.3, 2.4.5, and 2.4.7.

2.1. Hartree–Fock Theory

We will begin with a brief review of Hartree–Fock (HF) theory for three specific reasons. First, HF theory serves as the source of the orbitals and the reference wave function for the post-HF methods discussed in section 2.2. Second, HF theory provides the rationale for adding nonlocal exchange to the exchange–correlation density functional used in DFT. Third, HF theory is the simplest self-consistent field (SCF) method, and therefore, it provides a starting point for understanding the MCSCF and DFT approaches, both of which are discussed below. We note, however, that the energies predicted by HF theory are not useful in their own right as electron correlation energy (other than that associated with electron exchange, which is a correlation phenomenon) is neglected.

HF theory⁶⁴ was developed as one of the earliest methods for solving the electronic Schrödinger equation. In this theory, the wave function is taken to be a Slater determinant of orthonormal single-particle wave functions, typically referred to as orbitals (even though they are actually spin–orbitals), and each electron interacts only with the mean field of all of the other electrons (in other words, electronic motion is treated by a mean-field approximation). As a clarification, we note that the word “orbital” is used to refer to both the spin–orbitals themselves and the spatial parts of the spin–orbitals. As such, the meaning must usually be inferred from the context. The Slater determinant represents a convenient many-body wave function that satisfies the Pauli requirement that the wave function change sign with an exchange of particle indices (this is called antisymmetry). An HF theory calculation is in its very essence a variational optimization of the Slater determinantal wave function by finding the spin–orbitals that give the lowest energy. These spin–orbitals are the eigenfunctions of the Fock operator which actually also depends on the spin–orbitals. As a result, this eigenvalue equation must be solved by iterating until the orbitals are consistent with the operator and the operator is consistent with the orbitals. This is called self-consistency, and the mean-field determined self-consistently is called a self-consistent field (SCF). Practically, the spatial parts of the spin–orbitals are expanded in a set of basis functions. We refer to these as the one-electron or single-particle basis functions to distinguish them from the configuration state functions, CSFs (defined below). The difference between the energy obtained from HF theory, E_{HF} , and the (usually unknown) accurate solution to the electronic Schrödinger equation is usually called the correlation energy

$$E_{\text{corr}} = E_0 - E_{\text{HF}} \quad (2.7)$$

2.2. Post-HF Methods

The failure of a mean-field method to properly account for all correlated motions of electrons makes the electronic energy calculated by the HF approximation inaccurate. Indeed, a reading of section 2.1 makes it apparent that there are two critical assumptions in HF theory. The first is that the electrons are exposed only to a mean-field interaction with one another, that is, the motions of the electrons are uncorrelated, although their average densities optimize to reduce repulsive interactions. In a proper treatment, however, the motions of the electrons are coupled as a result of instantaneous electron–electron interactions. This is called dynamical electron correlation. The second critical assumption is sometimes associated with the terms nondynamical or static correlation and relates to a Slater determinant being only one of the many possible ways to construct a properly antisymmetric electronic wave function. For some cases, a single Slater determinant is insufficiently flexible for even a qualitatively accurate representation of the system.

The inaccuracy of the HF energies due to neglect of the electron correlation energy means that they are not usually used in modern work and have very rarely been used to describe the properties of MOFs. Recovering some of this correlation energy—ideally a substantial fraction—is required in most cases for accurate prediction of the properties of molecular and extended solid-state systems. Several approaches have been developed that build on an initial calculation with HF theory in order to calculate a posteriori some of the correlation energy that the HF level neglects. These are denoted as post-HF methods. Generally, HF orbitals are used to make many-electron basis functions, termed configuration state functions (CSFs), with each HF orbital having a *definite integer* occupancy. We review the approaches for recovering the correlation energy below.

2.2.1. Møller–Plesset Second-Order Perturbation Theory. In this method, an attempt is made to recover dynamical correlation by adding a perturbation, $\lambda\hat{H}'$, that is equal to the difference between the full Hamiltonian and the Hamiltonian of which the HF wave function is an eigenfunction

$$\hat{H} = \lambda\hat{H}' + \hat{H}^0 \quad (2.8)$$

The latter is the zeroth-order Hamiltonian, \hat{H}^0 , and is the sum of the one-electron Fock operators. Both the wave function and \hat{H} can then be expanded as a power series in λ

$$\Psi_i = \Psi_i^{(0)} + \lambda\Psi_i^{(1)} + \lambda^2\Psi_i^{(2)} + \dots \quad (2.9)$$

These equations are then inserted into the electronic Schrödinger equation, which is solved order by order. The first-order energy is the HF energy, and the higher order energies (orders 2, 3, ...) are called MP2, MP3,⁶⁵ ..., in recognition of the original derivation by Møller and Plesset.⁶⁶ The series is not necessarily convergent as one goes to higher orders of the MP n approaches, but stopping at an early term (MP2, MP3, or MP4) is usually most meaningful in the sense of an asymptotic series.⁶⁷ In practical terms, it is assumed that the perturbation to the zeroth-order Hamiltonian is small and becomes increasingly so at higher orders.

For MOFs, the MP2 approach has been largely used as a benchmarking model for the development of classical force fields, since, unlike HF theory, it provides a physical description of damped dispersion interactions that often dominate the attractive noncovalent forces that are particularly important for

predicting, for example, gas adsorption behavior. However, the cost of MP2 calculations is high compared to modern DFT methods that typically yield equal or better accuracy.

2.2.2. Coupled Cluster Theory. In coupled cluster (CC) theory, an energy expression is obtained by many-body theory exponential functions of cluster operators, $\check{T}_1, \check{T}_2, \check{T}_3, \dots, \check{T}_n$, that generate excited-state determinants excited by one, two, three, ..., n electrons from the reference ground-state HF wave function. If n were equal to the total number of electrons (in other words, full configuration interaction (CI)), the results would be exact, but in practice even $n = 3$ is often prohibitively expensive. Truncation of the included cluster operators at double and triple excitations leads to the coupled cluster singles and doubles (CCSD) theory and the coupled cluster singles, doubles, and triples (CCSDT) method, respectively. At the CCSD level, some triple, quadruple, and higher excitations are already included. This is due to the fact that some higher order excitations can be expressed as products of linked double excitations, eq 2.11

$$e^{\check{T}_1 + \check{T}_2} = 1 + \check{T}_1 + \check{T}_2 + \frac{\check{T}_1^2}{2} + \frac{\check{T}_2^2}{2} + \check{T}_1\check{T}_2 + \dots \quad (2.11)$$

The approximate CC approach that tends to be regarded as the best compromise between speed and accuracy is the CCSD(T) method. In this method, triple excitations are incorporated into the CCSD wave function in a perturbative manner rather than evaluated explicitly by full CC theory.⁶⁸ The CCSD method is less accurate than CCSD(T). In fact, the CCSD(T) approach has been shown to be very accurate for closed-shell systems and is often referred to as the gold standard of computational chemistry, although one should remain cautious because the errors can sometimes be larger than expected when the system cannot be reasonably described by a single Slater-determinantal wave function, which is the reference wave function. Even when CCSD(T) theory is adequate, practical calculations may be inadequate and prohibitive. This is because CCSD(T) requires large one-electron basis sets to achieve high accuracy and is thus generally far too expensive to be routinely used for studying extended or large systems such as MOFs.

For MOFs, CC calculations are most useful for benchmarking so-called first-principles force fields through calculations on small (or subnano) molecular clusters that are models of some portions of the MOF. We note that local correlation methods, such as the local pair natural-orbital coupled cluster single double (LPNO-CCSD) method,⁶⁹ have been developed to allow CC calculations on larger systems. The LPNO-CCSD approach has been used for studying some MOFs.⁷⁰

2.3. Beyond HF and Post-HF Methods

At the beginning of section 2.2 we noted that the two critical assumptions in HF theory are, first, that the electrons are exposed only to a mean-field interaction with one another (omission of the dynamic portion of the correlation energy) and, second, that the wave function can be represented by a single CSF (omission of the static component of the correlation energy). For cases in which a system cannot be truly described by a single Slater determinant, it is more accurate to use a multiconfigurational reference function (in other words, the wave function must contain more than one CSF). The MP n approaches have been generalized to the multireference case,⁷¹ leading to a variety of closely related methods called variously (multireference Møller–Plesset, MRMP n), multiconfiguration quasidegenerate perturbation theory, complete active space

second-order perturbation theory of various sorts, e.g., the CASPT2 model summarized in section 2.3.2, etc. The CC approaches have also been generalized to the multireference cases (multireference coupled cluster, MRCC), albeit at still higher computational costs.^{72,73} Their prohibitively large costs means that multireference CC methods are still only rarely used for practical work.

2.3.1. Complete Active Space Self-Consistent Field (CASSCF) Theory. Systems that cannot be correctly described by a single Slater determinant can be better approximated with a linear combination of *multiple* Slater determinants, as described in eq 2.12. In multiconfigurational self-consistent field (MCSCF) theory, the many-electron wave function, Φ_{MCSCF} , is taken as a linear combination of CSFs, Ψ_I , and the orbitals in terms of which the CSFs are defined are simultaneously optimized with the coefficients, c_I , of the CSFs.

$$\Phi_{\text{MCSCF}} = \sum_I c_I \Psi_I \quad (2.12)$$

The reference orbitals used to construct the CSFs are divided into inactive orbitals, active orbitals, and virtual orbitals. The virtual orbitals are unoccupied in all CSFs, and the inactive orbitals are doubly occupied in all CSFs. A full CI expansion that allows for all possible electronic configurations or occupancies (unoccupied, singly occupied, or doubly occupied) is then carried out, only within the active space of orbitals. An MCSCF wave function of this type is called a complete active space (CAS) wave function, and the procedure of optimizing the orbitals as well as the configuration coefficients for this wave function is called complete active space self-consistent (CASSCF) theory. The CI coefficients in the expansion are optimized while also performing orbital optimizations over the active orbitals and some subset or all of the inactive orbitals.⁷⁴ The choice of a good active space typically requires insights into the chemical nature of the system of interest. As a result, this method is not a black-box method, and it is rather challenging to employ.

Also, we note that dynamical correlation is not initially accounted for in CASSCF theory. It accounts for electronic correlation primarily driven by near degeneracies of CSFs (static correlation). In contrast, dynamical correlation converges slowly as the number of CSFs increases, and the CASSCF method is not an efficient way to converge it. However, the CASSCF approach can be used for generating orbitals for a post-SCF calculation of dynamical correlation. It should however be noted that there is really no precise distinction between the two kinds of correlation, and any attempt to include static correlation inevitably includes some portion of the dynamical correlation as well. Indeed, increasingly larger active spaces (in other words, larger numbers of active orbitals) will include increasing amounts of dynamical correlation as a full CI including all orbitals is approached.

2.3.2. Complete Active Space Second-Order Perturbation (CASPT2) Theory. In the CASPT2 approach, dynamical correlation is accounted for after an initial CASSCF step by using perturbation theory. The second-order energy is determined in a manner similar to that used in the MP2 method.⁷⁵ However, while for $\text{MP}n$ approaches based on HF theory the choice of a zeroth-order Hamiltonian is obvious, various options are available following a CASSCF calculation. As a result, some variations in multireference second-order perturbation theory exist in the literature. CASPT2 refers to a particular choice of zeroth-order CASSCF Hamiltonian, and it

is generally very accurate when combined with an adequate and well-chosen set of active orbitals as well as one-electron basis sets. For MOFs, CASSCF and CASPT2 calculations have typically been used primarily for computing accurate gas adsorption energies and in developing first-principle force fields.

2.4. Density Functional Theory (DFT)

DFT is based on two theorems from Hohenberg and Kohn, which we shall summarize here without the complication of using true mathematical rigor. In fact, our whole discussion of DFT will gloss over the mathematical subtleties. The first of the Hohenberg–Kohn theorems shows that there is a one-to-one (in other words, a unique) correspondence between the electron density, $\rho(r)$, and the external potential, $v(r)$, in which the electrons move. In the absence of any applied electromagnetic field, the external potential is simply that due to the nuclei. The density therefore uniquely determines the ground-state wave function and vice versa, and therefore, there is a universal functional of the density that gives the total energy. The second Hohenberg–Kohn theorem states that, given the exact universal density functional (i.e., the functional that takes the electron density as its argument and predicts the energy therefrom), the ground-state energy can be obtained variationally, eq 2.13

$$E_{v(r)}[\rho(r)] \geq E_{v(r)}[\rho_0(r)] = E_0 \quad (2.13)$$

where $\rho_0(r)$ is the exact density and E_0 is the exact energy.⁷⁶

However, the universal density functional is not known, and most modern DFT calculations are carried out within the formalism proposed by Kohn and Sham (KS).⁷⁷ The KS approach posits a system of noninteracting electrons having exactly the same density as the real system of interacting electrons. The wave function of the noninteracting system is a Slater determinant, and the kinetic energy of the electrons is computed from this Slater determinant. Then the orbitals of the Slater determinant can be determined by solving a set of eigenvalue equations similar to the Hartree–Fock equations. These equations are called the Kohn–Sham equations, the operator analogous to the Fock operator is called the Kohn–Sham operator, and the equations must be solved self-consistently. The Kohn–Sham operator contains an effective potential, $v_{\text{eff}}(r)$, that has three terms: the external potential v (which is usually simply the potential of the nuclei, although it can be more general), the classical Coulomb potential $\int ((\rho(r'))/(r-r))dr$ of the electron density (often called the Hartree potential), and a term called the exchange-correlation potential, $V_{\text{xc}}(r)$, thus

$$V_{\text{eff}}(r) = V_{\text{ext}}(r) + \int \frac{\rho(r')}{r-r'} dr + V_{\text{xc}}(r) \quad (2.14)$$

The energy of the KS system can then be written as

$$E_{\text{KS}}[\rho(r)] = \sum_i^N \varepsilon_i - \int \frac{\rho(r)\rho(r')}{r-r'} dr dr' + E_{\text{xc}}[\rho(r)] - \int V_{\text{xc}}(r)\rho(r) dr \quad (2.15)$$

where $V_{\text{xc}}(r)$ is a functional derivative of the exchange-correlation functional E_{xc} , i.e., $V_{\text{xc}}(r) = ((\delta E_{\text{xc}}[\rho(r)])/(\delta \rho(r)))$. The exchange-correlation functional, E_{xc} , is formally given by eq 2.16

$$E_{\text{xc}}[\rho(r)] = T[\rho(r)] - T_{\text{s}}[\rho(r)] + V_{\text{ee}}[\rho(r)] - J[\rho(r)] \quad (2.16)$$

In eq 2.16, $V_{\text{ee}}[\rho(r)]$ is the exact electron–electron interaction energy (which could be computed if we knew the exact wave function) and $J[\rho(r)]$ is the classical Coulomb energy (which is trivially computed). Notice that eq 2.16 contains the many-body effects on the electron kinetic energies (the difference in the kinetic energies of a system of interacting electrons and noninteracting KS electrons, $T[\rho(r)] - T_{\text{s}}[\rho(r)]$), as well as the difference between the quantum mechanical electron–electron interaction and the classical Coulomb interaction.

If the exact exchange–correlation term were used, the energy predicted from a DFT calculation would be exact. However, as it is not known, various approximations to the energy functional, $E_{\text{xc}}[\rho(r)]$, have been developed, and their varying strengths and weaknesses are the subject of many benchmarking studies in the literature.⁷⁸ These approximations are usually called density functionals, even though a more accurate name would be approximate density functionals or even more fully, approximate exchange–correlation functionals.

Depending on the particular property or properties of interest, periodic computations of the properties of a MOF can be carried out on the (frozen) experimentally determined crystal structure or on an optimized structure. KS-DFT theory is particularly advantageous for studying large molecular and periodic systems (e.g., MOFs) as well as systems containing heavy elements, because the computational cost for solving the KS equations is low compared to WFT methods, and the cost of DFT computations goes up (“scales”) much more slowly as the system size increases.^{64b} We do note that specially designed computational algorithms can reduce the scaling for both WFT and DFT methods to linear in system size for large enough systems, but often the systems of interest are not large enough to warrant using such algorithms, which can be slower than conventional algorithms for small- and moderate-sized systems and even many large systems.

For open-shell systems, one usually works with the spin-up and spin-down densities (which we call spin densities and label as ρ_{α} and ρ_{β}) rather than just their sum (ρ), which is the total density. When ρ_{α} does not equal ρ_{β} , a system is said to be spin polarized. A fully satisfactory treatment of spin-polarized systems requires a relativistic treatment,⁷⁹ but most practical work simply makes the exchange–correlation functional a functional of both ρ_{α} and ρ_{β} .

It is worth stressing here the formal nature of the results of Hohenberg and Kohn. They prove the existence of an exact, unique density functional, but they do not give a prescription for how to find that functional. To make progress, one often approximates the density functional using not only explicit functions of the density (or spin densities) but also functions of the gradients of the density (or spin densities), which are functions of the density or spin densities and also by using functions of the KS spin–orbitals, which are functionals of the density or spin densities. The functions of the orbitals can be nonlocal, that is, the energy density at a point in space can depend on more than just quantities evaluated at that point in space. Nonlocal exchange–correlation functionals are sometimes called hybrid, and local functionals are sometimes called pure. These are however poorly chosen descriptors as it is easily shown that the unknown exact functional is nonlocal.

2.4.1. Exchange–Correlation Functionals. The exchange–correlation energy functional is often decomposed into an

exchange functional, $E_{\text{x}}[\rho(r)]$, and a correlation functional, $E_{\text{c}}[\rho(r)]$, although this decomposition is not unique⁸⁰

$$E_{\text{xc}}[\rho(r)] = E_{\text{x}}[\rho(r)] + E_{\text{c}}[\rho(r)] \quad (2.17)$$

The earliest approximation of the exchange–correlation functional is called the local density approximation (LDA). It was based on the fictitious system of a uniform electron gas (UEG, a system with an infinite number of electrons and uniform density balanced by a corresponding positive background charge). For the UEG, the exchange energy can be determined as a relatively simple analytical functional of the electron density. In most modern computational chemistry packages, the correlation part of $E_{\text{xc}}[\rho(r)]$ is based on either the simulation work of Ceperley and Alder⁸¹ or modern modifications such as that of Vosko, Wilk, and Nusair.⁸² Its dependence on the density of a UEG means that LDA might be suitable for solid-state systems where the electron density varies only slowly. However, for molecular systems, LDA often overestimates bonding energies and underestimates bond lengths.^{64b} There have been reports in which LDA was used in calculating the vibrational frequencies of MOFs^{21a,83} and guest molecules in MOFs.⁸⁴ These will be discussed in later sections of this review.

A KS-DFT calculation with different orbitals for different spins is called a spin-polarized calculation or an unrestricted KS (UKS) calculation. Exchange–correlation functionals must be generalized to depend separately on spin-up and spin-down densities to be used in such calculations. When the LDA is generalized in this way, it is called the local spin-density approximation (LSDA). An LDA functional is a special case of an LSDA functional.

2.4.2. Gradient Approximation Functionals. Gradient approximations are functionals in which the exchange–correlation energy functional is derived as a functional not only of the local spin densities but also of the magnitudes of the spin-density gradient, $|\nabla\rho|$, as shown in eq 2.18

$$E_{\text{xc}}^{\text{GGA}}[\rho(r)] = \int \rho(r) E_{\text{xc}}^{\text{GGA}}(\rho, |\nabla\rho|) \text{d}r \quad (2.18)$$

There are two main categories of gradient approximations. Generalized gradient approximations (GGAs) are functionals in which one attempts to separately approximate exchange and correlation by imposing a factorizable functional form on the exchange that derives from a uniform scaling property of the exact exchange–correlation functional. GGA functionals have been widely used for studying molecular systems as they provide a better description than LSDA in regions where there are significant local variations in the electron density. They remain computationally cheaper than WFT methods and cheaper than some functionals found at higher levels of the so-called Jacob’s ladder of functionals⁸⁵ (in which functionals are organized by their ingredient lists), and they provide substantial improvements over LSDA for calculated ionization and atomization energies.^{64b} Their computational scalability (as a result of modern linear scaling approaches) and accuracy make them particularly suited for studying extended systems like MOFs. Many GGA functionals have been used in studying MOFs. Examples of the more popular choices are PBE,⁸⁶ revPBE,⁸⁷ PBEsol,⁸⁸ PW91,⁸⁹ BLYP,⁹⁰ OLYP,^{90b,91} and BP86.^{90a,92}

In nonseparable gradient approximations (NGAs), one does not attempt to separate exchange and correlation. An example of an NGA is the N12 functional, developed by one of us, which provides good accuracies for solid-state cohesive energies

and lattice constants on one hand and molecular atomization energies and bond lengths on the other.⁹³ These two sets of properties have generally been considered to be incompatible given the single set of parameters provided in conventional GGAs (see additional references in ref 93).

2.4.3. Meta-Gradient Approximation Functionals. In meta-GGA and meta-NGA functionals, gradient approximation functionals are augmented with a dependence on the Laplacian of the density, $\nabla^2\rho$, and/or the noninteracting kinetic energy, τ , eq 2.19

$$E_{\text{xc}}^{\text{GGA}}[\rho(r)] = \int \rho(r) E_{\text{xc}}^{\text{LDA}}(\rho, \nabla\rho, \nabla^2\rho, \tau) dr \quad (2.19)$$

Two examples of meta-GGA functionals that have been used for studying MOFs are the TPSS functional of Tao, Perdew, Staroverov, and Scuseria,⁹⁴ the Minnesota M06-L⁹⁵ functional and the Minnesota M11-L functional.⁹⁶ As will be discussed in later sections of this review, the M06-L functional performs quite well for predicting the structures of MOFs as well as the binding energies of physisorbed guest molecules and has been recommended for transition metals as well as inorganic and organometallic systems.⁹⁷

2.4.4. Hybrid Functionals. Local density approximations, gradient approximations, and meta-gradient approximations are all local, which means that the exchange-correlation density at a given point depends only on local properties at that point. A hybrid functional is derived through the combination of a local functional with a portion of the HF exchange; the latter is included in place of that derived only from the local exchange functional. HF exchange is a nonlocal functional of occupied orbitals, and inclusion of this nonlocal contribution to the energy often leads to improved predictions of reaction energies, reaction barriers, and redox energies of molecular systems.^{64b} Functionals including a portion of nonlocal exchange are called hybrid functionals. Examples of hybrid functionals that have been used in studying MOFs are B3LYP,^{90b,98} B3PW91,^{89,98} PBE0,⁹⁹ BHLYP,^{90b,100} X3LYP,¹⁰¹ M06,¹⁰² M06-2X,¹⁰² M06-HF,¹⁰³ and TPSSH.⁹⁴ B3LYP has been one of most widely used functionals to date. It combines 20% HF exchange with the B88 exchange and LYP correlation functionals according to

$$E_{\text{xc}} = (1 - a)(E_{\text{xc}}^{\text{LDA}}) + a(E_{\text{x}}^{\text{HF}}) + b(E_{\text{x}}^{\text{B88}}) + c(E_{\text{c}}^{\text{LYP}}) + (1 - c)(E_{\text{c}}^{\text{VWN}}) \quad (2.20)$$

In eq 2.20, the empirical parameters are $a = 0.20$, $b = 0.72$, and $c = 0.81$. The amounts of HF exchange in PBE0 and BHLYP are 25% and 50%, respectively. The M06, M06-2X, and M06-HF functionals are parametrized hybrid functionals that contain 27%, 54%, and 100% HF exchange, respectively.

2.4.5. DFT+U Approaches. Calculations with most density functionals suffer from the so-called self-interaction error (SIE), which arises from the interaction of a single electron with its own density in the classical Coulomb approximation. We note that although SIE is most clearly manifested by this single-electron self-interaction, it also has a many-electron component, which will not be discussed here.¹⁰⁴ Two practical consequences of the approximate exchange-correlation functionals of the LSDA and GGAs not canceling out the self-interaction present in the classical Coulomb term found in eq 2.15 are, first, a tendency of LSDA and GGA functionals to overdelocalize valence electrons and, second, a tendency to overstabilize metallic-like states.

Meta-gradient functionals can eliminate some SIE if the functional form is well chosen and hybrid functionals more directly eliminate a portion of the SIE (indeed, all of it, if 100% of the HF exchange is included), but they (especially the hybrid functionals) raise the computational costs for extended systems. A less expensive (and correspondingly less reliable) method that has been applied to MOFs for correcting some of these deficiencies is called DFT+U¹⁰⁵ (this includes LSDA+U and GGA+U). In the DFT+U approach, electrons in selected orbitals (e.g., localized valence d and f orbitals in transition metals and actinide systems, respectively, and sometimes p orbitals on oxygen atoms) are described with the Hubbard model¹⁰⁶ (to enforce localization of specific valence states), $E_{\text{Hub}}[(n_{mm}^{\text{I}\sigma})]$, while all other valence electrons are treated at the LSDA or GGA level leading, in one version, to the energy expression

$$E_{\text{LSDA/GGA+U}} = E_{\text{LSDA/GGA}} + E_{\text{Hub}}[(n_m^{\text{I}\sigma})] - E_{\text{dc}}[(n^{\text{I}\sigma})] \quad (2.21)$$

where $(n_m^{\text{I}\sigma})$ denotes the set of all orbital occupancies of orbitals that are corrected for self-interaction (n being the number of electrons in the orbital of angular momentum l and spin σ on atom I with orbital angular momentum projection quantum number m), and $(n^{\text{I}\sigma})$ being the set of all subshell occupancies (obtained by summing over m .) Note that the corresponding energy E_{Hub} is adjusted for double counting with the term E_{Hub} , which treats the self-interaction-corrected electrons interacting with a mean field. In most implementations of the DFT+U method, it is only necessary to give the effective Coulomb energy, $U-J$, where U and J are, respectively, the spherically averaged screened Coulomb and exchange energy used in defining the Hubbard model of correlated electrons (and $U-J$ is then usually relabeled as U). The +U correction may be considered as a way to include effects that could also be included by Hartree–Fock exchange^{107,108} but at a much lower cost, but also with the disadvantage that the empirical U parameter must be determined for each case.

The DFT+U approach has particular advantages from a computational standpoint. First, it is not very demanding of resources (about the same order as LDA and GGA calculations), and so it can be used to screen libraries of synthesized or potential MOFs. Second, implementations of the DFT+U approach are widely available in commercial and freely distributed software. In addition, first and second derivatives of the Hubbard-corrected energies can be easily implemented and computed, which permits facile computation of optimized geometries and vibrational frequencies. One significant disadvantage of the DFT+U approach is the degree to which the $U-J$ term in the Hubbard model varies with material. The U , J , and $U-J$ values of the correlated electrons for each atom type can be chosen based on comparison of some calculated reaction energies to experimental data¹⁰⁹ or to unrestricted Hartree–Fock or CI calculations on model systems.¹⁰⁷ However, the parameters can be quite sensitive to the environment (or even the state), so that a proper choice of model system (which is generally simpler than the target system) is not always trivial. This becomes a more particular concern when effective $U-J$ values cannot be determined from empirical data. For this reason, the DFT+U method has little predictive value for new systems where data on which to base the choice of the empirical, $U-J$, parameters are unavailable.

In general, DFT+U approaches are specified by adding the “+U” keyword to the name of the standard functional. For

example, one can perform calculations at the LDA+U, PBE+U, or vdW-DF2+U level by using the Hubbard model to correct for the SIE of correlated electrons at the LDA, PBE, or vdW-DF2 levels, respectively (the vdW-DF2 functional is described further below).

2.4.6. Screened Exchange Functionals. The HF exchange in hybrid functionals makes them more computationally demanding than local functionals. This is because the nonlocality of exact HF exchange requires the computation of Coulomb integrals even at very long range. However, it is well known that polarization-correlation effects screen interactions between distant electrons (as in the Debye–Hückel theory of electrolytic solutions). For this reason, Heyd, Scuseria, and Ernzerhof proposed a new functional, called HSE,¹¹⁰ that applies a modified Coulomb potential to the exchange so as to screen the long-range portion of the HF exchange

$$E_{\text{xc}}^{\text{HSE}} = a(E_{\text{x}}^{\text{HF,SR}}) + (1 - a)(E_{\text{x}}^{\text{PBE,SR}}) + (E_{\text{x}}^{\text{PBE,LR}}) + (E_{\text{c}}^{\text{PBE}}) \quad (2.22)$$

In this equation, $a = 0.25$, just as in the global hybrid PBE0 functional. The short-range (SR) and long-range (LR) portions of the Coulomb operator are split through the use of the error function according to

$$\frac{1}{r} = \frac{\text{erfc}(\omega r)}{r} + \frac{\text{erf}(\omega r)}{r} \quad (2.23)$$

In eq 2.23, the complementary error function is defined by $\text{erfc}(\omega r) = 1 - \text{erf}(\omega r)$ and ω is used to adjust the relative proportions of the long-range and short-range terms as a function of distance. In the original HSE functional, which is also called HSE03, $\omega = 0.106$ or 0.189 a_0^{-1} , depending on the term. However, in a later work, a single value, $\omega = 0.11 \text{ a}_0^{-1}$, was optimized.¹¹¹ The reoptimized functional is called HSE06. Most workers now use HSE06, which is the recommended version, although it is sometimes called HSE and sometimes called HSE06. To the extent that it is defined to be independent of material, it is more applicable than DFT+U. Calculations with HSE or HSE06 are more expensive than those with the LSDA and GGAs, with or without +U. Depending on the system size and software choice (as well as the choice of the fast Fourier transform grids for the exact exchange routines and the degree of parallelization over bands and k points), the cost of calculations with HSE may be higher than for GGAs by up to 2 orders of magnitude.

2.4.7. Dispersion-Corrected Functionals. It has been recognized for some time that early generation density functionals fail to describe medium- to long-range correlation effects correctly.¹¹² In the literature, such effects are often referred to all together as “dispersion”, although a more proper use of this term would be restricted to the longest range effects where the overlap of two subsystems can be neglected. For systems with no permanent charge, dipole moment, or quadrupole moment, the long-range potential in the non-overlap region varies asymptotically as r^{-6} , where r is the distance between the subsystems. Overlap cannot be neglected near van der Waals minima, where repulsion due to the overlap of the electronic clouds of the two systems is comparable in magnitude to attraction; this repulsion is usually called exchange repulsion. The continuation of the physical effect (instantaneous alignment of mutually induced dipole moments on the two subsystems) responsible for dispersion into closer distances of approach where exchange repulsion is not

negligible is sometimes called dispersion, but that label should strictly be reserved to the nonoverlap region. We will call this effect damped dispersion; it is an example of an attractive noncovalent interaction. Just as dispersion is a consequence of long-range electron correlation, damped dispersion is a consequence of medium-range electron correlation.

Failure to include damped-dispersion effects can have a significant impact since weak noncovalent interactions can be important in many chemical and biological phenomena including adsorption and molecular recognition.¹¹³ The extended structures of MOFs contain many organic linkers that are usually aromatic. Aromatic–aromatic interactions between these linkers and the physical adsorption processes between metal and organic sites in the framework and guest gas molecules all would be expected to include significant contributions from damped dispersion. It is critical that electronic structure calculations on MOFs are carried out with methods that can adequately describe damped-dispersion interactions when such nonbonded interactions play key roles in the chemistry under study.

There have been a number of attempts to develop DFT methods that accurately describe dispersion or damped-dispersion interactions.¹¹⁴ The three approaches that have been used in electronic structure calculations on MOFs are described in succeeding paragraphs.

- (1) The most fundamental approach to including dispersion in KS theory is to add a nonlocal term to the correlation functional. For example, in the vdW-DF¹¹⁵ methods, a nonlocal dispersion term, E_{c}^{nl} , is explicitly included in the density functional

$$E_{\text{xc}} = E_{\text{x}}^{\text{GGA}} + E_{\text{c}}^{\text{LDA}} - E_{\text{c}}^{\text{nl}} \quad (2.24)$$

The vdW-DF2¹¹⁶ and optPBE¹¹⁷ are two examples of density functionals that adopt this approach. As will be discussed later in this review, the vdW-DF and vdW-DF2 functionals have been used in computing the equilibrium lattice properties of MOFs, the adsorption energies of gases in MOFs, and the shifts in the vibrational frequencies of gas molecules upon adsorption in MOFs. In some cases, the nonlocal correlation term is based on virtual orbitals (a virtual orbital is another name for an unoccupied orbital). Methods including both nonlocal exchange based on occupied orbitals and nonlocal correlation functionals based on unoccupied orbitals have been called doubly hybrid functionals.¹¹⁸

- (2) Another approach to including dispersion is to develop local functionals that account semiquantitatively for medium-range correlation energy. Such functionals can model damped dispersion near van der Waals minima, but local functionals cannot predict true dispersion (in other words, dispersion in the overlap-free long-range regions). Examples of functionals designed to treat medium-range correlation are the Minnesota series of M06-type and M11-type functionals. The M06-2X version gives good results for the S22 set and for stacked aromatic systems, for example.¹¹⁹
- (3) The final way to include dispersion is to add atom-pair terms to estimate the corrections to an exchange-correlation functional due to its inadequate treatment of medium-range correlation energy, similar to the way this interaction is computed in molecular mechanics.¹¹⁴ The so-called DFT-D functionals are based on this

approach. As these DFT-D functionals are designed to be used for van der Waals distances (rather than the long-range overlap-free regions that are less important for chemistry), the parameters of such corrections depend on the functional to which they are appended since different functionals make different errors in the medium-range correlation energy. The most widely used approach involves combining sets of atom-pair terms (D1,¹²⁰ D2,¹²¹ or D3¹²²) provided by Grimme et al. with standard density functionals. For example, in the PBE-D2 approach, atom pairs are obtained from the D2 scheme and used to correct electronic energies obtained with the standard PBE functional. The D3 model is not purely pairwise additive because the parameters depend on coordination numbers; the D3 model exists in two versions called D3(0) and D3(BJ).¹²³ DFT-D methods have been widely applied for studying MOFs, but their ability to model dispersion interactions as a function of the charge or oxidation state of a metal ion is questionable.

2.4.8. Multiconfiguration Pair-Density Functional Theory. Although KS theory would be exact for all systems if one knew and used the exact (but probably unknowable) exchange-correlation function, with available approximate density functionals, it often shows larger errors for systems (such as many systems containing transition metals) whose wave function description is inherently multiconfigurational. Such systems are often called strongly correlated or multi-reference systems.

Attempts to combine the CASSCF method with DFT to obtain a method that treats multireference systems run into the difficulty that standard correlation functions are designed to include all the correlation energy. However, as there is no precise distinction between static and dynamical correlation, any attempt to include static correlation via CASSCF inevitably includes some portion of the dynamical correlation as well, and increasingly larger numbers of active orbitals will include increasing amounts of dynamical correlation, leading to a double-counting problem. Interestingly, some of us recently proposed and are working on a consistent way to combine these two theories (CASSCF and DFT) without overcounting dynamical correlation.¹²⁴ This method is called multiconfiguration pair-density functional theory (MC-PDFT), and we expect it will be useful for MOFs in the future. Even still, this approach might be inaccessible for systems in which a reasonable and chemically accurate active space size is beyond the capacities for current computational technology. In these cases, there is hope that a generalized active space (GAS)¹²⁵ or restricted active space¹²⁶ or SplitGAS¹²⁷ wave function could be used to partition the total active space, such that noncontributing CSFs ("deadwood" as famously termed by Ruedenberg and co-workers¹²⁸) can be removed. This, in some cases, can drastically reduce the number of CSFs in the configuration interaction performed on the active space, making MC-PDFT calculations much more amenable for studying large molecular systems.

2.5. Time-Dependent Density Functional Theory (TDDFT)

For MOFs with optical, luminescence, and sensing applications, it is often important to determine the natures and energies of their adsorption or emission processes. In most cases, this is done with TDDFT, an extension of static or ground-state DFT to treat the time-dependent or dynamical properties of many-body systems. The time-dependent properties of interest in

most investigations on MOFs are the optical gap as well as the absorption and emission spectra. A monograph¹²⁹ and many review articles¹³⁰ cover in detail the underlying principles, benchmarks,¹³¹ applications, and performance of TDDFT. Although TDDFT is formally exact, the accuracy of linear-response TDDFT within the adiabatic approximation generally depends strongly on the choice of density functionals. Many standard functionals, in particular, do not describe accurately long-range charge-transfer¹³² (CT) excitations and excitations to Rydberg¹³³ states, since the non-Coulomb part of their exchange potentials decays too rapidly and becomes inaccurate at long distances. Generally, this fast decay is exponential in contrast to the slow asymptotic $1/r$ decay of the true universal potential, and this contributes to the SIE in local exchange functionals. This leads to significant underestimations of the excitation energies to Rydberg and CT states, i.e., they are predicted to be red shifted relative to experiment, although a detailed examination of the problem shows that the origin of the problem is not precisely the same for Rydberg states and charge-transfer states. Such underestimation errors are reduced by adding a portion of exact exchange in the functional, i.e., by using hybrid functionals.⁹⁹ Substantial work has focused on the development of highly tuned functionals with full exact exchange (completely removing the SIE),^{103a} asymptotically corrected model potentials,¹³⁴ long-range-corrected (LC) functionals,¹³⁵ as well as local hybrid¹³⁶ functionals. The LC-BLYP¹³⁷ and CAM-B3LYP¹³⁸ functionals have been widely used in studies of the absorption and emission properties of MOFs.¹³⁹

2.6. Inclusion of Spin–Orbit Coupling Effects

Spin–orbit interactions derive from the magnetic interaction between the magnetic field due to orbital angular momentum, μ_l , and the magnetic spin angular momentum, μ_s , of an electron. Spin–orbit coupling separates the energies of one-electron energy levels that would be degenerate in the absence of electron spin angular momentum.¹⁴⁰ Splittings of formally degenerate levels in transition-metal d-orbital manifolds by crystal field effects can generally be expected to be larger than those from spin–orbit coupling effects, so for MOFs, the strongest motivation for examining spin–orbit coupling effects has derived from an interest in understanding specific magnetic properties.^{43f} To treat spin–orbit coupling effects, one typically computes the interacting states at the DFT, CASSCF, or CASPT2 level without including spin–orbit coupling.¹⁴¹ These states are then used as a basis for the solution of configuration interaction equations involving a Hamiltonian including spin–orbit coupling, a so-called spin–orbit state-interaction (SO-SI) calculation.

2.7. Performing Electronic Structure Calculations on MOFs

As previously noted, MOFs are crystalline systems. As such, they possess a repeating unit (unit cell) composed of tens to hundreds of atoms, sometimes belonging to space groups exhibiting a high degree of symmetry. Electronic structure calculations on MOFs can therefore be carried out in three ways: (i) on the unit cell by exploiting periodic boundary conditions (PBC) to model an infinite solid, (ii) by constructing smaller (super)molecular clusters that are sufficiently large for a region of central interest to behave as though it were embedded in the bulk solid, or (iii) by combined quantum mechanical and molecular mechanical (QM/MM) methods.¹⁴²

2.7.1. Molecular Cluster Calculations. As mentioned above, sometimes one approximates the MOF by a subnanomolecular cluster or even a nanoscale cluster. For simplicity, we shall refer to this class of model as a molecular cluster model. The physical justification of using cluster models when studying MOFs is that the phenomena of interest (catalysis, gas separation, etc.) are usually localized. Truncation of the extended solid-state MOF into a molecular cluster significantly reduces the computational costs and potentially allows for the use of, for example, post-HF wave function methods. This truncation can, however, introduce unphysical edge effects and spatial anisotropy in the model clusters, and if the cluster model is too small, one may miss non-negligible dispersion interactions in some cases, so truncated models must be constructed with special attention to such details. In Figures 5 and 6, we show two examples in which researchers

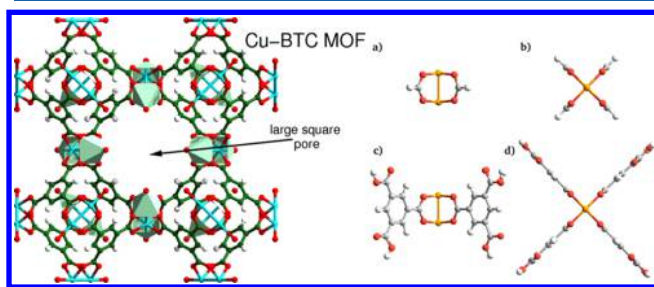


Figure 5. (Left) Side view of the periodic structure of Cu-BTC. (Right) To accelerate DFT calculations, the extended system was truncated into (top, a) side view and (top, b) top view $\text{Cu}_2(\text{HCOO})_4$ or (bottom, c) side view and (bottom, d) top view $\text{Cu}_2(\text{BTC})_4$ systems. The overall charges of the model clusters were made to be equal to that of the periodic unit cell by protonation as required. Reprinted with permission from ref 143. Copyright 2013 American Chemical Society.

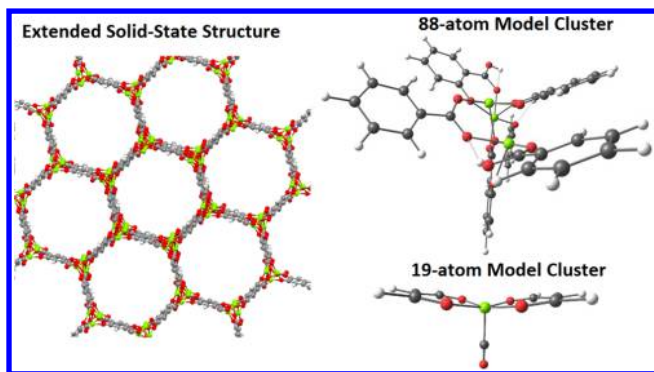


Figure 6. (Left) Extended structure of Fe-MOF-74. (Right) Two model clusters obtained from the periodic structure and designed to imitate bulk conditions for the central Fe atoms. The 19-atom model cluster was sufficiently small to allow for expensive LPNO-CCSD/CBS calculations. Fe, O, C, and H atoms are represented as green, red, gray, and white spheres, respectively.

constructed molecular clusters of increasing size for studying the interaction of gas molecules with MOFs. First, Supronowicz et al. studied the interactions of small gases (CO , CO_2 , NO , and SO_2 among others) with Cu-BTC.¹⁴³ Cu-BTC contains a binuclear copper (Cu) paddle-wheel unit that is connected to four BTC (benzene tricarboxylate ligands). To simplify and speed up their DFT computations, they constructed two molecular clusters of different sizes. The simplest of these is a

dicopper tetraformate, $(\text{Cu}_2(\text{HCOO})_4)$, Figure 5. This model captures the bimetallic nature of the paddle wheel but assumes that the four BTC ligands can be truncated into formate ions. Because small gas molecules might interact not only with the Cu sites but also with portions of the organic ligand, they also performed calculations on the model dicopper tetrabenzenetricarboxylate, $\text{Cu}_2(\text{BTC})_4$. It is however important to note that the original clusters cut from the periodic crystalline structure are highly charged. This is different from the overall zero charge of the unit cell of Cu-BTC. In nearly all molecular cluster calculations, otherwise charged clusters have to be protonated or deprotonated to ensure that they reach charge neutrality, as in the MOF's unit cell, with the size of the cluster being chosen to minimize the chemical impacts of such local charge adjustments.

In their study of N_2/CH_4 separation on V/Fe-MOF-74, Lee et al.¹¹⁶ also constructed two types of clusters centered on the metal sites, Figure 6. One model is a large cluster containing 88 atoms, of which 3 are metal sites reflecting the local structure of the MOF-74 framework but only the central metal atom was the focus of study for the analysis of interaction energies. The smaller cluster model contained 19 atoms and only a single metal center. Lee et al.¹¹⁶ performed DFT calculations (vdW-DF2+U, M06-L, M06, and M11-L^{96b}) as well as CASPT2 calculations on the 88-atom cluster model, Figure 6. However, it was practical to carry out calculations at the LPNO-CCSD level at the complete basis set (CBS) limit only on the 19-atom cluster model. We note that while we selected the construction of molecular clusters by Supronowicz et al.¹⁴³ and Lee et al.¹¹⁶ as illustrative examples, many electronic structure calculations on MOFs are carried out at the cluster model level,¹⁴⁴ and additional examples will be discussed in the main portion of the review.

A significant advantage of cluster models is that many levels of electronic structure theory are widely available for molecular cluster calculations but not for calculations employing periodic boundary conditions (PBC).

2.7.2. Periodic DFT and DFT+U Calculations. DFT and DFT+U calculations on the unit cell (or sometimes supercells) of MOFs, undertaken employing PBC, are becoming increasingly common. They are generally referred to as periodic DFT calculations. The necessary computational machinery for periodic DFT and DFT+U calculations has been implemented in several software packages. Usually these calculations are carried out with plane wave (PW) basis sets.¹⁴⁵ This is advantageous as the use of PW basis sets makes it simple to evaluate forces, stresses, and force constants, a situation that allows for the optimization of the atomic positions in the unit cell as well as the shape and volume of the unit cell. The construction of PW basis sets also permits fast Fourier transform techniques to speed solution of the electronic structure equations and also ensures completeness and orthonormality. As such there are no issues with basis set superposition errors (BSSE) or linear dependencies.

We note that PWs can be designed either to treat all electrons or to be used in conjunction with atomic pseudopotentials that replace the core electrons. All-electron calculations are extremely demanding because the core orbitals vary rapidly and therefore require high frequencies in the plane wave basis. The pseudopotential approach simplifies the description of atoms by constructing pseudoatoms in which a subset of typically valence electrons (usually only valence electrons or valence electrons and outer core electrons) is

involved in self-consistent calculations and the remaining electrons are replaced with pseudopotentials mimicking their influence on the overall electronic structure.¹⁴⁶ This simplification results in significant savings in computational costs and is grounded in the fact that most physical and chemical properties are defined by the properties of electrons in valence orbitals. In ultrasoft pseudopotentials (USPs),¹⁴⁷ the norm-conservation condition of norm-conserving pseudopotentials¹⁴⁸ is violated and localized atom-centered augmentation charges are used to correct for the deficit created by removing the charge associated with the extension of pseudopotential orbitals into the defined core radius. With pseudopotentials, the cutoff energy or basis set size can be reduced dramatically, leading to faster calculations. Many PW periodic DFT calculations on MOFs have used the pseudopotential approach. However, as the quality of PW basis sets is uniform at every point in space, a very large number of basis functions are needed to properly describe extended but sparsely packed systems (like MOFs and zeolites) in which the density is both nonuniform and strongly dependent on the local chemical environment.

A more accurate approach than pseudopotentials is the projector-augmented wave (PAW) method.¹⁴⁹ The PAW method combines ideas from USPs with the ideas from the linearly augmented plane wave method to achieve higher accuracy in a more convenient framework.¹⁴⁶ Kresse et al.¹⁴⁶ and Holzwarth et al.¹⁵⁰ described the formalism of the PAW plane wave method and reviewed its performance in comparison to other pseudopotential methods. Another approach to the accurate treatment of core electrons is the Gaussian and augmented-plane-wave density functional method in which the electron density close to the nuclei is expanded in Gaussian functions and the smoother density farther from the nuclei is expanded in plane waves.¹⁵¹

Periodic DFT calculations can also be carried out with traditional Gaussian basis functions¹⁵² or a combination of Slater-type orbitals and numerical basis functions.¹⁵³ Such calculations are usually slower than those with PW pseudopotential basis sets but permit many of the analysis tools employed for molecular calculations to be applied in the same fashion to periodic calculations. Another option is to use orbitals defined on real-space grids, an approach particularly well suited for parallelization.¹⁵⁴

One of the more recent developments in the computational study of MOFs is the use of *ab initio* molecular dynamics (AIMD)¹⁵⁵ approaches within the periodic DFT formalism to study the framework dynamics in flexible MOFs.¹⁵⁶ This method has also been used to generate trajectories for MOF systems over 1–50 ps time scales.¹⁵⁷ One can then obtain an average value for physical properties computed for each trajectory. Examples of such properties are core-edge X-ray absorption spectra,¹⁵⁷ extended X-ray absorption fine structure spectra,¹⁵⁸ dipole moments,¹⁵⁹ and interatomic distances.¹⁶⁰ Dynamically averaged values (as well their distribution) are more reflective of experimental values measured at equivalent temperatures and can sample not only the dynamic motions of the atoms in the MOF but also those of guest molecules when of interest. It is important, of course, that simulated trajectories truly sample a statistical ensemble that correlates to experimental conditions. In AIMD simulations, rather than use predefined analytical potentials as employed in classical MD, the forces are computed on the fly as the trajectories are generated.¹⁵⁵ However, the cost of treating the electronic

degrees of freedom makes AIMD simulations significantly more expensive than classical MD simulations. AIMD has also been combined with free energy approaches to compute the free energy barriers and pathways of reactions (including diffusion or acid/base speciation) in other nanoporous materials.¹⁶¹

2.7.3. Combined Quantum Mechanical and Molecular Mechanical (QM/MM) Methods. In QM/MM methods, the active subsystem is treated by quantum mechanical electronic structure methods and the rest of the system is treated by MM. In principle, this allows the use of larger models than the subnanomodels mentioned above. An example of an application to MOFs is the work of Yadnum et al.¹⁶² in which they compare Cu–ZSM-5 zeolites and Cu–MOF-505 for catalysis of the Mukaiyama aldol¹⁶³ reaction.

3. PROPERTIES OF METAL–ORGANIC FRAMEWORKS

A goal of computational methods is to predict accurately both the intrinsic properties of MOFs in the absence of adsorbates as well as their functional properties such as gas adsorption capacity, isosteric heats of gas adsorption, gas separation, gas diffusion, Brunauer–Emmett–Teller (BET) surface area, and catalytic properties. There are many reports in which electronic structure methods have been used to predict or complement available experimental data about the intrinsic properties of various MOFs. A few recent examples are listed in refs 30b and 164. Herein, we first review reports on two MOFs that have been studied extensively over the past few years: MOF-5 and MOF-74. We then review several studies of the properties of MOFs with flexible frameworks.

3.1. Structural, Mechanical, and Electronic Properties of MOFs

For most MOFs, the available experimental structural data is limited to a powder structure, which may be inaccurate and can contain solvent molecules. The reader is referred to refs 165 and 166, where researchers attempted to clean up problematic structures. Electronic structure calculations can play an important role with regard to obtaining accurate structural parameters as well as mechanical properties.

Periodic DFT calculations are best suited for determining the structural and mechanical properties of a MOF unit cell. A typical calculation involves optimization of the atomic positions and of the equilibrium lattice constants of the unit cell. After optimization of the atomic positions and lattice constants of a MOF, the mechanical and electronic properties can be obtained. An understanding of the mechanical properties of MOFs is essential as they are often pressurized into more compact forms during usage and also sometimes subjected to hydrostatic compressions when used in high-pressure gas storage applications. Some of the mechanical properties of MOFs that have been investigated with electronic structure calculations are bulk modulus, Young's modulus, and shear modulus. The bulk modulus, K , of a substance describes its resistance to uniform compression. It is described by the equation shown in eq 3.1

$$K = \rho \frac{dP}{d\rho} \quad (3.1)$$

In eq 3.1, ρ is the density and P is the pressure. The higher the bulk modulus, the less compressible is the material. The Young's modulus, E , is the measure of a material's stiffness under the effects of unidirectional loading, eq 3.2. In essence it

is the ratio of the stress along an axis over the strain along that particular axis

$$E = \frac{\text{stress}}{\text{strain}} = \frac{\text{force/area}}{\text{change in length/initial length}} \quad (3.2)$$

A material with a high(er) Young's modulus is stiff(er). In periodic DFT calculations, these mechanical properties can be calculated by applying to the unit cell small uniform/anisotropic infinitesimal pressures and fitting the resulting energy–volume curve to some equation of state.¹⁶⁷

Electronic properties of interest include the band structure, electronic density of states (DOS), and partial atomic charges. The band gap, which is the gap between the valence band and the conduction band, can be extracted from the band structure. It is closely related to the threshold for photons to be absorbed by the material, which is the optical gap, and to the difference between the electron affinity and the ionization potential, which is the fundamental gap. However, as MOFs are low-dielectric media, the optical gap can be considerably smaller than the fundamental gap due to significant exciton binding energies. Exciton effects may be calculated by the Bethe–Salpeter equation.¹⁶⁸

The DOS is the number of states per interval/unit of energy, and it can be decomposed into partial DOSs based on atomic numbers (e.g., C, H, N, O, Fe, ...), orbital angular momentum quantum numbers (s, p, d, f, ...), or a combination of atomic numbers and azimuthal quantum numbers (e.g., C-2p, Fe-3d, ...). The decomposition into atomic components depends on the radii assumed for the elements, although the significance of this dependence is often overlooked. Atomic partial charges obtained from electronic structure calculations are typically used in force fields for MD and MC simulations. They can also be used to rationalize trends in binding strengths between MOFs and adsorbates.

3.1.1. MOF-5. As noted above and in Table 1, MOF-5 has Zn₄O tetrahedral clusters joined by BDC linkers to form an extended 3D framework with interconnecting pores of 8 Å width and 12 Å diameter, Figure 7.²⁰ It has a space group of *Fm*3*m* and is also referred to as IR-MOF-1 in the literature. There has been and continues to be much interest in MOF-5 (as well as its analogues¹⁶⁹), largely because experimental measurements by Roswell et al. in 2004 suggested that it could

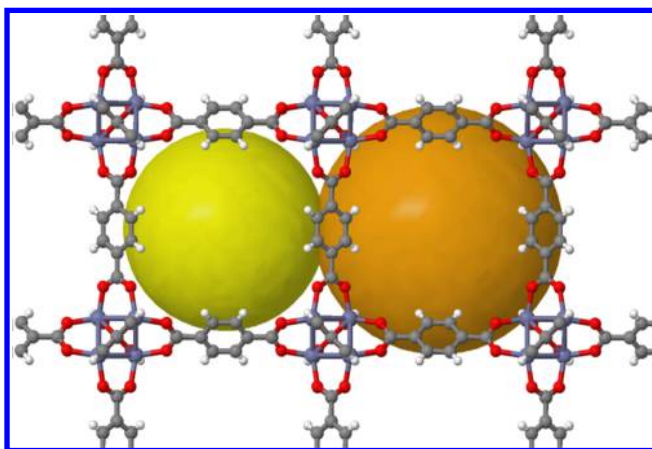


Figure 7. MOF-5 showing the two types of interconnecting pores. Zn₄O and BDC linkers are also visible. Zn, O, C, and H atoms are represented by purple, red, grey, and white spheres, respectively.

achieve a gravimetric hydrogen storage density of about 1.3% at 77 K and 1 atm H₂ partial pressure.^{41d} These experimental results motivated many computational studies,¹⁷⁰ not because MOF-5 attained the target of 6% gravimetric density set by the United States Department of Energy (DOE) at the time¹⁷¹ but because it was thought that an understanding of the properties of MOF-5 could provide insights into modifications or new MOFs that would attain these targets. Many of these computational studies focused on computing the adsorption isotherms of H₂ on MOF-5 in addition to discovering the H₂ adsorption sites in this particular MOF.¹⁷⁰ The structural properties of MOF-5, by itself, were optimized with periodic DFT in some of these early computational works, with Sagara et al.^{170d} and Mueller et al.^{170b} obtaining lattice constants of 25.77 and 26.14 Å, respectively, both using the PBE density functional. Sagara et al. used GTOs basis functions, while Mueller used PAW plane waves. The calculated values compare reasonably well with the experimental value of 25.91 Å.¹⁷²

A series of articles in which the intrinsic structural, mechanical, and electronic properties of MOF-5 were studied with electronic structure methods was published from 2006 onward. Mattesini et al.⁸³ studied the properties of MOF-5 with periodic LDA calculations using USPs. They obtained remarkable agreement (within 0.003 Å) between the calculated and the experimental lattice constants.¹⁷² Samanta et al.^{21c} used the PAW plane wave method while still using LDA and obtained an agreement of about 0.02 Å between experiment and theory. Bahr et al.^{21a} obtained lattice parameters of 25.59 and 26.04 Å with the LDA and PW91 functionals, respectively, also with PAW plane waves, which may be compared to the experimental value of 25.91 Å. In addition, Samanta et al.^{21c} obtained calculated Zn–Zn, Zn–O, and O–C bond lengths in the unit cell within 0.03 Å of the experimental values. After optimizing the unit cell, Zhou et al.¹⁷³ also calculated its phonon DOS and dispersion curves. These calculated properties were compared to experimental Raman/IR or neutron inelastic scattering (NIS) measurements. The calculated phonon DOS agreed well with the experimental NIS data.¹⁷³ Fuentes-Cabrera et al. replaced the Zn atoms in MOF-5 by Cd, Be, Mg, and Ca and found that the change in the equilibrium volume is correlated with the atomic radius of the substituent metal.¹⁷⁴

The calculation of the mechanical properties of MOF-5 has also been of interest. Samanta et al.^{21c} and Zhou et al.¹⁷³ calculated the shear modulus of MOF-5 to be 1.4 and 1.2 GPa, respectively. Bahr et al.^{21a} used the LDA and PW91 functionals with the PAW method and obtained an average value of 2.7 GPa. These low values suggest that MOF-5 might be structurally unstable and might yield other phases under high pressure and strain.¹⁷³ Zhou et al. explored the possibility of phase transitions occurring via the softest phonon modes of the unit cell. They found that although the softest mode corresponds to twisting of the linker, phase reorganization is probably precluded as a result of the high barrier (≥48.2 kJ/mol) associated with this mechanism.

MOF-5 is by no means the only MOF with a very low shear modulus. Tan et al. measured the mechanical properties of ZIF-8 using the Brillouin scattering technique.^{32b} ZIF-8 is a member of the zeolitic imidazolate frameworks (ZIFs) subfamily of MOFs. It contains Zn²⁺ ions and 2-methyl imidazolate organic linkers and has a sodalite topology, Table 1.³¹ They found that its shear modulus is also very low, about 1.1 GPa. The experimental investigations were complemented with DFT

(B3LYP functional) calculations at 0 K from which they also obtained a shear modulus of 1.1 GPa. Hegde et al. recently computed the energies and transition barriers required to induce faults in the structure of ZIF-8.^{32a}

Wu et al.³⁴ recently discovered that UiO-66 exhibits unusually high shear stability, with its minimal shear modulus being an order of magnitude higher than that of ZIF-8 and MOF-5. UiO-66 has a porosity of about 53% and contains $\text{Zr}_6\text{O}_4(\text{OH})_4$ metal clusters that are each linked to 12 BDC linkers.²⁵ The high shear modulus of the framework is maintained when the Zr atoms are replaced by Hf or Ti or when the organic linker is changed from BDC to BPDC (UiO-67) or TPDC (UiO-68), BPDC^{2-} = biphenyl-4,4'-dicarboxylate and TPDC^{2-} = terphenyl-dicarboxylate. Wu et al.³⁴ found that the high shear stability of the UiO-6X ($X = 6, 7$, and 8) MOFs is a direct result of the high degree of coordination of the Zr–O units to the organic linkers. We note that the UiO-6X MOFs have 12 metal–organic linker coordinations in comparison to 4–6 in MOF-5, ZIF-8, and Cu–BTC.

The calculated Young's moduli of MOF-5 obtained by Fuentes-Cabrera et al.,¹⁷⁴ Samanta et al.,^{21c} Mattesini et al.,⁸³ Zhou et al.,¹⁷³ and Bahr et al.^{21a} are 18.0, 21.1, 9.4, 21.9, and 21.6 GPa, respectively. These values are significantly different from the experimental value of 2.7 ± 1.0 GPa obtained by Bahr et al.^{21a} Even after applying a unitless anisotropic correction factor of about 2.9 to the experimental data, there is still substantial disagreement with the results obtained from DFT calculations.^{21a} The origin of this discrepancy between calculated and experimental values of the Young's modulus is unclear. We note, however, that similar large discrepancies have been reported for some zeolites.¹⁷⁵ It is possible that the discrepancies are due to the deficiencies of the LDA and GGA functionals used in these studies. Tan et al. obtained excellent agreement between experimental and calculated mechanical properties when they used the hybrid B3LYP functional, suggesting that the incorporation of HF exchange is important for accuracy.^{32b} Classical MD and MC simulations have predicted even larger values, and thus larger errors, for the Young's modulus of MOF-5.¹⁷⁶

The calculated bulk modulus of MOF-5 is generally around 16.3–18.5 GPa.¹⁷⁵ This indicates that MOF-5 is a very soft material. Unlike the shear modulus, which appears to be independent of linker size, Yang et al.¹⁷⁷ have shown that longer linkers generally tend to result in smaller bulk moduli. This conclusion was reached by comparing the calculated bulk moduli of MOF-5 to those of IR-MOF-10^{177b} and IR-MOF-14.^{177a} In IR-MOF-10, Zn_4O clusters similar to those in MOF-5 are coordinated to naphthalene-2,6-dicarboxylate (NDC) linkers,¹⁷⁸ while in IR-MOF-14 they are bound to pyrene-2,7-dicarboxylate (PDC) linkers.^{49c} These are much larger than the BDC linker found in MOF-5. Additionally, the calculated bulk moduli of MOF-5, IR-MOF-10, and IR-MOF-17 decrease monotonically as the metal centers are changed from Zn to Cd or from Be to Ba.¹⁷⁷

With respect to electronic properties, Samanta et al.^{21c} and Mattesini et al.⁸³ computed the electronic DOS of MOF-5 with LDA. They obtained a band gap of 2.7 and 2.5 eV, respectively. These values are about 0.8–1.0 eV less than the value of 3.5 eV obtained by Bordiga et al.¹⁷⁹ from UV–vis diffuse reflectance spectrometry. This underestimation of the electronic band gap is a well-known consequence of using local DFT functionals for band gap calculations. Surprisingly, Yang et al.¹⁸⁰ and Fuentes-Cabrera et al.¹⁷⁴ used GGA functionals (which are also local) to

calculate the electronic DOS of MOF-5, and both obtained a band gap of about 3.5 eV, in good agreement with experiment. It is not immediately clear why the chosen GGA functionals performed well for predicting the band gap of MOF-5. The calculated partial DOS of MOF-5 indicates that the 3d states of Zn are strongly hybridized with the 2p states of O and C at the top of the valence band, reflecting that there are strong interactions between the Zn and the O atoms of the Zn_4O metal clusters.

3.1.2. MOF-74. The members of the MOF-74 series have been widely studied. As noted in section 1, these MOFs have 3D topologies containing divalent metal sites and 2,5-dioxido-1,4-benzenedicarboxylate linkers.^{4,181} A general representation is shown in Figure 1. At the current moment, the Zn, Mn, Fe, Co, Ni, and Cu analogues of Mg–MOF-74 are also known with all members having open metal sites that can be created by removing coordinated solvent molecules. We also note that the synthesis and characterization of analogues containing two or more metals, i.e., a mixed-MOF-74, has been reported by Wang et al.¹⁸²

In general, there has been tremendous interest in the gas uptake and separation properties of the MOF-74 series, with particular emphasis on CO , CO_2 , CH_4 , and H_2 .^{4,7,22c,183} As additional examples, in 2009, Britt et al.^{37c} showed that Mg–MOF-74 could efficiently separate CO_2 and CH_4 , whereas other studies have shown that the isosteric heats of H_2 capture in the MOF-74 materials range from 8 to about 14 kJ/mol.¹⁸⁴ In section 4, we discuss theoretical studies that were focused on the adsorption of gases in MOF-74 materials. A few of these are listed in refs 22b, 70, and 185.

However, one of the intriguing questions about the MOF-74 materials (and other MOFs^{164c}) relates to their magnetic properties in the bulk phase as well as the nature(s) of the interactions between the well-ordered metal sites of the framework. The possibility of a quasi-1D (one-dimensional) magnetic behavior in these materials makes them tantalizing for electronic structure studies.^{43f,186} The effect of Jahn–Teller distortions on such quasi-1D behavior has been investigated in other MOFs.¹⁸⁷ The transition from ferromagnetic to antiferromagnetic ordering upon adsorption of alkenes by Fe–MOF-74 is another question that has been investigated using quantum mechanical approaches.¹⁸⁸ Park et al. noted that the geometrical changes that occur after adsorption of alkenes is the main driver of this magnetic transition, with electronic effects such as charge-transfer and orbital interactions playing only minor roles.¹⁸⁸ In contrast, Maximoff and Smit provided a detailed mechanism for how the adsorption of O_2 on Fe–MOF-74 occurs via charge-transfer-driven quasi-1D metal–insulator–metal transitions that affect the degree to which the quasi-1D electrons are delocalized or localized as well as whether the O_2 is adsorbed as a superoxide or a peroxide moiety.¹⁸⁹ Such temperature-dependent magnetic behavior¹⁹⁰ is not observed when N_2 (which is very much redox inactive in comparison to O_2) is adsorbed on Fe–MOF-74 or when either N_2 or O_2 is adsorbed on Zn–MOF-74.

In the cobalt member of the MOF-74 series, Co–MOF-74, the metal–metal (M–M) distance within a helical backbone chain is around 3.1 Å while the shortest distance between metal atoms in adjacent chains is about 7.4 Å, Figure 8.^{183d} Systems with large anisotropies in M–M distances have been found to behave as one-dimensional (1D) or linear magnets. Dietzel et al.^{183d} measured the magnetic susceptibility of this material and found no deviation from conventional 3D magnetic behavior.

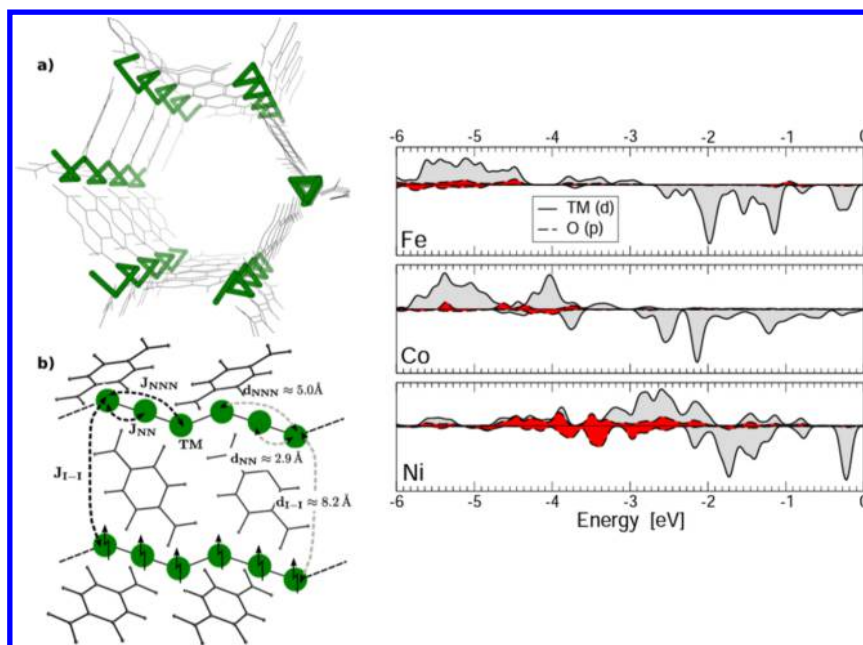


Figure 8. (Left top) Front view of Fe-MOF-74. Helix-like magnetic chains connecting the Fe centers are shown in green. (Left bottom) Side view of Fe-MOF-74 showing the distances and coupling constants between intrachain nearest neighbors (NN), next nearest neighbors (NNN), and chains (I-I). (Right) Calculated partial DOS of Fe-MOF-74, Co-MOF-74, and Ni-MOF-74. Reprinted with permission from ref 186. Copyright 2013 American Physical Society.

This material has helix-like magnetic chains formed by the transition metals interspaced by organic linkers, Figure 8. To elucidate the potential 1D magnetic properties of the MOF-74 framework, Canepa et al.¹⁸⁶ carried out periodic DFT calculations with the PBE functional on Fe-MOF-74, Co-MOF-74, and Ni-MOF-74 while using USPs. They initially computed the magnetic moments and used Löwdin analysis to calculate the charge density on each atom.^{64a} This is crucial as 1D-magnetism can only be displayed when each metal atom has a non-negligible magnetic moment. They predicted a magnetic moment of 3.3 μ_B for Co-MOF-74, which is lower than the experimental value of 4.7 μ_B . The discrepancy between the calculated and the experimental values is most likely a result of the tendency of GGA functionals, like PBE, to unphysically delocalize electronic charge density. It is reasonable to expect that functionals (like hybrids functionals) and approaches like DFT+U that enforce localization of 3d electrons might lead to better agreement between the calculated and the experimental values of the magnetic moment of Co-MOF-74, obtained also with the PBE functional by Canepa et al.¹⁸⁶

The calculated magnetic moments of Fe-MOF-74 and Ni-MOF-74 are 3.6 and 1.6 μ_B , respectively. Analysis of the calculated total and partial DOSs as well as partial atomic charges, Figure 8, indicates that the magnetization of each helix originates from the metal d electrons and that there is some hybridization with the 2p orbitals of neighboring oxygen atoms. The DOSs obtained with the PBE functional are qualitatively similar to those obtained at the PBE+U level by Zhang et al.¹⁹¹ To determine the existence of interactions between magnetic spin carriers, Canepa et al.¹⁸⁶ computed the interchain, J_{NN} and J_{NNN} , and intrachain, J_{I-I} , coupling constants using a 1D Ising model derived from the Heisenberg-Dirac-van Vleck Hamiltonian.¹⁹² Here, J_{NN} is the coupling constant between nearest neighbors, J_{NNN} is the coupling constant between next-nearest neighbors, and J_{I-I} describes the coupling between chains. The computed intrachain J coupling constants are larger

and more positive than J_{I-I} . This suggests the existence of linear ferromagnetism and is largely expected as the long interchain M-M distances quench intrachain spin interactions. The calculated J_{NN} value obtained for Fe-MOF-74 was $28.1 \pm 0.4 \text{ cm}^{-1}$, considerably overestimating the experimental value of 4.1 cm^{-1} . The interchain coupling constant, J_{I-I} , of Fe-MOF-74 was calculated as -1.2 cm^{-1} and agrees well with the experimental value of -1.12 cm^{-1} .^{183b}

In 2013, Maurice et al.^{43f} re-examined the magnetic properties of Fe-MOF-74 by combining theory with experimental measurements of the magnetic susceptibility data. Theoretical calculations were carried out at the cluster level using DFT (M06-L and M06) and the state-averaged CASSCF approach followed by multireference perturbation theory, NEVPT2, to account for dynamical correlation effects. Spin-orbit coupling effects were also accounted for with the spin-orbit state interaction, SO-SI, method. With the M06-L density functional, the isotropic coupling constants, J_{NN} and J_{NNN} , were calculated to be 10.3 and 2.0 cm^{-1} , respectively. The J values obtained by Maurice et al. using the M06-L functional and an 88-atom cluster model represent an improvement compared with the values obtained by Canepa et al.¹⁸⁶ using the PBE functional and a periodic unit cell. Further improvement is seen when the metahybrid M06 functional ($J_{NN} = 3.6 \text{ cm}^{-1}$ and $J_{NNN} = 0.5 \text{ cm}^{-1}$) is used, confirming that accurate localization of the unpaired 3d electrons is crucial to correct prediction of the magnetic moments of MOFs.

The magnitude of the J_{NN} coupling constants obtained by Canepa et al.¹⁸⁶ and Maurice et al.^{43f} as well as the experimental results suggest that the NN interactions are ferromagnetic but small. Maurice et al.^{43f} also examined the influence of anisotropy at the high-spin Fe^{II} centers on the magnetic properties of Fe-MOF-74. Anisotropic effects arise from the deviation of the first coordination sphere of the Fe centers from a perfect square pyramidal geometry, spin-orbit coupling effects, as well as long-range anisotropy in the crystal. For Fe-

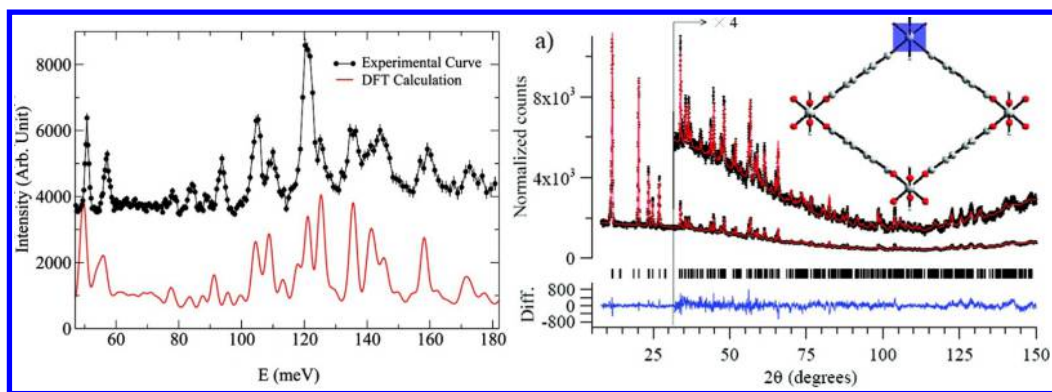


Figure 9. (Left) Comparison of the high-energy inelastic neutron scattering data for the room-temperature lp polymorph of MIL-53 to the predicted results obtained for the DFT-optimized structure. Peaks at 50.8 and 57.1 meV are dependent on the structural transition and correspond to the twisting modes of the benzene rings in the framework. (Right) Neutron powder diffraction of MIL-53(Al) collected at room temperature after heating to 450 K. Reprinted with permission from ref 15a. Copyright 2008 American Chemical Society.

MOF-74, the relevant anisotropy parameters are D , the axial zero-field splitting (ZFS) parameter, and E , the rhombic ZFS parameter. D and E were calculated to be around -12.0 and 3.5 cm^{-1} , respectively, and appear to be largely independent, to within $2\text{--}3 \text{ cm}^{-1}$, of second-order perturbation and spin–orbit coupling effects. Although D is quite large and negative, it does not result in permanent magnetization as it represents a mismatch with the calculated value of the J_{NN} isotropic coupling constant. This indicates that Fe–MOF-74 would most likely have fast magnetic relaxation pathways that would prevent it from behaving as a magnet. Experimental measurements reported in the same article confirm the absence of slow magnetic relaxation pathways and hysteresis in the magnetization field curves at very low temperatures.^{43f} Electronic structure calculations have been used in studying the magnetic properties of other MOFs¹⁹³ as well as the effect of guest molecules on the magnetic properties of Fe–MOF-74.^{183b,188}

3.2. Framework Flexibility in MOFs and Its Effects on Functional Properties

There are cases where the unit cell of a particular MOF can exist in different forms, shapes, and sizes. In these cases, optimization of equilibrium lattice constants and atomic positions is more involved than situations in which the MOF's unit cell has only a single (apparent) polymorph. In addition, the relative free energies of the polymorphs of a “bistable” (the unit cell has two known stable polymorphs) or “polystable” MOF (the unit cell has more than two known stable polymorphs) might vary with temperature, pressure, or strain. A comprehensive review of recent works on flexible MOFs has been provided by Schneemann et al.³³ In one of the earliest studies of a bistable MOF, Liu et al.^{15a} used a combination of neutron powder diffraction, inelastic neutron scattering, and periodic DFT/LDA calculations to characterize MIL-53(Al). The MIL-53 family of MOFs contains terephthalate linkers and trivalent metal ions, Table 1. Prior to the report of Liu et al.,^{15a} MIL-53(Al) had been shown to undergo reversible structural changes as a result of interactions between the framework and adsorbed molecules; the series of M–MIL-53 ($M = \text{Cr, Al, Fe, Sc, etc.}$) MOFs can undergo volume changes by as much as 40–270% upon gas adsorption.¹⁹⁴ MIL-53(Al) exists as a large pore (lp) polymorph when all solvent and adsorbed species are evacuated but exists as a narrow-pore (np) polymorph after adsorbing species like H_2O or CO_2 . This reversible behavior was labeled as the “breathing” of the

framework and reflects significant flexibility of the organic linker. The experimental results of Liu et al.^{15a} however showed that this breathing behavior could be induced by simply altering the temperature in the absence of guest molecules. To explain these experimental findings, the structure of the lp polymorph was optimized at the DFT level. From the optimized structure, the phonon DOS was computed and compared to the experimental inelastic neutron scattering data collected at room temperature. The calculated phonon DOS agreed well with the experimental data, Figure 9. Liu et al.^{15a} were able to identify two soft vibrational peaks in the experimental and calculated spectra that could trigger the structural transformation of the lp polymorph to the np polymorph, Figure 9. These peaks correspond to twisting modes of the benzene ring and suggest that the breathing behavior of the MIL-53 framework is a result of the twisting of the framework rings and an intrinsic property of the MOF. The existence of two polymorphs for MIL-53(Al) is not simply caused by the presence of guest molecules, as previously thought.¹⁹⁴ We note that Munn et al.¹⁹⁵ were able to assign the inelastic neutron scattering spectra of the closed and open forms (after exposure to methanol vapor) of MIL-53-Fe by comparison to the simulated spectra of MIL-53-Al obtained from periodic DFT calculations with USPs.

These results have been confirmed by Mendt et al.,¹⁹⁶ who carried out electron spin resonance (ESR) measurements of the polymorphs of the chromium analogue, MIL-53(Cr). Although the barrier associated with twisting of the benzene ring was not computed by Liu et al., they reported the results of nudged elastic band (NEB) calculations for the structural transformation of VO(BPDC) from the np form to the lp form.¹⁹⁷ The transition-state barrier of the lp–np transformation varies between 38 and 43 kJ/mol at 0–650 K. They were also able to predict a novel overstretched np geometry which is however higher in energy than the np and lp forms at 0 K.

Liu et al.^{15a} did not report the relative energies of the polymorphs of MIL-53(Al), because the LDA functional did not predict the np polymorph to be stationary. Simulations with classical force fields also failed to predict a stable np polymorph.¹⁹⁸ It was therefore unclear whether quantum mechanical calculations could accurately describe the lp polymorph as the high-temperature version and the np polymorph as the low-temperature version. In 2010, Walker et al.^{15b} reported a theoretical study of the relative energies of

the lp and np polymorphs using older generation density functionals and also dispersion-corrected functionals. They employed PBE, vdW-DF, PBE-D, B3LYP-D, and B3LYP-D* functionals in their calculations.^{15b} Perhaps not surprisingly, they found that dispersion effects are crucial to stabilizing the np polymorph. Without including dispersion effects, the PBE functional predicts that the lp polymorph is more stable than the np polymorph. This disagrees with the experimental results that show the np polymorph is the low-temperature phase.^{15a} PBE0 also failed to predict correctly the relative energies of the lp and np polymorphs of MIL-53(Cr).¹⁹⁹ However, when dispersion effects are included (with any of vdW-DF, PBE-D, B3LYP-D, or B3LYP-D*), the np polymorph becomes more stable than its lp analogue by 5.0–18.0 kJ/mol. Clearly, the stabilization energy provided by dispersion effects, the dispersion stabilization energy, is larger for the np polymorph.

Walker et al.^{15b} decomposed the dispersion stabilization energy by converting the phenyl rings of the terephthalate linkers to cyclohexane rings. This removes the aromatic–aromatic interactions from the dispersion effects that are captured by the dispersion-corrected functionals. They found that almost 50% of the dispersion energy comes from the phenyl rings, while more than 80% comes from overall organic C–C, C–H, and C–O interactions. They concluded that a full account of dispersion effects correctly predicts the np polymorph as the low-temperature phase. To determine why the lp polymorph is the preferred polymorph at ambient temperature, they computed the change in entropy associated with the lp–np transition and were able to show that the lp polymorph becomes entropically stabilized above 300 K.^{15b}

Although the framework flexibility of a “breathing” MOF is an intrinsic property, it can have also a significant impact on the functional properties of the MOF, specifically its gas adsorption and separation properties.²⁰⁰ In 2009, Coombes et al.¹⁹⁹ optimized the structures of lp and np MIL-53(Cr) using the PBE and PBE0 functionals. As noted above, these functionals do not correctly predict the np form as the lowest energy structure.^{15b} They also developed a force field for studying the adsorption of H₂O in the lp and np forms of the MOF. They found that the hydration energies are always higher for the np form regardless of H₂O loading. The relative stabilities of the lp and np forms of the hydrated MOF, however, are dependent on the loading of H₂O. When only one H₂O molecule is adsorbed, the lp form is still more stable than the np form. It is however only 18.9 kJ/mol more stable than the np form, compared to a value of 29.9 kJ/mol for the empty MOF. In contrast, when more H₂O molecules are adsorbed, the np form becomes more stable than the lp form. This is in agreement with the experimental observation of the np polymorph under ambient conditions after exposure to H₂O or CO₂.¹⁹⁴ The stabilization of the np form after hydration occurs because adsorbed H₂O molecules can interact with both sides of the pore in the narrower pores of the np geometry.^{14,201}

The relative energies of the lp and np polymorphs of bistable MIL-53 MOFs and consequently their gas adsorption and separation properties can be altered by functionalizing the organic linker. Couck et al.²⁰² reported that when the organic linker of MIL-53(Al) is functionalized with an amino group, the resulting MOF, labeled as NH₂-MIL-53(Al), performed excellently in separating CO₂ from CH₄. To explain these findings, Stavitski et al.²⁰³ carried out complementary experimental investigations and periodic DFT calculations on MIL-53(Al) and NH₂-MIL-53(Al), Figure 10. They used the

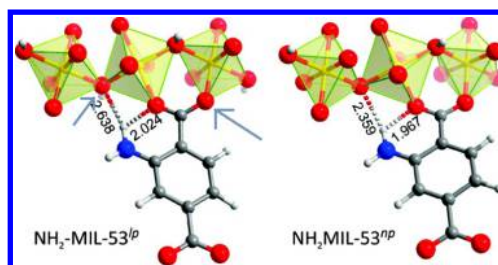


Figure 10. Inter-molecular contacts of the amino group of NH₂-MIL-53 with hydrogen-bonded carboxylate and OH groups (these two are indicated by arrows on the left). Structural metrics of the hydrogen bonds formed by the amine groups with the carboxylate and OH groups are shown for the lp (left) and np (right) polymorphs. Reprinted with permission from ref 202. Copyright 2009 American Chemical Society.

PBE and PBE-D2 approaches in their computations. They first examined the effect of functionalization on the empty frameworks in the absence of adsorbed gases. They found that the lp polymorph of MIL-53 is energetically preferred to the np polymorph by only 3 kJ/mol, suggesting that both polymorphs can exist at low temperatures. The opposite situation was obtained for NH₂-MIL-53(Al), with the np polymorph being favored by 14 kJ/mol over its lp counterpart. This result is in accord with the results of Devic et al., who carried out classical MD simulations with the universal force field²⁰⁴ (UFF) and showed that the attachment of Cl, Br, NH₂, and hydroxyl groups to the organic linker of MIL-53(Fe) increased the stability of the np polymorph relative to its lp counterpart.²⁰⁵

Examination of the optimized structures of the polymorphs of NH₂-MIL-53(Al), Figure 10, shows that the introduction of the amino group not only breaks the CH $\cdots\pi$ interactions of the organic linker but also provides opportunities for van der Waals contacts between different fragments of the organic linkers. The added amino groups decrease the basicity of the hydrogen-bonded carboxylic acid and bridging OH ligands that are directly coordinated to the [AlO₆] ∞ clusters. The decreased basicity of the carboxylic and bridging OH groups cause the [AlO₆] ∞ chains in NH₂-MIL-53(Al) to be more flexible than those in MIL-53(Al). The narrow pores of the np framework allow for more efficient interactions of the amino groups with the framework carboxylic or hydroxyl groups. For this reason, the monoclinic unit cell of the np polymorph is more stable for NH₂-MIL-53(Al) than for MIL-53(Al).

Stavitski et al.²⁰³ then computed the CO₂ adsorption energies of the lp and np polymorphs of NH₂-MIL-53 and MIL-53, Figure 11. The np polymorph of NH₂-MIL-53 has a greater affinity for CO₂ than its lp counterpart, suggesting that the decreased basicity of the hydrogen-bonded carboxylic acid and bridging OH ligands allows for a better capture of CO₂. Couck et al.²⁰² proposed that the higher CO₂ selectivity in NH₂-MIL-53(Al) is driven by its preference for the more flexible np polymorph. This greater flexibility of the np polymorph allows it to efficiently accommodate adsorbed molecules within certain pressure limits. The narrower pores of the np polymorph, however, become a disadvantage when there is a need to accommodate very large quantities of CO₂. On the other hand, adsorption of CO₂ to the lp version of MIL-53 also forms an np product, consistent with the existence of the lower volume polymorph under ambient atmospheric conditions and after exposure to H₂O or CO₂.¹⁹⁴ We note that Torrisi et al.²⁰⁶

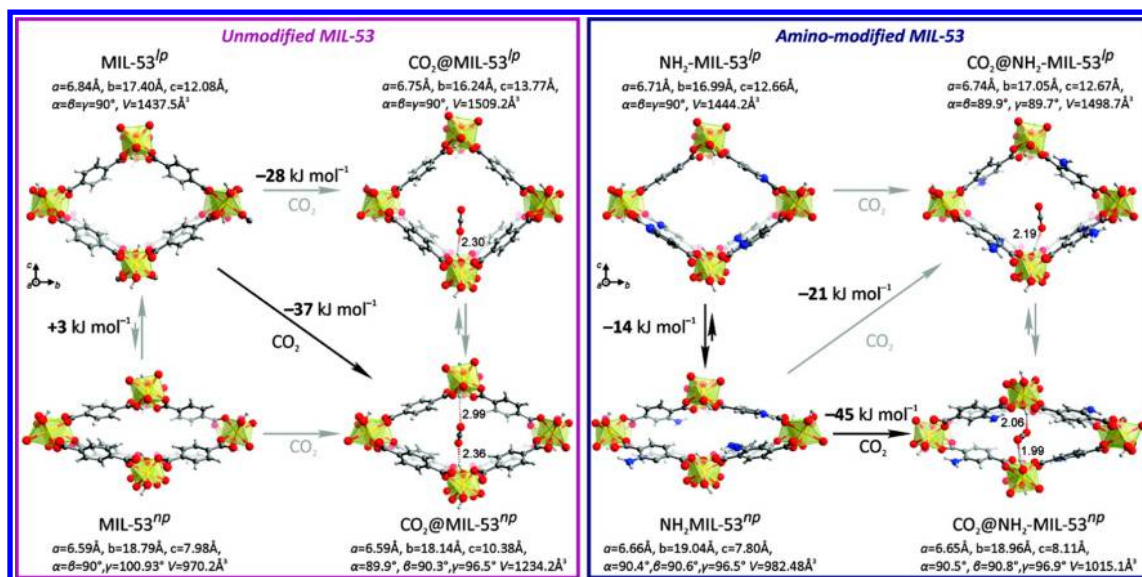


Figure 11. Calculated CO₂ adsorption energies for the lp and np polymorphs of MIL-53 (left) and NH₂-MIL-53 (right) obtained at the PBE-D2 level of theory. Reprinted with permission from ref 203. Copyright 2011 American Chemical Society.

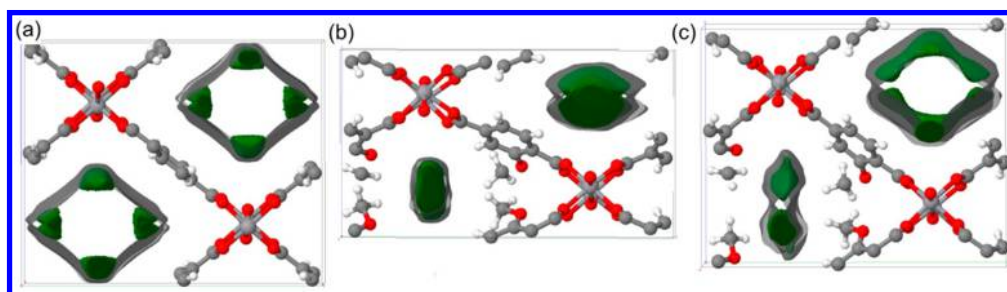


Figure 12. Isosurfaces of local excess chemical potential (gray, 0 kJ/mol; green, -15 kJ/mol) in (a) lp geometry of MIL-47(V⁴⁺), (b) fully relaxed np geometry of MIL-47(V⁴⁺)-OCH₃ (notice the availability of the larger negative potential for CO₂ capture in the np polymorph, and (c) MIL-47(V⁴⁺)-OCH₃ relaxed with its volume fixed at that of the lp polymorph. This constrained geometry reduces the available negative potential for CO₂ capture. Reprinted with permission from ref 208. Copyright 2013 American Chemical Society.

proposed, based on DFT calculations and GCMC simulations, that functionalization of the BDC linker by (CH₃)₂, (OH)₂, and COOH groups can also improve the CO₂ adsorption energies of MIL-53(Al). They used the PW91 functional in their DFT calculations and only considered the lp form of MIL-53(Al). It is therefore not clear whether the (CH₃)₂, (OH)₂, and COOH groups also stabilize the empty np polymorph, like the NH₂ group.

A complete explanation of framework breathing requires calculating free energies for the various states of the system. There has been some progress with an empirical free energy model,²⁰⁷ but it would be challenging to replace this model with one based on quantum mechanical calculations.

There are several other cases in which functional groups attached to the organic linker can alter the relative stabilities of the lp and np polymorphs as well as the gas adsorption properties of a breathing/flexible MOF. Biswas et al.²⁰⁸ synthesized and characterized the MIL-47(V⁴⁺)-X (X = -H, -Cl, -Br, -CH₃, -CF₃, -OH, and -OCH₃) series of MOFs. They found that the CO₂ adsorption capacities of the compounds depend on the size and nature of the attached functional groups, with MIL-47-OCH₃ exhibiting the highest capacity for CO₂. Computationally, they used the PBE-D3 method, damping the dispersion correction D3 scheme with the method proposed by Becke and Johnson.^{123,209} According

to their study the lp geometry is more stable for unsubstituted MIL-47(V⁴⁺). In contrast, full optimization of MIL-47-OCH₃ shows that the np geometry is slightly more stable (2.5–5.7 kJ/mol) than the lp geometry.

To explain the increased adsorption of CO₂ by MIL-47-OCH₃, they calculated Hirshfeld atomic charges as well as the local excess chemical potential isosurfaces of the different polymorphs. The calculated Hirshfeld charges of MIL-47 are generally similar to those of MIL-47-OCH₃, indicating that the methoxy group has only a local influence on the electron distribution of the organic linker. However, from Widom particle insertion simulations based on the optimized DFT structures and energetics it was found that CO₂ affinity is higher in MIL-47-OCH₃ for two reasons. First, the partially collapsed framework in the np polymorph allows CO₂ to interact simultaneously with all surrounding linkers and substituents. This is similar to the conclusion of Couck et al.²⁰² in their study on NH₂-MIL-53(Al). Second, the presence of the OCH₃ substituent provides favorable electrostatic interactions with the adsorbed CO₂ molecule, Figure 12. There have been several experimental confirmations of the influence of functional groups attached to the organic linker on the relative stabilities of the polymorphs of other bistable MOFs.²¹⁰

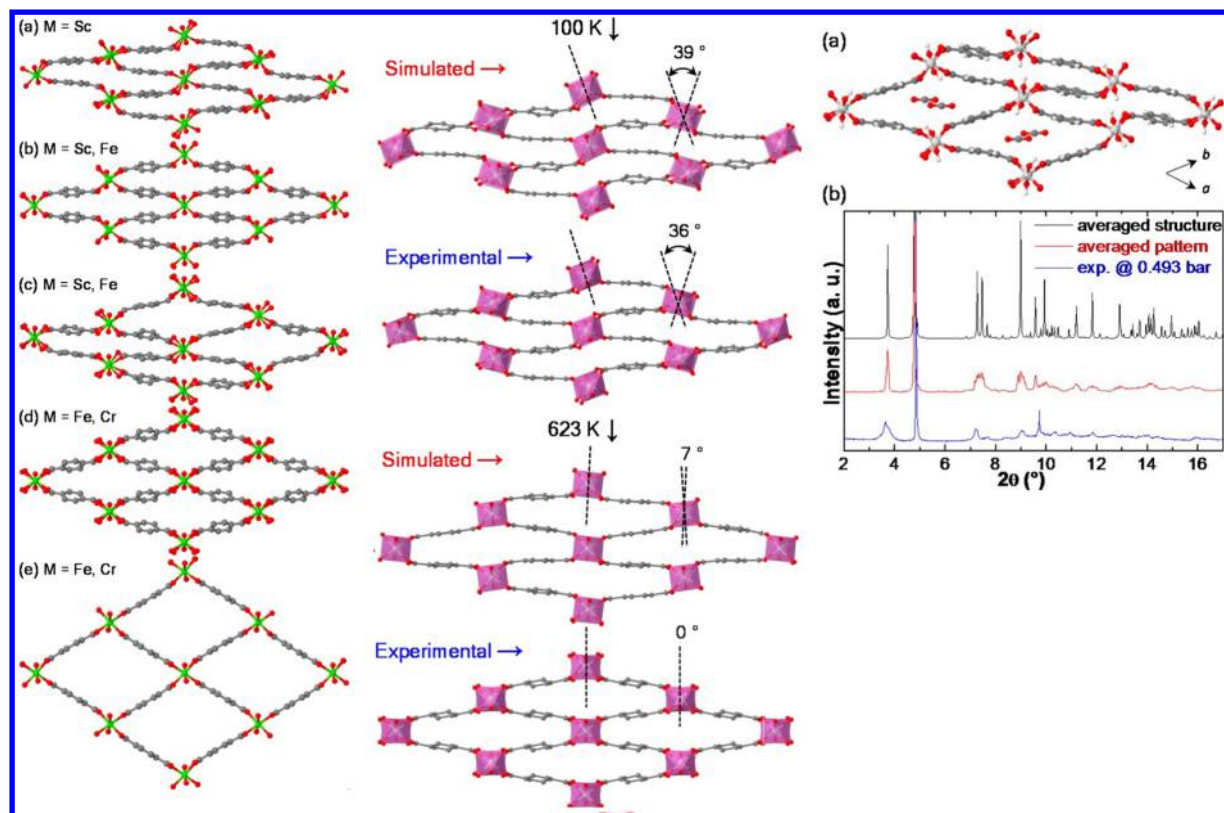


Figure 13. (Left) Schematic representations of five possible polymorphs of MIL-53 M^{3+} MOFs. (Middle) Orientations of the organic linker and $[\text{ScO}_6]_\infty$ chains in the cp geometry of MIL-53(Sc) at 100 K (top) and the vnp geometry at 623 K (bottom). (Right) The int structure obtained from AIMD simulations for CO_2 loading of 2.2 mmol/g. Reprinted with permission from ref 156. Copyright 2013 American Chemical Society.

Boutin et al.²¹¹ recently characterized MIL-53(Ga) for which the np polymorph is the most thermodynamically stable phase at ambient temperature. This is an exception within the MIL-53 family, which generally has the lp form as the stable phase at ambient conditions and the np form preferred only at much lower temperatures. Boutin et al.²¹¹ used periodic B3LYP-D3 calculations to confirm that the np form of MIL-53(Ga) is the stable geometry in the absence of adsorbed H_2O . A full explanation of the difference between MIL-53(Ga) and MIL-53(Al) has been provided by Coudert et al.,²¹² who carried out periodic DFT calculations as well as AIMD simulations. DFT calculations at 0 K indicated that while the np form is more stable than the lp form for both MIL-53(Ga) and MIL-53(Al), there is a further stabilization of the np form in the Ga MOF by about 4 kJ/mol. The equilibrium temperature of the np–lp transformation would therefore be expected to be higher for MIL-53(Ga) than for MIL-53(Al). Some rationalization of this phenomenon was attributed to the shape of the orbitals of Ga and Al. The more diffuse orbitals of Ga allow greater deformation of its coordination sphere, allowing its organic linkers to get closer in MIL-53(Ga) than in MIL-53(Al).

As noted above, polystable MOFs display more complex structural transformations than the apparent bistability found in MIL-53(Al/Cr) and MIL-47(V^{4+}). As an example, MIL-53(Fe) adopts a very-narrow-pore (vnp) geometry when it is evacuated and expands to an intermediate (int) form as it begins to take up CO_2 before opening up to its np and then lp forms.^{205,213} A recent experimental and theoretical characterization of MIL-53(Sc) by Chen et al.¹⁵⁶ revealed an even more complex breathing sequence. MIL-53(Sc) can exist as a closed-pore (cp) geometry after evacuation that is different from the vnp form.

The cp geometry has no accessible porosity to N_2 or CO_2 . This geometry can be reversibly converted to the vnp form by raising the temperature from 100 to 573 to 623 K. Chen et al. carried out AIMD simulations with BLYP-D3 to understand the temperature and adsorbed CO_2 -induced transformations of MIL-53(Sc).¹⁵⁶ This appears to be the first attempt to study the breathing phenomenon in MOFs with AIMD simulations. The experimentally observed rotation of the $[\text{ScO}_6]_\infty$ chains at higher temperature, confirmed by the AIMD simulations, is responsible for the reversible cp–vnp transformation, Figure 13. The AIMD simulations almost quantitatively reproduce the rotations of the $[\text{ScO}_6]_\infty$ chains, indicating that the entropic effects associated with molecular motion at higher temperatures are well captured. It was also found that the AIMD simulations correctly describe the cp–int transition that occurs after a CO_2 loading of 2.2 mmol/g is adsorbed at 196 K. The powder diffraction pattern obtained from the simulations match with the experimental data. The CO_2 molecules form electron donor–acceptor complexes with the framework in the int polymorph. The suitability of AIMD for studying breathing in MOFs was confirmed by showing that at even higher CO_2 loadings the simulated powder diffraction pattern matches the experimental pattern obtained at a CO_2 pressure of 0.9 bar.

Interestingly, Haigis et al.²¹⁴ also reported AIMD simulations on hydrated MIL-53(Cr). By examining the distribution of the adsorbed H_2O molecules in the np and lp forms, they were able to discern differences in their adsorption dynamics. In the np form, the adsorbed molecules occupy specific crystalline sites, whereas they show a more disordered and bulk-like structure in the lp form. More recently, Haigis et al.²¹⁵ carried out an interesting methodological study of constant pressure (NPT

ensemble) AIMD simulations on MIL-53(Ga). The transition of the polymorphs of MIL-53(Ga) was found to depend crucially on the description of dispersion interactions. This is unlike the previously noted findings of Walker et al.^{15b} The coordination chemistry of the Ga atoms favors the lp polymorph, while dispersion interactions favor the np polymorph. Haigis et al.²¹⁵ also examined the performance of some commonly used dispersion-corrected functionals, with prescriptions about their performance, modifications, and use in future AIMD studies on flexible MOFs. They also found that large Gaussian basis sets and plane wave cutoffs, larger than the settings used in most investigations, are crucial for accurate calculation of stresses and atomic forces.

We note that Ghoufi et al.²¹⁶ have been able to use parameterized force fields to capture the temperature-, pressure-, and chemical-induced lp–np transformation in MIL-53(Cr), suggesting that classical MD simulations can be used when there are accurate force fields or when AIMD simulations are excessively expensive.

There have been several attempts at predicting the conditions required for a MOF to display framework flexibility associated with bistability or polystability.²¹⁷ There are however only a few attempts in which electronic structure calculations have been used to correlate the mechanical and framework flexibility properties of MOFs. Ortiz et al. have shown that the possibility of structural transitions between polymorphs can be deciphered by looking at the local elastic properties of MOFs.²¹⁸ They showed that flexible MOFs have very large anisotropies in their Young's and shear moduli, compared to nonflexible MOFs. As examples, the anisotropies in the Young's moduli of MOF-5 and ZIF-8 are 2.1 and 1.4, respectively compared to 105 and 444 for MIL-53(Al) and MIL-53(Ga), respectively. These principles have been used to predict the existence of framework flexibility in two recently synthesized MOFs.²¹⁹

4. GAS ADSORPTION AND SEPARATION

There is a large body of literature in which electronic structure methods are used to study the adsorption and separation of gas molecules (e.g., Ar, H₂, H₂O, CO, CO₂, N₂, CH₄, C₂H₆, and C₂H₄) by MOFs. These reports are reviewed in this section. Researchers generally attempt to determine the various binding sites of guest molecules in MOFs, the adsorption energies at the binding sites, and the selective adsorption of some guest molecules over others. In addition, researchers often use first-principles calculations to generate force field parameters that are then employed in classical MD and GCMC simulations. Indeed, the earliest instance of the use of electronic structure methods to study gas adsorption/diffusion in a MOF involved computation of atomic charges at the DFT level of theory for the Cu–BTC²²⁰ and MOF-5²²¹ frameworks. These partial charges were used in GCMC simulations to study the separation of gas mixtures in Cu–BTC and the diffusion of several gases in MOF-5.²²¹

A complication in considering adsorption is that as the gases start to adsorb one needs to consider only sorbate–sorbent interactions. However, if the pores are large enough, as adsorption proceeds one must consider both sorbate–sorbent interactions as more molecules attach to the framework as well as sorbate–sorbate interactions as the guest molecules fill the pores.²²²

4.1. Computing Adsorption Energetics with Electronic Structure Methods

In this section, we provide a review of the more methodological/benchmarking aspects of using electronic structure methods for studying the adsorption of gases in MOFs. To be specific, what degree of accuracy can one expect from DFT and WFT approaches, especially in cases where physisorption plays an important role in adsorption (section 4.1.1)? Additionally, we examine the effects of using periodic unit cells and cluster models on the computed properties of adsorbed gases (section 4.1.2) as well as whether capturing the relative trends in gas adsorption energies is sufficient to accurately describe gas separation phenomena in MOFs (section 4.1.3). Overall, section 4.1 describes the degree of accuracy of modern electronic structure methods when used to study gas adsorption in MOFs. It lays the background for describing electronic structure effects on adsorption (section 4.2), the influence of trace gases on gas adsorption (section 4.3), coadsorption and diffusion of gases in MOFs (section 4.4), as well as the adsorption of gases by guest ligands or reagents in MOFs (section 4.5).

4.1.1. Physisorption and Choice of Electronic Structure Method. As noted earlier, periodic DFT and molecular cluster calculations with DFT or ab initio methods are commonly used approaches for studying MOFs. The suitability of various approximate exchange–correlation functionals for studying the adsorption of gases on MOFs is however a crucial question. This is important as in many MOFs, gas molecules are adsorbed by physical interactions with open metal sites as well as with framework organic functionality. Kristyan and Pulay¹¹² have shown that most standard local and semilocal functionals do not correctly capture dispersion interactions, which are crucial in describing physisorption and diffusion of gases in nanoporous materials, and this is now widely understood in the community.

Poloni et al.^{185b} recently examined the performance of the PBE and PBE+D2 functionals as well as several derivatives of vdW-DF proposed by Dion et al.¹¹⁵ in predicting the adsorption energy of CO₂ on Mg–MOF-74 and Ca–BTT (H₂Ca[(C₄Cl)₃(BTT)]₈ where BTT^{3–} is 1,3,5-benzenetristetrazolate ligand). They carried out periodic DFT calculations with these functionals while employing norm-conserving Trouiller–Martins pseudopotentials. PBE predicts an adsorption enthalpy of 18.2 kJ/mol for CO₂ on Mg–MOF-74 in comparison to an experimental value of 39–40 kJ/mol. Addition of the D2 empirical dispersion correction from Grimme¹²¹ brings the calculated value to within 0.5–1.5 kJ/mol of the experimental value. A similar difference of about 20.3 kJ/mol was found between the calculated adsorption enthalpies of CO₂ on Ca–BTT obtained with the PBE and PBE+D2 approaches. Among the vdW-DF-type methods (vdW-DF, vdW-DF2, vdW-PBE, vdW-CO9x, and vdW-optB88) that were also tested by Poloni et al.,^{185b} it was found that only the vdW-DF and vdW-DF2 functionals could accurately predict the adsorption energy of CO₂ on Mg–MOF-74. The inclusion of dispersion in the PBE-D2, vdW-DF, and vdW-DF2 approaches is crucial. PBE fails because it does not fully account for the dispersion effects that are involved in the physisorption of CO₂ at the Mg and Ca sites of Mg–MOF-74 and Ca–BTT, respectively.

Valenzano et al.^{144c} also arrived at this conclusion in their study of the adsorption of CO and CO₂ on M–MOF-74 (M = Mg, Ni, and Zn). They found that the mean error for the

B3LYP+D* approach is about 5.6 kJ/mol, while a hybrid MP2:B3LYP+D* (see ref 144c for details) approach provides a smaller mean absolute error of 3.8 kJ/mol. Yu et al.¹⁸¹ reported that LDA and other GGA functionals such as PW91 and even hybrid functionals such as B3LYP all fail to accurately predict the CO₂ binding energies to several M–MOF-74 frameworks (M = Mg, Mn, Fe, Co, Ni, Cu, and Zn).

We note that there is no guarantee that the good performance of the PBE+D2, vdW-DF, and vdW-DF2 functionals for CO₂ adsorption on Mg–MOF-74 will necessarily extend to the adsorption of other gases on other MOFs. As an example, Grajciar et al.²²³ examined the performance of 3 GGA (PBE, RPBE, and BLYP), a meta-GGA (TPSS), and two hybrid (B3LYP and BHLYP) functionals for predicting the binding energy of H₂O to a paddle-wheel cluster model of the Cu–BTC MOF. They also computed the binding energies predicted by these density functionals augmented with the empirical D2 and D3 dispersion correction.^{114,120,121} As seen in Figure 14, the

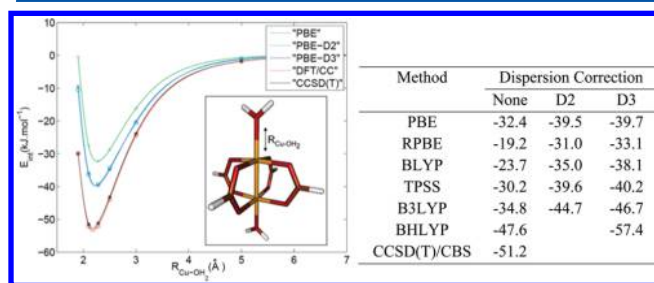


Figure 14. (Left) Interaction energy of H₂O with Cu₂(HCOO)₄, a model cluster of Cu–BTC, at various levels of theory. (Right) Full list of the calculated values of the adsorption energy of H₂O on Cu₂(HCOO)₄ obtained with several density functionals and at the CCSD(T)/CBS level. All energies are given in kJ/mol. Reprinted with permission from ref 223. Copyright 2010 American Chemical Society.

GGAs and meta-GGAs as well as the GGA+D2/D3 and TPSS+D2/D3 approaches significantly underestimate the results obtained at the CCSD(T)/CBS level as well as the experimental result (-51 ± 3 kJ/mol) obtained by Henninger et al.²²⁴ at 318 K. BHLYP (50% exact exchange) binds H₂O more tightly than B3LYP (20% exact exchange), a situation expected from the tendency of exact exchange to lead to shorter bonds. Grajciar et al.²²³ noted that addition of dispersion corrections on top of the density functionals is unreliable as it leads to either underestimation errors (significant for the GGAs and metaGGAs but slight for B3LYP) or an overestimation error of 6.2 kJ/mol (in the case of BHLYP), Figure 14. Similarly, Chavan et al.²²⁵ reported that computations at the B3LYP-D*/TZVP level underestimate the heat of adsorption of water and H₂S on Ni–MOF-74 by about 32 and 10 kJ/mol, respectively.

The results in Figure 14 were obtained by considering adsorption of H₂O at only one site in Cu–BTC. As a result, they should not be directly compared to experiments as Castillo et al.²²⁶ had previously shown with GCMC simulations that there are three types of adsorption sites in Cu–BTC. To correct for this, Grajciar et al.²²³ carried out further periodic calculations with PBE and a parametrized DFT/CC approach in which two sites in the MOF are occupied by H₂O molecules. They obtained an average binding energy of -30.6 kJ/mol with PBE, still significantly off from the experimental value. The

DFT/CC approach of Nachtigall et al.²²⁷ corrects the errors in DFT by representing them in a pairwise fashion as a sum of atom–atom correction functions and assuming that these correction functions are transferable from small reference systems to the systems of interest, in particular

$$\Delta E = E_{\text{CCSD(T)}} - E_{\text{DFT}} = \sum_{ij} e_{ij} R_{ij} \quad (4.1)$$

In eq 4.1, $E_{\text{CCSD(T)}}$ and E_{DFT} are the energies from CCSD(T) and DFT, respectively, R_{ij} is the distance between atoms i and j , and e_{ij} is a reproducible Hilbert space interpolation. After parametrizing the DFT/CC approach on smaller systems, Grajciar et al.²²³ obtained an average binding energy of -50.3 kJ/mol for the two binding sites. The physical manifestation of the dispersion effect can be seen in the calculated Cu–OH₂ bond lengths: 2.21 and 2.23 Å for DFT/CC versus 2.27 and 2.31 Å for PBE and 2.17 Å from experiment.^{12b} The correction functions obtained for the DFT/CC approach in this work have been used to successfully identify the adsorption sites of C₃H₈ and C₃H₆ on Cu–BTC.²²⁸ Hermann and Bludsky proposed a new vdW-DF/CC scheme with simplified correction functions.²²⁹ This method has been used to study adsorption of gas species on zeolites. The advantage of the DFT/CC approach is that it ensures that calculations on large systems with standard functionals attain the accuracy of CC theory by using error functions obtained from high-level calculations on small systems. It might yet be that while dispersion-corrected DFT methods can accurately predict the binding energies of gases to MOFs, one might need dispersion parameters obtained by fitting to high-level wave function approaches to obtain accurate predictions of the bond distances between open metal sites and guest gas molecules. As an example, we contrast the good performance of the DFT/CC method for the Cu–OH₂ bond length in Cu–BTC (2.21–2.23 Å)²²³ versus the rather wide range of “errors” (0.01–0.41 Å and 3–14°)^{22c} in the calculated metal–oxygen (M–O) distances and M–O–C angles obtained from vdW-DF2+U calculations on CO₂ adsorbed in the MOF-74 series. Interestingly, the M–O distances were accurately predicted for Mn–, Co–, and Cu–MOF-74, while rather larger errors were obtained for their Mg, Fe, Ni, and Zn analogues.

We note that although correction of existing functionals with the empirical D1, D2, or D3 schemes of Grimme et al. or the DFT/CC approach are rather inexpensive ways of including dispersion effects, there are modern functionals (beyond the aforementioned vdW-DF and vdW-DF2) that implicitly incorporate dispersion effects and that are applicable to a wide range of systems. Toda et al.²³⁰ re-examined the adsorption of H₂O on Cu–BTC with 15 functionals as well as with MP2. After full optimization of their cluster model with MP2, they obtained excellent agreements with the experimental adsorption energy (deviation of ~ 1.5 kJ/mol) and structural properties (0.02–0.08 Å); Yu et al. used a similar approach in their study on CO₂ adsorption by several M–MOF-74 frameworks.¹⁸¹ Among the functionals examined by Toda et al., M05-2X and B2PLYPD,²³¹ a double hybrid functional with empirical D2 corrections, provided the best energetic and geometric data. They noted that the M06-L, M06, and LC-BLYP¹³⁷ functionals as well as the combined M06-L/M05-2X approach represent the best compromise between the accuracy of calculated data and the computational cost with the local M06-L functional being cheapest for both energies and geometry optimizations.

The good performance of the M06-L functional is not limited to interactions between metal sites and guest gas molecules. Witte et al.²³² recently studied the interaction of guest gas molecules with organic linkers in MOFs by using the benzene–CO₂ model. This is a reasonable model given that the organic linkers in most MOFs are either aromatic or highly conjugated. They compared results obtained at the MP2 and CCSD(T) levels to those obtained with 16 density functionals as well as their D2- and D3-corrected counterparts. They used the aug-cc-pVTZ basis set for all DFT calculations. Of the standard GGA and meta-GGA functionals that were tested, ω B97X and M06-L had the best performance.

4.1.2. Periodic and Truncated Cluster Models. Intuitively, one would expect that calculations based on periodic unit cells or on larger and relaxed cluster models would provide better results than those based on small clusters. The studies that we describe in the following show that when the phenomena under investigation are localized, smaller clusters can be also be quantitatively accurate. In most cases, though, one cannot separate errors due to truncation to a cluster model from those errors that are due to the inexactness of the density functional or incompleteness of the wave function method.

Verma et al.^{144d} carried out a systematic study of the adsorption of C1–C3 hydrocarbons on Fe–MOF-74. They used a cluster model containing three Fe atoms, Figure 15, and

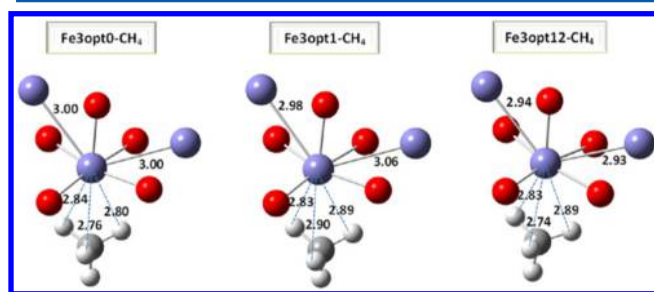


Figure 15. Three computational scenarios of a cluster model of CH₄ adsorbed at the Fe centers of Fe–MOF-74. See text for description of these scenarios. Reprinted with permission from ref 144d. Copyright 2013 American Chemical Society.

examined three different scenarios: when only the geometry of the guest molecule is optimized (Fe3opt0-guest), when the positions of the Fe atom and the guest molecule are optimized (Fe3opt1-guest), and when the positions of the Fe atom, the guest molecule, and 11 atoms in the first coordination sphere around the metal are optimized (Fe3opt12-guest). The cluster was obtained from the crystal structure of Fe–MOF-74. They used the M06-L functional with the def2-TZVP basis set. For CH₄ and C₃H₈, they found that as more atoms are optimized, the calculated adsorption enthalpies get closer to the experimental values. For CH₄, they obtained 28, 23, and 23 kJ/mol for the Fe3opt0-guest, Fe3opt1-guest, and Fe3opt12-guest models, respectively, in comparison to the experimental value of 20 kJ/mol. In contrast, no tangible change in the calculated adsorption enthalpy was obtained for C₂H₆, while for the unsaturated hydrocarbons the binding actually becomes much stronger as more atoms are optimized. As a result, the Fe3opt12-guest model overestimates the experimental adsorption energies of C₂H₂, C₂H₄, and C₃H₆ by 13–21 kJ/mol. Despite this large overestimation of the binding energies of the unsaturated hydrocarbons in the Fe3opt12-guest model, all

cluster models considered were able to reproduce the trend in the experimental adsorption enthalpies (CH₄ < C₂H₆ < C₃H₈ < C₃H₆ < C₂H₄ < C₂H₂). The trends in the calculated energies explain the experimental separation of ethylene/ethane and propylene/propane mixtures that were previously reported by Bloch et al.^{183b}

Kim et al.²³³ reported periodic DFT calculations with PBE+D2 and RPBE+D2 on the adsorption of the C1–C3 hydrocarbons by Fe–MOF-74. They obtained similar trends to those of Verma et al.^{144d} However, their results generally underestimate the experimental data, while those of Verma et al.^{144d} generally give overestimates.

In cases where guest–MOF interactions are completely localized on the metal site, the organic linker can be truncated to allow for only a good description of the first coordination sphere around the metal. Supronowicz et al.¹⁴³ studied the effect of cluster model sizes on the computed adsorption energies of several gases by Cu–BTC. Their BTC linker was truncated to a formate ligand in their model cluster, Cu₂(HCOO)₄. They also carried out calculations that used the complete BTC ligand in Cu₂(BTC)₄. In nearly all cases, the energy difference is small (1–4 kJ/mol), suggesting that a reasonable truncation of the organic linker can provide correct adsorption energies and trends while significantly reducing computational costs.

4.1.3. Gas Separation and Trends in Adsorption Energies. For gas separation and purification purposes, it is important that the chosen level of theory captures the correct trends in the adsorption energies of the constituents of a gas mixture on the MOF. More desirable still, of course, is the prediction of accurate *absolute* energies of adsorption. In a recent study, Lee et al.⁷⁰ predicted that a V(II) analog of Fe–MOF-74 will have a considerably higher enthalpy of adsorption for N₂ than for CH₄ and as such could be used in separating a mixture of these gases. They used three models: periodic DFT calculations with the vdW-DF2+U approach; DFT (M06-L, M06, and M11-L) and counterpoise-corrected CASPT2 (CASPT2-CP) calculations on an 88-atom cluster model; and finally calculations with the vdW-DF2+U, M06-L, CASPT2-CP, and LPNO-CCSD/CBS approaches on an even smaller cluster model. All methods used in this work predict that V–MOF-74 adsorbs N₂ more strongly than CH₄ with differential adsorption energies, $\Delta(N_2/CH_4)$, ranging from 9 to 42 kJ/mol. All methods also predict that the V²⁺ MOF moreover adsorbs N₂ more strongly than the Fe²⁺ MOF. Lastly, all methods predict that the Fe²⁺ MOF would *not* be efficient for separating N₂ and CH₄. The agreement between the DFT and the WFT approaches as well as the agreement between the periodic and the cluster models increases confidence in the predictions and can be recommended as a best practice. While synthesis of V–MOF-74 remains to be realized, comparison of the calculated and experimental absolute binding energies of N₂ and CH₄ to Fe–MOF-74 shows that the results obtained with the periodic model are within 6.0 kJ/mol of the experimental results.

In a similar predictive spirit, Kim and Jung²³⁴ proposed, based entirely on first-principle calculations, that Fe–MOF-74 can be used to separate 1-butene from other isomers of butene. They obtained a binding energy of –55 kJ/mol for 1-butene and only –31, –41, and –42 kJ/mol for *trans*-2-butene, *cis*-2-butene, and isobutene, respectively. They used the RPBE+D2 approach in their periodic DFT calculations. Although it was previously known that several MOFs (e.g., ZIF-7²³⁵ and Cu–

BTC²³⁶) and zeolites (RUB-41²³⁷) could selectively adsorb some isomers of butene while excluding others, this is the first evidence that high-purity 1-butene gas could be obtained in a one-step process.

Watanabe et al.²³⁸ reported that Cu(HFIPBB)-(H₂HFIPBB)_{0.5} (H₂HFIPBB = 4,4'-[hexafluoroisopropylidene]-bis[benzoic acid]), a microporous MOF membrane, could be used to separate CO₂ from CH₄. The calculated adsorption energies for these two gases on the MOF only differ by about 4 kJ/mol (−10 kJ/mol for CO₂ and −6 kJ/mol for CH₄). The calculations were carried out with the PW91 functional in a periodic DFT framework. This standard GGA does not account for dispersion forces, and it is therefore possible that these energies underestimate the correct binding energies of the gas molecules on this MOF. The potential of this MOF for separating CO₂ and CH₄ appears to lie in the relative activation energies for gas diffusion from the center of the MOF to the adsorption site. Gas diffusion is significantly faster for CO₂ (activation barrier of 16 kJ/mol) than for CH₄ (activation barrier of 45 kJ/mol). The computations showed that the MOF membrane is 10⁴–10⁵ times more selective for CO₂ than CH₄.

In some cases, selective gas adsorption at different sites in a MOF may occur for different reasons. Ray et al.²³⁹ recently studied CO₂/CH₄ separation in a set of five ZIFs with the vdW-DF2 functional. They showed that selectivity at different sites in these ZIFs arise from three factors: differential electrostatic interactions, hydrogen bonding with CO₂, and steric constraints. Steric constraints are more important for CH₄ as it largely binds to the ZIFs through dispersion interactions. They also reported that CO₂ diffuses more readily in ZIF-93 than CH₄, despite the fact that it is more strongly bound to the framework. This was also the case in the aforementioned report of Watanabe et al.²³⁸ It was determined from NEB calculations that this MOF has a large electrostatic potential in its channel, a fact that contributes to lower CO₂ transport barriers.²⁴⁰

4.2. Influence of Electronic Structure on Adsorption Energetics

After predicting that V–MOF-74 binds N₂ more strongly than CH₄ during their study of its potential for efficiently separating these gases, an electronic structure understanding of this differential was provided.⁷⁰ Lee et al.⁷⁰ used three approaches, all based on their model clusters. First, they computed the total charges on the adsorbed N₂ and CH₄ species using the charge model 5 (CMS) method developed by Marenich et al.²⁴¹ In their 88-atom cluster, they found that the partial charge of the V center increases by 0.07 upon adsorption of N₂ but decreases by 0.07 upon adsorption of CH₄, a situation that would be consistent with the existence of larger π -back-bonding in the case of V–N₂ adsorption. In contrast, the charge on the Fe center of Fe–MOF-74 is fairly insensitive to the presence of N₂ or CH₄. Second, they analyzed the covalent portion of the interaction energy between the MOFs and the guest molecules using the natural orbitals for chemical valence (NOCV) theory developed by Ziegler's group.²⁴² This approach decomposes the orbital overlap energy obtained from the extended transition-state method (ETS)²⁴² into components based on orbitals that are easily understood within chemical valence theory. The results of these analyses are shown in Figure 16. Briefly, the σ donation and π^* back-bonding interactions are much weaker for Fe–N₂ than for V–N₂. The results of these NOCV analyses were confirmed with a natural bond orbital

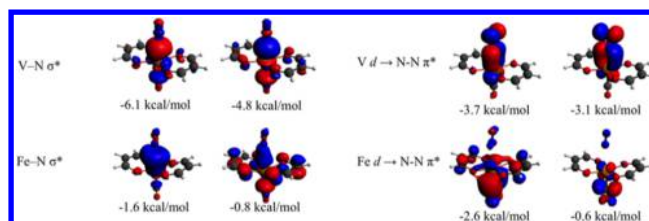


Figure 16. Strongest four NOCV orbitals found to contribute most to the interaction of N₂ with the metal sites in V–MOF-74 (top) and Fe–MOF-74 (bottom). Eigenvalues of the NOCVs are shown below them. Reprinted with permission from ref 70. Copyright 2014 American Chemical Society.

analysis (NBO).²⁴³ In the NBO analysis, the adsorption of N₂ on the V centers of V–MOF-74 includes identification of a localized V–N σ bond, while no analogous bond was predicted for the Fe–N₂ system. Second-order perturbation theory in the KS matrix of the natural bond orbitals indicates that the back-bonding ($\pi \rightarrow \pi^*$ of guest NBO orbitals) is roughly about 134 kJ/mol for V–N₂ and only about 54 kJ/mol for Fe–N₂ (For this analysis, the absolute values of the back-bonding are not expected to be quantitative but the significant difference in values is expected to reflect accurately the relative importance of the phenomenon).

Poloni et al.^{22b} also used charge and molecular orbital analyses to interpret the trends in the binding energies of CO₂ to the open metal sites (specifically Mg, Ca, Ti, V, Cr, Mn, Fe, Co, Ni, Cu, and Zn) of the BTT and MOF-74 frameworks. To study the ionic/electrostatics contribution to binding, they examined the relationship between the binding energy and a Q/r parameter. Q/r is the ratio of the M lliken charge of the metal or the ligand nitrogen closest to CO₂ to the distance between the CO₂ oxygen and the metal or the CO₂ carbon and the organic linker. They found that the calculated binding energies are independent of the Q/r contributions of the ligand but strongly depend on the Q/r values for the metal center, Figure 17. The only exceptions to the correlation between binding energy and the metal's contribution to the Q/r parameter were Ti and V. Rather than using a Q/r parameter, Koh et al.²⁴⁴ simply used the calculated partial charges (Q) at the metal centers and arrived at essentially the same conclusion for M–MOF-74 and M–BTC. Ti and V displayed significantly stronger binding of CO₂ than would be expected from the computed Q/r or Q .

To explain why Ti and V do not follow the simple Q/r model, Poloni et al.^{22b} noticed that after coordination of CO₂ (through an oxygen atom), the approximately square pyramidal symmetry of the unsaturated metal site is transformed into a pseudo-octahedral site as a result of the interaction between the d_{z^2} orbital of the metal and one of the lone pairs of the oxygen atom, Figure 17b. This mixing and imposition of pseudo-octahedral symmetry results in the stabilization of the oxygen lone pair orbitals and a destabilization of the d_{z^2} orbital. For Ti (d^2) and V (d^3), the d_{z^2} orbital is actually empty, such that the overall result of CO₂ adsorption is a net stabilization due to the stabilization of the oxygen lone pair orbitals. In contrast, for metals in which the d_{z^2} orbital is singly occupied, CO₂ adsorption is associated with both stabilization of the oxygen lone pairs and destabilization of the d_{z^2} orbital. This explains why the CO₂ binding energy to Fe–BTT is 47.2 kJ/mol, about one-half the binding energy to V–BTT. An additional (albeit modest) destabilization is found when the d_{z^2} orbital is doubly

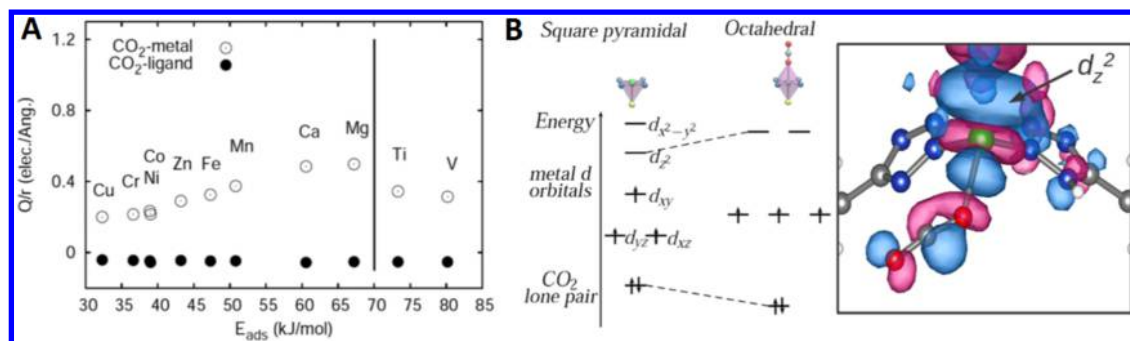


Figure 17. (A) Relationship between the calculated binding energies of CO₂ to several M-BTT MOFs and the calculated Q/r (Mülliken charge to distance ratio) parameter. (B) CO₂ capture alters the crystal field splitting pattern of the V (d³) site from square pyramidal to octahedral. (C) Plot of the metal–CO₂ antibonding orbital showing interaction of the metal's d_{z²} orbital with the adsorbed CO₂ guest. Reprinted with permission from ref 22b. Copyright 2014 American Chemical Society.

occupied, as in Cu (d⁹) and Zn (d¹⁰). This orbital stabilization/destabilization interpretation notwithstanding, there is still a significant role for electrostatics in determining the overall binding energy. For example, the greater Q/r parameter of Zn-BTT ensures that it binds CO₂ more strongly than Cr-BTT, Co-BTT, and Ni-BTT, Figure 17a.

Zhou et al.²⁴⁵ had previously shown that H₂ adsorption on two different MOFs with open metal sites is dominated by Coulomb attraction and strongly correlated with ionic radius of the metal site. They used the PBE functional in their calculations and arrived at similar conclusions as Poloni et al.,^{22b} who employed the vdW-DF2 functional. This suggests that although medium-range correlation energy is crucial to obtaining accurate adsorption energies, standard GGA functionals adequately capture the dominant charge-transfer and electrostatic attraction portions of the total interaction energy that can dominate in polar instances. Park et al.²⁴⁶ have shown that the trends in the calculated binding energies of CO₂ to MOF-74, Figure 18, arise mainly from the electrostatic

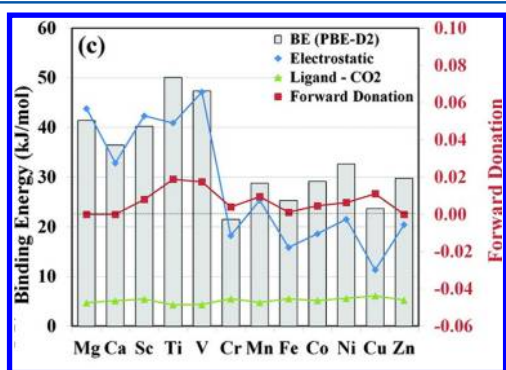


Figure 18. Decomposition of the binding energies of CO₂ to M-MOF-74 obtained at the PBE-D2 level of theory into electrostatic energy, ligand–CO₂ interaction energy, and forward donation terms. The forward-donation term describes the mixing of the lone pairs of CO₂ with the empty metal d orbitals. Reprinted with permission from ref 246. Copyright 2012 American Chemical Society.

interactions, with M = Ti being an exception to this correlation. The ligand–CO₂ interaction is essentially constant for all M-MOF-74, but the Ti-, V-, Mn-, and Cu-MOFs have appreciable spikes in orbital contributions, Figure 18. The calculations of Park et al.²⁴⁶ and Poloni et al.^{22b} show that dispersion effects might contribute up to 50% of the total adsorption energy of CO₂ to MOF-74.

The effect of an approximate octahedral ligand field on the splitting, stabilization, and destabilization of the 4d manifold of transition metals was also observed by Verma et al.^{144d} in their aforementioned work on the separation of C1–C3 hydrocarbons by Fe-MOF-74. By comparing the NBOs obtained for the Fe–C₂H₄ and Fe–C₂H₆ systems, they found weak electron donation from the π -bonding orbital of C₂H₄ to the 3d, 4p, and 4d orbitals of Fe whereas donation to the metal orbitals arises from the σ (C–H) bonding orbital of C₂H₆. The calculated eigenvalues of the natural atomic orbitals (NAOs) shows that there is far greater stabilization of the d_{xz} and d_{xy} orbitals upon adsorption of C₂H₄ compared to when C₂H₆ is adsorbed. Kim et al.²³³ also reported that the π -bonding orbital of C₂H₂ interacts strongly with the Fe centers of Fe-MOF-74.

Although the energy difference between fragment orbitals plays a significant role in determining orbital overlap, it should be noted that spatial overlap also contributes to determining the degree of interaction between two fragments. We illustrate with an example of how the localization of an orbital can determine its overlap with the orbitals of a guest molecule. After inelastic neutron diffraction experiments and capacity measurements²⁴⁷ showed that H₂ is strongly adsorbed by several Cu-MOFs with paddle-wheel frameworks, Kim et al.²⁴⁸ carried out periodic DFT/PBE calculations on the Cu₂-tetrabenzenecarboxylate (Cu₂-TBC) molecule in search of an atomistic explanation. They found that the diatomic paddle-wheel arrangement of the metal centers in this model MOF causes a strong localization of the 4s orbital, a situation that allows for (σ -s)-type coupling, Figure 19, between the occupied σ orbital of H₂ and the unoccupied 4s orbital of Cu²⁺. They then hypothesized that Zn and Mg would allow for better interactions with H₂ as the s orbitals of these metals have lower eigenvalues and are more localized. This hypothesis was confirmed by calculations on Zn and Mg analogues of their Cu₂-TBC system.

Subsequent to this report, Bak et al.²⁴⁹ examined the influence of electronic structure on the H₂ adsorption properties at the metal sites of M₂(HCOO)₄ (M = Sc to Zn) paddle-wheel frameworks. They found that the early transition metals (Sc to Cr) interact weakly with H₂ because of strong covalent metal–metal interactions in the paddle wheel. In contrast, for the late transition metals (Mn–Ni), although the filling of the metal–metal antibonding orbitals weakens the metal–metal bonds, the strong ferromagnetic coupling of the metal sites lowers the interaction with H₂. The strong σ -4s orbital overlap previously reported by Kim et al.²⁴⁸ is observed

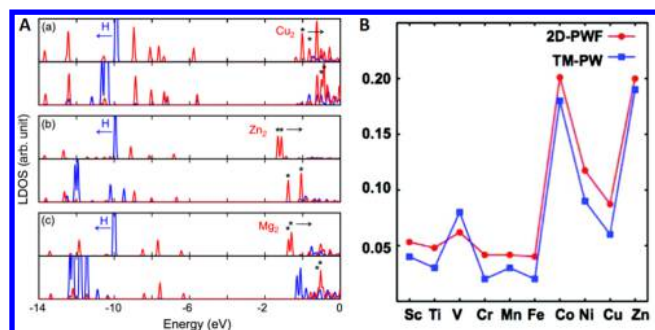


Figure 19. (A) Local s-orbital density of states obtained for M_2 -TBC ($M = \text{Cu}$, Zn , and Mg) MOFs before (top) and after (bottom) two equivalents of H_2 adsorption per node. Responsive unoccupied s-derived metal states are marked (*). (B) Computed H_2 adsorption energies (eV) on $M_2(\text{HCOO})_4$ ($M = \text{Sc}$ – Zn) paddle-wheel frameworks. Notice the sweet spots at Co and Zn. Reprinted with permission from refs 248 and 249. Copyright 2010 American Physical Society.

in the post-transition metals (Cu and Zn). Comparisons of the adsorption of H_2 or pyridine (a far stronger Lewis base) to these $M_2(\text{HCOO})_4$ paddle wheels show the latter to be adsorbed more strongly with concomitant weakening of the covalent bonds between the metal centers. On the basis of the study of Verma et al.,^{144d} this is likely due to electron donation from the aromatic π -ring orbitals of pyridine.

Although several studies have shown the importance of attractive electrostatic interactions as well as orbital overlap interactions, the binding energy between a MOF and a guest molecule can be decomposed into more than two terms. Hijikata and Sakaki²⁵⁰ recently examined the binding energy of MeNC , H_2O , C_2H_4 , C_2H_2 , CO , CO_2 , N_2 , CH_4 , and H_2 on paddle-wheel frameworks at the MP4(SDQ) and M06-L levels of theory. For cases with available experimental data, the adsorption energies obtained with M06-L and MP4(SDQ) were both within 5.0 kJ/mol of experimental values. This is another example of the apparent accuracy of the M06 family of meta-GGA functionals for such types of interactions. They then performed a localized molecular orbital (LMO) analysis of the HF wave function. This approach decomposes the binding energy into 5 terms: electrostatic interaction energy (ES), exchange repulsion energy (EX), charge transfer (CT) + polarization (Pol) interaction energy, and electron correlation effects. They found that the binding energy has a positive linear relationship with ES and a negative linear relationship with EX. As a result, the binding energy increases with the CT + Pol term. This suggests that more care should be taken in describing the role of electrostatic and orbital overlap interactions in determining the magnitudes and trends in binding energies. It also remains to be seen whether the results of the LMO analysis (and the relative roles of the different components) reported by Hijikata and Sakaki²⁵⁰ extend to KS theory.

We note that H_2 is generally adsorbed weakly by most MOFs with binding energies typically around 0–15 kJ/mol. Sastre²⁵¹ discussed the physical features of the hydrogen adsorption interactions in quantum-chemical terms, and Gomez and Sastre²⁵² performed MP2 calculations to determine the optimal H_2 adsorptions per metal site as well as the metal atom density in a MOF that will result in optimal adsorption for the 2015 storage targets.¹⁷¹ This follows on from earlier work by Lochan and Head-Gordon, who estimated that the storage material

must have an H_2 binding energy of 20–40 kJ/mol to meet the Department of Energy (DOE) target.²⁵³ They noted that storage materials that relied solely on van der Waals interactions are unlikely to achieve this challenge. MOFs that have no unsaturated metal sites are likely to have significant contributions from dispersion forces in their H_2 adsorption energies. Sillar et al.²⁵⁴ have shown through PBE, PBE+D, and MP2 calculations that dispersion contributes about 50% of the adsorption energy of H_2 to MOF-5. They showed that quantitative agreement with experimental results can be achieved by including zero-point energy (ZPE) corrections and assuming that H_2 molecules retain their rotational degree of freedom after adsorption. In a detailed study of the intermolecular potential between a MOF and a guest molecule as well as the quantum dynamics of H_2 adsorbed in MOFs, Matanovic et al.²⁵⁵ reported the results of rigorous quantum five-dimensional calculations of the coupled translation–rotation eigenstates of H_2 adsorbed on MOF-5.

4.3. Effects of Trace Gases on Gas Adsorption and Separation

There have been a few reports in which electronic structure methods were used to probe the effect(s) of trace gas contaminants on the adsorption properties of MOFs. This is particularly relevant given that gases such as N_2 , H_2O , as well as trace amounts of sulfur oxides (SO_x) and nitrogen oxides (NO_x) are known to be present in flue gases emitted from coal-fired plants. It is important that the effects of these gases on MOFs are properly understood before their large-scale adoption for capturing CO_2 from industrial flue gases.

Yu et al.^{17b} studied the impact of CO , H_2O , N_2 , NO , NO_2 , SO_2 , SO_3 , H_2SO_3 , H_2SO_4 , HNO_2 , and HNO_3 on the adsorption of CO_2 by Mg–MOF-74 and MIL-101. MIL-101 contains Cr_3O trimers and the BDC linker. They computed the structures of the guest–MOF systems and determined the binding energies of each of these gases at the unsaturated metal sites of the MOFs using the B3LYP-D and $\omega\text{B97X-D}$ functionals (for both MOFs) as well as MP2 (for only Mg–MOF-74). The adsorption free energies were then used in a single-site Langmuir model to estimate the occupancy of the unsaturated metal sites by the different gaseous species at finite pressures. They found that the poisoning of the MOFs by SO_x species is an important issue and that the strongly adsorbed H_2SO_3 and H_2SO_4 are particularly potent poisons for both MOFs. The strong binding of these species to the MOFs is large enough to overcome the kinetic effect of their low partial pressures relative to that of CO_2 .

Ding and Yazaydin²⁵⁶ performed similar calculations for the adsorption of NO_2 , NO , SO_2 , CO , and O_2 on M–MOF-74 ($M = \text{Mg}$, Ni , and Co), Cu–BTC, and two other MOFs as poisons for CO_2 capture, and their general results (SO_x species poison Mg–MOF-74 and prevents CO_2 adsorption) agree with those of Ding and Yazaydin.²⁵⁶ Yu and Schmidt²⁵⁷ have since commented that they overestimated the binding energy of SO_2 to Mg–MOF-74 by considering it as a quintet rather than expected closed-shell singlet state of Mg^{2+} . However, there is still a need for further theoretical and experimental research regarding the effects of contaminant gases on the adsorption properties of MOFs with unsaturated metal sites. This is in light of a recent report by Liu et al.,²⁵⁸ who found that MIL-101 actually retains its adsorption capacity for CO_2 after addition of H_2O , SO_2 , and NO to a 10 vol % CO_2/N_2 feed flow. Han et al.²⁵⁹ showed that the CO_2/N_2 selectivity remains largely

unchanged in several zeolites after exposure to humid air, SO₂, and NO₂. They also found a MOF for which short-term exposure to SO₂ and NO₂ actually caused an increase in CO₂ adsorption capacity.²⁵⁹

There have been a few electronic structure studies of the effects of contaminant gases on MOFs that have no open metal sites. Liu et al.²⁶⁰ carried out a combined DFT-GCMC study of the effects of H₂O, O₂, and SO₂ on CO₂ adsorption and CO₂/N₂ separation by ZIF-68. They arrived at the same conclusion as that of Yu et al.^{17b} for Mg-MOF-74: SO₂ poisons the MOF and inhibits both CO₂ adsorption and CO₂/N₂ separation. In contrast, O₂ has a negligible effect on the properties of the MOF, while H₂O can have a deleterious effect (by competing for adsorption sites) as well as a positive effect (by forming new adsorption sites for CO₂) on the properties of ZIF-68. However, Ding and Yazaydin²⁶¹ have since suggested that cooperative interactions between SO₂ and CO₂ molecules could actually have little or no effect on CO₂ adsorption by ZIF-10, ZIF-68, ZIF-69, and ZIF-71. They used the Universal Force Field (UFF) modified with electrostatic charges computed with DFT in GCMC simulations of CO₂ uptake by these MOFs.

Chen et al.²⁶² have shown through GCMC simulations based on electrostatic charge parameters obtained from DFT that the terminal water molecules in hydrated MIL-101 actually act as additional sites and enhance the adsorption of CO₂ more so than that of CH₄. Overall, these studies suggest that the ability of a trace gas to poison a MOF depends on two factors: first, the strength of its interaction with the MOF and, second, the strength of its interactions with other guest molecules after it has been adsorbed on the MOF. The GCMC simulations of Huang et al. also demonstrate this concept.²⁶³

It is also possible in some cases for a trace gas to replace some portions of the organic linker. In the M(BDC)(TED)_{0.5} systems (where TED is triethylenediamine and M = Cu, Zn, Ni, Co), the TED linker can be removed from the framework and replaced by water. Replacement of the TED linkers by water ligands converts the M(BDC)(TED)_{0.5} MOFs to M-MOF-2 structures. Tan et al.²⁶⁴ reported a combined experimental and theoretical examination of the stability of these MOFs in the presence of water. They found that the stability of the MOF depends critically on the identity of the central metal ions. While water displaces the TED linkers in the Zn and Co MOFs, the Ni analogue maintains its structure after exposure to water. In order to explain these experimental results, the energies required to replace a TED linker by 2, 4, 6, 8, and 10 water molecules were calculated with the vdW-DF functional for the Zn and Co MOFs. They found that while the hydration of Zn(BDC)(TED)_{0.5} is a spontaneous process, this is not the case for its Ni analogue. The Ni analogue is more resistant to hydration. Spontaneous hydration of the Ni MOF does not occur until 6 or more water molecules are used to replace one TED ligand.

The issue of stability to the presence of water has also been raised for UiO-66 and UiO-67.²⁶⁵ DeCoste et al.'s experimental work suggested an increase in chemical degradation by water (and hydrochloric acid) as the linker is changed from BDC (UiO-66) to BPDC (UiO-67).^{265a} A recent work by Mondloch et al.²⁶⁶ has however shown that UiO-67 (and NU-1000) are actually stable toward linker hydrolysis. Their experimental work revealed that with UiO-67 these MOFs collapse when activated from H₂O as a result of capillary forces. To support this, they carried out cluster model DFT calculations, which

showed that linker hydrolysis is overall an endoergic process (about 109 kJ/mol). To add to the evidence against hydrolysis, the ejection of the linker was calculated to have a barrier of about 118 kJ/mol. Additional empirical work by Mondloch et al.²⁶⁶ revealed that the framework collapse can be overcome by using solvents that exhibit lower capillary forces.

In MOFs with hydrophobic walls, it is likely that hydration will lead to formation of water clusters at the center of the cavities rather than to adsorption or hydrolysis. The advantage of hydrophobicity lies in the fact that other guest molecules can be adsorbed at the adsorption sites that were not occupied by water. Indeed, it has been shown that fluorinated MOFs (FMOFs), a class of MOFs with hydrophobic walls, have a high volumetric uptake of gaseous hydrocarbons relative to water vapor.²⁶⁷ In FMOFs, all hydrogen atoms of the organic linker are replaced by fluorine atoms. Nijem et al.²⁶⁸ recently carried out a joint experimental-theoretical investigation of the formation of water clusters in FMOF-1 (Ag₂[Ag₄TZ₆])_n, where TZ is 3,5-bis(trifluoromethyl)-[1,2,4-triazolate]. They carried out periodic DFT calculations and Born–Oppenheimer AIMD simulations with the vdW-DF functional while using USPs. Theoretically they found that while adsorption of one water molecule from the gas phase into the major pore is exothermic (~20 kJ/mol), adsorption from liquid water is endothermic (~35 kJ/mol). The single water molecule apparently migrates to the center of the pores from the initial docking positions during geometry optimization. This suggests that the water molecule is trying to avoid the hydrophobic walls of the pore that is dominated by fluorine entities.

A similar situation was observed when water clusters (dimer–pentamers) were embedded in the pores. Compared to liquid water, embedding small water clusters in the pores is an endothermic process. However, as the clusters become increasingly larger, they become more stable in the pores (17 kJ/mol for dimer, 12 kJ/mol for trimer, 5 kJ/mol for tetramer, and –12 kJ/mol for pentamer). This suggests that the water clusters formed away from the hydrophobic walls are stabilized by increased hydrogen bonding as they become larger. The walls of the MOF also likely confine the water clusters and impose a limit on their sizes. Indeed, by comparing calculated and experimental vibrational spectra of the embedded water clusters, it was deduced that the clusters contain less than six molecules. Interestingly, it was found that since water molecules are not strongly bound to the walls of the framework, CH₄ can penetrate and adsorb at its favored sites, the organic linker decorated with fluorine atoms. The results obtained from this study suggest the possibilities of using MOFs as reaction media (for performing reactions in the clusters localized at the centers of pores) and to clean up liquid hydrocarbon spills.^{267,268} We note that it is also possible to localize protonated water clusters in MOFs.²⁶⁹

4.4. Coadsorption and Diffusion of Gases in MOFs

Nijem et al.²⁷⁰ and Canepa et al.²⁷¹ recently studied the effect of gas loading on the computed adsorption energies, diffusion behavior, and IR spectroscopic signatures of H₂, H₂O, and CO₂ on Mg-MOF-74. They considered two cases: one gas molecule per unit cell or six guest molecules occupying the six metal sites. They found that while the computed adsorption energies of H₂ and CO₂ are insensitive to the gas loading, there is a decrease of about 3 kJ/mol when the loading of H₂O is increased from 1 to 6. This presumably occurs because of the repulsions between the hydrogen atoms of adjacent adsorbed H₂O molecules.

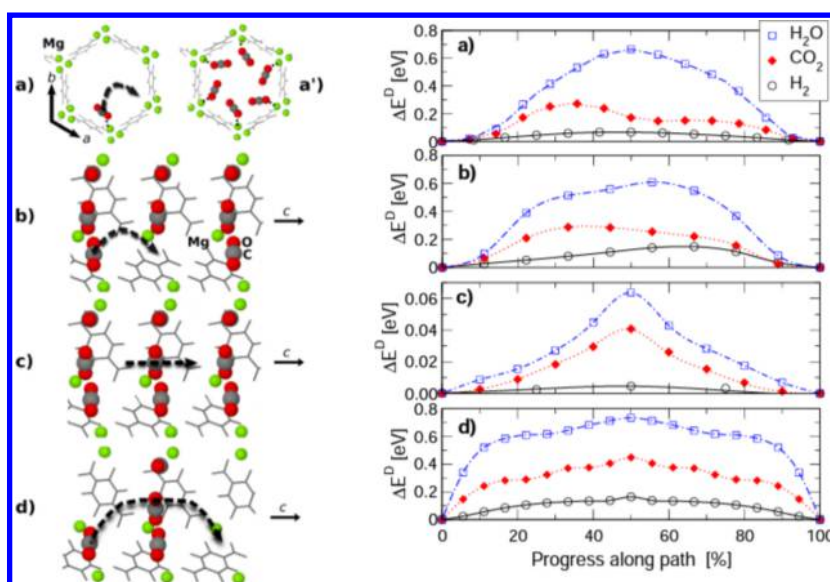


Figure 20. (Left) Schematic of the proposed diffusion mechanisms in Mg-MOF-74. View along the *c* axis when the number of CO₂ in the Mg-MOF-74 unit cell is 1 (a) or 6 (a'). Views perpendicular to the *c* axis are shown in b, c, and d. Diffusion paths are shown with dashed arrows. (Right) Energy profiles of the diffusion mechanisms shown on the left. These profiles were obtained with the NEB approach. Reprinted with permission from ref 271. Copyright 2013 American Physical Society.

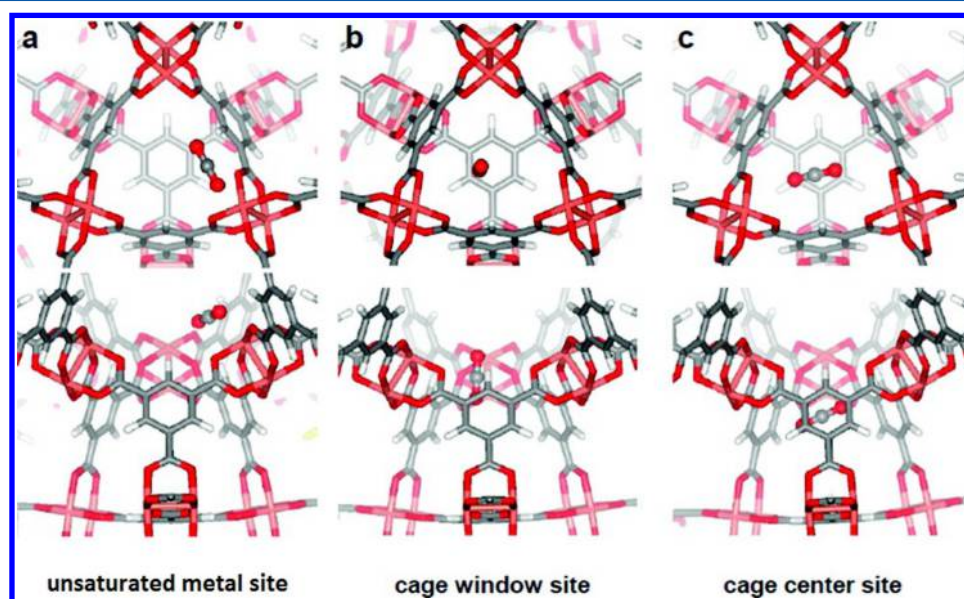


Figure 21. CO₂ adsorption in the three domains of Cu-BTC. Adsorption sites in the three domains are the unsaturated metal site, cage window site, and cage center sites. The latter two are occupied only at high CO₂ loadings. Reprinted with permission from ref 274. Copyright 2011 American Chemical Society.

Nijem et al.²⁷⁰ and Canepa et al.²⁷¹ found that the gas loading could also have an effect on the vibrational frequencies of the adsorbed gas. For CO₂, they computed a slight red shift ($\Delta\nu = -2 \text{ cm}^{-1}$) in the stretching mode when the loading is increased from 1 to 6. This slight red shift was confirmed experimentally. The vdW-DF functional was used in these calculations. The diffusion of H₂, H₂O, and CO₂ in Mg-MOF-74 at different loadings was also investigated. The NEB approach was employed in these calculations. Some of the results are presented in Figure 20. Four possible diffusion mechanisms were considered: (a) direct hopping from one Mg²⁺ site to the adjacent one, (b) longitudinal hopping from one Mg²⁺ site to the equivalent one in the next unit cell, (c) longitudinal motion of a molecule through MOF-74 loaded

with the same molecule, and (d) one previously adsorbed molecule moves through a barrier made by 6 molecules and binds again at an equivalent site two unit cells away. The latter two mechanisms are representative of molecular flow in the MOF-74 framework. In all cases, H₂O has the highest barrier to diffusion, Figure 20.

For the first two mechanisms, the barriers to hopping are essentially equivalent to the adsorption energies of the guest molecules at the Mg²⁺ centers. This is not unexpected, as these mechanisms require extraction of the adsorbed molecules. When the MOF is fully loaded with guest molecules, the diffusion barrier of an unadsorbed molecule (mechanism c in Figure 20) is very low, essentially barrierless for H₂. This indicates that the interactions between the diffusing molecules

in the middle of the MOF-74 channel and the adsorbed molecules at the metal sites are minimal. Lastly, it remains very difficult for a preadsorbed molecule to diffuse further into a fully filled MOF-74 framework (mechanism d), again likely because of the initially established coordination with a metal site. These results were shown to agree excellently with the results of time-resolved IR diffusion experiments. The calculated diffusion barrier of 0.04 eV (0.03 eV after correction for ZPE corrections) agrees quantitatively with the 0.03 eV barrier experimentally determined by Bao et al.²⁷²

Although Canepa²⁷¹ found that the binding energy of H₂ and CO₂ is insensitive to loading, this does not extend to MOFs in which additional sites can be occupied at high loadings or when the adsorbed molecules can interact in a cooperative fashion. Tan et al.²⁷³ found that the calculated adsorption energy of SO₂ on M(BDC)(TED)_{0.5} (M = Zn, Ni; TED = triethylenediamine) increases slightly with loading. When only 1, 2, 4, 6, and 8 SO₂ molecules are found in the unit cell, the calculated binding energies are -70, -68, -70, -75, and -77 kJ/mol, respectively.

Grajciar et al. employed the DFT/CC method as well as periodic calculations with the PBE functional to find that CO₂ adsorption energies on Cu-BTC increase from -23.1 kJ/mol at 1:12 (one CO₂ per Cu) coverage to -30.0 kJ/mol at 20:12 coverage.²⁷⁴ This was supported by experimental microcalorimetry measurements. The most interesting result is that Cu-BTC has several CO₂ capture domains, Figure 21. Up to a 12:12 coverage, only the open metal sites are occupied. Between the 13:12 and the 20:12 coverages, the cage window sites are occupied, while beyond 20:12 coverage, the centers of the small cages and large pores begin to be occupied. For this particular reason, one must take care when comparing experimentally measured isosteric heats of gas adsorption to calculated binding energies. To calculate the isosteric heat of adsorption, one would need to compute the adsorption energy of the guest molecule at all sites and the relative contributions of each binding site would be required. By trying various arrangements, orientations, and interaction sites of the guest molecule with the MOF, one can use DFT²⁷⁵ calculations or AIMD simulations^{170b} to probe the existence of multiple binding sites in a MOF.

4.5. Ligand-Assisted Adsorption in MOFs with Open Metal Sites

Poloni et al.²⁷⁶ studied the binding mechanism of CO₂ on Ca-BTT using periodic DFT calculations with the PBE and vdW-DF functionals. They found that CO₂ could bind to this MOF in two ways: first, by direct coordination to the unsaturated metal centers (A site) and, second, through the N₂ atoms of the tetrazole molecule found in the linker (B site, Figure 22). After determining the optimal positions of the extra-framework cations, they calculated the adsorption energies of CO₂ according to these two mechanisms. They found that CO₂ is more strongly adsorbed at the B site than at the A site, with the latter increasing the adsorption energy by up to 50%. The enhanced binding at the B site is a result of a 3-fold binding of CO₂ to the framework. The oxygen atoms of CO₂ interact with the H and Ca atoms of the framework, while the carbon atom is attracted to the negatively charged N atom of the tetrazole ligand, Figure 22. Poloni et al.²⁷⁶ then computed the CO₂ binding geometries and energetics when the tetrazole molecule of the BTT linker is replaced by oxazole (N atom of tetrazole is replaced by O) or triazole (N atom of tetrazole is replaced by

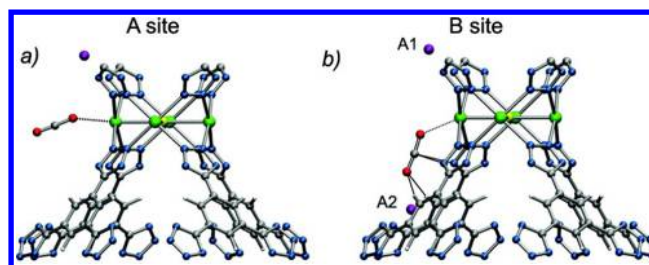


Figure 22. Coordination of CO₂ in Ca-BTT through (a) the A site or the unsaturated metal site and (b) the B site or a ligand-assisted adsorption. A1 and A2 sites are two of three extraframework metal atoms (purple) required to balance the overall negative charge of the framework. Reprinted with permission from ref 276. Copyright 2012 American Chemical Society.

CH). In both cases, the adsorption energy is reduced compared to the original tetrazole MOF. The larger partial negative charge on the nitrogen atom, compared to the oxygen atom of oxazole, allows for greater interaction between an oxygen atom of CO₂ and the correspondingly more positive protons of the tetrazole.

4.6. Gas Adsorption by Guest Molecules or Functionalizing Reagents

As previously noted, modification of the organic linker by inserting functional groups (e.g., amine, nitro, alcohol, etc.) can lead to improved adsorption energetics and capacity for specific gases by altering the structure of the MOF or by altering the local environment at absorption sites (see section 3.2). As another example, Halder et al.²⁷⁷ reported the synthesis of two interpenetrated MOFs containing Cd²⁺, aminobenzenedicarboxylic acid (NH₂-BDC), and 1,2-bis(4-pyridylmethylene)hydrazine). These MOFs show excellent selectivity for CO₂ over other gases as a result of specific interactions with the amino group of the NH₂-BDC linkers and the =N-N= group of 1,2-bis(4-pyridylmethylene)hydrazine. Periodic DFT calculations were carried out on one of these MOFs with the PBE-D2 approach. Halder et al.²⁷⁷ obtained an adsorption energy of 36 kJ/mol for CO₂, in good agreement with the experimental value of 38 kJ/mol. The presence of the amino group was exploited to catalyze a Knoevenagel condensation reaction.

It is however also possible to improve gas adsorption in MOFs by incorporating additional functionalities or guest molecules into the pore channels. As exposed metal sites are generally attractive to gas molecules, they can be used to improve adsorption by depositing them as dopants on the organic linker or by chemical insertion into the molecular structure of the organic linker. Another possibility that has been explored in the literature involves attachment of amine ligands to the open metal sites of several MOFs. This is due to the propensity of aqueous amines to adsorb gases like CO₂ as well as SO_x or NO_x gases. These are discussed below.

4.6.1. Amine Ligands at Open Metal Sites. In 2009, Demessence et al.²⁷⁸ successfully grafted ethylenediamine (NH₂CH₂CH₂NH₂) functionalities onto the open metal centers in Cu-BTT. Without the amine, Cu-BTT has an isosteric heat of adsorption of 21 kJ/mol for CO₂, a value only slightly above the enthalpy of liquefaction of CO₂. However, after grafting amines to the metal sites, the adsorption energy of CO₂ increased dramatically to about 90 kJ/mol. To our knowledge, this remains a record heat of adsorption for CO₂ by a MOF. This experimental result demonstrates that incorpo-

ration of guest molecules can actually be used to alter the adsorption properties of MOFs.

In 2012, Choi et al.²⁷⁹ employed experimental measurements and periodic DFT calculations to characterize Mg–MOF-74 with ethylenediamine (ED) molecules grafted to the Mg^{2+} centers. They used the PW91-D2 approach in their calculations. The calculated binding energies of 1, 3, 6, and 18 amine molecules to the metal sites in the unit cell of Mg–MOF-74 are 71, 95, 98, and 125 kJ/mol, respectively. Strong binding is expected given that the amines coordinate to the MOF through the interaction of their nucleophilic nitrogen atoms to the electrophilic open Mg^{2+} sites. However, the measured CO_2 adsorption capacity of the amine-functionalized MOF, ED-Mg–MOF-74, is only slightly above that of Mg–MOF-74. Choi et al. did not report any calculations exploring the adsorption energies of CO_2 to the amine-functionalized MOF or the reasons behind the similarity in the adsorption capacities of Mg–MOF-74 and ED-Mg–MOF-74.

However, in 2012, McDonald et al.^{38a} reported a study having similar conclusions to those of Demessence et al.²⁷⁸ Their experimental characterization showed that *N,N'*-dimethylethylenediamine (*mmen* = $\text{CH}_3\text{NHCH}_2\text{CH}_2\text{NHCH}_3$) functionalized $\text{Mg}_2(\text{dobpdc})$ has a high adsorption enthalpy for CO_2 and that the *mmen* groups are bound to almost every open metal site in the framework, Figure 23. At a first glance, one

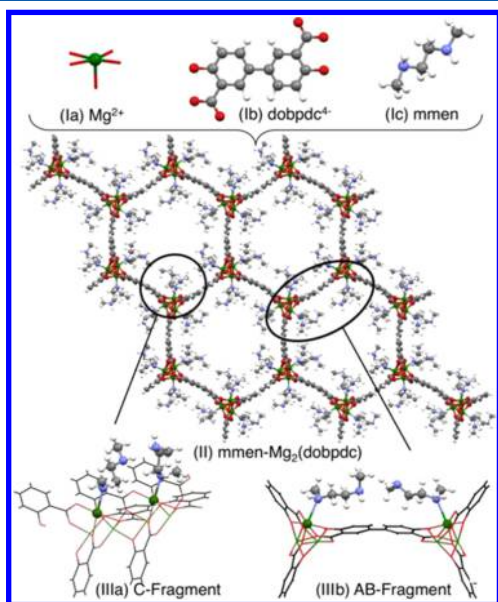


Figure 23. *mmen*– $\text{Mg}_2(\text{dobpdc})$ MOF contains Mg^{2+} metal sites (Ia), *dobpdc* organic linkers (Ib), and *mmen* ligands (Ic) grafted to the metal sites. Planas et al.^{144b} used cluster models to cut along the *c* axis (IIIa) or across the *ab* plane (IIIb) in their calculations. Reprinted with permission from ref 144b. Copyright 2013 American Chemical Society.

would surmise that the grafted amine ligands are involved in CO_2 adsorption. However, the experiments also suggested that adsorption occurs through a 1:1 amine: CO_2 stoichiometry, indicating that only one amine group is required per CO_2 molecule. This is completely different from the 2:1 amine: CO_2 stoichiometry expected from conventional aqueous alkylamine chemistry.²⁸⁰ In 2013, Planas et al.^{144b} proposed a mechanism that reconciles the high CO_2 adsorption energy of *mmen*– $\text{Mg}_2(\text{dobpdc})$ with the experimentally observed 1:1 amine: CO_2 stoichiometry.

To reduce the computational expense of their calculations, they designed two cluster models selected from optimized crystalline geometries, Figure 23. The clusters were cut either along the plane linking adjacent metal–*mmen* groups, *c* axis, or across the plane of the organic linkers, *ab* plane. The geometries of the cluster models were optimized with the PBE+D method while using a combination of def-SV(P) and def-TZVPP basis sets. In these geometry optimizations, the geometry of the MOF was held fixed while the positions of the *mmen* moieties and CO_2 were optimized. The effects of relaxing the positions of the Mg^{2+} sites and its neighboring oxygen atoms, Figure 23, were also explored. The proposed mechanism is shown in Figure 24. Two CO_2 molecules are inserted into the dangling ends of the *mmen* ligands grafted to the Mg^{2+} sites. The overall effect is that a dicarbamic acid product is formed across the *ab* plane of the MOF, with the COOH groups of each carbamic acid moiety interacting across the organic linker. The CO_2 :amine stoichiometry in this proposed mechanism is 2:2, as a second CO_2 group is recruited after the adsorption of the first one, Figure 24. The transition-state barriers of the steps in the proposed mechanism range from 0.1 to 40 kJ/mol, indicating that the adsorption of both CO_2 molecules is feasible under ambient conditions. In addition, the overall reaction energy is –138 kJ/mol for adsorbing two CO_2 molecules (average adsorption energy of –69 kJ/mol). This is consistent with the experimental isosteric heat of adsorption of –71 kJ/mol.

It should however be noted that a recently published experimental and theoretical work has indicated that adsorption of CO_2 by *mmen*– $\text{Mg}_2(\text{dobpdc})$ occurs via an insertion into magnesium–nitrogen bonds along the *c*-axis.²⁷⁸ This study demonstrated that the formation of interacting adjacent ammonium and carbamate groups results in an adsorption isotherm containing signatures of phase change behavior. It is possible that quantum-mechanical calculations and Monte-Carlo simulations will eventually be used to provide insights into the relative energies of this newly proposed chain-like ammonium-carbamate product and the paired carbamic acid species proposed by Planas et al.^{38b} as well as their relative contributions to the total adsorption isotherm.

4.6.2. Decorating MOFs with Metal Atoms. Functionalities that improve gas adsorption characteristics are not limited to amine groups coordinated to unsaturated metal sites. One strategy for increasing H_2 adsorption involves doping by heteroatoms or the decoration of MOFs with metal atoms. In 2007, Han and Goddard²⁸¹ showed through a combination of DFT calculations and GCMC simulations that doping of MOFs with lithium, a light electropositive metal, can be used as a strategy for increasing H_2 storage. They used the hybrid X3LYP¹⁰¹ density functional to determine the favored sites for Li atoms in five MOFs. After the geometry optimizations, the H_2 binding strengths of the metal oxide clusters and organic linkers of the lithium-decorated MOFs were computed at the MP2 level while employing a mix of QZVPP and TZVPP basis sets. In the pure MOFs, H_2 binds to the metal oxide clusters and organic linkers with binding energies of 6.3 and 3.8 kJ/mol, respectively. This only leads to high H_2 uptake below 77 K. In contrast, for the lithium-decorated MOFs, the H_2 binding energies are much higher, making them more relevant for H_2 storage at higher temperatures. The results of these computations were used to generate force field parameters that were subsequently used in GCMC simulations. Similar to the DFT calculations, the GCMC simulations show that

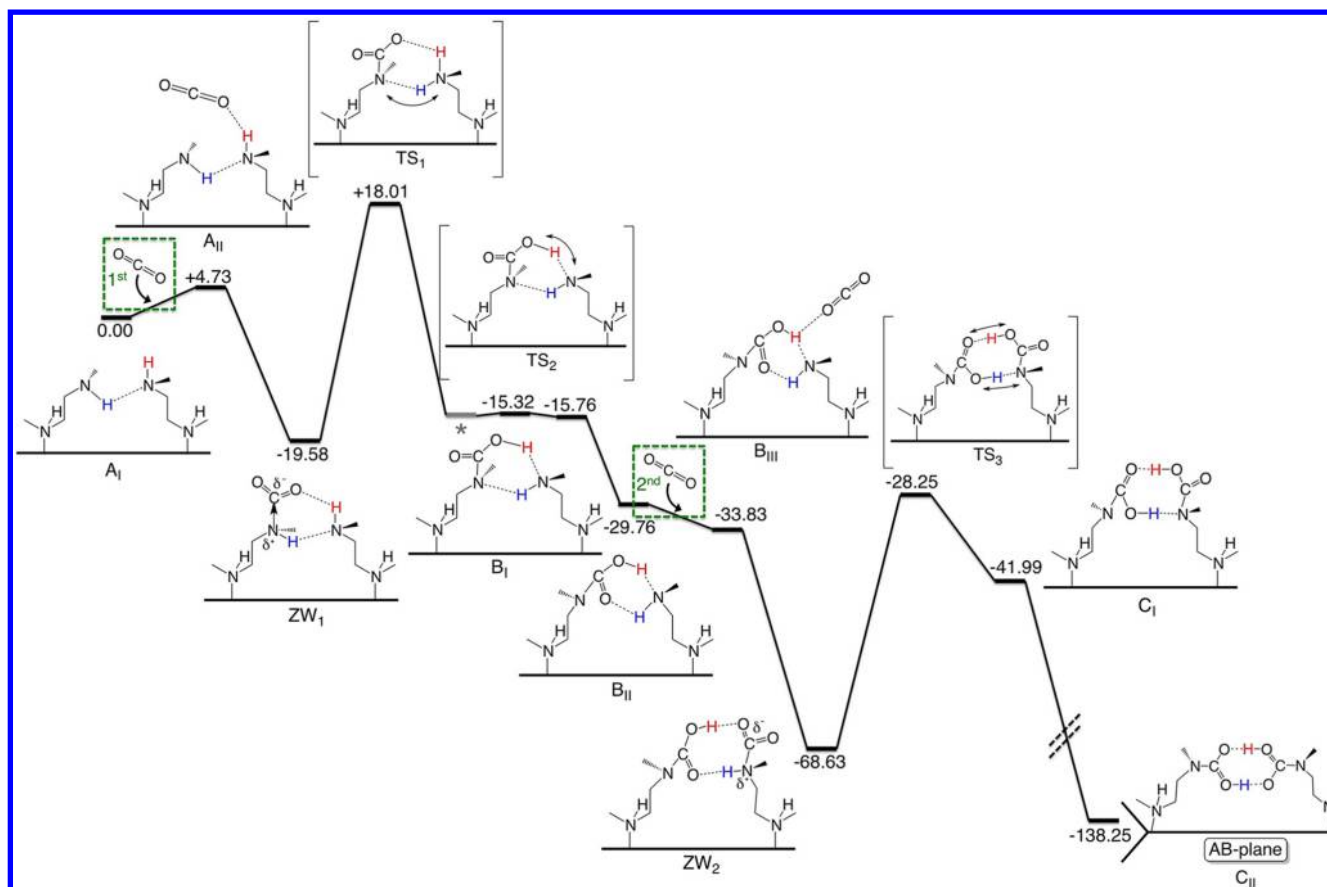


Figure 24. Proposed mechanism for CO_2 adsorption by $\text{mmen-Mg}_2(\text{dobpdc})$. Reaction energies and transition barriers were obtained at the PBE+D level of theory. The mechanism involves uptake of two CO_2 molecules with the final product being a dicarbamic acid species with the acid groups interacting across the *ab* plane through hydrogen bonds. Reprinted with permission from ref 144b. Copyright 2013 American Chemical Society.

decoration of MOFs with Li dramatically increases the H_2 adsorption capabilities of the five MOFs. Indeed, the simulations show that one of the MOFs, Li-MOF-30, can reach the 6.0 wt % gravimetric ratio at 243 K and 100 bar, the 2010 DOE target. Han et al. extended this approach to other MOFs.²⁸²

Periodic DFT calculations with a GGA functional by Blomqvist et al.,²⁸³ also reported in 2007, showed that the BDC linker of MOF-5 can bind two Li atoms and that each of these can bind up to 3 H_2 molecules. Their calculations showed that the formation of Li clusters inside the pores was unlikely due to energetic considerations. The binding energy per H_2 molecule is about 12 kJ/mol, significantly higher than that in pure BDC. AIMD simulations also reported in this work²⁸³ however showed that Li is coordinated with only 2 H_2 molecules at about 200 K. This amount is reduced at 300 K. Since then, several workers have shown that H_2 storage in MOF-5 storage can be strongly enhanced by decorating with Al, Sc, and Pd clusters under ambient conditions.²⁸⁴ Mavrandonakis et al.²⁸⁵ showed similar enhancement of H_2 storage capacity occurs after Li doping of IR-MOF-14. They noted that the enhanced storage capacity arises from strong polarization effects between the Li atoms and the adsorbed H_2 molecules. Dalach et al.²⁸⁶ studied two paddle-wheel Zn_2 complexes at the DFT and MP2 levels of theory. They found that the Li atoms enhance the H_2 adsorption energies and are associated with some oxygen atoms around the Zn_2 dimer, rather than with the organic linker as reported in previous

studies.^{281,283} Beyond decorating the aromatic linker with Li atoms, Sun et al.²⁸⁷ suggested a strategy that involves lithiation of the tetrazolidine moieties found in some MOFs. The lithium tetrazolidine groups provide 14 binding sites for H_2 and are much more stable than the alkoxide moieties in the MOF.

4.6.3. Organic Linkers Functionalized with Lithium Atoms. In 2008, Klontzas et al.²⁸⁸ reported computations on the H_2 adsorption properties of IR-MOF-8 and IR-MOF-14 modified with lithium alkoxide. In these systems, a Li atom is added to the naphthalene rings of IR-MOF-8 and to the pyrene rings of IR-MOF-14. Essentially, an alcohol group in the original organic linkers is converted into a lithium alkoxide moiety. This chemical transformation was later achieved experimentally by Mulfort et al.^{247a} in 2009. The binding energies of H_2 on IR-MOF-8 and IR-MOF-14 functionalized with Li were computed as 9–13 kJ/mol in each case. The calculations were carried out at the PBE/TZVPP level of theory. These values are about 2–3 times higher than those in the pure MOFs. The high adsorption energies in the lithiated MOFs are likely a result of charge-induced dipoles between the positively charged Li atoms and H_2 .

In 2011 Getman et al.²⁸⁹ reported the results of electronic structure calculations and GCMC simulations that appear to conflict with the results of Klontzas et al.²⁸⁸ After studying the effects of Li–, Mg–, Mn–, Ni–, and Cu–alkoxides on the H_2 storage properties of several MOFs including MOF-5, IR-MOF-10, IR-MOF-16 (Zn_4O metal clusters and 1,1':4,4''-terphenyl]-4,4''-dicarboxylate organic linker),^{49c} and UiO-68,

they concluded that Li-alkoxide functionalization of the organic ligand results in negligible enhancement of the uptake at 243 K. According to their calculations, Li and Mn physically bind H₂ with initial binding energies of −10 and −22 kJ/mol, respectively. The binding energy in the lithiated MOFs is however too weak to overcome thermal effects at 243 K. As a result, Li functionalization of the organic linker cannot strongly enhance H₂ adsorption at this temperature.

In contrast, Ni- and Cu-alkoxides bind H₂ chemically with initial binding energies of −78 and −84 kJ/mol. Although this will lead to high uptake at low pressures, Getman et al.²⁸⁹ found that the alkoxide sites are quickly saturated at pressures beyond 1 bar. This happens because adsorption of subsequent (second, third, fourth, ...) H₂ molecules at the metal alkoxide sites is only weakly exothermic, by about −10 kJ/mol. Their overall prediction is that Ni- and Cu-alkoxide-functionalized MOFs will have poor H₂ delivery properties. The discrepancy between the results of Getman et al.²⁸⁹ and those of Klontzas et al.²⁸⁸ likely arises from the quality of the force fields used to model the interactions between H₂ and the lithiated organic linkers. They showed that there is little enhancement of H₂ uptake after Li alkoxide functionalization if these interactions are fit to the potential energy surfaces obtained at the MP2/6-311+G** level of theory. In contrast, when Lennard–Jones parameters taken from Klontzas et al.²⁸⁸ were used, significant uptake of H₂ was computed. The simulations with the force field generated at the MP2/6-311+G** level of theory are supported by the experimental results of Mulfort et al.^{247a} and Himsl et al.,²⁹⁰ who reported heats of H₂ adsorption of only 6.6–11.6 kJ/mol for two different MOFs after Li alkoxide functionalization.

Beyond H₂ storage in functionalized MOFs, Bae et al.²⁹¹ experimentally showed that Li alkoxide functionalization of the organic linker as well as doping with Li atoms can enhance separation of CO₂ from CH₄. Their work was carried out on three Zn-based MOFs and reported in 2010. This discovery appears to have been motivated by the computations of Xu et al.,²⁹² who examined the influence of Li decoration or Li alkoxide functionalization of the BDC ligand in MOF-5 using DFT calculations and GCMC simulations. They found that the location of the Li atoms in the framework can not only change the adsorption sites for CO₂ but also improve selectivity for CO₂ by enhancing the electrostatic potentials in the material. Although it might be very difficult to reduce the benzene struts in the BDC ligand of MOF-5 with Li, the underlying principle of differential interactions of the electrostatic charge of Li with the quadrupole moments of CO₂ and CH₄ was demonstrated by the experiments of Bae et al.²⁹¹

5. CATALYSIS AND REACTIVITY

MOFs have several properties that make them excellent platforms for heterogeneous catalysis. Paramount among these are their high porosity and large pore sizes. For this reason, there is significant interest in designing and synthesizing MOFs with large pores in order to allow reaction substrates to enter freely into their pores/channels where they could undergo catalyzed reactions and exit as products. In addition, MOFs offer an opportunity to ensure greater catalyst stabilities as the individual catalytic sites in the framework, while dense, can be isolated from one another by the framework.

A key issue in MOF catalysis is the diversity of possible structures at, around, and leading up to the immobilized metal sites. These provide unparalleled opportunities for design and tuning. By changing the linker and the metal, one can change,

for example, the sizes, shapes, and functionalities of the pores, the accessibility of the catalytic site, the coordination number and bite angles of the metal, the recognition profile, the oxidative or reductive power, and the acidity or basicity and pH. Such tuning can give rise to enormous variations in catalytic activity. Thus, for example, the MOFs NU-1000 and UiO-66 are based on the same Zr₆O₈ node structures. However, the greater accessibility of the nodes in the former MOF as well as their ability to offer open Zr coordination sites upon dehydration cause NU-1000 to be dramatically more effective for the hydrolysis of chemical weapons agents.²⁹³ In designing MOF catalysts, it is especially noteworthy that one can achieve ligand environments of the active metal site that would be impossible in homogeneous catalysis.²⁹⁴

There are many MOFs with reported catalytic properties associated with the presence of unsaturated metal sites or reactive ligand sites and in some cases by catalytic species incorporated into the pores of the MOF. The reader is referred to the reviews by Corma et al.,^{48c} Dhakshinamoorthy et al.,²⁹⁵ and Lee et al.⁴⁵ for detailed descriptions of reactions in which MOFs have been used as catalysts. Herein, we review electronic structure calculations for three classes of reactions catalyzed by MOFs: oxidation, hydrogenation, and Knoevenagel condensation reactions. We have chosen these classes of reactions as they have been well studied experimentally and computationally and thereby offer opportunities for more in-depth consideration.

5.1. Oxidation Reactions

Several oxidation reactions for selectively converting hydrocarbons and alcohols to higher value feedstocks have been catalyzed by MOFs. These reactions generally use O₂ from air or organic hydroperoxides as oxidizing agents that are environmentally more benign than the other oxidation catalysts in current use in industry. In many cases, computational studies have been focused on computing the binding energies of the oxidizing agents to the MOF or on elucidating the electronic structure of the (reactive) intermediately oxidized MOF. For example, Tuci et al.²⁹⁶ carried out DFT calculations with the PBE functional in order to understand the oxidation of several alkenes by a Co (II) (*R,R*)-thiazoline-2,4-dicarboxylate MOF that has the form [Co(L-OL)(H₂O).H₂O)], where OL is the organic linker. They calculated the adsorption energy and configuration of O₂ at the Co(II) centers in this MOF. They found that some charge is transferred from the metal site to the adsorbed O₂ as a result of back-donation, which is consistent with their experimental results that indicated a mechanism involving η^1 -superoxo species. The strong adsorption of O₂ precludes significant interaction of the olefin with the metal center, a result also supported by their experiments.

Results of a DFT study on a superoxo complex formed with a MOF have also been reported by Tonigold et al.²⁹⁷ Interestingly, they were able to compare the results obtained from calculations with the PBE+D and B3LYP+D functionals with experimental measurements of the isosteric heat of adsorption of O₂ on two MOFs, MFU-1 and MFU-2. MFU-1 and MFU-2 are similar to MOF-5 but contain Co^{II}₄O clusters linked with 1,4-bis[3,5-dimethyl-pyrazol-4-yl]benzene linkers. O₂ binds to MFU-1 as either a van der Waals (vdW) complex or an η^2 -superoxo complex (i.e., side-on O₂ binding). For the vdW complex, the calculated heats of adsorption obtained with the two functionals are within 3.5 kJ/mol of the experimental value. A rather disconcerting disagreement between the

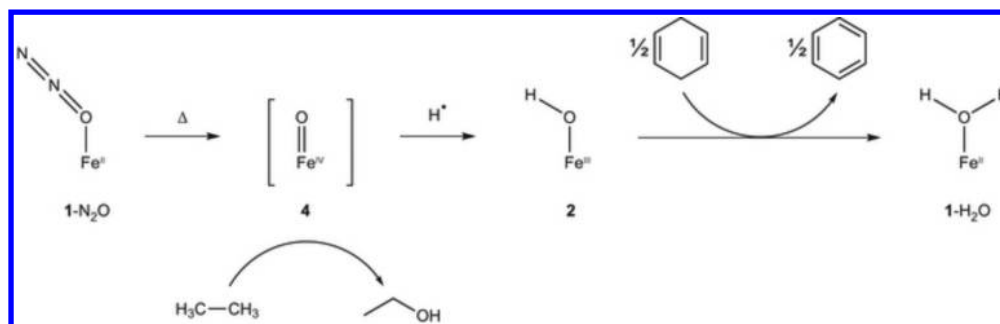


Figure 25. N_2O activation and reactivity of Fe–MOF-74 in the oxidation of ethane and 1,4-cyclohexadiene. Reprinted with permission from ref 304. Copyright 2014 Nature Publishing Group.

functionals was reported, however, when the heat of adsorption of O_2 as a η^2 -superoxo species was calculated. PBE+D predicts a stable complex (-52.7 kJ/mol), whereas B3LYP+D predicts an unstable complex ($+64.9$ kJ/mol). The result obtained from the GGA functional is likely wrong as the experimental data show that only a vdW complex can be formed below 120°C . For the GGA functional to be correct, the formation of the η^2 -superoxo complex would have to be prevented by a very high energy barrier.

Given the poor performance of the GGA functional and the possibility of conflicting results between GGA and hybrid functionals in the report by Tonigold et al.,^{297,298} it is interesting that Jelic et al.²⁹⁹ used the calculated O_2 binding energies as a screening parameter in the search for possible metal/linker combinations that can catalyze oxidation reactions more efficiently than the $\text{Co}^{2+}/\text{Cl}^-$ combination found in MFU-41. Jelic et al.²⁹⁹ examined the origin of the discrepancy in the GGA and hybrid functionals for the calculated O_2 binding energy as a η^2 -superoxo species to the Co^{2+} centers in MFU-41. They noted that since the discrepancy between the GGA and hybrid functionals is independent of the type of ligand, its origin has to lie in the treatment of the Co metal center. Essentially, the description of the fully occupied d orbitals in the high-spin state of the tetrahedrally coordinated Co^{2+} centers in MFU-41 is different when GGA or hybrid functionals are used. As there is no guarantee that the errors associated with the high-spin state of the Co^{2+} site in MFU-41 by GGA functionals will be reproducible for different metal centers, additional calculations were carried out with the hybrid B3LYP functional. Dispersion corrections were added to both functionals using the scheme of Tkatchenko and Scheffler.³⁰⁰ Using the hybrid functional, they were able to identify metal/linker combinations for which O_2 adsorption was more exothermic than in the case in MFU-71. The most promising candidates were Mn^{2+} or Fe^{2+} centers combined with NH_2 ligands.

After Xamena et al.⁴⁶¹ experimentally demonstrated that the oxidation of tetralin to ketones and alcohols could be catalyzed by ZIF-9 and a copper MOF formed with 2-hydroxypyrimidinolate linkers (Cu–2HP), Ryan et al.³⁰¹ performed cluster model calculations with the B3LYP functional to determine the reaction pathway. Interestingly, they found that metal sites within the MOFs could not be the active sites for catalysis. This is because the surrounding organic linkers sterically prevent direct interaction of the tetralin reactant with the metal centers. This plus the fact that the MOFs' small pore sizes are too small to allow for diffusion of tetralin suggested that the catalytic reaction occurs at surface sites. Such surface-dominated reactivity has been reported in other instances as well; for

instance, experimental investigations as well as DFT computations by Chizallet et al. demonstrated that the acidic/basic sites in ZIF-8 responsible for the catalysis of observed transesterification reactions are located at the external surface.³⁰²

Cu–2HP has two important limitations with respect to its activity.⁴⁶¹ First, there is an accumulation of tetralinhydroperoxide at the early stages. In addition, the regioselectivity with respect to the product ketone of tetralin is quite low. A different MOF, however, studied by Luz et al.³⁰³ has been found to overcome these limitations, and it is additionally active for the catalytic oxidation of cumene and ethylbenzene. The MOF in this case is $[\text{Cu}(\text{im})_2]$, formed between Cu^{2+} ions and imidazolate (im).³⁰³ Experimentally, $[\text{Cu}(\text{im})_2]$ is also more efficient of a catalyst than Cu–2HP.

Luz et al.³⁰³ also carried out cluster model DFT computations (B3PW91 functional with the 6-311G** basis set) to determine the origins of the different reactivities of Cu–2HP and $[\text{Cu}(\text{im})_2]$. A significant difference was found in the abilities of Cu–2HP and $[\text{Cu}(\text{im})_2]$ to decompose the hydroperoxide feedstock and to coordinate the resulting radical hydroxyl species. The coordination sphere of $[\text{Cu}(\text{im})_2]$ can be expanded to coordinate the OH radical, whereas in Cu–2HP the coordination of this radical would have to be accompanied by the decoordination of one of the organic linkers. As such, the hydroperoxide is accumulated freely during catalysis with Cu–2HP, in agreement with experimental observations, whereas it is consumed in further oxidation reactions in $[\text{Cu}(\text{im})_2]$, also in good agreement with experiment.

More recently, Xiao et al.³⁰⁴ were able to activate ethane to ethanol by using Fe–MOF-74 oxidized with nitrous oxide, N_2O . The primary question in this study appears to be whether the MOF-74 framework could afford the high-spin iron–oxo species found in enzymatic heme systems that can activate strong C–H bonds, Figure 25. This is particularly important given the hypothesis that ethane oxidation occurs at these iron–oxo sites, created by initial oxidation of the open-metal sites of Fe–MOF-74. To assess this question, the geometries of the singlet, triplet, and quintet states of $\text{Fe}(\text{O})$ –MOF-74, 4, were optimized at the periodic DFT level while using the PBE+U approach and plane wave basis sets. The quintet state was predicted to be the ground state. For this state, a short Fe–O bond length of about 1.64 Å was predicted, consistent with previous reports on iron(IV) oxo complexes.³⁰⁵ Further support for the results of the periodic PBE+U calculations was provided by molecular cluster calculations employing the CASSCF and CASPT2 approaches. The cluster models were all optimized with the PBE and M06-L density functionals. All theories employed in this study predict a quintet ground state

for 4, which confirms the ability of the MOF-74 framework to support a mononuclear high-spin iron(IV) oxo center. In a similar fashion, the Fe(III) hydroxo species formed after hydrogen abstraction from the alkane, 2 in Figure 25, was found to have a sextet ground state. The good performance of GGA functionals in correctly predicting the ground states of the Fe(IV) oxo and Fe(III) hydroxo species is different from the experience of Tonigold et al.^{297,298} and Jelic et al.,²⁹⁹ indicating the degree to which DFT can be sensitive to the nature of the metal and the ligand field in an individual MOF.

5.2. Hydrogenation Reactions

There are many reports of MOFs being used as efficient catalysts during the hydrogenation of the double or triple bonds of alkenes, alkynes, or aromatic compounds. The possibility of converting gases related to global climate change (like CO₂ and SO₂) to more valuable compounds is an important topic of research for the future.

Maihom et al.³⁰⁶ used the M06-L functional to study the mechanism by which CO₂ is converted to formic acid over MOF-5 functionalized with copper alkoxide. To begin, the benzene strut of the BDC linker is converted from C₆H₄ to the copper catecholate C₆H₂(O₂Cu). As noted earlier, the incorporation of metal alkoxides into the organic linkers of MOFs is a viable strategy for increasing their gas storage properties. As expected, the CO₂ adsorption energy at the copper oxide functionality is higher than that in Cu-BTC. After optimizing the structures of their model clusters, Maihom et al.³⁰⁶ explored two reaction mechanisms for CO₂ hydrogenation: a stepwise mechanism and a concerted mechanism, Figure 26. These two mechanisms occur near the copper

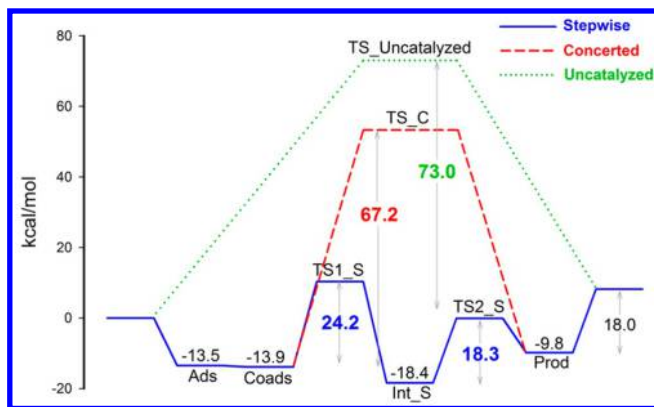


Figure 26. Computed reaction pathway for CO₂ hydrogenation in the gas phase on MOF-5 functionalized by copper alkoxide groups. Reprinted with permission from ref 306. Copyright 2013 American Chemical Society.

catecholate site. They also studied the hydrogenation mechanism in the absence of the MOF catalyst. They found that the stepwise mechanism through a formate intermediate is associated with lower transition state energies, Figure 26. In contrast, the concerted mechanism has a larger barrier of about 67.2 kcal/mol. In the absence of the MOF active site, an even larger activation barrier was computed, Figure 26.

5.3. Knoevenagel Condensation Reactions

A Knoevenagel condensation involves nucleophilic addition of a compound with an activated methylene to an aldehyde or ketone to form a substituted alkene in the presence of an amine catalyst, Figure 27. Several MOFs, such as IR-MOF-3, with

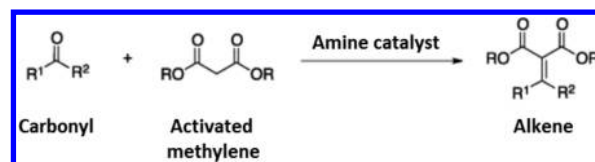


Figure 27. Schematic representations of the reactants, catalysts, and products of the Knoevenagel condensation reaction.

basic centers in or attached to their organic ligands have been used to catalyze such reactions.³⁰⁷ IR-MOF-3 contains the Zn₄O cluster found in MOF-5 but has 2-amino-1,4-benzenedicarboxylate linkers. After Gascon et al.³⁰⁷ discovered that not only IR-MOF-3 acts as a catalyst for Knoevenagel condensations but also the basicity and catalytic activity of aniline-like systems were enhanced when incorporated into MOFs, Cortese and Duca³⁰⁸ carried out MP2, DFT, and QM/MM³⁰⁹ calculations to explore reaction paths. They used cluster models to study the condensation of benzaldehyde and ethylcyanoacetate. They found that while water could poison the catalytically active amino sites in simpler catalysts, this situation is avoided in IR-MOF-3 because its Zn centers interact more strongly with the water molecules produced during the condensation reaction. Second, the larger basicity of IR-MOF-3 was assigned to the formation of protonated conjugate derivatives. The higher basicity in IR-MOF-3 together with its resistance to water poisoning of its amino sites makes it superior to simpler catalysts.

5.4. Electronic Structure Effects on Catalysis and Reactivity

The efficiency of any catalyst, including MOF catalysts, can be altered through structural changes, electronic changes, or both. A thorough demonstration of this concept was reported in 2012 by Vermoortele et al. for catalysis at the Zr₆O₄(OH)₄ nodes of UiO-66.³¹⁰ They synthesized several analogues of UiO-66 in which the BDC linkers were modified with various substituents (NH₂, CH₃, OCH₃, F, Cl, Br, and NO₂). They then compared the potency of these modified MOFs as catalysts to that of parent UiO-66 for the cyclization of citronella. They found that the reaction rate is dramatically enhanced by electron-withdrawing groups on the organic linker with UiO-66-NO₂ being the most active material. To explain this observation, they carried out geometry optimizations and transition-state searches with the B3LYP functional while employing a cluster model containing formates rather than the terephthalates found in UiO-66. To assess the kinetic properties, they added the empirical D3 correction of Grimme¹²² and computed single-point energies based on optimized structures. They found that not only is citronella adsorbed more strongly on UiO-66-NO₂ than on UiO-66 (−24 versus −16 kJ/mol) but also the relevant transition-state barrier is lower for the former (37 kJ/mol) than for the latter (56 kJ/mol). The nitro group allows for stronger binding of citronella as it increases the Lewis acidity of the active site and also has favorable electrostatic interactions with the adsorbate in the transition-state structure.

Vandichel et al.³¹¹ recently reported an experimental and theoretical study of the epoxidation of cyclohexene by MIL-47-V containing terephthalate linkers functionalized by OH, F, Cl, Br, CH₃, or NH₂. Experimentally, it was found that these substituents led to an increase in the catalytic performance relative to parent MIL-47-V. To explain these findings and provide more insights into the nature and mechanism of heterogeneous catalysis by MOFs, Vandichel et al.³¹¹ carried

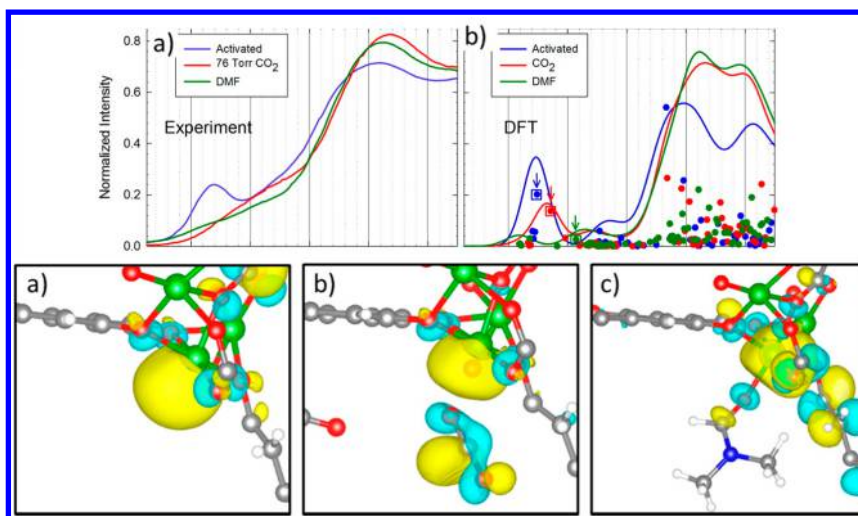


Figure 28. (Top) (a) NEXAFS spectra of activated Mg-MOF-74 (blue), Mg-MOF-74 with 76 Torr CO₂ (red), and Mg-MOF-74 with DMF (green). (b) Calculated NEXAFS spectra (lines) and transition intensities for individual absorptions (circles) of activated Mg-MOF-74 (blue), Mg-MOF-74 with adsorbed CO₂ (red), and Mg-MOF-74 with adsorbed DMF (green). (Bottom) Excited-state wave functions of activated Mg-MOF-74, Mg-MOF-74 with adsorbed CO₂, and Mg-MOF-74 with adsorbed DMF in the calculated spectra presented in the top section. Reprinted with permission from ref 157. Copyright 2013 American Chemical Society.

out a suite of DFT calculations on periodic and extended cluster models on MIL-47-V and its derivatives. After using theory to identify an alkyl-peroxy species as the active site for the epoxidation of cyclohexene in the MIL-47-V MOFs, it was found that all substituents indeed increase the catalytic efficiency. The largest increase was obtained for -OH, in agreement with experiment. Specifically, the substituents were able to modulate catalytic performance through interactions, such as hydrogen bonds, in the transition state. These interactions lead to more stable transition states (and thus lower barriers), just as was reported by Vermoortele et al.³¹⁰ in their work on cyclization of citronella by functionalized derivatives of UiO-66.

The ability of remote electron-withdrawing groups to increase metal-guest interactions applies to catalyst substrates as well as other (nonsystem) systems. We previously noted (in section 3.2) the examples of improved CO₂ selectivity in NH₂-MIL-53(Al) relative to MIL-53(Al) that were reported by Couck et al.²⁰² as well as the report of Torrisi et al.²⁰⁶ on the improvement of CO₂ adsorption energies by functionalization of the BDC linker of MIL-53(Al) by (CH₃)₂, (OH)₂, and COOH groups. As another example, we note that Fischer et al.³¹² reported that the adsorption energy of H₂ by a Cu₂(benzene-monocarboxylate)₄ cluster model is significantly increased when electron-withdrawing groups are added to the para position of the benzene rings; by contrast, adsorption energy is significantly reduced in the case of electron-donating groups. The ability of the electron-withdrawing groups to induce Lewis acidity at the Cu center was assessed by computing Cu Hirshfeld charges in the presence and absence of the substituent groups.

Mu et al.³¹³ demonstrated the same principle for MOF-5. Following up on a study³¹⁴ that showed that the imidazole linkers were the optimal adsorption sites for H₂ in ZIFs, Liu et al. showed that nitro functionalization of the linkers in ZIFs leads to stronger binding of CO₂.³¹⁵ This conclusion agrees with the conclusions of Torrisi et al.³¹⁶ in their more general search for functional groups that improve interactions between CO₂ and benzene.

Lastly, we note that there is significant interest in using MOFs to support catalytic small metal nanoparticles or nanoclusters.³¹⁷ Guo et al. demonstrated chemoselective hydrogenation of cinnamaldehyde using Pt nanoclusters confined in UiO-66-NH₂.³¹⁸ In this MOF, an amino group is attached to the organic linker. Dang et al. synthesized several amides and ketones by using ZIF-8 loaded with Pd nanoparticles in carbonylative coupling catalysis.³¹⁹ These reports are however not accompanied by electronic structure calculations. This is most likely because of the enormous costs of such computations. The modeling of such systems will pose interesting challenges associated with modeling the electronic structure of nanoparticles, with their associated quantum confinement effects and emerging band structures.

6. SPECTROSCOPIC PROPERTIES

In this section, we review some studies of the spectroscopic properties of MOFs. We focus in particular on X-ray absorption spectroscopy, vibrational (IR/Raman) spectroscopy, as well as UV-vis optical absorption properties.

6.1. X-ray Absorption Spectroscopy

X-ray absorption near-edge structure spectroscopy (XANES) can provide information regarding the electronic configuration and stereochemistry of the metal sites in MOFs. Extended X-ray absorption fine structure spectroscopy (EXAFS) can provide additional information regarding the structural arrangement and degree of thermal disorder in condensed-phase systems.³²⁰ For example, the oxidation states of the Cr atoms in MIL-101 were characterized as divalent centers with a coordination number of about 5.4 through XANES and EXAFS experiments.³²¹ In another example, Goesten et al. used XANES to characterize the sulfur oxidation state in sulfated MIL-101(Cr) and MIL-53(Al) as 6.³²² The introduction of such highly acidic sulfate groups into these MOFs increases proton conductivity and the activity of acid-catalyzed reactions.

While many experimental X-ray absorption spectroscopy studies of MOFs have been undertaken, only a few theoretical X-ray absorption studies of MOFs have been reported. This is

generally the case for complex systems and not limited to MOFs. The XANES spectra of complex systems are usually interpreted qualitatively rather than with computational calculations. This is due to a special challenge associated with the presence of multiple absorbers at each photon energy. Drisdell et al.¹⁵⁷ recently used a combination of experimental and theoretical investigations to study the different adsorption processes of CO₂ and N,N'-dimethylformamide (DMF) on Mg-MOF-74. In addition, they examined how the bindings of these ligands to Mg-MOF-74 differ from their binding to its expanded analogue, Mg₂(dobpdc). By also studying amine-functionalized Mg₂(dobpdc), they were able to obtain insights into the effects of coordinating *mmen* ligands to the metal sites on the core-edge spectra of Mg₂(dobpdc). The X-ray absorption spectra were computed with the PBE density functional, exciting from the 1s orbital of Mg as the initial state and using the excited electron and Core-Hole approximation (XCH)³²³ to represent the final states. In the XCH approximation, the excited-state density and energy are determined self-consistently within the KS-DFT formalism while retaining a hole in the core orbital and an electron in the final orbital. The transition amplitudes to each excited state are approximated as effective single-particle matrix elements. The reader is referred to ref 323 for a full description of the approach used in computing the transition amplitudes.

The XANES spectra calculated by Drisdell et al.¹⁵⁷ generally agree well with the experimentally measured spectra. The structural changes induced by the adsorption of CO₂ and DMF on Mg-MOF-74 were adequately reproduced by the computations. In both Mg-MOF-74 and Mg₂(dobpdc), as a result of the unsaturated nature of the metal sites, several transitions are observed in the pre-edge region, experimentally as well as computationally, which would otherwise be forbidden due to dipole-selection rules. They are however allowed in the activated MOFs either because the final orbitals associated with the transitions extend into the unoccupied apical site or because it is strongly mixed or hybridized with the orbitals of the organic ligand, Figure 28. The coordination of DMF to Mg-MOF-74 or *mmen* to Mg₂(dobpdc), however, reduces the intensities of these pre-edge structures in the computed XANES spectra. This is because adsorption imposes a pseudo-octahedral symmetry around the metal center and thus reimposes the strictness of the dipole selection rules, Figure 28. Computationally, a correlation between the reduction of the pre-edge features and the strength of the bond between the metal and adsorbent was found. CO₂ is adsorbed to the Mg centers in Mg-MOF-74 much more weakly than DMF. As a result, imposition of octahedral symmetry at the Mg sites is weaker when CO₂ is adsorbed than when DMF is adsorbed. The calculated spectra show that the pre-edge features are significantly weakened when DMF is adsorbed by the MOF than when CO₂ is adsorbed, Figure 28. This difference between the spectral changes observed after adsorption of CO₂ and DMF is, however, not observed experimentally. The researchers suggested that the thermal motion of the adsorbed species at the metal sites, compared to the static minima employed in the calculations, could possibly mask the influence of the adsorbate on the electronic transitions sampled in the X-ray absorption experiments.

Calculated XANES spectra were also reported by Borfecchia et al.³²⁴ in their study of the adsorption of ammonia, NH₃, at the dicopper paddle-wheel sites of Cu-BTC. They computed the XANES spectra of the activated MOF, hydrated MOF, and

NH₃-MOF adsorbate complex with the FEF code³²⁵ while using a muffin-tin potential and the Hedin-Lundqvist exchange-correlation functional to account for the presence of the core-hole in a self-consistent fashion.³²⁶ The resulting XANES spectra were then optimized (by altering the atomic positions) to validate the bond distances obtained empirically by EXAFS. This shows that computed XANES spectra can be used to complement structural data obtained from EXAFS, X-ray diffraction, and infrared spectroscopy.

Finally, Mattesini et al.⁸³ reported the calculated C and O core edge spectra for MOF-5. The C core edge is dominated by spectral signatures typical of unsaturated graphitic systems, while the O core edge has different fingerprints for the carboxylate and Zn₄O cluster oxygen atoms.

6.2. Infrared Spectroscopy

6.2.1. Calculation of IR Spectra. Harmonic vibrational frequencies of molecular and condensed-phase systems are related to the second derivatives of the total energy with respect to the motion of the nuclei. To predict *anharmonic* vibrational frequencies, which in principle more accurately reflect experiment, one requires higher order (≥ 3) derivatives of the total energy. Computation of analytical second derivatives of the total energy is possible for many electronic structure approaches and relatively inexpensive, albeit significantly more demanding of computational resources than a simple energy calculation. Even in those instances where analytical second derivatives are not available, numerical differentiation of analytical first derivatives typically provides a tractable approach to computing harmonic frequencies.

By contrast, computation of the higher order derivatives needed to include *anharmonic* effects is much more computationally expensive, whether analytical formulas are available or not. For this reason, the harmonic approximation is used in most theoretical studies. In addition, since the intensities of vibrational modes are related to a mixed-dipole derivative that is typically available analytically, the IR spectra of molecular clusters and periodic systems can be readily determined.^{64b}

The IR spectral signatures of MOFs reveal the vibrations of their constituent atoms and are direct indicators of their structural properties. Many quantum mechanical studies of the IR spectra of MOFs and species adsorbed on MOFs have been performed. We discuss representative examples in two classes, namely, IR spectral studies of MOFs alone and then those undertaken in the presence of guest molecules.

6.2.2. IR Spectra of Bare MOFs. The vibrational frequencies of a MOF can be calculated from the periodic unit cell by using density functional perturbation theory (DFPT)³²⁷ or from a representative cluster model by truncating some portions of the unit cell. Generally, vibrational frequencies are slightly underestimated by GGA functionals and overestimated by hybrid functionals (since pure Hartree-Fock theory generally overestimates vibrational frequencies by about 10%).^{64b,328} For GGA functionals, underestimation of experimental frequencies by about 100 cm⁻¹ is not unusual.³²⁹ However, the agreement between the calculated and the experimental vibrational frequencies depends on the balance of errors arising from the harmonic approximation, choice of density functional, choice of basis set(s), and periodic or cluster model(s) used in the calculations. As an example, Ji et al.^{139b} truncated the crystal structure of MOF-5 into a representative fragment containing a Zn₄O cluster coordinated to 6 BDC ligands. This fragment fully captures the first coordination

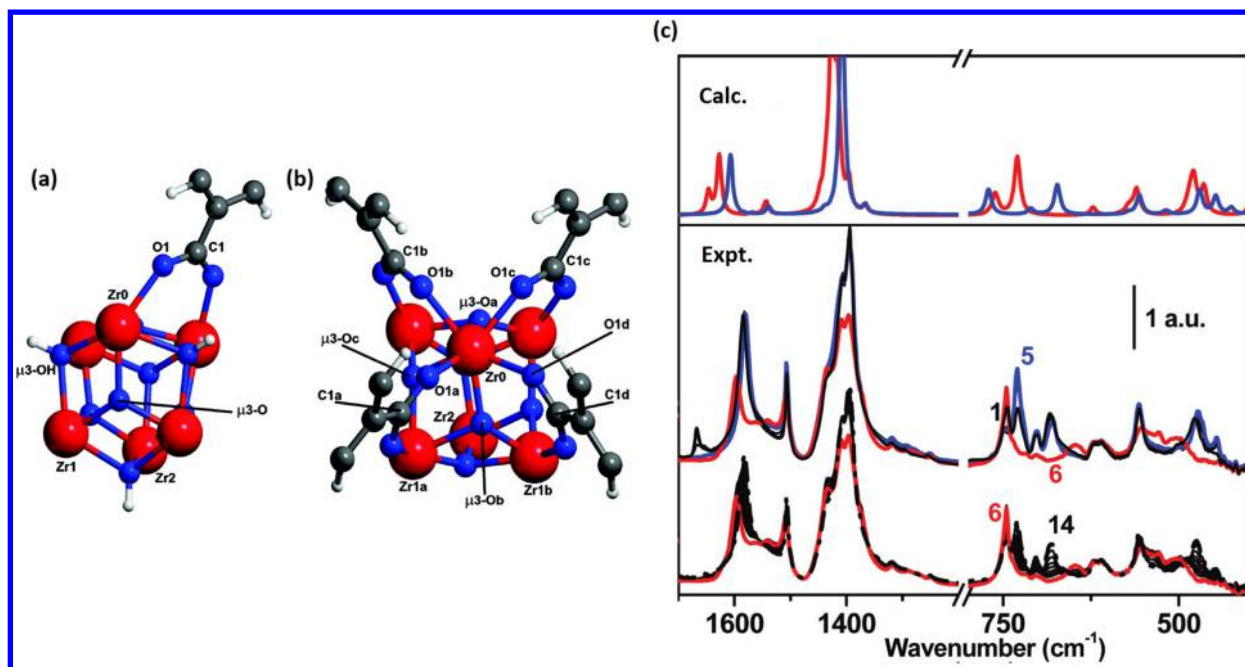


Figure 29. Inner Zr_6 clusters in the (a) hydroxylated and (b) dehydroxylated forms of UiO-66. (c) Calculated and experimental IR spectra of the hydrated (blue) and dehydrated forms (red) of UiO-66. Reprinted with permission from ref 26. Copyright 2011 American Chemical Society.

sphere around the Zn atoms of MOF-5. The calculated Zn–O, C–O, and C–H bonds in the cluster model are within 0.03 Å of the experimental values, and the Zn–O–Zn and O–Zn–O angles are within 1° of experimental values. The calculated frequencies of the Zn–O stretching modes obtained with the PBE functional agree with the experimental data to within 8–9 cm^{-1} , which is so good as to be fortuitous. By contrast, Civalleri et al.³³⁰ carried out periodic DFT calculations on the unit cell of MOF-5 with the B3LYP functional. Their results overestimate the experimental values by 41–71 cm^{-1} . The degree of accuracy obtained by Ji et al.^{139b} is likely due to error cancellations.

Calculated IR spectra can be useful for elucidating the complex structures of MOFs. Valenzano et al. and Chavan et al. used the B3LYP and B3LYP-D approaches to compute the IR spectra of Ni–MOF-74,^{152b} UiO-66,^{26,28} and UiO-67.²⁸ The UiO-6X (X = 6, 7 and 8) MOFs are of great interest as a result of their high thermal and chemical stabilities. Valenzano et al.^{26,28} used a combination of X-ray diffraction, EXAFS, IR, and UV–vis spectroscopies as well as periodic DFT/B3LYP calculations to study the hydrated, hydroxylated, and dehydroxylated structures of UiO-66, Figure 29. They confirmed that the metal cluster is a $Zr_6O_4(\text{OH})_4$ unit, Figure 29a, that is converted to a Zr_6O_6 cluster, Figure 29b, by elimination of two water molecules upon thermal treatment at 300 °C. Calculated structural data obtained from geometry optimizations were combined with data from X-ray diffraction and EXAFS experiments to resolve the $\mu_3(\text{Zr}-\text{OH})$ and $\mu_3(\text{Zr}-\text{O})$ distances in the $Zr_6O_4(\text{OH})_4$ and Zr_6O_6 clusters.

The calculated IR spectra were unambiguously assigned and used to provide insights into empirical IR spectra collected during successive solvent removal, dehydration, and rehydration experiments. In particular, Valenzano et al.^{26,28} found that between the hydroxylated and the dehydroxylated forms of UiO-66 the bands at 470 (assigned as the HO–Zr–OH bending mode), 672 ($\mu_3\text{-Zr}-\text{O}$ stretching in hydroxylated form), and 730 cm^{-1} ($\mu_3\text{-Zr}-\text{O}$ stretching in hydroxylated

form) are well replicated by both experiment and theory. Chavan et al.²⁸ performed analogous experiments and computations on UiO-67. Importantly, the agreement between the experimental and the computed spectra for UiO-66 and UiO-67 allows for a comprehensive assignment of the vibrational modes. Second, comparison of the spectra of UiO-66 and UiO-67 shows that the only major difference arises from bending modes of the hydrogen atoms of the BPDC linker found in the latter. The presence of these modes in the spectra of UiO-67 is replicated both experimentally and theoretically. In these studies, the experimental and calculated spectra generally agree well after the latter is shifted to remove the overestimation error due to the use of the hybrid functional ($\sim 30 \text{ cm}^{-1}$).

A similar approach of comparing experimental and computed IR spectra was employed by Planas et al.^{24b} to assign the proton topology of the octahydrated Zr_6O_8 core in NU-1000. While formally similar to the core in the UiO-6n series, a smaller number of coordinating carboxylate linkers leaves open Zr sites to which water molecules may coordinate. By combining spectra for various tautomers, Boltzmann-weighted based on computed energies, Planas et al. successfully reproduced detailed spectral features between 2400 and 2800 cm^{-1} associated with strongly hydrogen-bonded OH stretches and established the overall topology of the NU-1000 node as $Zr_6(\mu_3\text{-O})_4(\mu_3\text{-OH})_4(\text{OH})_4(\text{OH}_2)_4$.

Calculated and experimental IR/Raman spectra can also be used in studying structural changes in flexible MOFs. In 2011, Nijem et al.³³¹ studied both experimentally and computationally the preferential adsorption of CO_2 over N_2 in a mixed-ligand flexible MOF, $\text{Zn}_2(\text{BDC})_2(\text{BPDE})$, where BPDE is 1,2-bis(4-pyridyl)ethylene. The theoretical calculations were used to show that particular shifts in the Raman spectra of the MOF could be correlated with specific structural changes. The Raman spectrum of $\text{Zn}_2(\text{BDC})_2(\text{BPDE})$ was measured at room temperature as well as at much lower temperatures (–120/–190 °C) in the presence and absence of CO_2 or N_2 . The

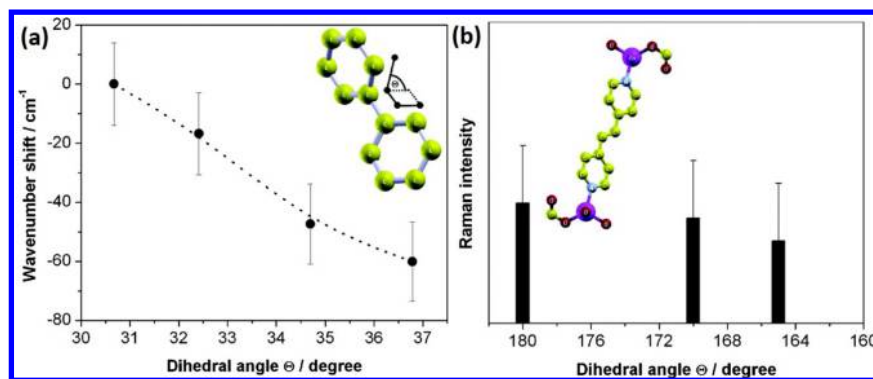


Figure 30. (a) Dependence of the vibrational frequencies of the interlink C–C band on the angle between the two benzene rings of the BPDC ligand. (b) Dependence of the intensity of the free C=O band on the dihedral angle between the free C=O groups at the top and bottom of the BPDC ligand. Reprinted with permission from ref 331. Copyright 2011 American Chemical Society.

experimental data collected under these conditions show that adsorption is associated with structural changes in the MOF.

As previously noted in this review, structural transformations between polymorphs of flexible MOFs are generally correlated with soft vibrational modes often related to twisting/bending of the organic linker. For instance, Nijem et al.³³¹ assigned the ~ -3 cm^{-1} red shift of the experimental 1286 cm^{-1} band on adsorption to likely be associated with the C–C inter-ring twisting of the BPDC ligand. To further assess this, DFT calculations were carried out to determine if variations of the angle between the planes of the benzene rings of BPDC could actually induce a shift in the C–C inter-ring vibrational frequency. As shown in Figure 30a, a 1 – 2° shift in the BDC benzene–benzene plane angle can induce about a 15 cm^{-1} red shift in the C–C inter-ring vibration, which is consistent with the experimental observation, although also much larger in magnitude. Additionally, the twisting of the BPDC linker occurs with the simultaneous shortening of the C–O bond and decrease in the intensity of the C=O mode. The dependence of the intensity of the C=O mode on twisting of the BPDC ligand at the top and bottom of the BPDC ligand is also supported by DFT calculations, Figure 30.

6.2.3. IR Spectra of Adsorbed Species in MOFs.

Vibrational frequencies of adsorbed gas molecules in MOFs are reported in several studies and compared to those of the isolated gas molecules. Poloni et al.^{185b} computed the vibrational frequencies of molecular CO and CO₂ both isolated and adsorbed on Mg–MOF-74 and Ca–BTT with the PBE and vdW-DF2 functionals. Upon adsorption at a MOF's metal site, the vibrational frequencies of CO₂ change and the degeneracy of the bending modes is broken. Experimentally, there is a blue shift of about 4 – 12 cm^{-1} in the asymmetric stretching mode of CO₂ adsorbed on Mg–MOF-74 compared to gaseous CO₂. This experimental result is well replicated with the PBE (6 cm^{-1}),^{185b} vdW-DF2 (17 – 21 cm^{-1}),^{185b,270,332} and B3LYP-D (10 – 15 cm^{-1})³³³ functionals. Wu et al., by contrast, obtained a red shift of about 13 cm^{-1} with LDA, which illustrates a limitation of this older level of DFT.⁸⁴ Finally, Valenzano et al.³³³ used the B3LYP-D approach to successfully predict the shifts in the vibrational frequencies of N₂ and CO adsorbed in Mg–MOF-74.

In general, one would expect GGA and hybrid functionals to correctly predict the directions of the shifts in the IR frequencies of adsorbed gases. There are exceptions, however. For example, while vdW-DF2 correctly predicts the blue shift in the asymmetric stretching mode of CO₂ adsorbed on Mg–

MOF-74, it incorrectly predicts a blue shift (56 cm^{-1}) for the CO₂ bending mode in Ni–MOF-74, to be compared to the experimentally observed red shift (-9 to -17 cm^{-1})³³³ and also the result obtained with the PBE functional (-13 cm^{-1}).^{185b} The vdW-DF2+U (in which the 3d electrons are localized with a U – J parameter of 6.4 eV) approach correctly predicts a blue shift in the vibrational frequency of CO adsorbed to Ni–MOF-74, even though it underestimates the shift by about 21 cm^{-1} (generally 10 – 22 cm^{-1} for M–MOF-74, M = Mg, Mn, Fe, Co, Ni, and Zn).^{183a}

6.2.4. Origins of the Shifts in Vibrational Frequencies of Adsorbed Gases.

By comparing experimental IR spectral data to those calculated for different binding modes/sites, the calculated shifts in the vibrational frequencies of adsorbed gases can be used to determine the configuration mode and location of an adsorbed molecule in a MOF. With respect to the former, Noei et al.³³⁴ studied the adsorption of CO on a mixed-valence ruthenium MOF, [Ru^{II,III}(BTC)₂Cl_{1.5}]. After discovering significant mismatches between the experimentally measured spectra and the computed vibrational frequencies of the structure in which CO is coordinated in a straightforward manner to the chloride portion of the mixed-valence paddle wheel, they explored other possible configuration modes. The best agreement with experiment is obtained with a structure in which a chloride is transferred to a neighboring paddle wheel, leading to charge separation and alternating cationic and anionic SBUs.

In another example, Chizallet et al.³⁰² reported that ZIF-8 is able to catalyze the transesterification of vegetable oil with significant activity. The exact location of the catalytic sites was however unclear as the organic linkers in ZIF-8 are not functionalized and the Zn metal sites in the MOF are saturated in a favorable tetrahedral coordination. To rationalize the catalytic behavior and determine the catalytic active sites, Chizallet et al.³⁰² studied the adsorption of CO in ZIF-8 with Fourier transform IR (FTIR) measurements complemented with DFT calculations using cluster and periodic models. The inherent assumption is that CO and the reactant in the catalysis reaction are adsorbed at similar sites. Chizallet et al.³⁰² constructed models in which CO interacts with the bulk of ZIF-8 or with external groups at the surface of the MOF. They then computed the shifts in the vibrational frequency of CO adsorbed at each site. They found that the sites that have a significant impact on the vibrational properties of CO are those from the external surface of ZIF-8 rather than those in the porous portions of the MOF. This is consistent with the weak

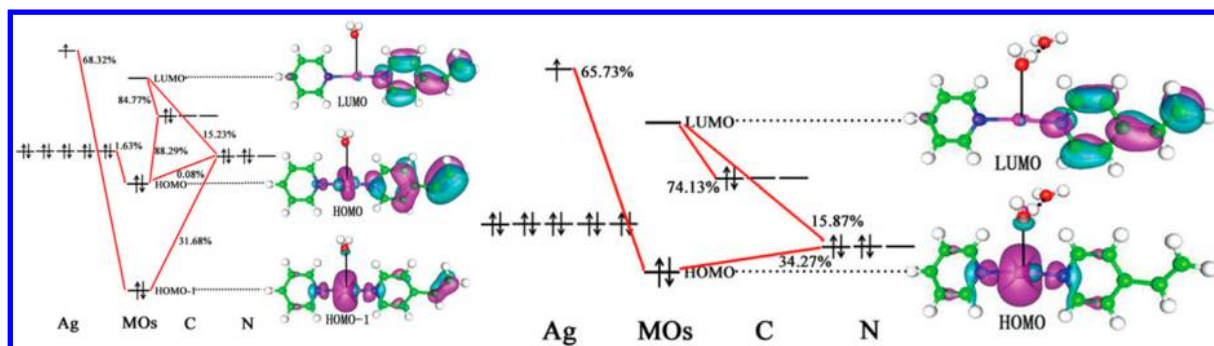


Figure 31. Frontier MOs of (left) model a and (right) model b for a silver-containing MOF. The S_1 excitation in model a comprises of the HOMO–1 \rightarrow LUMO and HOMO \rightarrow LUMO transitions conferring a LLCT + LMCT on the emission behavior. In contrast, the emission behavior is modified to a LMCT transition in model b due to the presence of a second sphere water molecule. Reprinted with permission from ref 139a. Copyright 2013 American Chemical Society.

interaction between CO and the tetrahedrally coordinated Zn centers of the bulk material.

Liu et al.³³⁵ used the vibrational frequencies of CO adsorbed in two MOFs as well as local structural properties and NBO analysis to characterize the relative strengths of the Lewis acid sites in two MOFs, Cu–BTC and Cu–MIPT. Cu–MIPT has the same dicopper paddle-wheel inorganic SBU as Cu–BTC. It however has 5-methyl-isophthalate linkers rather than the BTC linkers found in Cu–BTC. Calculated CO vibrational frequencies have also been used to evaluate the local electronic properties of sites in zeolites.³³⁶

Although calculated shifts in the vibrational frequencies of adsorbed species are informative, it is important to bear in mind that GGA and hybrid functionals can significantly underestimate and overestimate, respectively, the absolute frequencies. As an example, Tan et al.³³⁷ computed the asymmetric and symmetric stretches of SO₂ adsorbed on Ni(BDC)(TED)_{0.5} as 1217 and 1053 cm^{−1}, respectively, with the vdW-DF functional. These frequencies represent shifts of about −39 and −20 cm^{−1} from the calculated gas-phase frequencies of 1256 and 1073 cm^{−1}. Experimentally, the frequencies of SO₂ in the MOF are found at 1326 and 1144 cm^{−1} and 1362 and 1151 cm^{−1} for gaseous SO₂. Thus, vdW-DF2 underestimates the experimental frequencies by up to 100 cm^{−1}. Fortunately, it much more accurately predicts the shifts between the free and the adsorbed molecules to about 3–13 cm^{−1}. Using the vdW-DF functional, Kong et al.³³⁸ predicted a shift of about 25–28 cm^{−1} in the vibrational frequency of H₂ adsorbed in Zn₂(BDC)(TED); this agrees reasonably with the measured shift of 35 cm^{−1}.

6.3. UV–vis Absorption and Emission Spectroscopy

The luminescence properties of MOFs have attracted a great deal of attention. Of particular interest is the fact that the luminescence behavior of a MOF can be sensitive to the structural and electronic properties of the metal sites and the organic linkers. Interactions of the MOF with adsorbent molecules through coordination bonds, π -stacking interactions, and hydrogen bonds have also been shown to affect the luminescence properties of various MOFs.³⁵ For a full description of the available experimental data on luminescent MOFs and their uses, we note the recent reviews by Cui et al.^{42h} and Allendorf et al.^{42a}

On the theoretical front, most efforts have focused on determining the nature of the electronic transitions involved in the absorption/emission process. Ji et al. studied the luminescence properties of [Ag₂(PDA)(DPE)₂(H₂O)]_n·

4nH₂O^{139a} (DPE is 1,2-di(4-pyridyl)ethylene and PDA is 1,2-phenylenediacetic acid) and MOF-5^{139b} with TDDFT. Prior to this theoretical study, Bordiga et al.^{144a} proposed that the luminescent behavior of MOF-5 is due to a O^{2−}–Zn⁺ \rightarrow O[−]–Zn⁺ charge-transfer excitation within its zinc oxide (Zn₄O₁₃) metal clusters. Subsequent experimental measurements by Feng et al.³³⁹ showed that pure MOF-5 has a single emission at 397 nm after it is excited at 345 nm. By comparison, the organic linker H₂BDC emits at 382 nm, while ZnO nanoclusters emit at around 560 nm.

The studies of Bordiga et al.^{144a} and Feng et al.³³⁹ ultimately had conflicting assignments for the emission process in MOF-5, which Ji et al.^{139b} attempted to understand using TDDFT. To ascertain the degree of accuracy of the TDDFT calculations, they initially computed the absorption spectra of MOF-5 and the organic H₂BDC linker with the LC-BLYP¹³⁷ functional and a triple- ζ -polarized basis set. This computational approach quantitatively reproduces the experimental spectral measurements, with the single intense peak observed at 350 nm in the absorption spectrum of the H₂BDC ligand predicted to be at 349 nm. They also found that the highest occupied molecular orbital (HOMO) and lowest unoccupied molecular orbital (LUMO) of MOF-5 contain no contributions from the Zn₄O₁₃ clusters. The HOMO is delocalized over all six BDC linkers, while the LUMO is delocalized over only four BDC linkers. As a result of Kasha's rule,³⁴⁰ the emission properties of MOF-5 should be dominated by ligand–ligand charge transfer (LLCT) associated with the emission of an electron from the LUMO to the HOMO, assuming that the lowest excited singlet state is indeed the HOMO \rightarrow LUMO excitation.

The accuracy of the calculated absorption spectrum of H₂BDC improves confidence in the emission spectra computed for MOF-5, H₂BDC, and ZnO clusters at the same level of theory. The computations indicate that MOF-5 and H₂BDC have emission peaks at 390 and 350 nm, respectively, in very good agreement with the experimental data. Ji et al.^{139b} concluded that the luminescence properties of MOF-5 arise from LLCT rather than charge transfer within the organic linker or within the ZnO clusters.

Ji et al.^{139a} also studied the luminescent properties of [Ag₂(PDA)(DPE)₂(H₂O)]_n·4nH₂O at the TDDFT level. They used the Coulomb-attenuated CAM-B3LYP¹³⁸ functional. With the aim of determining the influence of the water ligands in the second coordination sphere on the luminescence properties of the MOF, they constructed two models. In the first model (model a), a water ligand is directly coordinated to the Ag

center, while in the second model (model **b**), there is a hydrogen bond between model **a** and a water ligand in the second coordination sphere. Model **a** can be said to approximate $[\text{Ag}_2(\text{PDA})(\text{DPE})_2(\text{H}_2\text{O})]_n$, while model **b** approximates $[\text{Ag}_2(\text{PDA})(\text{DPE})_2(\text{H}_2\text{O})]_n \cdot 4n\text{H}_2\text{O}$. Ji et al.^{139a} found that the luminescence behavior of model **a** arises from ligand-to-metal charge transfer (LMCT) coupled with LLCT and LMCT+LLCT, Figure 31. Interestingly, however, it was found that the presence of a water molecule in the second coordination sphere significantly impacts the luminescence properties of model **b**. Specifically, the Ag–O bonds between the metal centers and the coordinated water ligands as well as the hydrogen bonds between the coordinated water ligands and the second-sphere water molecules are strengthened in the first electronic excited singlet state, S_1 . These structural changes convert the LMCT+LLCT emission in model **a** to just LMCT in model **b**, Figure 31.^{139a}

Similar results were observed experimentally by Chen et al.³⁴¹ in a system where several anionic ligands were found to increase the luminescence properties of MOF-76b in methanol. The anionic ligands induce the spectral changes by forming hydrogen bonds with terminal methanol molecules found in the MOF. The number of water molecules in the second coordination sphere can also play a strong role in the location and intensities of the emission spectra of MOFs. Sui et al.³⁴² showed that at least three water ligands must be included in cluster models before good agreement can be obtained between the experimental and the calculated absorption and emission spectra of $\text{Zn}(3\text{-TZBA})(2,2'\text{-BIPY})(\text{H}_2\text{O}) \cdot n\text{H}_2\text{O}$; they used the CAM-B3LYP and LC-BLYP¹³⁷ functionals in their calculations, the results with CAM-B3LYP being more consistent with experimental data than those with LC-BLYP.

Liu et al.³⁴³ recently characterized a gallium MOF that is isostructural with MOF-253.³⁴⁴ This MOF is designated COMOC-4 and contains octahedral $\text{GaO}_4(\text{OH})_2$ units bound to four BPYDC (2,2'-bipyridine-5,5'-dicarboxylate) linkers and two μ_2 -hydroxide anions. In a subsequent study, the emission band of COMOC-4 was found to be sensitive to the solvent environment as well as to the incorporation of Eu^{3+} ions.³⁴⁵ This is interesting given the widespread usage of lanthanide-doped materials in sensing, nonlinear optics, and biomedical analysis.

To understand the guest-responsive excited-state properties of COMOC-4, Liu et al.³⁴⁵ carried out TDDFT calculations with the HCTH,³⁴⁶ B3LYP, and CAM-B3LYP¹³⁸ functionals which, respectively, have 0%, 20%, and long-range correction with 63% exact exchange. By comparing the experimental absorption spectra to the calculated spectra obtained for different cluster models, they found that the UV–vis absorption is likely a LMCT process. Also, by comparing the experimental spectra to the spectra obtained for neutral or cationic clusters, they found that the surface of COMOC-4 contains cationic defects. Eu^{3+} functionalization enhances the luminescence of the material by coupling the ligand-based luminescence of the parent structure to that of the incorporated Eu^{3+} ions. On the methodological front, HCTH³⁴⁶ and CAM-B3LYP underestimate the calculated excitation energies of the organic linker, while B3LYP agrees quite well with experiment. This is somewhat surprising given the charge-transfer nature of the excitations, but it is always possible that the good agreement is due to fortuitous cancellation of errors associated with choice of functional, basis set, solvent model, etc.

Zhang et al.³⁴⁷ performed DFT and TDDFT calculations to determine the energy gaps between the first singlet and triplet excited states of the organic linker in strongly luminescent lanthanide–carboxylate MOFs. The LMCT luminescence behavior of the MOFs requires a resonance between the triplet state of the linker and the lanthanide ion. They found that charge transfer from the ligand to the lanthanide centers is optimal if the energy difference between the first singlet and triplet excited states of the linker is around $2500\text{--}4500\text{ cm}^{-1}$. The magnitudes of the energy gaps between these excited states of the linker were used to rationalize the differences in the energy transfer observed for the $\text{Eu}(\text{III})$ and $\text{Tb}(\text{III})$ MOFs. In some cases, the metal center can quench the LMCT emission intensity either as a result of the energy gap with the linker's triplet excited state or due to its magnetic nature. Lu et al.³⁴⁸ employed DFT and TDDFT to determine the origin of the emission spectra of several MOFs containing 4-sulfosalicylic acid. Their data showed that Cd^{2+} enhances the emission intensity, while paramagnetic Mn^{2+} quenches it.

6.4. Band Gaps

As noted above, in 2005 Fuentes-Cabrera et al.¹⁷⁴ used GGA functionals to calculate the electronic DOS of MOF-5 as well as those of its Be, Mg, Ca, and Cd analogs. In these analogs, the Zn_4O tetrahedra of MOF-5 are replaced by Be_4O , Mg_4O , Ca_4O , and Cd_4O , respectively. Their calculations suggested that the band gap is invariant to the identity of the metal clusters found in MOF-5, indicating that it might be difficult to modify the optical properties of MOFs by simply exchanging the metals in their inorganic SBUs with other metals. It should also be noted that substitution of the metal clusters in MOFs is not a trivial process. There is always the possibility that such processes can lead to a completely different topology, precluding direct comparison of MOF systems. This is another disadvantage to the metal-substitution route of tuning the band gaps of MOFs.

However, there have been many reports regarding the tunability of the band gaps in MOFs since the study of Fuentes-Cabrera et al.¹⁷⁴ First, Gascon et al.³⁰⁷ measured the band gaps of MOFs with organic linkers other than the BDC linker found in MOF-5 while retaining its metal clusters and framework topology. They found that the band gap changes dramatically upon changing the organic linker. This result had already been predicted by the calculations of Civalieri et al.,³³⁰ who showed that replacement of the BDC linker by either NDC or BPDC reduces the computed band gap from about 5.0 to 4.0 eV; these calculations use the hybrid B3LYP functional and so overestimate the experimental band gap, but the influence of the organic linker is manifest. The tunability of the band gap by altering the organic linker suggests that the top of the valence band and the bottom of the conduction band are dominated by contributions from the organic linker.

The sensitivity of the band gap to the attachment of electron-donating and electron-withdrawing groups to the organic linker is also evident in the calculation of the electronic band gap properties of hydroxylated and dehydroxylated forms of UiO-66 and UiO-67 as well as $\text{UiO-66-Cr}(\text{CO})_3$ and UiO-66-NH_2 . Chavan et al.²⁸ calculated electronic band gaps of these MOFs with the B3LYP functional and compared their results to experimental values. A general overestimation of the absolute values of the band gaps by about 22% was obtained. Despite this overestimation, the calculations excellently reproduce the band gap trend of $\text{UiO-66} > \text{UiO-66-Cr}(\text{CO})_3 > \text{UiO-66-NH}_2 > \text{UiO-67}$ obtained experimentally. In all cases, it was

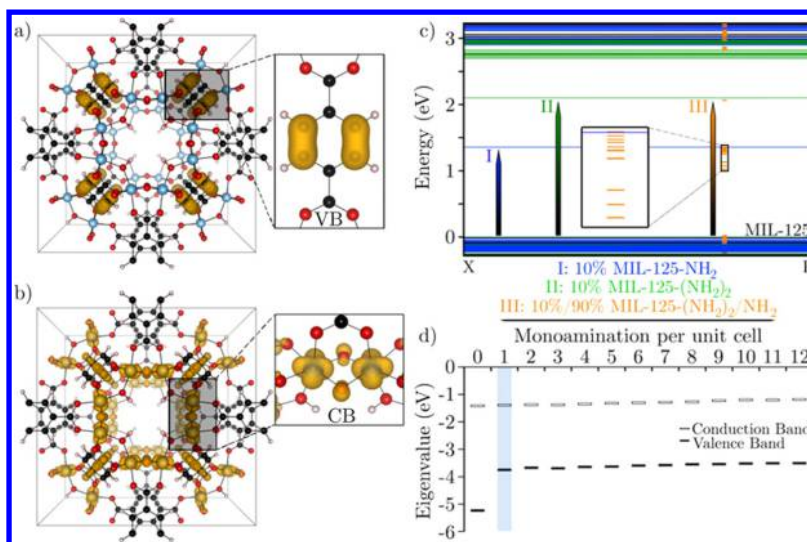


Figure 32. (a) Frontier orbitals of the valence band of substituted MIL-125. This is mostly composed of C 2p orbitals of the BDC linker. (b) Frontier orbitals of the conduction band of unsubstituted MIL-125. This is mostly composed of O 2p and Ti 3d orbitals. (c) Calculated band structures (PBEsol level) of 10% MIL-125-NH₂ (one BDC-NH₂ linker in unit cell, the others are BDC), 10% MIL-125-(NH₂)₂ (one BDC-(NH₂)₂ linker in unit cell, the others are BDC), and 10%/90% MIL-125-(NH₂)₂/NH₂ (one BDC-(NH₂)₂ linker in unit cell, the others are BDC-NH₂). (d) Calculated valence and conduction band energies of MIL-125-NH₂ containing increasing numbers of BDC-NH₂ linkers obtained at the HSE06 level of theory. Notice that the band gap does not change after one BDC-NH₂ group has been incorporated into the framework. Reprinted with permission from ref 349. Copyright 2013 American Chemical Society.

found that the band gap is of π - π^* character with no contributions from the Zr centers. This is similar to the results of Civalleri et al.'s computation for MOF-5.³³⁰ In addition, the calculations of Chavan et al.²⁸ reproduced the observation that Cr(CO)₃ and NH₂ reduce the band gaps, a result that suggests that functionalization of the organic linkers as well as adsorption of guest molecules can be used to engineer desirable band gap properties.

Hendon et al.³⁴⁹ reported similar experiments and computations on MIL-125 MOFs with aminated linkers. MIL-125 contains cyclic octamers of TiO₂ octahedra with BDC linkers and has a band gap of about 3.6 eV. Band structure calculations were carried out with the PBEsol⁸⁸ and HSE06¹¹⁰ density functionals on MIL-125 and MIL-125-(NH₂)_{*n*}, where *n* = 1–12 and denotes the number of BDC linkers that are amino-substituted. In MIL-125, the top of the valence band is dominated by contributions from the organic linker (Figure 32a), while the bottom of the conduction band is based largely on the TiO₂ octahedra (Figure 32b). This would initially suggest that the conduction band is “immune” to alterations of the organic linker. It was found however that as *n* is gradually increased from 1 to 12, the amino-substituted linkers contribute to a new adsorption band that intervenes *below* the conduction band found in MIL-125. As a result, inclusion of a single BDC-NH₂ linker is enough to drastically decrease the optical band gap to around 2.6 eV, Figure 32d. Computations with the HSE06 functional show that band gaps intermediate between those of MIL-125 and MIL-125-(NH₂)_{*n*} can be achieved by attaching OH, CH₃, or Cl groups to the BDC linkers.

Further calculations and experiments by Hendon et al.³⁴⁹ showed that diamination of the linker (to form MIL-125-((NH₂)₂)_{*n*}) could be used further to reduce the band gap to about 1.3 eV, Figure 32d. This is of great interest as most MOFs have large electronic band gaps (in excess of 3.4 eV), which limits their use in the visible region of the electromagnetic spectrum, where they could otherwise be used in lighting and sensing applications.

Lin et al.³⁵⁰ carried out a joint experimental–theoretical study in which the conjugation of the organic linker of MOF-5 was altered by either replacing the benzene moiety of the BDC ligand with naphthalene (IR-MOF-8) or by a carbon–carbon double bond (MOF-FMA, FMA = fumaric acid) while retaining the same topology as MOF-5. Experimentally, MOF-FMA and IR-MOF-8 have band gaps of 4.1 and 3.0 eV, respectively, while MOF-5 has a band gap of about 3.6 eV. Although DFT calculations with the PBE functional deviated from the experimental values by 0.3–0.5 eV, the trends between the MOFs were well reproduced. The initial motivation of this work was based on the results of the density functional tight binding calculations of Kuc et al.³⁵¹ in which they reported that the band gap can be altered by changing the organic linker coordinated to the same inorganic SBU.

Flarge-Larsen et al.³⁵² explored the effects of ligand size and ligand functionalization on the band gaps of the UiO-6X (X = 6, 7, 8) systems in a combined experimental and computational study. They also examined the effect of the torsion in the middle aromatic ring of the TPDC linker on the band gap.³⁵³ Further confirmation that the degree of conjugation in the ligand exhibits significant control over the band gap was reported by Yang et al.^{177a} by comparing the calculated band gaps of M-MOF-5, M-IR-MOF-10,^{177b} and M-IR-MOF-14. Pham et al. also carried out a systematic examination of the effects of halogen atoms and the introduction of antiaromatic linkers on the calculated band gaps of MOFs.³⁵⁴

While hybrid functionals generally tend to overestimate band gaps and GGA functionals tend to underestimate them, there are a few reported cases where computations with GGAs unexpectedly predict rather accurate experimental values. One example is the study of MOF-5 reported by Fuentes-Cabrera et al.¹⁷⁴ Gao et al.³⁵⁵ recently measured a value of about 1.7 eV for the band gap of the Ti⁴⁺ and DOBDC-based NTU-9 MOF. Their calculations with the PBE functional and USPs predicted the band gap of NTU-9 to be about 1.7 eV, in good agreement with experiments. The particular features of these systems that

lead to such surprisingly good agreement between theory and experiment remain unclear.

Irrespective of the so-called “band gap problem” afflicting many density functionals, quantum chemical calculations have a great potential for the design of MOFs that not only have interesting optical properties but that will also be feasible from a synthetic standpoint. To illustrate this point, we note that Foster et al.³⁵⁶ recently suggested a series of modular conjugated linkers suitable for visible light harvesting. They calculated the absorption spectra, fundamental gaps, and optical gaps of these organic linkers at the DFT/TDDFT level while using the tuned LC-BLYP¹³⁷ functional. The choice of the LC-BLYP functional is deliberate as it can be tuned such that the negative of the eigenvalue of the HOMO, $-\epsilon_{\text{HOMO}}$, yields the ionization potential of the system being studied. At the optimal tuning points (where $-\epsilon_{\text{HOMO}}$ matches the ionization potential), the functional generally describes charge-transfer and Rydberg excitations with greater accuracy than standard GGA and hybrid functionals.

Foster et al.³⁵⁶ discovered that the electronic structures of the dioxidorephthalate-type (DOT) linkers in the MOF-74 series are not well suited for photovoltaic applications, largely because of their large optical gaps (3.3–4.1 eV). The DOT linkers containing 1, 2, 3, 4, ... benzene struts were labeled as DOT(I), DOT(II), DOT(III), DOT(IV), ... A series of linkers was subsequently proposed, containing alternating electron-deficient benzo[*c*][1,2,5]thiadiazole (BT) and electron-rich thieno[3,2-*b*]thiophene (TT) blocks (i.e., TT-TT, BT-BT, BT-TT-BT, BT-TT-BT-TT-BT). The optical gaps for these proposed linkers are about 1.9–3.1 eV, and they achieve orbital alignments with electron acceptors such as PCBM. The band gaps and DOS of MOF-74 containing the various linkers were then calculated at the periodic DFT level using the HSE06 functional. The frontier bands in the crystal structures are dominated by C 2p orbitals from the linker. As a result, the band gaps computed on the modified MOF-74 frameworks follow the same trend (systematically shifted by about 0.5 eV) as those obtained from molecular calculations on the isolated BT-BT, BT-TT-BT, and BT-TT-BT-TT-BT linkers. These proposed BT-BT, BT-TT-BT, and BT-TT-BT-TT-BT derivatives of MOF-74 derivatives may therefore be used for visible light applications.

While linker modifications and functionalizations have been demonstrated as viable routes to tune the band gaps of MOFs, the metal substitution strategy (replacing metals while retaining framework topology) has received less experimental attention. The predictions of Fuentes-Cabrera et al.¹⁷⁴ that replacement of the Zn centers in MOF-5 by Be, Mg, Ca, or Cd has little effect on the band gap offers some cause for pessimism. However, recent computations have demonstrated the possibility of tuning the band gaps of some MOFs by either changing the metal centers or by changing the sizes of their inorganic SBUs. With respect to the latter option, Lin et al.³⁵⁰ determined the experimental and theoretical band gaps of IR-MOF-9, Zn₅-BPDC, and CPO-7, three MOFs that differ in the sizes of their Zn SBUs (Zn₄O₁₃, Zn₅O₂₂, and Zn₄₋₆O, respectively) but otherwise retain the same organic linker. The PBE functional adequately reproduces the reduction of the band gap as the size of the metal cluster increases. This reduction is probably due to the greater interactions with the organic linker which modulate the frontier orbitals of both the organic and the inorganic components, thereby possibly

altering the band gap. It is difficult to draw general conclusions, however, insofar as these MOFs have different topologies.

Yang et al.³⁵⁷ recently explored the effect of substitution engineering on the band gap of MOF-5 by substituting new atoms (X and Y) for the corner elements in MOF-5. The set of structurally analogous and isostructural MOFs resulting from these substitutions was labeled as X₄Y-MOF-5, X = Zn, Cd, Be, Mg, Ca, Sr, and Ba and Y = O, S, Se, and Te. The structural, electronic, and band gap properties of the X₄Y-MOF-5 series were computed at the periodic DFT level using the PBE functional. This approach is relatively cheap computationally and facilitates the experimental screening procedure. The band gaps of the X₄Y-MOF-5 series ranged from 1.7 to about 3.6 eV, and the threshold absorption wavelengths ranged from 345 to 724 nm. These results suggest the possibility of systematically tuning the optical and response properties of MOFs.

Choi et al.³⁵⁸ reported that simple substitution of the oxygen anions in the Zn₄O clusters of MOF-5 with sulfur or selenium anions will result in MOFs expected to absorb light in the visible region of the spectrum. They also predicted an even more radical possibility³⁵⁹ based on periodic DFT calculations with the PBE functional; they reported that MOF-5 can be converted from a semiconductor to a metallic system by replacing its Zn²⁺ sites with Co²⁺.³⁵⁹ For intermediate substitutions, the band gap was found to depend on the ratio of the Zn²⁺/Co²⁺ ions.

Experimental evidence of the influence of the Zn²⁺/Co²⁺ ratio on the band gap was obtained for a different MOF, MOF-74, by Botas et al.³⁶⁰ Sippel et al.³⁶¹ demonstrated with theory and experiment that replacement of the Zn atoms in MFU-4 by Co results in the reduction of the band gap by about 1 eV. In this case substitution of Zn by Co leads to empty 3d bands that are below the bottom of the conduction band in MFU-4. Similar to the reports of Foster et al.³⁵⁶ and Hendon et al.,³⁴⁹ an understanding of the relative energy levels of the inorganic and organic components as they relate to the locations of the valence and conduction bands will permit either linker modification/substitution or a metal substitution strategy for tuning band gaps.

7. FIRST-PRINCIPLES FORCE FIELDS

Quantum chemical calculations have been widely used to develop force fields employed in classical simulations of MOF systems and their chemistry. As noted in section 1.4, force fields based on underlying electronic structure data are often referred to as first-principles force fields. Quantum mechanical calculations can be used directly for dynamics calculations without fitting to force fields^{155,362} (this is called direct dynamics), but—as also noted above—while electronic structure calculations have been tremendously useful in describing the behavior and properties of MOFs at the molecular scale, they are less frequently used for predicting macroscopic properties—particularly dynamical ones—as a result of their high computational costs. Some examples of these macroscopic properties are adsorption isotherms, gas diffusivity, and isosteric heats of gas adsorption. These properties have been experimentally measured and reported for many gas/MOF systems, making it easy, in principle, to compare theoretical and empirical data.

GCMC³⁶³ and MD³⁶⁴ simulations find use for determining various macroscopic observables. GCMC is perhaps the main technique for studying adsorption equilibria in nanoporous materials. In a GCMC simulation, adsorption occurs in a model

Table 2. Representative List of Recently Published Reports in Which Force Fields Were Used in Simulating of the Properties of MOFs

	aim(s)	method(s)	ref
reviews			
1	high-throughput screening of MOFs		367
2	suitability and development of MOFs for gas storage and separation		368
methane capture, storage, and delivery			
3	examination of the possibility that MOFs can attain the DOE targets for CH ₄ delivery capacity	GCMC simulations	369
4	methane storage in metal-substituted MOF-74	GCMC simulations	370
5	investigation of the effect of amine functionalization of the organic linker in MIL-53-Al on CO ₂ /CH ₄ separation	GCMC simulations	371
noble gases			
6	adsorption of noble gases in MOFs with open metal sites	GCMC simulations	372
7	predicting separation of noble gases by various MOFs	several levels of theory including MD and GCMC simulations	373
8	investigation of the adsorption of noble gases and N ₂ by 16 MOFs	GCMC simulations	374
hydrogen adsorption, storage, and delivery			
9	screening of about 140 000 MOFs for H ₂ storage	GCMC simulations	375
10	improvement of the modeling of Mg–H ₂ interactions in Mg–MOF-74 by including many-body polarization interactions	GCMC simulations	376a
11	large-scale screening of MOFs using classical DFT and GCMC simulations with emphasis on the performance of four free-energy functionals	classical DFT and GCMC simulations	377
12	influence of Li doping and fullerene impregnation on H ₂ storage by MOFs	GCMC simulations	378
13	determination of the role of quantum effects on the adsorption of H ₂ in MOFs	explicit inclusion of quantum effects using various levels of theory	379
14	investigation of the H ₂ sorption properties of an rht-MOF containing amide units in place of the alkyne group found in the original rht-MOF	partial charges from DFT calculations. Several force field models were used to describe H ₂	185a
15	H ₂ adsorption on UiO-66	GCMC simulations	380
16	H ₂ adsorption by several MOFs functionalized with Mg/Fe catecholates on the organic linkers; this work aimed to discover design strategies that maximize volumetric deliverable capacity	GCMC simulations	381
CO₂ adsorption, storage, and separation			
17	high pressure and supercritical CO ₂ adsorption on Basolite MOFs (Cu–BTC, MIL-53-Al, and MIL-100-Fe)	GCMC simulations	382
18	investigation of the stability of MOF polymorphs under solvothermal conditions; this involved computation of the free energy of immersion	MD simulations combined with thermodynamic integration and the osmotic framework adsorbed solution theory (OFAST)	383
19	adsorption of C ₂ H ₂ , CO ₂ , and CH ₄ on Mg–MOF-74 and Zn–MOF-74	GCMC simulations	384
20	impact of functionalized ligands on CO ₂ adsorption by the lp polymorph of MIL-53-Al	GCMC simulations	385
21	impact of functionalized ligands on CO ₂ -selective adsorption over N ₂ and CH ₄ by UiO-67	GCMC simulations	386
22	screening of nanoporous materials for desulfurizing or decarburizing biogas, natural gas, and flue gas	GCMC simulations	387
aromatic compounds			
23	screening of 32 MOFs for recovering aniline from aqueous solutions	Monte Carlo simulations	388
24	examination of the effect of framework flexibility on the adsorption and separation of aniline/phenol mixtures from aqueous solutions by MIL-53-Al	configurational-bias Monte Carlo (CBMC) simulations ³⁸⁹	61b
25	separation of <i>p</i> -xylene from mixtures of xylene isomers	Monte Carlo simulations	390
26	adsorption of benzene in cation-containing MOFs with the aim of studying the effect of the extraframework cations on adsorption	MD and Monte Carlo simulations	391
27	screening of biocompatible MOFs as potential drug carriers; ibuprofen was considered as the prototypical drug	GCMC simulations	392
other gases			
28	adsorption of hydrogen sulfide on three (Cu–BTC, MIL-47, and MOF-5) MOFs	Monte Carlo simulations	393
29	demonstration of the strong influence of adsorption thermodynamics on the diffusivities of guest molecules inside crystalline nanoporous materials	CBMC simulations	394
30	modeling adsorption of water and ammonia in hydrophobic MOFs with the aim of capturing the latter and not the former	GCMC simulations	61a
31	investigation of SO ₂ gas adsorption in MOFs	GCMC simulations	395
32	investigation of the structural properties, diffusion, and adsorption of various alkanes and gaseous refrigerants on Ni–MOF-74	MD and GCMC simulations as well as the free energy perturbation ³⁹⁶ approach	397
33	investigation of the structural response to methanol uptake by a scandium terephthalate MOF and its nitro-functionalized derivative at extreme pressures	MD and GCMC simulations	398

system where the MOF is in contact with a gas reservoir. Gas molecules partition between this reservoir and the MOF. The

temperature, chemical potential of the gas reservoir (or the reservoir pressure), and structure of the MOF are used as

inputs. A statistical mechanical ensemble is created by making random changes to the positions, orientations, and conformations of the species found in the gas–MOF system. Average values of the heat of adsorption and gas uptake are then obtained from the equilibrated statistical ensemble.

The ability of GCMC simulations to connect to these experimental observables has led to an explosion in the number of studies in which the technique is used to study gas adsorption; a similar situation is obtained using MD simulations to predict diffusion constants in MOFs for comparison to available experimental data. In evaluating the energy of each MOF/adsorbate configuration, computationally efficient classical simulations use force fields to describe all interactions in the system. The accuracy of the GCMC simulation critically depends on the accuracy of the chosen force fields, which—given the physical nature of the adsorption processes—must include a good ability to handle nonbonded interactions. We noted above (section 4.6.3) a case in which researchers arrived at different conclusions with respect to the effect of Li decoration on gas adsorption as a result of differences in the quality of force field parameters used to describe the guest–MOF interactions.^{60b,288,289} In addition, the failure of generic force fields to match experimental adsorption data for some ZIFs³⁶⁵ and to capture accurately interactions at open metal sites is well documented.^{22a,366} Indeed, while some early generation force fields included parameters for metals that were designed to make those force fields “universal” in terms of being readily applicable to any problem, those force fields necessarily sacrificed accuracy for transferability, in part because the very large experimental data sets that have permitted highly tuned organic force fields to be developed with, say, 20 or more individual carbon atom types are less available for metal-containing compounds, which certainly exhibit enormous variation in structure and property as a function of oxidation state, coordination number, etc. In some sense, each new MOF, unless it is a trivial variation on an already known MOF, becomes a new force field parametrization problem.

There continues to be a significant amount of research interest in developing accurate first-principles force fields suitable for studying gas adsorption in MOFs, among other things. In developing first-principles force fields, the potentials that describe the interactions between the adsorbed gas and MOF are first computed at some more computationally demanding QM level, which is itself demonstrated to be sufficiently accurate either through comparison to relevant experimental observables or by demonstration of convergence with respect to model approximations. Force field parameters that reproduce the QM potentials as well as, possibly, local first and second derivatives of the potential are subsequently generated by fitting to a functional form that contains an electrostatic component as well as a vdW component. The bonded and nonbonded interactions existing in the MOF also have to be described in the overall force field to be used in the GCMC simulations if the framework is to be treated as flexible (or if the adsorption is so strong at some sites as to include a substantial degree of covalency). Fang et al.^{60a} and Getman et al.^{60b} provided recent and comprehensive reviews of the protocols involved in generating first-principles force fields as well as their applications to MOFs. For this reason, we only highlight a few recent methodological developments in deriving first-principles force fields as well as their applications to MOFs. We restrict ourselves to reports that were not included in the aforementioned reviews. Even with these restrictions, there are

still many recent reports in which force fields have been used to study the properties of MOFs. In Table 2 we compile a representative list of such reports.^{61,185,367–398} We then highlight the development of new force fields and their applications to studying gas adsorption, separation, and storage in MOFs.

An especially promising approach^{376c–e} to force field development for MOFs (and other kinds of systems) is the use of so-called physically motivated force fields in which the individual terms in the force field correspond to specific individual physical effects such as exchange repulsion, correct electrostatics, induction, and dispersion.

7.1. Recent Force Fields—Development and Validation

In 2013, Rudenko et al.³⁹⁹ carried out a multiscale study of the adsorption of water on Mg–MOF-74. This study is selected for review as it involves a guest molecule that is outside the well-studied series of CO₂, CO, and H₂. It also highlights the need to generate first-principles force fields that more accurately describe guest interactions with the open metal sites of MOFs, compared to existing generic force fields. Rudenko et al.³⁹⁹ carried out DFT calculations, AIMD simulations, and classical MD and GCMC simulations. In the MD and GCMC simulations, they used Lennard–Jones parameters from UFF²⁰⁴ and electrostatic charges from the work of Dzubak et al.^{22a} to describe the framework atoms. The adsorbed water was described either with the TIP n P ($n = 3, 4$, or 5) models⁴⁰⁰ or with a DFT-derived force field. The DFT-derived force field has a pairwise additive functional form that contains electrostatic, repulsive, and attractive components.

In generating the DFT-derived force field, the researchers considered interactions of the adsorbed water molecule with the metal center, the center of the benzene strut of the BDC linker, and also one of the carboxylate ends of linker. They used cluster models in the DFT calculations. The interactions between the water molecules and these sites were fitted based on energy decompositions of the DFT electronic energy at each single point. The DFT-derived force field was validated by comparing the radial distribution functions (RDFs) obtained from MD simulations to those obtained from AIMD simulations at several temperatures, Figure 33. While the DFT-derived force field faithfully reproduces the RDF obtained from the AIMD simulations, Figure 33, the TIP n P+UFF models had significant shortcomings with regard to reproducing the results of the AIMD simulations. The predicted 300 K Mg²⁺–OH₂ interaction energy is about –71 kJ/mol for the DFT-derived force field and around –41 kJ/mol with TIP3P, for example (we note that Canepa et al.²⁷¹ previously obtained a value of –76.2 kJ/mol from DFT calculations). Such large discrepancies in interaction energies are responsible for significant differences in predicted adsorption isotherms; the first-principles force field provides a much closer agreement with experiment than do the TIP n P+UFF models, Figure 33.

In another study involving MOF-74 that demonstrates the advantage of using first-principles force fields over their generic counterparts, Borycz et al.⁴⁰¹ developed a force field for describing the interactions of CO₂ with Fe–MOF-74. The force field parameters in that case were fit to a potential defined by restricted open-shell MP2 calculations of the gas–MOF interactions. The predicted isotherm and isosteric heat of adsorption curves agreed very well with experimental data.

Lin et al.⁴⁰² suggested a particular protocol for deriving accurate nonpolarizable force fields from periodic DFT

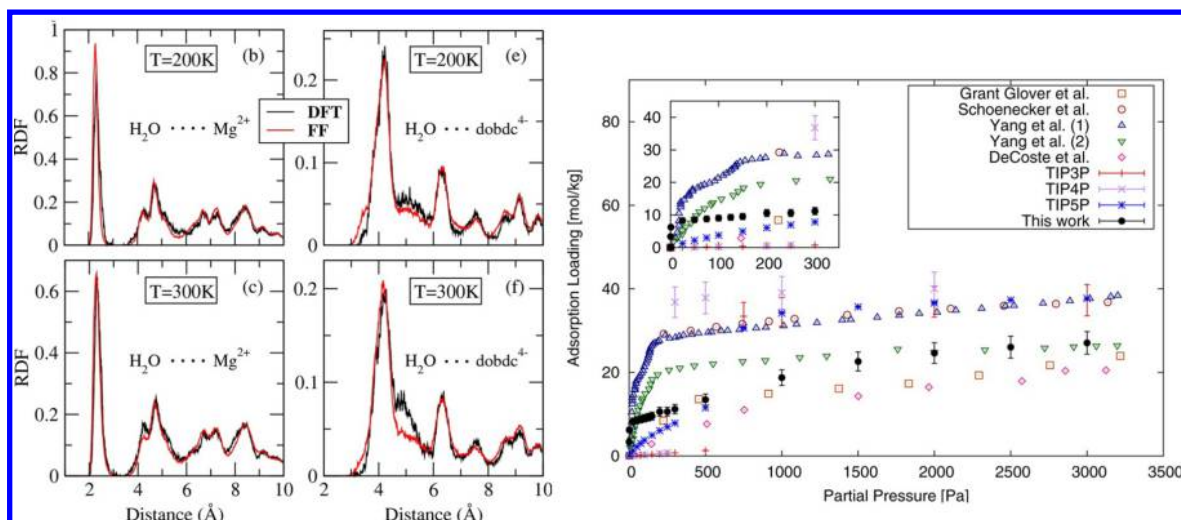


Figure 33. (Left) RDFs describing the interactions between water and the Mg²⁺ or ligands in Mg–MOF-74 derived from AIMD simulations (black) and from MD simulations with the DFT-derived force field (red). (Right) Comparison of experimental and GCMC adsorption isotherms at 300 K. Notice that the DFT-derived force field performs well at high pressures but overestimates experimental data at 0.1–1.0 Pa, a situation likely due to the perfect crystal structure used in the simulations. See ref 399 for references to the experimental data. Reprinted with permission from ref 399. Copyright 2014 American Chemical Society.

calculations. One advantage of their proposed approach is that periodic DFT calculations are computationally cheaper than the MP2 or coupled-cluster calculations often used to generate force fields from cluster models, which may themselves be subject to truncation artifacts. The methodology of Lin et al.⁴⁰² uses specific paths that are most sensitive to the interactions between approaching pairs of atoms and also includes a self-consistent optimization loop that allows the fitting of only 2 variables at each step. The specific paths are generated from initial computations using UFF,²⁰⁴ and the final force field is parametrized so that it minimizes deviation from the energies computed with periodic DFT. Lin et al.⁴⁰² demonstrated that a force field derived from this approach accurately described CO₂ interactions (adsorption isotherm and binding geometries) with Mg–MOF-74 as well as the dynamics of the adsorbed CO₂ in the MOF. By also examining CO₂ interactions with Zn–MOF-74 they demonstrated that the protocol used in deriving their force field was transferable.

After their studies of Mg– and Zn–MOF-74, Lin et al.⁴⁰² also examined the adsorption of water on Mg–MOF-74 using the same approach, and several predictions were made regarding the abilities of Zn–MOF-74 and Mg–MOF-74 to separate a CO₂/H₂O mixture. They found that water could poison both MOFs and reduce their CO₂ adsorption capabilities, as a result of its strong adsorption at the open metal sites. These conclusions are similar to those previously reached by several workers.^{17b,256,261} Yu et al.⁴⁰³ have also recently shown from DFT calculations and GCMC simulations that water reduces CO₂ adsorption on Mg–MOF-74. Interestingly, they predicted that CO₂/N₂ separation is actually enhanced in the hydrated MOF; water adsorbed at the open metal sites interacts more strongly with CO₂ than with N₂.

The derivation of force field parameters from periodic DFT calculations by Lin et al.⁴⁰² follows on their previous report demonstrating that accurate adsorption properties can be obtained by correcting generic force fields with single-point energy values from a few electronic structure calculations.⁴⁰⁴ Here the generic force field provides the number and location of the gas adsorption sites. The use of the generic force field to

determine the adsorbed fraction and adsorption sites crucially differentiates this protocol from that previously proposed by Sillar et al.²⁵⁴ in which a multisite isotherm estimate of the adsorption isotherm is constructed from prior knowledge.

Another approach to modifying generic force fields has been taken by Addicoat et al.,⁴⁰⁵ who extended the original UFF²⁰⁴ parameter set by including 18 additional atom types for the inorganic metal clusters found in MOFs. They only considered intramolecular interactions within MOFs, i.e., it is designed for improved simulations of flexible MOFs. The reference geometries used in deriving the force field parameters of the atom types were obtained from experimental data or from DFT calculations. The new force field is labeled as UFF4MOF and complementary to the atom-type table in the original UFF.²⁰⁴ They found that for the organic linkers, it was very important that chemically reasonable bond orders were chosen. For the metal/metal clusters, good accuracy was sometimes obtained by error cancellations.

Bristow et al. also recently developed a new set of potentials.⁴⁰⁶ They used periodic DFT calculations on an initial parametrization set (MOF-5, IR-MOF-10, IR-MOF-14, UiO-66, UiO-67, and Cu–BTC) as the reference for deriving their new interatomic potentials. The interatomic potentials are transferable (regardless of metal or ligand identity) and adequately reproduce the bulk moduli and vibrational frequencies as well as other structural properties of the MOFs in the parametrization set. It remains to be seen whether this force field can be useful for MOFs outside the parametrization set and whether they can perform well for other material properties. As UFF4MOF⁴⁰⁵ and the force field of Bristow et al.⁴⁰⁶ provide satisfactory predictions of the structural properties of MOFs, they open up a path toward large-scale screening of MOFs, as one can in principle mix them with high-quality first-principles force field parameters of guest gas molecules through combining rules. New transferable and accurate potentials that can be used in simulations have been developed for CO₂ and N₂ from first-principles calculations.⁴⁰⁷

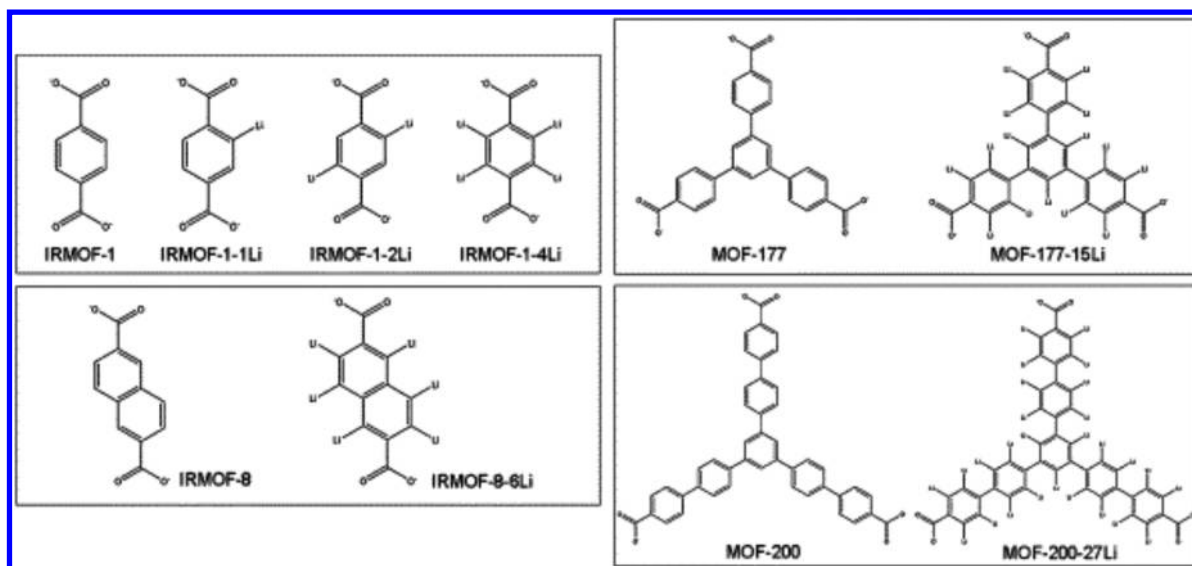


Figure 34. Functionalization of the aromatic rings in several MOFs. Reprinted with permission from ref 408. Copyright 2013 Wiley-VCH.

7.2. Applications of First-Principles Force Fields

On the basis of computational modeling, Han et al.⁴⁰⁸ proposed a new class of MOFs functionalized with Li groups that can show H₂ uptake in excess of 10 wt % H₂ at ambient temperature. In these MOFs, the Li atoms are the counterions to phenyl poly(anions) derived from the benzene struts of the framework linker (Figure 34). This is different from those other cases noted above in which Li atoms are used to decorate the framework or in which they are associated with the organic linker as counterions in alkoxide moieties.

The interaction potentials of H₂ with the Li functional groups were described at the MP2 level of theory with large basis sets. The C–Li bond parameters between the aromatic rings and the Li atoms were fit to a Morse potential based on underlying DFT data, and the remaining required force field parameters were obtained from the literature. GCMC simulations of the H₂ uptake by MOF-5-*n*Li (where *n* is the number of Li atoms and is 1, 2, 3, or 4), IRMOF-8-6Li, MOF-177-15Li, and MOF-200-27Li show that the adsorption energy increases when the framework contains more Li atoms. All these MOFs contain the same Zn₄O metal cluster. It was found that the highly porous MOF-200-27Li has a total uptake of 10.3 wt % H₂ and an excess uptake of 8.3 wt % H₂ at 298 K and 100 bar. This exceeds the 2015 target set by the DOE.¹⁷¹ In addition, these functionalized MOFs are predicted to have higher delivery amounts of adsorbed H₂ than Li-doped MOFs. Of course, experimental confirmation of this promising study will depend on the availability of synthetic routes to the highly lithiated aromatic struts in these MOFs, the stability of the framework after insertion of up to 27 C–Li bonds, and the enormous reactivity that would be expected with gases like CO₂ or H₂O if they are even trace contaminants in an H₂ gas stream.

The porosity of a MOF is correlated with the length of its organic linker. Longer linkers should intuitively lead to larger pores. The caveat, however, is that they may also lead to interwoven, interpenetrating, entangled, or collapsed frameworks. In interwoven frameworks, two or more separate frameworks assemble within each other leading usually to a substantial reduction in their porosities.⁴⁰⁹ QM studies of interwoven MOFs are quite expensive as one must consider a supercell containing portions of the unit cells of each

component framework. This makes classical GCMC and MD simulations attractive alternatives for studying these systems. Han et al.⁴¹⁰ recently examined CO₂ capture and H₂ purification in two MOFs and their interwoven counterparts. The framework atomic positions were optimized with the DREIDING⁴¹¹ generic force field, but first-principles force fields were used to describe the interactions between the guest molecules and MOFs. The researchers found that although porosity is decreased in interwoven MOFs, these MOFs can still have high CO₂ uptake at low pressures. The interpenetration of frameworks resulted in the formation of new adsorption sites with high affinity for CO₂. The decrease in porosity becomes detrimental to CO₂ uptake at high pressures though. At very high pressures, greater porosity simply allows more CO₂ to be packed into a MOF. Barbarao et al.⁴¹² have recently shown through experimental and theoretical investigations that functionalization of the organic linkers in interwoven MOFs results in *decreased* affinity for CO₂. This is not only counterintuitive but also contrary to the results obtained for noninterpenetrating MOFs, where functionalization increases adsorption.^{202,413} In the interwoven frameworks it appears that linker interactions between the different frameworks begin to compete with linker–gas interactions, thereby reducing the number of high-affinity sites available to adsorb CO₂ at low pressures.

Ideally, GCMC simulations provide clear insights into the adsorption mechanism, statistics, and energetics of a gas in MOFs. This is however not always straightforward. Not only is it possible that different force fields can lead to different conclusions regarding predicted adsorption equilibria but they can also more vexingly provide contrasting agreement with different sets of experimental data, which may *themselves* not be fully consistent. To resolve differences between the measured CO₂ uptakes of rht-MOF-7 by two experimental groups, Pham et al.⁴¹⁴ carried out GCMC simulations of CO₂ and H₂ adsorption on said MOF. The MOFs found in the rht family contain supramolecular building blocks containing three coplanar isophthalate groups connected to 24 square paddle-wheel M₂(COO)₄ units, forming a cuboctahedron, truncated tetrahedron, or truncated octahedron cluster.⁴¹⁵ They used the different atomic positions reported in the crystallographic data

of both experimental groups and found that these different atomic positions led to different electrostatic parameters associated with the metal sites. When high-quality first-principles force field^{407b} parameters were used to describe the CO₂ molecules in the GCMC simulations, the adsorption isotherm and isosteric heat of adsorption agreed best with one set of experimental data. However, agreement with the other set of experimental data could be obtained by describing CO₂ with a force field that was fit to empirical vapor–liquid equilibria data for CO₂.⁴¹⁶ Remarkably, the two force fields result in completely different pictures of the sorption mechanism: In one model CO₂ is adsorbed at open metal sites, while in the other sorption is dominated by van der Waals interactions with the framework. These results highlight the sensitivity of GCMC simulations to small modifications in the crystal structures and model parameters and the need for models that more robustly describe the physical system(s) under consideration.

8. CONCLUSIONS AND PROSPECTS

Over the past decade, there has been broad and intense research interest in understanding the properties of MOFs due to their wide range of potential applications and industrial practical uses. CO₂ adsorption and separation from industrial flue gases as well as onboard fuel-gas storage in automotive vehicles represent just two opportunities to exploit the unique properties of MOFs. Finding practical ways to achieve the design/discovery, synthesis, characterization, and widespread adoption of environmentally benign MOFs with optimal performance for specific applications (be it in gas storage and separation, catalysis, sensing, or magnetism) is a long-term goal for researchers in this field. At the moment, most investigations are geared toward correlating the properties of extant, novel, or even hypothetical MOFs with their performance for various applications. It is hoped that insights from such correlations can be used to guide future experimental synthetic priorities.

Electronic structure calculations and simulations have been used in parallel with experimental investigations to provide improved molecular-level understanding of MOFs and their properties and reactivities. Here, we discussed how these calculations and simulations have been used to predict the structural, magnetic, mechanical, gas adsorption and separation, catalytic, and spectroscopic properties of MOFs. In addition, we discussed the derivation of force fields from first principles so as better to describe the interactions between guest molecules and MOFs during classical GCMC simulations of gas adsorption or classical MD simulations of gas (or liquid) diffusion. Methodologically, for QM modeling, there has always been a need to choose between accurate but computationally expensive post-SCF wave function approaches and much faster but sometimes less accurate DFT approaches. The development and adoption of new meta, hybrid, dispersion-corrected, nonlocal-correlation, screened-exchange, and long-range corrected density functionals by the wider computational chemistry community have been paralleled by application of new model chemistries based on these methods to MOFs. These methods generally reproduce well the trends in the calculated properties and when combined with first-principles force fields have opened up opportunities for rapid screening of MOF properties requiring simulations. In addition, advances in hardware have made AIMD simulations feasible for studying structural transformations in breathing MOFs.

For post-SCF approaches, there is a growing maturity in the way researchers (i) choose cluster models that accurately mimic the positions of specific atoms or groups of atoms in the bulk framework or (ii) bootstrap multiple models from smaller to larger in order to demonstrate consistency in chemical and theoretical models. The introduction of faster hardware and algorithms as well as the development of local correlation methods (like the LPNO-CCSD method) have also increased the range of post-SCF methods that can be used for studying large systems such as MOFs.

8.1. Creation and Large-Scale Screening of a MOF Database

Compared to the Materials Project,⁴¹⁷ which has been mainly focused on inorganic materials for use in rechargeable energy storage architectures, database initiatives for MOFs are, at the time of this writing, still in early stages of development. Three examples of such database initiatives are given in ref 418. We emphasize that there is strong interest in developing databases or libraries for both existing and hypothetical MOFs, and much has already been done in this direction. Specifically, in addition to the initiatives given in ref 418, Wilmer et al.^{50e} generated a large number of hypothetical MOFs while Chung et al.¹⁶⁵ provided a compilation of computation-ready experimental (CoRE) MOFs. Also, these are in addition to the work of Martin et al. on MOF-5 analogues,^{21b} Lin et al. on ZIFs,⁴¹⁹ and Bao et al.⁴²⁰

However, a truly “universal database of MOFs” (and we say this to encourage ongoing efforts mentioned above) will likely contain experimental and computed structural, surface area, and gas adsorption data for existing MOFs as well as hypothetical MOFs. The underlying insight is that an open-source and widely disseminated database will not only encourage screening of materials for specific applications but also lead to more intelligently and specifically designed MOFs. This is because advances in the intelligent design of optimally performing MOFs are likely to arise from a combinatorial, screening, and supercomputing framework that may also be able to take advantage of machine-learning algorithms, rather than just from small-scale intuition-driven crystal design, synthesis, and characterization efforts and the development of more accurate and faster electronic structure or classical simulation methods.

For this reason, a useful database will need to have front-end tools that provide easy access to various research groups as well as algorithms and hardware architectures that can be used to compute the gas storage/adsorption, optical, and spectroscopic properties of large data sets. A collaborative spirit between experimental and theoretical research groups will lead to timely submission of their available data to the database. It will be beneficial to have automated applications that can design hypothetical frameworks for not yet synthesized MOFs, generate inputs for electronic structure computations, generate inputs for classical simulations, and ultimately present the final data or results in readily accessible forms. Automation of such activities will be particularly useful.

For electronic structure computations, the research community will benefit from a decision to adopt generally a reduced suite of methods to be used for initial optimizations of structures of MOFs to be stored in the database. It will also be important to develop algorithms and methods that correlate physical observables or computed quantities with the performance of MOFs for specific applications. Parameters for screening the database for particular properties or applications

as well as a widely accepted and adopted naming convention would accelerate progress in this area as well.

8.2. Electronic Structure Methods and Computing Architectures

Over the past decade, the story of computational MOF chemistry has largely been the story of the wider computational chemistry community as well, that is, the number of particles that can be included in electronic structure calculations is still limited by the speed (as well as accessibility and cost) of modern parallel computers as well as the inherently expensive scaling behavior of post-SCF wave function methods. There have been, however, some encouraging developments. First, it has been demonstrated that electronic structure calculations and simulations can be orders of magnitude faster on graphical processing units (GPUs) than on central processing units (CPUs), thus making larger systems and longer time scales more tractable.⁴²¹ Second, there are initiatives for achieving exascale computing in most advanced facilities.⁴²² Third, the development of fast embedding methods^{423a–d} and other fragment methods^{423e–i} promises to significantly accelerate computations on extended systems while not only providing the accurate picture necessary for localized phenomena but also incorporating in various fashions the influence of the embedding fragment/environment on the site of interest.⁴²³ It is possible that some combination of these developments will result in significant reduction in the computational costs of calculations and simulations on MOFs and other large systems. In addition, calculations at post-SCF wave function levels of theory will invariably become more accessible for larger systems with faster and larger computing platforms. In the short and medium terms, the further development of local correlation methods⁴²⁴ might usher in affordable linear scaling for large systems.

Periodic DFT calculations on MOFs are still mostly carried out with standard and dispersion-corrected GGA and meta-GGA density functionals. As we discussed in this review, there are niches where hybrid density functionals can provide improved results for MOFs. In addition, damped-dispersion effects have been shown to be crucial to describing gas adsorption phenomena in MOFs. Density functionals that better incorporate such effects are becoming increasingly mature and are now being widely applied to MOFs. In the short term, pragmatic techniques like the DFT/CC approach of Nachtigall et al.^{223,227,274} are also promising as they provide results at the degree of accuracy of highly correlated post-SCF wave function methods at essentially the cost of DFT. Development of analogous techniques that can be used for open-shell systems and to some extent for multireference systems will be a positive step. Another possibility might be the development of more specific dispersion corrections for the different atom types found in the most common MOFs and topologies.

With respect to simulations, AIMD simulations are often limited to small and mid-sized systems and short time scales due to the need to compute energies and gradients at the quantum mechanical level. As supercomputing capabilities and density functionals continue to improve, it should become easier to model larger systems with reliable electronic structure methods and to attain AIMD simulation times that are sufficient for proper description of phenomena with longer relaxation times. Free-energy approaches like metadynamics⁴²⁵ and umbrella sampling⁴²⁶ can be used to avoid the very long

simulation times needed for rare events. To carry out free-energy AIMD simulations on flexible MOFs, one needs to construct collective variables that describe structural transformations at different temperatures and external pressures as well as in the presence of different number densities of guest molecules.

8.3. Improving Grand Canonical Monte Carlo (GCMC) Simulations

There is rarely a perfect match between experimental gas adsorption isotherms and isotherms predicted from GCMC simulations. This is not necessarily a theory problem, per se, as there are often significant differences between adsorption isotherms obtained by different experimental groups. It also needs to be further acknowledged that molecular calculations and simulations generally assume that MOFs exist as perfect crystals without any defects and that all available adsorption sites are accessible to guest molecules. As MOFs in the laboratory are far less ideal, it is possible that perfect agreement between empirical data and data obtained from GCMC simulations is illusory. (This, of course, is a problem of all theory–experiment comparisons, not just those involving GCMC simulations.) That, however, should not cause the community to overlook that there are significant opportunities for improving GCMC simulations of MOFs. Some of these opportunities include fitting first-principles force fields to larger and more accurate sets of electronic structure data, inclusion of polarizabilities in the force fields,³⁷⁶ accounting for framework flexibility during gas adsorption, employing longer simulation times, and exploring more sophisticated algorithms for accounting for the screened nature of electrostatic interactions in condensed phases.⁴²⁷ It should also be possible to systematically account for defects (such as missing ligands, missing metal clusters, occlusion of adsorption sites) in MOF crystal structures during simulations. Currently, the empirical adsorption isotherm is generally scaled with a numerical factor that is related to the proportion of available adsorption sites in the MOF, which is at best an ad hoc approach.⁴²⁸

8.4. Prediction and Scoring of Synthetic Pathways for MOFs

Even under the extremely optimistic scenario that a large, accessible, efficient, and “screenable” database of MOFs has been developed and electronic structure methods and computers are more accurate and orders of magnitude faster than they are currently, it will still be crucially important that experimentalists can actually synthesize and characterize hypothetical MOFs that have been predicted by theory to have potentially optimal performances for specific applications. Electronic structure calculations can assess reaction energetics and transition-state barriers for possible synthetic routes to MOFs as well as those for imagined competing side reactions (all including the effects of solvent environment, dissolved ions, working temperature, etc., on the proposed synthetic routes). However, obtaining a MOF in the laboratory involves more than simply mixing an inorganic compound with an organic linker in a solvent. One has to consider the effects of the solvent and also consider the initial nucleation process as well as crystal growth mechanisms. Experimental and computational researchers have to come up with a framework for generating possible synthetic routes to MOFs and scoring their likelihood of success. This is likely to be the greatest challenge of all.

AUTHOR INFORMATION

Corresponding Authors

*E-mail: sodoh@umn.edu.

*E-mail: gagliardi@umn.edu.

Notes

The authors declare no competing financial interest.

Biographies



Samuel Odoh received his B.Sc. degree at the University of Ibadan, Nigeria, before moving to Canada for his M.Sc. degree at the University of New Brunswick, Fredericton. He obtained his Ph.D. degree in Chemistry, December 2012, from the University of Manitoba under the direction of Professor Georg Schreckenbach studying actinide compounds with electronic structure and classical simulation methods. He spent some time (January–August 2013) at the Pacific Northwest National Laboratory as a postdoctoral research fellow with Dr. Bert de Jong before joining the group of Professor Laura Gagliardi at the University of Minnesota in September 2013. His research interests involve computational modeling of nanoporous materials and actinides with particular emphasis on gas storage, catalysis, and novel reactivity.



Chris Cramer earned his A.B. degree from Washington University in St. Louis and his Ph.D. degree (Chemistry) from the University of Illinois. His professional career began with 4 years of service as an officer in the United States Army, including combat duty in Operation Desert Storm. In 1992, he began his academic career at the University of Minnesota, where he is currently a Distinguished McKnight and University Teaching Professor and also Associate Dean for Academic Affairs in the College of Science & Engineering. He has been recognized as a fellow by the American Chemical Society as well as by the Alfred P. Sloan and John Simon Guggenheim foundations. He is a recipient of the Arthur S. Flemming award and also the author of the

textbook *Essentials of Computational Chemistry, Theories and Models*. His research interests encompass the development and application of models that include condensed-phase effects on structure and reactivity as well as the application of computational methods for both catalyst and materials design, with special interest in water splitting, oxygen activation, and sustainable polymers.



Don Truhlar is Regents Professor in the Chemistry Department at the University of Minnesota, Twin Cities, where he has been on the faculty since 1969. He was born in Chicago, IL, received his B.A. degree in Chemistry from St. Mary's College in Winona, Minnesota, and his Ph.D. degree in Chemistry from Caltech. He is a Fellow of the APS, AAAS, WATOC, RSC, and ACS and a member of the International Academy of Quantum Molecular Science and the National Academy of Sciences of the United States of America. He was director of the Minnesota Supercomputing Institute from 1988 to 2006. He is a recipient of the ACS Award for Computers in Chemical and Pharmaceutical Research, Peter Debye Award in Physical Chemistry, Minnesota Award, NAS Award for Scientific Reviewing, Schrödinger Medal of WATOC, Lisa Meitner Award, Dudley Herschbach Award for Collision Dynamics, Doctor honoris causa of Technical University of Lodz, Distinguished Alumnus Award of St. Mary's College, and RSC Chemical Dynamics Award. His research interests are centered on chemical dynamics and quantum mechanics.



Laura Gagliardi is a Distinguished McKnight University professor at the University of Minnesota. She obtained her Ph.D. degree from the University of Bologna, Italy, in Theoretical Chemistry. After a postdoctoral appointment at Cambridge, U.K., she began her independent career as an assistant professor at the University of Palermo, Italy, in 2002. She then moved to the University of Geneva, Switzerland, in 2005 as Associate Professor. Her move to the University of Minnesota came in 2009, where she is now Distinguished McKnight University Professor in the Department of Chemistry. Her research interests are in the area of theoretical and computational

chemistry, with special focus on inorganometallic materials and molecular systems. In 2004 she won the annual award of the International Academy of Quantum Molecular Science to scientists under 40, with citation “for her innovative contributions to prediction and understanding of new inorganic molecules using quantum chemical methods”. She is currently the director of the Energy Frontier Research Center named Inorganometallic Catalyst Design Center, based at the University of Minnesota.

ACKNOWLEDGMENTS

This work was funded by the Office of Basic Energy Sciences of the U.S. Department of Energy Division of Chemical Sciences, Geosciences, and Biosciences under award DE-FG02-12ER16362.

ACRONYMS AND ABBREVIATIONS

1D	one-dimensional
3D	three-dimensional
AIMD	ab initio molecular dynamics
BIPY	bipyridine
BPDC	biphenyldicarboxylate
BSSE	basis set superposition error
BDC	benzenedicarboxylate
BTC	benzenetricarboxylate
BTT	benzenetristetrazolate
CASSCF	complete active space self-consistent field method
CASPT2	complete active space second-order perturbation theory
CASPT2-CP	counterpoise-corrected complete active space second-order perturbation theory
CC	coupled cluster
CCSD	coupled cluster singles and doubles
CCSDT	coupled cluster singles, doubles, and triplets
CCSD(T)	coupled cluster singles, doubles with perturbative triples
CI	configuration interaction
CMS	charge model 5
CP	counterpoise corrected
CT	charge transfer
DOE	Department of Energy of the United States of America
DFT	density functional theory
DFT+U	DFT with Hubbard U term
DMF	<i>N,N'</i> -dimethylformamide
DOBDC	dioxidobenzenedicarboxylate
DOBPDC	dioxido-biphenyl dicarboxylate
DOS	density of states
DOT	dioxidoterephthalate
DPE	1,2-di(4-pyridyl)ethylene
ES	electrostatic interaction
ESR	electron spin resonance
ETS	extended transition state
EX	exchange repulsion
FMA	fumarate acid group
FTIR	Fourier transform infrared
GCMC	grand canonical Monte Carlo
GGA	generalized gradient approximation
GTO	Gaussian-type orbital
HF	Hartree–Fock
H ₂ HFIPBB	4,4'-[hexafluoroisopropylidene]bis[benzoic acid]

HSE	Heyd, Scuseria, Ernzerhof
IR	infrared
J_{NN}	magnetic coupling constant between nearest neighbors
J_{NNN}	magnetic coupling constant between next nearest neighbors
$J_{\text{I-1}}$	intrachain magnetic coupling constant
KS	Kohn–Sham
LDA	local density approximation
LLCT	ligand-to-ligand charge transfer
LLCT+LMCT	ligand-to-ligand charge transfer and ligand-to-metal charge transfer
LMCT	ligand-to-metal charge transfer
LMO	localized molecular orbital
lp	large pore
LPNO–CCSD	local pair natural orbital–coupled cluster singles doubles
LYP	Lee–Yang–Parr
M–M	metal–metal
MD	molecular dynamics
MC	Monte Carlo
<i>mme</i>	1,4-dimethylamine
MOFs	metal–organic frameworks
MP n	Møller–Plesset perturbation theory truncated at the n th order
MRMP n	multireference Møller–Plesset perturbation theory truncated at the n th order
MRCC	multireference coupled cluster
NAO	natural atomic orbital
NBO	natural bond orbital
NDC	naphthalenedicarboxylate
NEB	nudged elastic band
NH ₂ –BDC	amino benzenedicarboxylate
NIS	neutron inelastic scattering
NN	nearest neighbor
NNN	next nearest neighbor
NOCV	natural orbitals for chemical valence
np	narrow pore
PAW	projector-augmented wave
PBC	periodic boundary conditions
PBE	Perdew, Burke, Ernzerhof
PDA	1,2-phenylenediacetic acid
PDC	pyrenedicarboxylate
Pol	polarization
Post-HF	post-Hartree–Fock
PW	plane wave
QM/MM	combined quantum mechanical and molecular mechanical method
RDF	radial distribution function
S1	first singlet electronic excited state
SBU	structural building unit
SIE	self-interaction error
SO-SI	spin–orbit state interaction
STO	Slater-type orbital
TDDFT	time-dependent density functional theory
TPDC	terphenyldicarboxylate
TPSS	Tao, Perdew, Staroverov, Scuseria
TBC	tetrabenzenecarboxylate
TED	triethylenediamine
TZ	3,5-bis(trifluoromethyl)-(1,2,4-triazolate)
TZBA	3-(<i>SH</i> -tetrazolyl)benzoic acid
UEG	uniform electron gas
UFF	universal force field

USP	ultrasoft potential
UV–vis	ultraviolet–visible
vdW	van der Waals
vnp	very narrow pore
WFT	wave function theory
XANES	X-ray absorption near-edge spectroscopy
EXAFS	extended X-ray absorption fine structure
XC	exchange correlation
XCH	excited electron and core–hole approximation
ZIF	zeolitic imidazolate framework
ZFS	zero field splitting
ZPE	zero point energy

REFERENCES

- (1) Keskin, S.; Liu, J.; Rankin, R. B.; Johnson, J. K.; Sholl, D. S. *Ind. Eng. Chem. Res.* **2009**, *48*, 2355.
- (2) Coudert, F.-X. *Chem. Mater.* **2015**, 1905.
- (3) (a) Eddaoudi, M.; Moler, D. B.; Li, H. L.; Chen, B. L.; Reineke, T. M.; O’Keeffe, M.; Yaghi, O. M. *Acc. Chem. Res.* **2001**, *34*, 319. (b) Rowsell, J. L. C.; Yaghi, O. M. *Microporous Mesoporous Mater.* **2004**, *73*, 3.
- (4) Dietzel, P. D. C.; Panella, B.; Hirscher, M.; Blom, R.; Fjellvag, H. *Chem. Commun.* **2006**, 959.
- (5) Farha, O. K.; Yazaydin, A. O.; Eryazici, I.; Malliakas, C. D.; Hauser, B. G.; Kanatzidis, M. G.; Nguyen, S. T.; Snurr, R. Q.; Hupp, J. T. *Nat. Chem.* **2010**, *2*, 944.
- (6) Murray, L. J.; Dinca, M.; Long, J. R. *Chem. Soc. Rev.* **2009**, *38*, 1294.
- (7) Rosi, N. L.; Kim, J.; Eddaoudi, M.; Chen, B. L.; O’Keeffe, M.; Yaghi, O. M. *J. Am. Chem. Soc.* **2005**, *127*, 1504.
- (8) Horcajada, P.; Surlle, S.; Serre, C.; Hong, D. Y.; Seo, Y. K.; Chang, J. S.; Greneche, J. M.; Margiolaki, I.; Ferey, G. *Chem. Commun.* **2007**, 2820.
- (9) Gu, Z. Y.; Yan, X. P. *Angew. Chem., Int. Ed.* **2010**, *49*, 1477.
- (10) Duan, X.; Cai, J. F.; Yu, J. C.; Wu, C. D.; Cui, Y. J.; Yang, Y.; Qian, G. D. *Microporous Mesoporous Mater.* **2013**, *181*, 99.
- (11) (a) Furukawa, H.; Cordova, K. E.; O’Keeffe, M.; Yaghi, O. M. *Science* **2013**, *341*, 974. (b) Zhou, H. C.; Long, J. R.; Yaghi, O. M. *Chem. Rev.* **2012**, *112*, 673.
- (12) (a) Chen, B. L.; Ockwig, N. W.; Millward, A. R.; Contreras, D. S.; Yaghi, O. M. *Angew. Chem., Int. Ed.* **2005**, *44*, 4745. (b) Chui, S. S. Y.; Lo, S. M. F.; Charmant, J. P. H.; Orpen, A. G.; Williams, I. D. *Science* **1999**, *283*, 1148. (c) Eddaoudi, M.; Kim, J.; Wachter, J. B.; Chae, H. K.; O’Keeffe, M.; Yaghi, O. M. *J. Am. Chem. Soc.* **2001**, *123*, 4368. (d) Lin, X.; Jia, J. H.; Zhao, X. B.; Thomas, K. M.; Blake, A. J.; Walker, G. S.; Champness, N. R.; Hubberstey, P.; Schroder, M. *Angew. Chem., Int. Ed.* **2006**, *45*, 7358. (e) Lin, X.; Telepeni, I.; Blake, A. J.; Dailly, A.; Brown, C. M.; Simmons, J. M.; Zoppi, M.; Walker, G. S.; Thomas, K. M.; Mays, T. J.; Hubberstey, P.; Champness, N. R.; Schroder, M. *J. Am. Chem. Soc.* **2009**, *131*, 2159. (f) Moulton, B.; Lu, J. J.; Mondal, A.; Zaworotko, M. J. *Chem. Commun.* **2001**, 863.
- (13) He, Y.; Li, B.; O’Keeffe, M.; Chen, B. L. *Chem. Soc. Rev.* **2014**, *43*, 5618.
- (14) Loiseau, T.; Serre, C.; Huguenard, C.; Fink, G.; Taulelle, F.; Henry, M.; Bataille, T.; Ferey, G. *Chem.—Eur. J.* **2004**, *10*, 1373.
- (15) (a) Liu, Y.; Her, J.-H.; Dailly, A.; Ramirez-Cuesta, A. J.; Neumann, D. A.; Brown, C. M. *J. Am. Chem. Soc.* **2008**, *130*, 11813. (b) Walker, A. M.; Civalieri, B.; Slater, B.; Mellot-Drazniaks, C.; Cora, F.; Zicovich-Wilson, C. M.; Roman-Perez, G.; Soler, J. M.; Gale, J. D. *Angew. Chem., Int. Ed.* **2010**, *49*, 7501.
- (16) (a) Ferey, G. *Science* **2005**, *310*, 1119. (b) Ferey, G.; Mellot-Drazniaks, C.; Serre, C.; Millange, F.; Dutour, J.; Surlle, S.; Margiolaki, I. *Science* **2005**, *309*, 2040.
- (17) (a) Hou, X.-J.; Li, H.; He, P. *Comput. Theor. Chem.* **2015**, 1055, 8. (b) Yu, K.; Kiesling, K.; Schmidt, J. R. *J. Phys. Chem. C* **2012**, *116*, 20480.
- (18) Li, H.; Eddaoudi, M.; Groy, T. L.; Yaghi, O. M. *J. Am. Chem. Soc.* **1998**, *120*, 8571.
- (19) Yaghi, O. M.; Davis, C. E.; Li, G. M.; Li, H. L. *J. Am. Chem. Soc.* **1997**, *119*, 2861.
- (20) Yaghi, O. M.; O’Keeffe, M.; Ockwig, N. W.; Chae, H. K.; Eddaoudi, M.; Kim, J. *Nature* **2003**, *423*, 705.
- (21) (a) Bahr, D. F.; Reid, J. A.; Mook, W. M.; Bauer, C. A.; Stumpf, R.; Skulan, A. J.; Moody, N. R.; Simmons, B. A.; Shindel, M. M.; Allendorf, M. D. *Phys. Rev. B* **2007**, *76*, 184106. (b) Martin, R. L.; Lin, L. C.; Jariwala, K.; Smit, B.; Haranczyk, M. *J. Phys. Chem. C* **2013**, *117*, 12159. (c) Samanta, A.; Furuta, T.; Li, J. *J. Chem. Phys.* **2006**, *125*, 084714.
- (22) (a) Dzubak, A. L.; Lin, L.-C.; Kim, J.; Swisher, J. A.; Poloni, R.; Maximoff, S. N.; Smit, B.; Gagliardi, L. *Nat. Chem.* **2012**, *4*, 810. (b) Poloni, R.; Lee, K.; Berger, R. F.; Smit, B.; Neaton, J. B. *J. Phys. Chem. Lett.* **2014**, *5*, 861. (c) Queen, W. L.; Hudson, M. R.; Bloch, E. D.; Mason, J. A.; Gonzalez, M. I.; Lee, J. S.; Gygi, D.; Howe, J. D.; Lee, K.; Darwish, T. A.; James, M.; Peterson, V. K.; Teat, S. J.; Smit, B.; Neaton, J. B.; Long, J. R.; Brown, C. M. *Chem. Sci.* **2014**, *5*, 4569.
- (23) Deria, P.; Mondloch, J. E.; Tylanakis, E.; Ghosh, P.; Bury, W.; Snurr, R. Q.; Hupp, J. T.; Farha, O. K. *J. Am. Chem. Soc.* **2013**, *135*, 16801.
- (24) (a) Beyzavi, M. H.; Klet, R. C.; Tussupbayev, S.; Borycz, J.; Vermeulen, N. A.; Cramer, C. J.; Stoddart, J. F.; Hupp, J. T.; Farha, O. K. *J. Am. Chem. Soc.* **2014**, *136*, 15861. (b) Planas, N.; Mondloch, J. E.; Tussupbayev, S.; Borycz, J.; Gagliardi, L.; Hupp, J. T.; Farha, O. K.; Cramer, C. J. *J. Phys. Chem. Lett.* **2014**, *5*, 3716.
- (25) Cavka, J. H.; Jakobsen, S.; Olsbye, U.; Guillou, N.; Lamberti, C.; Bordiga, S.; Lillerud, K. P. *J. Am. Chem. Soc.* **2008**, *130*, 13850.
- (26) Valenzano, L.; Civalieri, B.; Chavan, S.; Bordiga, S.; Nilsen, M. H.; Jakobsen, S.; Lillerud, K. P.; Lamberti, C. *Chem. Mater.* **2011**, *23*, 1700.
- (27) Schaate, A.; Roy, P.; Godt, A.; Lippke, J.; Waltz, F.; Wiebcke, M.; Behrens, P. *Chem.—Eur. J.* **2011**, *17*, 6643.
- (28) Chavan, S.; Vitillo, J. G.; Gianolio, D.; Zavorotynska, O.; Civalieri, B.; Jakobsen, S.; Nilsen, M. H.; Valenzano, L.; Lamberti, C.; Lillerud, K. P.; Bordiga, S. *Phys. Chem. Chem. Phys.* **2012**, *14*, 1614.
- (29) Huang, X.; Zhang, J.; Chen, X. *Chin. Sci. Bull.* **2003**, *48*, 1531.
- (30) (a) Goesten, M.; Stavitski, E.; Pidko, E. A.; Gucuyener, C.; Boshuizen, B.; Ehrlich, S. N.; Hensen, E. J. M.; Kapteijn, F.; Gascon, J. *Chem.—Eur. J.* **2013**, *19*, 7809. (b) Ryder, M. R.; Civalieri, B.; Bennett, T. D.; Henke, S.; Rudic, S.; Cinque, G.; Fernandez-Alonso, F.; Tan, J. C. *Phys. Rev. Lett.* **2014**, *113*, 215502.
- (31) Moggach, S. A.; Bennett, T. D.; Cheetham, A. K. *Angew. Chem., Int. Ed.* **2009**, *48*, 7087.
- (32) (a) Hegde, V. I.; Tan, J. C.; Waghmare, U. V.; Cheetham, A. K. *J. Phys. Chem. Lett.* **2013**, *4*, 3377. (b) Tan, J. C.; Civalieri, B.; Lin, C. C.; Valenzano, L.; Galvelis, R.; Chen, P. F.; Bennett, T. D.; Mellot-Drazniaks, C.; Zicovich-Wilson, C. M.; Cheetham, A. K. *Phys. Rev. Lett.* **2012**, *108*, 095502.
- (33) Schneemann, A.; Bon, V.; Schwedler, I.; Senkovska, I.; Kaskel, S.; Fischer, R. A. *Chem. Soc. Rev.* **2014**, *43*, 6062.
- (34) Wu, H.; Yildirim, T.; Zhou, W. *J. Phys. Chem. Lett.* **2013**, *4*, 925.
- (35) Kuppler, R. J.; Timmons, D. J.; Fang, Q. R.; Li, J. R.; Makal, T. A.; Young, M. D.; Yuan, D. Q.; Zhao, D.; Zhuang, W. J.; Zhou, H. C. *Coord. Chem. Rev.* **2009**, *253*, 3042.
- (36) James, S. L. *Chem. Soc. Rev.* **2003**, *32*, 276.
- (37) (a) Babarao, R.; Hu, Z. Q.; Jiang, J. W.; Chempath, S.; Sandler, S. I. *Langmuir* **2007**, *23*, 659. (b) Bae, Y. S.; Mulfort, K. L.; Frost, H.; Ryan, P.; Punathanam, S.; Broadbelt, L. J.; Hupp, J. T.; Snurr, R. Q. *Langmuir* **2008**, *24*, 8592. (c) Britt, D.; Furukawa, H.; Wang, B.; Glover, T. G.; Yaghi, O. M. *Proc. Natl. Acad. Sci. U.S.A.* **2009**, *106*, 20637. (d) Chen, B. L.; Liang, C. D.; Yang, J.; Contreras, D. S.; Clancy, Y. L.; Lobkovsky, E. B.; Yaghi, O. M.; Dai, S. *Angew. Chem., Int. Ed.* **2006**, *45*, 1390. (e) Dietzel, P. D. C.; Besikiotis, V.; Blom, R. J. *Mater. Chem.* **2009**, *19*, 7362. (f) Keskin, S.; van Heest, T. M.; Sholl, D. S. *ChemSusChem* **2010**, *3*, 879. (g) Lee, J. Y.; Olson, D. H.; Pan, L.; Emge, T. J.; Li, J. *Adv. Funct. Mater.* **2007**, *17*, 1255. (h) Li, J. R.; Kuppler, R. J.; Zhou, H. C. *Chem. Soc. Rev.* **2009**, *38*, 1477. (i) Li, J. R.; Ma, Y. G.; McCarthy, M. C.; Sculley, J.; Yu, J. M.; Jeong, H. K.; Balbuena, P. B.; Zhou, H. C. *Coord. Chem. Rev.* **2011**, *255*, 1791. (j) Li,

- K. H.; Olson, D. H.; Seidel, J.; Emge, T. J.; Gong, H. W.; Zeng, H. P.; Li, J. *J. Am. Chem. Soc.* **2009**, *131*, 10368. (k) Mason, J. A.; Sumida, K.; Herm, Z. R.; Krishna, R.; Long, J. R. *Energy Environ. Sci.* **2011**, *4*, 3030. (l) Pan, L.; Olson, D. H.; Ciemmolonski, L. R.; Heddy, R.; Li, J. *Angew. Chem., Int. Ed.* **2006**, *45*, 616. (m) Venna, S. R.; Carreon, M. A. *J. Am. Chem. Soc.* **2010**, *132*, 76. (n) Yang, C.; Wang, X. P.; Omary, M. A. *J. Am. Chem. Soc.* **2007**, *129*, 15454.
- (38) (a) McDonald, T. M.; Lee, W. R.; Mason, J. A.; Wiers, B. M.; Hong, C. S.; Long, J. R. *J. Am. Chem. Soc.* **2012**, *134*, 7056. (b) McDonald, T. M.; Mason, J. A.; Kong, X.; Bloch, E. D.; Gygi, D.; Dani, A.; Crocella, V.; Giordanino, F.; Odoh, S. O.; Drisdell, W. S.; Vlasisavljevich, B.; Dzubak, A. L.; Poloni, R.; Schnell, S. K.; Planas, N.; Lee, K.; Pascal, T.; Wan, L. F.; Prendergast, D.; Neaton, J. B.; Smit, B.; Kortright, J. B.; Gagliardi, L.; Bordiga, S.; Reimer, J. A.; Long, J. R. *Nature* **2015**, *519*, 303–308.
- (39) (a) Lee, C. Y.; Bae, Y.-S.; Jeong, N. C.; Farha, O. K.; Sarjeant, A. A.; Stern, C. L.; Nickias, P.; Snurr, R. Q.; Hupp, J. T.; Nguyen, S. T. *J. Am. Chem. Soc.* **2011**, *133*, 5228. (b) Li, K.; Olson, D. H.; Seidel, J.; Emge, T. J.; Gong, H.; Zeng, H.; Li, J. *J. Am. Chem. Soc.* **2009**, *131*, 10368.
- (40) Ma, S. Q.; Zhou, H. C. *Chem. Commun.* **2010**, 46, 44.
- (41) (a) Choi, S.; Drese, J. H.; Jones, C. W. *ChemSusChem* **2009**, *2*, 796. (b) Liu, C.; Li, F.; Ma, L. P.; Cheng, H. M. *Adv. Mater.* **2010**, *22*, E28. (c) Morris, R. E.; Wheatley, P. S. *Angew. Chem., Int. Ed.* **2008**, *47*, 4966. (d) Rowsell, J. L. C.; Millward, A. R.; Park, K. S.; Yaghi, O. M. *J. Am. Chem. Soc.* **2004**, *126*, 5666. (e) Rosi, N. L.; Eckert, J.; Eddaoudi, M.; Vodak, D. T.; Kim, J.; O'Keeffe, M.; Yaghi, O. M. *Science* **2003**, *300*, 1127. (f) Millward, A. R.; Yaghi, O. M. *J. Am. Chem. Soc.* **2005**, *127*, 17998.
- (42) (a) Allendorf, M. D.; Bauer, C. A.; Bhakta, R. K.; Houk, R. J. T. *Chem. Soc. Rev.* **2009**, *38*, 1330. (b) Bauer, C. A.; Timofeeva, T. V.; Settersten, T. B.; Patterson, B. D.; Liu, V. H.; Simmons, B. A.; Allendorf, M. D. *J. Am. Chem. Soc.* **2007**, *129*, 7136. (c) Chandler, B. D.; Cramb, D. T.; Shimizu, G. K. H. *J. Am. Chem. Soc.* **2006**, *128*, 10403. (d) Chen, B. L.; Wang, L. B.; Xiao, Y. Q.; Fronczek, F. R.; Xue, M.; Cui, Y. J.; Qian, G. D. *Angew. Chem., Int. Ed.* **2009**, *48*, 500. (e) Chen, B. L.; Yang, Y.; Zapata, F.; Lin, G. N.; Qian, G. D.; Lobkovsky, E. B. *Adv. Mater.* **2007**, *19*, 1693. (f) Chen, B. L.; Yang, Y.; Zapata, F.; Qian, G. D.; Luo, Y. S.; Zhang, J. H.; Lobkovsky, E. B. *Inorg. Chem.* **2006**, *45*, 8882. (g) Cui, Y. J.; Xu, H.; Yue, Y. F.; Guo, Z. Y.; Yu, J. C.; Chen, Z. X.; Gao, J. K.; Yang, Y.; Qian, G. D.; Chen, B. L. *J. Am. Chem. Soc.* **2012**, *134*, 3979. (h) Cui, Y. J.; Yue, Y. F.; Qian, G. D.; Chen, B. L. *Chem. Rev.* **2012**, *112*, 1126. (i) Della Rocca, J.; Liu, D. M.; Lin, W. B. *Acc. Chem. Res.* **2011**, *44*, 957. (j) Lan, A. J.; Li, K. H.; Wu, H. H.; Olson, D. H.; Emge, T. J.; Ki, W.; Hong, M. C.; Li, J. *Angew. Chem., Int. Ed.* **2009**, *48*, 2334. (k) Rocha, J.; Carlos, L. D.; Paz, F. A. A.; Ananias, D. *Chem. Soc. Rev.* **2011**, *40*, 926.
- (43) (a) Biswas, C.; Mukherjee, P.; Drew, M. G. B.; Gomez-Garcia, C. J.; Clemente-Juan, J. M.; Ghosh, A. *Inorg. Chem.* **2007**, *46*, 10771. (b) Kurmoo, M. *Chem. Soc. Rev.* **2009**, *38*, 1353. (c) Li, Q. P.; Jiang, X.; Du, S. W. *RSC Adv.* **2015**, *5*, 1785. (d) Li, Q. P.; Tian, C. B.; Zhang, H. B.; Qian, J. J.; Du, S. W. *CrystEngComm* **2014**, *16*, 9208. (e) MasPOCH, D.; Ruiz-Molina, D.; Veciana, J. *J. Mater. Chem.* **2004**, *14*, 2713. (f) Maurice, R.; Verma, P.; Zadrozny, J. M.; Luo, S.; Borycz, J.; Long, J. R.; Truhlar, D. G.; Gagliardi, L. *Inorg. Chem.* **2013**, *52*, 9379. (g) Ricco, R.; Malfatti, L.; Takahashi, M.; Hill, A. J.; Falcaro, P. J. *Mater. Chem. A* **2013**, *1*, 13033.
- (44) (a) Black, C. A.; Costa, J. S.; Fu, W. T.; Massera, C.; Roubeau, O.; Teat, S. J.; Aromi, G.; Gamez, P.; Reedijk, J. *Inorg. Chem.* **2009**, *48*, 1062. (b) Coronado, E.; Espallargas, G. M. *Chem. Soc. Rev.* **2013**, *42*, 1525. (c) Habib, H. A.; Sanchiz, J.; Janiak, C. *Inorg. Chim. Acta* **2009**, *362*, 2452. (d) Jia, H. P.; Li, W.; Ju, Z. F.; Zhang, J. *Eur. J. Inorg. Chem.* **2006**, 4264. (e) Jia, Q. X.; Sun, W. W.; Yao, C. F.; Wu, H. H.; Gao, E. Q.; Liu, C. M. *Dalton Trans.* **2009**, 2721. (f) Wang, Z. M.; Hu, K. L.; Gao, S.; Kobayashi, H. *Adv. Mater.* **2010**, *22*, 1526. (g) Zeng, M. H.; Wang, B.; Wang, X. Y.; Zhang, W. X.; Chen, X. M.; Gao, S. *Inorg. Chem.* **2006**, *45*, 7069.
- (45) Lee, J.; Farha, O. K.; Roberts, J.; Scheidt, K. A.; Nguyen, S. T.; Hupp, J. T. *Chem. Soc. Rev.* **2009**, *38*, 1450.
- (46) (a) Beier, M. J.; Kleist, W.; Wharmby, M. T.; Kissner, R.; Kimmeler, B.; Wright, P. A.; Grunwaldt, J. D.; Baiker, A. *Chem.—Eur. J.* **2012**, *18*, 887. (b) Carson, F.; Agrawal, S.; Gustafsson, M.; Bartoszewicz, A.; Moraga, F.; Zou, X. D.; Martin-Matute, B. *Chem.—Eur. J.* **2012**, *18*, 15337. (c) Czaja, A. U.; Trukhan, N.; Muller, U. *Chem. Soc. Rev.* **2009**, *38*, 1284. (d) Dang, D. B.; Wu, P. Y.; He, C.; Xie, Z.; Duan, C. Y. *J. Am. Chem. Soc.* **2010**, *132*, 14321. (e) Dhakshinamoorthy, A.; Garcia, H. *Chem. Soc. Rev.* **2012**, *41*, 5262. (f) Janiak, C. *Dalton Trans.* **2003**, 2781. (g) Leus, K.; Liu, Y. Y.; Van Der Voort, P. *Catal. Rev.* **2014**, *56*, 1. (h) Liu, Y.; Xuan, W. M.; Cui, Y. *Adv. Mater.* **2010**, *22*, 4112. (i) Mueller, U.; Schubert, M.; Teich, F.; Puetter, H.; Schierle-Arndt, K.; Pastre, J. *J. Mater. Chem.* **2006**, *16*, 626. (j) Ranocchiari, M.; van Bokhoven, J. A. *Phys. Chem. Chem. Phys.* **2011**, *13*, 6388. (k) Xamena, F.; Abad, A.; Corma, A.; Garcia, H. *J. Catal.* **2007**, *250*, 294. (l) Xamena, F.; Casanova, O.; Tailleux, R. G.; Garcia, H.; Corma, A. *J. Catal.* **2008**, *255*, 220.
- (47) (a) Canivet, J.; Aguado, S.; Schuurman, Y.; Farrusseng, D. *J. Am. Chem. Soc.* **2013**, *135*, 4195. (b) Zhang, D. M.; Guan, Y. J.; Hensen, E. J. M.; Chen, L.; Wang, Y. M. *Catal. Commun.* **2013**, *41*, 47.
- (48) (a) Cohen, S. M. *Chem. Rev.* **2012**, *112*, 970. (b) Cook, T. R.; Zheng, Y.-R.; Stang, P. J. *Chem. Rev.* **2013**, *113*, 734. (c) Corma, A.; Garcia, H.; Xamena, F. *Chem. Rev.* **2010**, *110*, 4606. (d) Stock, N.; Biswas, S. *Chem. Rev.* **2012**, *112*, 933.
- (49) (a) Burnett, B. J.; Barron, P. M.; Hu, C. H.; Choe, W. J. *Am. Chem. Soc.* **2011**, *133*, 9984. (b) Dinca, M.; Yu, A. F.; Long, J. R. *J. Am. Chem. Soc.* **2006**, *128*, 8904. (c) Eddaoudi, M.; Kim, J.; Rosi, N.; Vodak, D.; Wachter, J.; O'Keeffe, M.; Yaghi, O. M. *Science* **2002**, *295*, 469. (d) Evans, O. R.; Lin, W. B. *Acc. Chem. Res.* **2002**, *35*, 511. (e) Farha, O. K.; Hupp, J. T. *Acc. Chem. Res.* **2010**, *43*, 1166. (f) Ferey, G. *Chem. Soc. Rev.* **2008**, *37*, 191. (g) Lee, Y. R.; Kim, J.; Ahn, W. S. *Korean J. Chem. Eng.* **2013**, *30*, 1667. (h) Li, H.; Eddaoudi, M.; O'Keeffe, M.; Yaghi, O. M. *Nature* **1999**, *402*, 276. (i) Parnham, E. R.; Morris, R. E. *Acc. Chem. Res.* **2007**, *40*, 1005. (j) Perry, J. J.; Perman, J. A.; Zaworotko, M. J. *Chem. Soc. Rev.* **2009**, *38*, 1400. (k) Pichon, A.; Lazuen-Garay, A.; James, S. L. *CrystEngComm* **2006**, *8*, 211. (l) Shekhah, O.; Wang, H.; Kowarik, S.; Schreiber, F.; Paulus, M.; Tolan, M.; Sternemann, C.; Evers, F.; Zacher, D.; Fischer, R. A.; Woll, C. J. *Am. Chem. Soc.* **2007**, *129*, 15118. (m) Sumida, K.; Hill, M. R.; Horike, S.; Dailly, A.; Long, J. R. *J. Am. Chem. Soc.* **2009**, *131*, 15120.
- (50) (a) Farrusseng, D.; Daniel, C.; Gaudillere, C.; Ravon, U.; Schuurman, Y.; Mirodatos, C.; Dubbeldam, D.; Frost, H.; Snurr, R. Q. *Langmuir* **2009**, *25*, 7383. (b) Frost, H.; Snurr, R. Q. *J. Phys. Chem. C* **2007**, *111*, 18794. (c) Martin, R. L.; Haranczyk, M. *Chem. Sci.* **2013**, *4*, 1781. (d) Wilmer, C. E.; Farha, O. K.; Bae, Y. S.; Hupp, J. T.; Snurr, R. Q. *Energy Environ. Sci.* **2012**, *5*, 9849. (e) Wilmer, C. E.; Leaf, M.; Lee, C. Y.; Farha, O. K.; Hauser, B. G.; Hupp, J. T.; Snurr, R. Q. *Nat. Chem.* **2012**, *4*, 83.
- (51) Brunauer, S.; Emmett, P. H.; Teller, E. *J. Am. Chem. Soc.* **1938**, *60*, 309.
- (52) (a) Kohanoff, J. *Electronic structure calculations for solids and molecules: Theory and computational methods*; Cambridge University Press: New York, 2006. (b) Springborg, M. *Methods of electronic-structure calculations: from molecules to solids*; Wiley: New York, 2000.
- (53) (a) Frenkel, D.; Smit, B. *Understanding Molecular Simulation*, 2nd ed.; Academic Press, Inc.: Orlando, FL, 2001. (b) Hansen, J. P.; McDonald, I. R. *Theory of simple liquids*, 3rd ed.; Academic Press Inc.: New York, 2006.
- (54) (a) Huang, L. L.; Joshi, K. L.; van Duin, A. C. T.; Bandosz, T. J.; Gubbins, K. E. *Phys. Chem. Chem. Phys.* **2012**, *14*, 11327. (b) van Duin, A. C. T.; Dasgupta, S.; Lorant, F.; Goddard, W. A. *J. Phys. Chem. A* **2001**, *105*, 9396.
- (55) Zhao, M.; Iron, M. A.; Staszewski, P.; Schultz, N. E.; Valero, R.; Truhlar, D. G. *J. Chem. Theory Comput.* **2009**, *9*, 594.
- (56) Rapaport, D. C. *The Art of Molecular Dynamics Simulations*; Cambridge University Press: Cambridge, U.K., 1995.
- (57) Siepmann, J. I. *Adv. Chem. Phys.* **1999**, *105*, 1.
- (58) Garrett, B. C.; Truhlar, D. G. In *Encyclopedia of Computational Chemistry*; Schleyer, P. v. R., Allinger, N. L., Clark, T., Gasteiger, J.,

Kollman, P. A.; Schaefer, H. F., III, Eds.; John Wiley & Sons: Chichester, U.K., 1998; Vol. 5, p 3094.

(59) Chipot, C.; Pohorille, A. *Free Energy Calculations*; Springer-Verlag: Heidelberg, 2007.

(60) (a) Fang, H. J.; Demir, H.; Kamakoti, P.; Sholl, D. S. *J. Mater. Chem. A* **2014**, 2, 274. (b) Getman, R. B.; Bae, Y. S.; Wilmer, C. E.; Snurr, R. Q. *Chem. Rev.* **2012**, 112, 703.

(61) (a) Ghosh, P.; Kim, K. C.; Snurr, R. Q. *J. Phys. Chem. C* **2014**, 118, 1102. (b) Xiao, Y.; Han, T.; Xiao, G.; Ying, Y.; Huang, H.; Yang, Q.; Liu, D.; Zhong, C. *Langmuir* **2014**, 30, 12229.

(62) (a) Mead, C. A. In *Mathematical Frontiers in Computational Chemical Physics*; Truhlar, D. G., Ed.; Springer-Verlag: New York, 1988. (b) Simons, J.; Nichols, J. *Quantum Mechanics in Chemistry*; Oxford University Press: New York, 1997.

(63) Jasper, A. W.; Kendrick, B. K.; Mead, C. A.; Truhlar, D. G. In *Modern Trends in Chemical Reaction Dynamics: Experiment and Theory (Part 1)*; Yang, X.; Liu, K., Eds.; World Scientific: Singapore, 2004.

(64) (a) Szabo, A.; Ostlund, N. S. *Modern Quantum Chemistry*; Dover Publishing: Mineola, NY, 1996. (b) Cramer, C. J. *Essentials of Computational Chemistry*; Wiley: Chichester, 2002. (c) Levine, I. N. *Quantum Chemistry*, 4th ed.; Prentice Hall: Englewood Cliffs, NJ, 1991.

(65) Binkley, J. S.; Pople, J. A. *Int. J. Quantum Chem.* **1975**, 9, 229.

(66) Møller, C.; Plesset, M. S. *Phys. Rev.* **1934**, 46, 618.

(67) (a) Leininger, M. L.; Allen, W. D.; Schaefer, H. F.; Sherrill, C. D. *J. Chem. Phys.* **2000**, 112, 9213. (b) Olsen, J.; Christiansen, O.; Koch, H.; Jorgensen, P. *J. Chem. Phys.* **1996**, 105, 5082.

(68) (a) Raghavachari, K.; Anderson, J. B. *J. Phys. Chem.* **1996**, 100, 12960. (b) Raghavachari, K.; Trucks, G. W.; Pople, J. A.; Headgordon, M. *Chem. Phys. Lett.* **1989**, 157, 479.

(69) Neese, F.; Hansen, A.; Liakos, D. G. *J. Chem. Phys.* **2009**, 131, 064103.

(70) Lee, K.; Isley, W. C.; Dzubak, A. L.; Verma, P.; Stoneburner, S. J.; Lin, L. C.; Howe, J. D.; Bloch, E. D.; Reed, D. A.; Hudson, M. R.; Brown, C. M.; Long, J. R.; Neaton, J. B.; Smit, B.; Cramer, C. J.; Truhlar, D. G.; Gagliardi, L. *J. Am. Chem. Soc.* **2014**, 136, 698.

(71) Hirao, K. *Chem. Phys. Lett.* **1992**, 190, 374.

(72) Pittner, J. *J. Chem. Phys.* **2003**, 118, 10876.

(73) Yang, K. R.; Jalan, A.; Green, W. H.; Truhlar, D. G. *J. Chem. Theory Comput.* **2013**, 9, 418.

(74) Roos, B. O.; Taylor, P. R.; Siegbahn, P. E. M. *Chem. Phys.* **1980**, 48, 157.

(75) Andersson, K.; Malmqvist, P. A.; Roos, B. O. *J. Chem. Phys.* **1992**, 96, 1218.

(76) Hohenberg, P.; Kohn, W. *Phys. Rev. B* **1964**, 136, B864+.

(77) Kohn, W.; Sham, L. J. *Phys. Rev.* **1965**, 140, 1133.

(78) (a) Cramer, C. J.; Truhlar, D. G. *Phys. Chem. Chem. Phys.* **2009**, 11, 10757. (b) Goerigk, L.; Grimme, S. *Phys. Chem. Chem. Phys.* **2011**, 13, 6670. (c) Peverati, R.; Truhlar, D. G. *Philos. Trans. R. Soc., Ser. A: Math. Phys. Eng. Sci.* **2014**, 372, 20120476. (d) Zhang, W.; Truhlar, D. G.; Tang, M. *J. Chem. Theory Comput.* **2013**, 9, 3965.

(79) (a) Barth, U. v.; Hedin, L. *J. Phys. C: Solid State Phys.* **1972**, 5, 1629. (b) Rajagopal, A. K.; Callaway, J. *Phys. Rev. B* **1973**, 7, 1912. (c) van Wullen, C. *J. Comput. Chem.* **2002**, 23, 779.

(80) Engel, E.; Dreizler, R. M. *Density Functional Theory*; Springer-Verlag: Berlin, 2011.

(81) Ceperley, D. M.; Alder, B. J. *Phys. Rev. Lett.* **1980**, 45, 566.

(82) Vosko, S. H.; Wilk, L.; Nusair, M. *Can. J. Phys.* **1980**, 58, 1200.

(83) Mattesini, M.; Soler, J. M.; Yndurain, F. *Phys. Rev. B* **2006**, 73, 09411.

(84) Wu, H.; Simmons, J. M.; Srinivas, G.; Zhou, W.; Yildirim, T. *J. Phys. Chem. Lett.* **2010**, 1, 1946.

(85) Perdew, J. P.; Ruzsinszky, A.; Tao, J. M.; Staroverov, V. N.; Scuseria, G. E.; Csonka, G. I. *J. Chem. Phys.* **2005**, 123, 062201.

(86) Perdew, J. P.; Burke, K.; Ernzerhof, M. *Phys. Rev. Lett.* **1996**, 77, 3865.

(87) Zhang, Y. K.; Yang, W. T. *Phys. Rev. Lett.* **1998**, 80, 890.

(88) Perdew, J. P.; Ruzsinszky, A.; Csonka, G. I.; Vydrov, O. A.; Scuseria, G. E.; Constantin, L. A.; Zhou, X. L.; Burke, K. *Phys. Rev. Lett.* **2008**, 100, 136406.

(89) (a) Perdew, J. P. *Physica B* **1991**, 172, 1. (b) Perdew, J. P.; Chevary, J. A.; Vosko, S. H.; Jackson, K. A.; Pederson, M. R.; Singh, D. J.; Fiolhais, C. *Phys. Rev. B* **1992**, 46, 6671.

(90) (a) Becke, A. D. *Phys. Rev. A* **1988**, 38, 3098. (b) Lee, C. T.; Yang, W. T.; Parr, R. G. *Phys. Rev. B* **1988**, 37, 785.

(91) Cohen, A. J.; Handy, N. C. *Mol. Phys.* **2001**, 99, 607.

(92) Perdew, J. P. *Phys. Rev. B* **1986**, 33, 8822.

(93) Peverati, R.; Truhlar, D. G. *J. Chem. Theory Comput.* **2012**, 8, 2310.

(94) Tao, J. M.; Perdew, J. P.; Staroverov, V. N.; Scuseria, G. E. *Phys. Rev. Lett.* **2003**, 91, 146401.

(95) Zhao, Y.; Truhlar, D. G. *J. Chem. Phys.* **2006**, 125, 194101.

(96) (a) Peverati, R.; Truhlar, D. G. *J. Chem. Phys.* **2012**, 136.

(b) Peverati, R.; Truhlar, D. G. *J. Phys. Chem. Lett.* **2012**, 3, 117.

(97) (a) Averkiev, B. B.; Truhlar, D. G. *Catal. Sci. Technol.* **2011**, 1,

1526. (b) Averkiev, B. B.; Zhao, Y.; Truhlar, D. G. *J. Mol. Catal. A: Chem.* **2010**, 324, 80. (c) Gusev, D. G. *Organometallics* **2013**, 32, 4239.

(d) Luo, S. J.; Averkiev, B.; Yang, K. R.; Xu, X. F.; Truhlar, D. G. *J. Chem. Theory Comput.* **2014**, 10, 102.

(98) Becke, A. D. *J. Chem. Phys.* **1993**, 98, 5648.

(99) Adamo, C.; Barone, V. *J. Chem. Phys.* **1999**, 110, 6158.

(100) Becke, A. D. *J. Chem. Phys.* **1993**, 98, 1372.

(101) Xu, X.; Goddard, W. A. *Proc. Natl. Acad. Sci. U.S.A.* **2004**, 101, 2673.

(102) Zhao, Y.; Truhlar, D. G. *Theor. Chem. Acc.* **2008**, 120, 215.

(103) (a) Zhao, Y.; Truhlar, D. G. *J. Phys. Chem. A* **2006**, 110, 13126.

(b) Zhao, Y.; Truhlar, D. G. *J. Phys. Chem. A* **2006**, 110, 5121.

(104) Mori-Sanchez, P.; Cohen, A. J.; Yang, W. *J. Chem. Phys.* **2006**, 125, 201102.

(105) (a) Anisimov, V. I.; Aryasetiawan, F.; Liechtenstein, A. I. *J. Phys.: Condens. Matter* **1997**, 9, 767. (b) Dudarev, S. L.; Liechtenstein, A. I.; Castell, M. R.; Briggs, G. A. D.; Sutton, A. P. *Phys. Rev. B* **1997**, 56, 4900. (c) Himmetoglu, B.; Floris, A.; de Gironcoli, S.; Cococcioni, M. *Int. J. Quantum Chem.* **2014**, 114, 14.

(106) Hubbard, J. *Proc. R. Soc. A* **1964**, 276, 238.

(107) (a) Mosey, N. J.; Carter, E. A. *Phys. Rev. B* **2007**, 76, 155123.

(b) Mosey, N. J.; Liao, P.; Carter, E. A. *J. Chem. Phys.* **2008**, 129, 014103.

(108) Sorkin, A.; Iron, M. A.; Truhlar, D. G. *J. Chem. Theory Comput.* **2008**, 4, 307.

(109) Hu, Z.; Metiu, H. *J. Phys. Chem. C* **2011**, 115, 5841.

(110) (a) Heyd, J.; Scuseria, G. E.; Ernzerhof, M. *J. Chem. Phys.* **2003**, 118, 8207. (b) Heyd, J.; Scuseria, G. E.; Ernzerhof, M. *J. Chem. Phys.* **2006**, 124, 219906.

(111) Krukau, A. V.; Vydrov, O. A.; Izmaylov, A. F.; Scuseria, G. E. *J. Chem. Phys.* **2006**, 125, 224106.

(112) Kristyan, S.; Pulay, P. *Chem. Phys. Lett.* **1994**, 229, 175.

(113) Burley, S. K.; Petsko, G. A. *Science* **1985**, 229, 23.

(114) Grimme, S. *Wiley Interdiscip. Rev. Comput. Mol. Sci.* **2011**, 1, 211.

(115) Dion, M.; Rydberg, H.; Schroder, E.; Langreth, D. C.; Lundqvist, B. I. *Phys. Rev. Lett.* **2004**, 92, 246401.

(116) Lee, K.; Murray, E. D.; Kong, L. Z.; Lundqvist, B. I.; Langreth, D. C. *Phys. Rev. B* **2010**, 82, 081101.

(117) Klimes, J.; Bowler, D. R.; Michaelides, A. *J. Phys. Condens. Matter* **2010**, 22, 022201.

(118) (a) Zhao, Y.; Lynch, B. J.; Truhlar, D. G. *J. Phys. Chem. A* **2004**, 108, 4786. (b) Goerigk, L.; Grimme, S. *J. Chem. Theory Comput.* **2011**, 7, 291.

(119) (a) Hohenstein, E. G.; Chill, S. T.; Sherrill, C. D. *J. Chem. Theory Comput.* **2008**, 4, 1996. (b) Zhao, Y.; Truhlar, D. G. *J. Phys. Chem. C* **2008**, 112, 4061.

(120) Grimme, S. *J. Comput. Chem.* **2004**, 25, 1463.

(121) Grimme, S. *J. Comput. Chem.* **2006**, 27, 1787.

(122) Grimme, S.; Antony, J.; Ehrlich, S.; Krieg, H. *J. Chem. Phys.* **2010**, 132, 154104.

- (123) Grimme, S.; Ehrlich, S.; Goerigk, L. *J. Comput. Chem.* **2011**, *32*, 1456.
- (124) (a) Carlson, R. K.; Li Manni, G.; Sonnenberger, A. L.; Truhlar, D. G.; Gagliardi, L. *J. Chem. Theory Comput.* **2014**, *11*, 82. (b) Li Manni, G.; Carlson, R. K.; Luo, S.; Ma, D.; Olsen, J.; Truhlar, D. G.; Gagliardi, L. *J. Chem. Theory Comput.* **2014**, *10*, 3669.
- (125) Ma, D. X.; Manni, G. L.; Gagliardi, L. *J. Chem. Phys.* **2011**, *135*, 044128.
- (126) Sauri, V.; Serrano-Andres, L.; Shahi, A. R. M.; Gagliardi, L.; Vancoillie, S.; Pierloot, K. *J. Chem. Theory Comput.* **2011**, *7*, 153.
- (127) Manni, G. L.; Ma, D. X.; Aquilante, F.; Olsen, J.; Gagliardi, L. *J. Chem. Theory Comput.* **2013**, *9*, 3375.
- (128) (a) Bytautas, L.; Ruedenberg, K. *Chem. Phys.* **2009**, *356*, 64. (b) Ivanic, J.; Ruedenberg, K. *Theor. Chem. Acc.* **2001**, *106*, 339. (c) Ivanic, J.; Ruedenberg, K. *Theor. Chem. Acc.* **2002**, *107*, 220.
- (129) Marques, M. A. L.; Ullrich, C. A.; Nogueira, F.; Rubio, A.; Burke, K.; Gross, E. K. U. *Time-Dependent Density Functional Theory*; Springer-Verlag, Berlin, 2006.
- (130) (a) Casida, M. E. *J. Mol. Struct. THEOCHEM* **2009**, *914*, 3. (b) Casida, M. E.; Huix-Rotllant, M. *Annu. Rev. Phys. Chem.* **2012**, *63*, 287. (c) Marques, M. A. L.; Gross, E. K. U. *Annu. Rev. Phys. Chem.* **2004**, *55*, 427. (d) Runge, E.; Gross, E. K. U. *Phys. Rev. Lett.* **1984**, *52*, 997.
- (131) Laurent, A. D.; Jacquemin, D. *Int. J. Quantum Chem.* **2013**, *113*, 2019.
- (132) (a) Autschbach, J. *ChemPhysChem* **2009**, *10*, 1757. (b) Kuritz, N.; Stein, T.; Baer, R.; Kronik, L. *J. Chem. Theory Comput.* **2011**, *7*, 2408.
- (133) (a) Casida, M. E.; Salahub, D. R. *J. Chem. Phys.* **2000**, *113*, 8918. (b) Hirata, S.; Zhan, C. G.; Apra, E.; Windus, T. L.; Dixon, D. A. *J. Phys. Chem. A* **2003**, *107*, 10154. (c) Tozer, D. J.; Handy, N. C. *J. Chem. Phys.* **1998**, *109*, 10180.
- (134) (a) Gruning, M.; Gritsenko, O. V.; van Gisbergen, S. J. A.; Baerends, E. J. *J. Chem. Phys.* **2001**, *114*, 652. (b) Vanleeuwen, R.; Baerends, E. J. *Phys. Rev. A* **1994**, *49*, 2421.
- (135) Tawada, Y.; Tsuneda, T.; Yanagisawa, S.; Yanai, T.; Hirao, K. *J. Chem. Phys.* **2004**, *120*, 8425.
- (136) Jaramillo, J.; Scuseria, G. E.; Ernzerhof, M. *J. Chem. Phys.* **2003**, *118*, 1068.
- (137) Iikura, H.; Tsuneda, T.; Yanai, T.; Hirao, K. *J. Chem. Phys.* **2001**, *115*, 3540.
- (138) Yanai, T.; Tew, D. P.; Handy, N. C. *Chem. Phys. Lett.* **2004**, *393*, 51.
- (139) (a) Ji, M.; Hao, C.; Wang, D.; Li, H.; Qiu, J. *Dalton Trans.* **2013**, *42*, 3464. (b) Ji, M.; Lan, X.; Han, Z.; Hao, C.; Qiu, J. *Inorg. Chem.* **2012**, *51*, 12389.
- (140) Goodenough, J. B. *Phys. Rev.* **1968**, *171*, 466.
- (141) (a) Malmqvist, P. A.; Roos, B. O.; Schimmelpfennig, B. *Chem. Phys. Lett.* **2002**, *357*, 230. (b) Roos, B. O.; Malmqvist, P. A. *Phys. Chem. Chem. Phys.* **2004**, *6*, 2919. (c) vanLenthe, E.; Snijders, J. G.; Baerends, E. J. *J. Chem. Phys.* **1996**, *105*, 6505.
- (142) *Combined Quantum Mechanical and Molecular Mechanical Methods*; Gao, J.; Thompson, M. A., Eds.; American Chemical Society: Washington, DC, 1998.
- (143) Supronowicz, B.; Mavrandonakis, A.; Heine, T. *J. Phys. Chem. C* **2013**, *117*, 14570.
- (144) (a) Bordiga, S.; Vitillo, J. G.; Ricchiardi, G.; Regli, L.; Cocina, D.; Zecchina, A.; Arstad, B.; Bjorgen, M.; Hafizovic, J.; Lillerud, K. P. *J. Phys. Chem. B* **2005**, *109*, 18237. (b) Planas, N.; Dzubak, A. L.; Poloni, R.; Lin, L. C.; McManus, A.; McDonald, T. M.; Neaton, J. B.; Long, J. R.; Smit, B.; Gagliardi, L. *J. Am. Chem. Soc.* **2013**, *135*, 7402. (c) Valenzano, L.; Civalieri, B.; Sillar, K.; Sauer, J. *J. Phys. Chem. C* **2011**, *115*, 21777. (d) Verma, P.; Xu, X. F.; Truhlar, D. G. *J. Phys. Chem. C* **2013**, *117*, 12648.
- (145) (a) Kresse, G.; Furthmuller, J. *Phys. Rev. B* **1996**, *54*, 11169. (b) Kresse, G.; Furthmuller, J. *Comput. Mater. Sci.* **1996**, *6*, 15.
- (146) Kresse, G.; Joubert, D. *Phys. Rev. B* **1999**, *59*, 1758.
- (147) Vanderbilt, D. *Phys. Rev. B* **1990**, *41*, 7892.
- (148) Hamann, D. R.; Schluter, M.; Chiang, C. *Phys. Rev. Lett.* **1979**, *43*, 1494.
- (149) (a) Blochl, P. E. *Phys. Rev. B* **1994**, *50*, 17953. (b) Blochl, P. E.; Forst, C. J.; Schimpl, J. *Bull. Mater. Sci.* **2003**, *26*, 33.
- (150) Holzwarth, N. A. W.; Matthews, G. E.; Dunning, R. B.; Tackett, A. R.; Zeng, Y. *Phys. Rev. B* **1997**, *55*, 2005.
- (151) Lippert, G.; Hutter, J.; Parrinello, M. *Theor. Chem. Acc.* **1999**, *103*, 124.
- (152) (a) Dovesi, R.; Civalieri, B.; Roetti, C.; Saunders, V. R.; Orlando, R. *Reviews in Computational Chemistry*; John Wiley & Sons, Inc.: New York, 2005. (b) Valenzano, L.; Vitillo, J. G.; Chavan, S.; Civalieri, B.; Bonino, F.; Bordiga, S.; Lamberti, C. *Catal. Today* **2012**, *182*, 67.
- (153) Van Lenthe, E.; Baerends, E. J. *J. Comput. Chem.* **2003**, *24*, 1142.
- (154) (a) Alemany, M. M. G.; Jain, M.; Tiago, M. L.; Zhou, Y.; Saad, Y.; Chelikowsky, J. R. *Comput. Phys. Commun.* **2007**, *177*, 339. (b) Enkovaara, J.; Rostgaard, C.; Mortensen, J. J.; Chen, J.; Dulak, M.; Ferrighi, L.; Gavnholt, J.; Glinvad, C.; Haikola, V.; Hansen, H. A.; Kristoffersen, H. H.; Kuisma, M.; Larsen, A. H.; Lehtovaara, L.; Ljungberg, M.; Lopez-Acevedo, O.; Moses, P. G.; Ojanen, J.; Olsen, T.; Petzold, V.; Romero, N. A.; Stausholm-Møller, J.; Strange, M.; Tritsarlis, G. A.; Vanin, M.; Walter, M.; Hammer, B.; Hakkinen, H.; Madsen, G. K. H.; Nieminen, R. M.; Norskov, J.; Puska, M.; Rantala, T. T.; Schiøtz, J.; Thygesen, K. S.; Jacobsen, K. W. *J. Phys. Condens. Matter* **2010**, *22*, 253202. (c) Mortensen, J. J.; Hansen, L. B.; Jacobsen, K. W. *Phys. Rev. B* **2005**, *71*, 035109.
- (155) Marx, D.; Hutter, J. In *Modern Methods and Algorithms of Quantum Chemistry*; Grotendorst, J., Ed.; John von Neumann Institute for Computing: Jülich, 2000; Vol. 1.
- (156) Chen, L.; Mowat, J. P. S.; Fairen-Jimenez, D.; Morrison, C. A.; Thompson, S. P.; Wright, P. A.; Dueren, T. *J. Am. Chem. Soc.* **2013**, *135*, 15763.
- (157) Drisdell, W. S.; Poloni, R.; McDonald, T. M.; Long, J. R.; Smit, B.; Neaton, J. B.; Prendergast, D.; Kortright, J. B. *J. Am. Chem. Soc.* **2013**, *135*, 18183.
- (158) (a) Cauet, E.; Bogatko, S.; Weare, J. H.; Fulton, J. L.; Schenter, G. K.; Bylaska, E. J. *J. Chem. Phys.* **2010**, *132*, 194502. (b) Vjunov, A.; Fulton, J. L.; Huthwelker, T.; Pin, S.; Mei, D. H.; Schenter, G. K.; Govind, N.; Camaioni, D. M.; Hu, J. Z.; Lercher, J. A. *J. Am. Chem. Soc.* **2014**, *136*, 8296.
- (159) Thomas, M.; Brehm, M.; Fligg, R.; Vohringer, P.; Kirchner, B. *Phys. Chem. Chem. Phys.* **2013**, *15*, 6608.
- (160) (a) Atta-Fynn, R.; Bylaska, E. J.; Schenter, G. K.; de Jong, W. A. *J. Phys. Chem. A* **2011**, *115*, 4665. (b) Pozzo, M.; Alfe, D.; Lacovig, P.; Hofmann, P.; Lizzit, S.; Baraldi, A. *Phys. Rev. Lett.* **2011**, *106*, 135501.
- (161) Mace, A.; Laasonen, K.; Laaksonen, A. *Phys. Chem. Chem. Phys.* **2014**, *16*, 166.
- (162) Yadum, S.; Choomwattana, S.; Khongpracha, P.; Sirijaraensre, J.; Limtrakul, J. *ChemPhysChem* **2013**, *14*, 923.
- (163) Mukaiyama, T.; Narasaka, K.; Banno, K. *Chem. Lett.* **1973**, *2*, 1011.
- (164) (a) Amirjalayer, S.; Tafipolsky, M.; Schmid, R. *J. Phys. Chem. Lett.* **2014**, *5*, 3206. (b) Cai, Y.; Kulkarni, A. R.; Huang, Y. G.; Sholl, D. S.; Walton, K. S. *Cryst. Growth Des.* **2014**, *14*, 6122. (c) Vanpoucke, D. E. P.; Jaeken, J. W.; De Baerdemacker, S.; Lejaeghere, K.; Van Speybroeck, V. *Beilstein J. Nanotechnol.* **2014**, *5*, 1738.
- (165) Chung, Y. G.; Camp, J.; Haranczyk, M.; Sikora, B. J.; Bury, W.; Krungelvicute, V.; Yildirim, T.; Farha, O. K.; Sholl, D. S.; Snurr, R. Q. *Chem. Mater.* **2014**, *26*, 6185.
- (166) Goldsmith, J.; Wong-Foy, A. G.; Cafarella, M. J.; Siegel, D. J. *Chem. Mater.* **2013**, *25*, 3373.
- (167) (a) Le Page, Y.; Saxe, P. *Phys. Rev. B* **2002**, *65*, 104014. (b) Ziambaras, E.; Schroder, E. *Phys. Rev. B* **2003**, *68*, 064112. (c) Wallace, D. C. *Thermodynamics of crystals*; Wiley: New York, 1972.
- (168) (a) Louie, S. G. *Conceptual Foundations of Materials: A Standard Model for Ground- and Excited-State Properties*; Elsevier

- Science: Amsterdam, 2006. (b) Onida, G.; Reining, L.; Rubio, A. *Rev. Mod. Phys.* **2002**, *74*, 601.
- (169) (a) Brozek, C. K.; Dinca, M. *J. Am. Chem. Soc.* **2013**, *135*, 12886. (b) Venkataramanan, N. S.; Sahara, R.; Mizuseki, H.; Kawazoe, Y. *Int. J. Mol. Sci.* **2009**, *10*, 1601.
- (170) (a) Garberoglio, G.; Skoulidas, A. I.; Johnson, J. K. *J. Phys. Chem. B* **2005**, *109*, 13094. (b) Mueller, T.; Ceder, G. *J. Phys. Chem. B* **2005**, *109*, 17974. (c) Mulder, F. M.; Dingemans, T. J.; Wagemaker, M.; Kearley, G. J. *Chem. Phys.* **2005**, *317*, 113. (d) Sagara, T.; Klassen, J.; Ganz, E. *J. Chem. Phys.* **2004**, *121*, 12543. (e) Sagara, T.; Klassen, J.; Ortony, J.; Ganz, E. *J. Chem. Phys.* **2005**, *123*, 014701. (f) Sagara, T.; Ortony, J.; Ganz, E. *J. Chem. Phys.* **2005**, *123*, 214707. (g) Yildirim, T.; Hartman, M. R. *Phys. Rev. Lett.* **2005**, *95*, 215504.
- (171) DOE <http://www1.eere.energy.gov/hydrogenandfuelcells/mypp/>.
- (172) Eddaoudi, M.; Li, H. L.; Yaghi, O. M. *J. Am. Chem. Soc.* **2000**, *122*, 1391.
- (173) Zhou, W.; Yildirim, T. *Phys. Rev. B* **2006**, *74*, 180301.
- (174) Fuentes-Cabrera, M.; Nicholson, D. M.; Sumpter, B. G.; Widom, M. *J. Chem. Phys.* **2005**, *123*, 124713.
- (175) Astala, R.; Auerbach, S. M.; Monson, P. A. *J. Phys. Chem. B* **2004**, *108*, 9208.
- (176) (a) Greathouse, J. A.; Allendorf, M. D. *J. Phys. Chem. C* **2008**, *112*, 5795. (b) Han, S. S.; Goddard, W. A. *J. Phys. Chem. C* **2007**, *111*, 15185.
- (177) (a) Yang, L.-M.; Ravindran, P.; Vajeeston, P.; Tilset, M. *Phys. Chem. Chem. Phys.* **2012**, *14*, 4713. (b) Yang, L.-M.; Ravindran, P.; Vajeeston, P.; Tilset, M. *RSC Adv.* **2012**, *2*, 1618.
- (178) Feldblyum, J. I.; Wong-Foy, A. G.; Matzger, A. J. *Chem. Commun.* **2012**, *48*, 9828.
- (179) Bordiga, S.; Lamberti, C.; Ricchiardi, G.; Regli, L.; Bonino, F.; Damin, A.; Lillerud, K. P.; Bjorgen, M.; Zecchina, A. *Chem. Commun.* **2004**, 2300.
- (180) Yang, L.-M.; Vajeeston, P.; Ravindran, P.; Fjellvag, H.; Tilset, M. *Inorg. Chem.* **2010**, *49*, 10283.
- (181) Yu, D. C.; Yazaydin, A. O.; Lane, J. R.; Dietzel, P. D. C.; Snurr, R. Q. *Chem. Sci.* **2013**, *4*, 3544.
- (182) Wang, L. J.; Deng, H. X.; Furukawa, H.; Gandara, F.; Cordova, K. E.; Peri, D.; Yaghi, O. M. *Inorg. Chem.* **2014**, *53*, 5881.
- (183) (a) Bloch, E. D.; Hudson, M. R.; Mason, J. A.; Chavan, S.; Crocellà, V.; Howe, J. D.; Lee, K.; Dzubak, A. L.; Queen, W. L.; Zadrozny, J. M.; Geier, S. J.; Lin, L.-C.; Gagliardi, L.; Smit, B.; Neaton, J. B.; Bordiga, S.; Brown, C. M.; Long, J. R. *J. Am. Chem. Soc.* **2014**, *136*. (b) Bloch, E. D.; Queen, W. L.; Krishna, R.; Zadrozny, J. M.; Brown, C. M.; Long, J. R. *Science* **2012**, *335*, 1606. (c) Dietzel, P. D. C.; Georgiev, P. A.; Eckert, J.; Blom, R.; Straessle, T.; Unruh, T. *Chem. Commun.* **2010**, *46*, 4962. (d) Dietzel, P. D. C.; Morita, Y.; Blom, R.; Fjellvag, H. *Angew. Chem., Int. Ed.* **2005**, *44*, 6354. (e) Geier, S. J.; Mason, J. A.; Bloch, E. D.; Queen, W. L.; Hudson, M. R.; Brown, C. M.; Long, J. R. *Chem. Sci.* **2013**, *4*, 2054. (f) Herm, Z. R.; Swisher, J. A.; Smit, B.; Krishna, R.; Long, J. R. *J. Am. Chem. Soc.* **2011**, *133*, 5664. (g) Rowsell, J. L. C.; Yaghi, O. M. *J. Am. Chem. Soc.* **2006**, *128*, 1304.
- (184) (a) Liu, Y.; Kabbour, H.; Brown, C. M.; Neumann, D. A.; Ahn, C. C. *Langmuir* **2008**, *24*, 4772. (b) Vitillo, J. G.; Regli, L.; Chavan, S.; Ricchiardi, G.; Spoto, G.; Dietzel, P. D. C.; Bordiga, S.; Zecchina, A. *J. Am. Chem. Soc.* **2008**, *130*, 8386.
- (185) (a) Pham, T.; Forrest, K. A.; Nugent, P.; Belmabkhout, Y.; Luebke, R.; Eddaoudi, M.; Zaworotko, M. J.; Space, B. *J. Phys. Chem. C* **2013**, *117*, 9340. (b) Poloni, R.; Smit, B.; Neaton, J. B. *J. Phys. Chem. A* **2012**, *116*, 4957.
- (186) Canepa, P.; Chabal, Y. J.; Thonhauser, T. *Phys. Rev. B* **2013**, *87*, 094407.
- (187) (a) Stroppa, A.; Jain, P.; Barone, P.; Marsman, M.; Perez-Mato, J. M.; Cheetham, A. K.; Kroto, H. W.; Picozzi, S. *Angew. Chem., Int. Ed.* **2011**, *50*, 5847. (b) Wang, Z. X.; Jain, P.; Choi, K. Y.; van Tol, J.; Cheetham, A. K.; Kroto, H. W.; Koo, H. J.; Zhou, H.; Hwang, J. M.; Choi, E. S.; Whangbo, M. H.; Dalal, N. S. *Phys. Rev. B* **2013**, *87*, 224406.
- (188) Park, J.; Kim, H.; Jung, Y. *J. Phys. Chem. Lett.* **2013**, *4*, 2530.
- (189) Maximoff, S. N.; Smit, B. *Nat. Commun.* **2014**, *5*, 4032.
- (190) Bloch, E. D.; Murray, L. J.; Queen, W. L.; Chavan, S.; Maximoff, S. N.; Bigi, J. P.; Krishna, R.; Peterson, V. K.; Grandjean, F.; Long, G. J.; Smit, B.; Bordiga, S.; Brown, C. M.; Long, J. R. *J. Am. Chem. Soc.* **2011**, *133*, 14814.
- (191) Zhang, Q. J.; Li, B. H.; Chen, L. *Inorg. Chem.* **2013**, *52*, 9356.
- (192) (a) Dirac, P. A. M. *Proc. R. Soc. London, Ser. A* **1929**, *123*, 714. (b) Heisenberg, W. *Z. Phys.* **1928**, *49*, 619. (c) van Vleck, J. H. *Rev. Mod. Phys.* **1945**, *17*, 27.
- (193) (a) Di Sante, D.; Stroppa, A.; Jain, P.; Picozzi, S. *J. Am. Chem. Soc.* **2013**, *135*, 18126. (b) Zhuang, G. L.; Tan, L.; Chen, W. L.; Bai, J. Q.; Zhong, X.; Wang, J. G. *CrystEngComm* **2014**, *16*, 6963.
- (194) (a) Serre, C.; Mellot-Draznieks, C.; Surble, S.; Audebrand, N.; Filinchuk, Y.; Ferey, G. *Science* **2007**, *315*, 1828. (b) Serre, C.; Millange, F.; Thouvenot, C.; Nogués, M.; Marsolier, G.; Louer, D.; Ferey, G. *J. Am. Chem. Soc.* **2002**, *124*, 13519.
- (195) Munn, A. S.; Ramirez-Cuesta, A. J.; Millange, F.; Walton, R. I. *Chem. Phys.* **2013**, *427*, 30.
- (196) Mendt, M.; Jee, B.; Stock, N.; Ahnfeldt, T.; Hartmann, M.; Himsl, D.; Poepl, A. *J. Phys. Chem. C* **2010**, *114*, 19443.
- (197) Liu, Y. Y.; Couck, S.; Vandichel, M.; Grzywa, M.; Leus, K.; Biswas, S.; Vollmer, D.; Gascon, J.; Kapteijn, F.; Denayer, J. F. M.; Waroquier, M.; Van Speybroeck, V.; Van der Voort, P. *Inorg. Chem.* **2013**, *52*, 113.
- (198) (a) Salles, F.; Ghoufi, A.; Maurin, G.; Bell, R. G.; Mellot-Draznieks, C.; Ferey, G. *Angew. Chem., Int. Ed.* **2008**, *47*, 8487. (b) Serre, C.; Bourrelly, S.; Vimont, A.; Ramsahye, N. A.; Maurin, G.; Llewellyn, P. L.; Daturi, M.; Filinchuk, Y.; Leynaud, O.; Barnes, P.; Ferey, G. *Adv. Mater.* **2007**, *19*, 2246.
- (199) Coombes, D. S.; Cora, F.; Mellot-Draznieks, C.; Bell, R. G. *J. Phys. Chem. C* **2009**, *113*, 544.
- (200) Rosenbach, N., Jr.; Ghoufi, A.; Deroche, I.; Llewellyn, P. L.; Devic, T.; Bourrelly, S.; Serre, C.; Ferey, G.; Maurin, G. *Phys. Chem. Chem. Phys.* **2010**, *12*, 6428.
- (201) (a) Bourrelly, S.; Llewellyn, P. L.; Serre, C.; Millange, F.; Loiseau, T.; Ferey, G. *J. Am. Chem. Soc.* **2005**, *127*, 13519. (b) Llewellyn, P. L.; Bourrelly, S.; Serre, C.; Filinchuk, Y.; Ferey, G. *Angew. Chem., Int. Ed.* **2006**, *45*, 7751.
- (202) Couck, S.; Denayer, J. F. M.; Baron, G. V.; Remy, T.; Gascon, J.; Kapteijn, F. *J. Am. Chem. Soc.* **2009**, *131*, 6326.
- (203) Stavitski, E.; Pidko, E. A.; Couck, S.; Remy, T.; Hensen, E. J. M.; Weckhuysen, B. M.; Denayer, J.; Gascon, J.; Kapteijn, F. *Langmuir* **2011**, *27*, 3970.
- (204) Rappe, A. K.; Casewit, C. J.; Colwell, K. S.; Goddard, W. A.; Skiff, W. M. *J. Am. Chem. Soc.* **1992**, *114*, 10024.
- (205) Devic, T.; Salles, F.; Bourrelly, S.; Moulin, B.; Maurin, G.; Horcajada, P.; Serre, C.; Vimont, A.; Lavalley, J.-C.; Leclerc, H.; Clet, G.; Daturi, M.; Llewellyn, P. L.; Filinchuk, Y.; Ferey, G. *J. Mater. Chem.* **2012**, *22*, 10266.
- (206) Torrisi, A.; Bell, R. G.; Mellot-Draznieks, C. *Cryst. Growth Des.* **2010**, *10*, 2839.
- (207) Ghysels, A.; Vanduyfhuys, L.; Vandichel, M.; Waroquier, M.; Van Speybroeck, V.; Smit, B. *J. Phys. Chem. C* **2013**, *117*, 11540.
- (208) Biswas, S.; Vanpoucke, D. E. P.; Verstraeten, T.; Vandichel, M.; Couck, S.; Leus, K.; Liu, Y.-Y.; Waroquier, M.; Van Speybroeck, V.; Denayer, J. F. M.; Van der Voort, P. *J. Phys. Chem. C* **2013**, *117*, 22784.
- (209) (a) Becke, A. D.; Johnson, E. R. *J. Chem. Phys.* **2005**, *123*, 154101. (b) Johnson, E. R.; Becke, A. D. *J. Chem. Phys.* **2005**, *123*, 024101. (c) Johnson, E. R.; Becke, A. D. *J. Chem. Phys.* **2006**, *124*, 174104.
- (210) (a) Gaudin, C.; Cunha, D.; Ivanoff, E.; Horcajada, P.; Cheve, G.; Yasri, A.; Loget, O.; Serre, C.; Maurin, G. *Microporous Mesoporous Mater.* **2012**, *157*, 124. (b) Horcajada, P.; Salles, F.; Wuttke, S.; Devic, T.; Heurtaux, D.; Maurin, G.; Vimont, A.; Daturi, M.; David, O.; Magnier, E.; Stock, N.; Filinchuk, Y.; Popov, D.; Riekel, C.; Ferey, G.; Serre, C. *J. Am. Chem. Soc.* **2011**, *133*, 17839. (c) Lescouet, T.; Kockrick, E.; Bergeret, G.; Pera-Titus, M.; Aguado, S.; Farrusseng, D. *J. Mater. Chem.* **2012**, *22*, 10287. (d) Pera-Titus, M.; Farrusseng, D. *J. Phys. Chem. C* **2012**, *116*, 1638. (e) Serra-Crespo, P.; Gobechiya, E.;

- Ramos-Fernandez, E. V.; Juan-Alcaniz, J.; Martinez-Joaristi, A.; Stavitski, E.; Kirschhock, C. E. A.; Martens, J. A.; Kapteijn, F.; Gascon, J. *Langmuir* **2012**, *28*, 12916.
- (211) Boutin, A.; Bousquet, D.; Ortiz, A. U.; Coudert, F. X.; Fuchs, A. H.; Ballandras, A.; Weber, G.; Bezverkhyy, I.; Bellat, J. P.; Ortiz, G.; Chaplais, G.; Paillaud, J. L.; Marichal, C.; Nouali, H.; Patarin, J. *J. Phys. Chem. C* **2013**, *117*, 8180.
- (212) Coudert, F. X.; Ortiz, A. U.; Haigis, V.; Bousquet, D.; Fuchs, A. H.; Ballandras, A.; Weber, G.; Bezverkhyy, I.; Geolfroy, N.; Bellat, J. P.; Ortiz, G.; Chaplais, G.; Patarin, J.; Boutin, A. *J. Phys. Chem. C* **2014**, *118*, 5397.
- (213) Millange, F.; Guillou, N.; Walton, R. I.; Greneche, J.-M.; Margiolaki, I.; Fereya, G. *Chem. Commun.* **2008**, 4732.
- (214) Haigis, V.; Coudert, F. X.; Vuilleumier, R.; Boutin, A. *Phys. Chem. Chem. Phys.* **2013**, *15*, 19049.
- (215) Haigis, V.; Belkhdja, Y.; Coudert, F.-X.; Vuilleumier, R.; Boutin, A. *J. Chem. Phys.* **2014**, *141*, 064703.
- (216) Ghoufi, A.; Subercaze, A.; Ma, Q.; Yot, P. G.; Ke, Y.; Puente-Orench, I.; Devic, T.; Guillermin, V.; Zhong, C.; Serre, C.; Ferey, G.; Maurin, G. *J. Phys. Chem. C* **2012**, *116*, 13289.
- (217) (a) Coudert, F. X.; Boutin, A.; Fuchs, A. H.; Neimark, A. V. *J. Phys. Chem. Lett.* **2013**, *4*, 3198. (b) Coudert, F. X.; Boutin, A.; Jeffroy, M.; Mellot-Draznieks, C.; Fuchs, A. H. *ChemPhysChem* **2011**, *12*, 247. (c) Llewellyn, P. L.; Maurin, G.; Devic, T.; Loera-Serna, S.; Rosenbach, N.; Serre, C.; Bourrelly, S.; Horcajada, P.; Filinchuk, Y.; Ferey, G. *J. Am. Chem. Soc.* **2008**, *130*, 12808. (d) Neimark, A. V.; Coudert, F. X.; Boutin, A.; Fuchs, A. H. *J. Phys. Chem. Lett.* **2010**, *1*, 445. (e) Wang, Z. Q.; Cohen, S. M. *J. Am. Chem. Soc.* **2009**, *131*, 16675.
- (218) Ortiz, A. U.; Boutin, A.; Fuchs, A. H.; Coudert, F. X. *Phys. Rev. Lett.* **2012**, *109*, 195502.
- (219) Ortiz, A. U.; Boutin, A.; Coudert, F. X. *Chem. Commun.* **2014**, 50, 5867.
- (220) Yang, Q. Y.; Zhong, C. L. *ChemPhysChem* **2006**, *7*, 1417.
- (221) Skoulidas, A. I.; Sholl, D. S. *J. Phys. Chem. B* **2005**, *109*, 15760.
- (222) Yuan, D.; Getman, R. B.; Wei, Z.; Snurr, R. Q.; Zhou, H.-C. *Chem. Commun.* **2012**, 48, 3297.
- (223) Grajciar, L.; Bludsky, O.; Nachtigall, P. *J. Phys. Chem. Lett.* **2010**, *1*, 3354.
- (224) Henninger, S. K.; Schmidt, F. P.; Henning, H. M. *Appl. Therm. Eng.* **2010**, *30*, 1692.
- (225) Chavan, S.; Bonino, F.; Valenzano, L.; Civalleri, B.; Lamberti, C.; Acerbi, N.; Cavka, J. H.; Leistner, M.; Bordiga, S. *J. Phys. Chem. C* **2013**, *117*, 15615.
- (226) Castillo, J. M.; Vlught, T. J. H.; Calero, S. J. *Phys. Chem. C* **2008**, *112*, 15934.
- (227) Bludsky, O.; Rubes, M.; Soldan, P.; Nachtigall, P. *J. Chem. Phys.* **2008**, *128*, 114102.
- (228) Rubes, M.; Wiersum, A. D.; Llewellyn, P. L.; Grajciar, L.; Bludsky, O.; Nachtigall, P. *J. Phys. Chem. C* **2013**, *117*, 11159.
- (229) Hermann, J.; Bludsky, O. *J. Chem. Phys.* **2013**, *139*, 034115.
- (230) Toda, J.; Fischer, M.; Jorge, M.; Gomes, J. R. B. *Chem. Phys. Lett.* **2013**, 587, 7.
- (231) Grimme, S. *J. Chem. Phys.* **2006**, *124*, 034108.
- (232) Witte, J.; Neaton, J. B.; Head-Gordon, M. *J. Chem. Phys.* **2014**, *140*, 104707.
- (233) Kim, H.; Park, J.; Jung, Y. *Phys. Chem. Chem. Phys.* **2013**, *15*, 19644.
- (234) Kim, H.; Jung, Y. *J. Phys. Chem. Lett.* **2014**, *5*, 440.
- (235) van den Bergh, J.; Gucuyener, C.; Pidko, E. A.; Hensen, E. J. M.; Gascon, J.; Kapteijn, F. *Chem.—Eur. J.* **2011**, *17*, 8832.
- (236) Alaerts, L.; Maes, M.; van der Veen, M. A.; Jacobs, P. A.; De Vos, D. E. *Phys. Chem. Chem. Phys.* **2009**, *11*, 2903.
- (237) Tijsebaert, B.; Varszegi, C.; Gies, H.; Xiao, F. S.; Bao, X. H.; Tatsumi, T.; Muller, U.; De Vos, D. *Chem. Commun.* **2008**, 2480.
- (238) Watanabe, T.; Keskin, S.; Nair, S.; Sholl, D. S. *Phys. Chem. Chem. Phys.* **2009**, *11*, 11389.
- (239) (a) Ray, K. G.; Olmsted, D.; He, N.; Houndonougbo, Y.; Laird, B. B.; Asta, M. *Phys. Rev. B* **2012**, *85*, 085410. (b) Ray, K. G.; Olmsted, D. L.; Houndonougbo, Y.; Laird, B. B.; Asta, M. *J. Phys. Chem. C* **2013**, *117*, 14642.
- (240) Ray, K. G.; Olmsted, D. L.; Burton, J. M. R.; Houndonougbo, Y.; Laird, B. B.; Asta, M. *Chem. Mater.* **2014**, *26*, 3976.
- (241) Marenich, A. V.; Jerome, S. V.; Cramer, C. J.; Truhlar, D. G. *J. Chem. Theory Comput.* **2012**, *8*, 527.
- (242) (a) Michalak, A.; Mitoraj, M.; Ziegler, T. *J. Phys. Chem. A* **2008**, *112*, 1933. (b) Mitoraj, M. P.; Michalak, A.; Ziegler, T. *J. Chem. Theory Comput.* **2009**, *5*, 962.
- (243) Reed, A. E.; Curtiss, L. A.; Weinhold, F. *Chem. Rev.* **1988**, *88*, 899.
- (244) Koh, H. S.; Rana, M. K.; Hwang, J.; Siegel, D. J. *Phys. Chem. Chem. Phys.* **2013**, *15*, 4573.
- (245) (a) Zhou, W.; Wu, H.; Yildirim, T. *J. Am. Chem. Soc.* **2008**, *130*, 15268. (b) Zhou, W.; Yildirim, T. *J. Phys. Chem. C* **2008**, *112*, 8132.
- (246) Park, J.; Kim, H.; Han, S. S.; Jung, Y. *J. Phys. Chem. Lett.* **2012**, *3*, 826.
- (247) (a) Mulfort, K. L.; Farha, O. K.; Stern, C. L.; Sarjeant, A. A.; Hupp, J. T. *J. Am. Chem. Soc.* **2009**, *131*, 3866. (b) Peterson, V. K.; Liu, Y.; Brown, C. M.; Kepert, C. J. *J. Am. Chem. Soc.* **2006**, *128*, 15578.
- (248) Kim, Y. H.; Kang, J.; Wei, S. H. *Phys. Rev. Lett.* **2010**, *105*, 236105.
- (249) Bak, J. H.; Le, V.-D.; Kang, J.; Wei, S.-H.; Kim, Y.-H. *J. Phys. Chem. C* **2012**, *116*, 7386.
- (250) Hijikata, Y.; Sakaki, S. *Inorg. Chem.* **2014**, *53*, 2417.
- (251) Sastre, G. *Theor. Chem. Acc.* **2010**, *127*, 259.
- (252) Gomez, D. A.; Sastre, G. *Phys. Chem. Chem. Phys.* **2011**, *13*, 16558.
- (253) Lochan, R. C.; Head-Gordon, M. *Phys. Chem. Chem. Phys.* **2006**, *8*, 1357.
- (254) Sillar, K.; Hofmann, A.; Sauer, J. *J. Am. Chem. Soc.* **2009**, *131*, 4143.
- (255) Matanovic, I.; Belof, J. L.; Space, B.; Sillar, K.; Sauer, J.; Eckert, J.; Bacic, Z. *J. Chem. Phys.* **2012**, *137*, 014701.
- (256) Ding, L. F.; Yazaydin, A. O. *J. Phys. Chem. C* **2012**, *116*, 22987.
- (257) Yu, K.; Schmidt, J. R. *J. Phys. Chem. C* **2013**, *117*, 3192.
- (258) Liu, Q.; Ning, L. Q.; Zheng, S. D.; Tao, M. N.; Shi, Y.; He, Y. *Sci. Rep.* **2013**, *3*, 2916.
- (259) Han, S. S.; Kim, D.; Jung, D. H.; Cho, S.; Choi, S. H.; Jung, Y. *J. Phys. Chem. C* **2012**, *116*, 20254.
- (260) Liu, Y.; Liu, J.; Lin, Y. S.; Chang, M. *J. Phys. Chem. C* **2014**, *118*, 6744.
- (261) Ding, L. F.; Yazaydin, A. O. *Phys. Chem. Chem. Phys.* **2013**, *15*, 11856.
- (262) Chen, Y. F.; Babarao, R.; Sandler, S. I.; Jiang, J. W. *Langmuir* **2010**, *26*, 8743.
- (263) Huang, H. L.; Zhang, W. J.; Liu, D. H.; Zhong, C. L. *Ind. Eng. Chem. Res.* **2012**, *51*, 10031.
- (264) Tan, K.; Nijem, N.; Canepa, P.; Gong, Q.; Li, J.; Thonhauser, T.; Chabal, Y. J. *Chem. Mater.* **2012**, *24*, 3153.
- (265) (a) DeCoste, J. B.; Peterson, G. W.; Jasuja, H.; Glover, T. G.; Huang, Y. G.; Walton, K. S. *J. Mater. Chem. A* **2013**, *1*, 5642. (b) Shearer, G. C.; Forselv, S.; Chavan, S.; Bordiga, S.; Mathisen, K.; Bjorgen, M.; Svelle, S.; Lillerud, K. P. *Top. Catal.* **2013**, *56*, 770.
- (266) Mondloch, J. E.; Katz, M. J.; Planas, N.; Semrouni, D.; Gagliardi, L.; Hupp, J. T.; Farha, O. K. *Chem. Commun.* **2014**, 50, 8944.
- (267) Ma, S. Q.; Sun, D. F.; Simmons, J. M.; Collier, C. D.; Yuan, D. Q.; Zhou, H. C. *J. Am. Chem. Soc.* **2008**, *130*, 1012.
- (268) Nijem, N.; Canepa, P.; Kaipa, U.; Tan, K.; Roodenko, K.; Tekarli, S.; Halbert, J.; Oswald, I. W. H.; Arvapally, R. K.; Yang, C.; Thonhauser, T.; Omary, M. A.; Chabal, Y. J. *J. Am. Chem. Soc.* **2013**, *135*, 12615.
- (269) (a) Duan, C. Y.; Wei, M. L.; Guo, D.; He, C.; Meng, Q. J. *J. Am. Chem. Soc.* **2010**, *132*, 3321. (b) Wei, M. L.; He, C.; Hua, W. J.; Duan, C. Y.; Li, S. H.; Meng, Q. J. *J. Am. Chem. Soc.* **2006**, *128*, 13318.
- (270) Nijem, N.; Canepa, P.; Kong, L. Z.; Wu, H. H.; Li, J.; Thonhauser, T.; Chabal, Y. J. *J. Phys. Condens. Matter* **2012**, *24*, 424203.

- (271) Canepa, P.; Nijem, N.; Chabal, Y. J.; Thonhauser, T. *Phys. Rev. Lett.* **2013**, *110*, 026102.
- (272) Bao, Z. B.; Yu, L. A.; Ren, Q. L.; Lu, X. Y.; Deng, S. G. *J. Colloid Interface Sci.* **2011**, *353*, 549.
- (273) Tan, K.; Canepa, P.; Gong, Q. H.; Liu, J.; Johnson, D. H.; Dyevoich, A.; Thallapally, P. K.; Thonhauser, T.; Li, J.; Chabal, Y. J. *Chem. Mater.* **2013**, *25*, 4653.
- (274) Grajciar, L.; Wiersum, A. D.; Llewellyn, P. L.; Chang, J. S.; Nachtigall, P. J. *Phys. Chem. C* **2011**, *115*, 17925.
- (275) Ramsahye, N. A.; Maurin, G.; Bourrelly, S.; Llewellyn, P. L.; Serre, C.; Loiseau, T.; Devic, T.; Ferey, G. *J. Phys. Chem. C* **2008**, *112*, 514.
- (276) Poloni, R.; Smit, B.; Neaton, J. B. *J. Am. Chem. Soc.* **2012**, *134*, 6714.
- (277) Haldar, R.; Reddy, S. K.; Suresh, V. M.; Mohapatra, S.; Balasubramanian, S.; Maji, T. K. *Chem.—Eur. J.* **2014**, *20*, 4347.
- (278) Demessence, A.; D'Alessandro, D. M.; Foo, M. L.; Long, J. R. *J. Am. Chem. Soc.* **2009**, *131*, 8784.
- (279) Choi, S.; Watanabe, T.; Bae, T.-H.; Sholl, D. S.; Jones, C. W. *J. Phys. Chem. Lett.* **2012**, *3*, 1136.
- (280) Rochelle, G. T. *Science* **2009**, *325*, 1652.
- (281) Han, S. S.; Goddard, W. A. *J. Am. Chem. Soc.* **2007**, *129*, 8422.
- (282) (a) Han, S. S.; Choi, S.-H.; Goddard, W. A. *J. Phys. Chem. C* **2011**, *115*, 3507. (b) Han, S. S.; Goddard, W. A. *J. Phys. Chem. C* **2008**, *112*, 13431.
- (283) Blomqvist, A.; Araujo, C. M.; Srepusharawoot, P.; Ahuja, R. *Proc. Natl. Acad. Sci. U.S.A.* **2007**, *104*, 20173.
- (284) (a) Dixit, M.; Maark, T. A.; Ghatak, K.; Ahuja, R.; Pal, S. *J. Phys. Chem. C* **2012**, *116*, 17336. (b) Dixit, M.; Maark, T. A.; Pal, S. *Int. J. Hydrogen Energy* **2011**, *36*, 10816. (c) Wang, T.; Zhang, Q.; Ma, B.; Chen, H.; Chen, L. *Int. J. Hydrogen Energy* **2012**, *37*, S081.
- (285) Mavrandonakis, A.; Tylanakakis, E.; Stubos, A. K.; Froudakis, G. E. *J. Phys. Chem. C* **2008**, *112*, 7290.
- (286) Dalach, P.; Frost, H.; Snurr, R. Q.; Ellis, D. E. *J. Phys. Chem. C* **2008**, *112*, 9278.
- (287) Sun, Y.; Ben, T.; Wang, L.; Qiu, S.; Sun, H. *J. Phys. Chem. Lett.* **2010**, *1*, 2753.
- (288) Klontzas, E.; Mavrandonakis, A.; Tylanakakis, E.; Froudakis, G. E. *Nano Lett.* **2008**, *8*, 1572.
- (289) Getman, R. B.; Miller, J. H.; Wang, K.; Snurr, R. Q. *J. Phys. Chem. C* **2011**, *115*, 2066.
- (290) Himsl, D.; Wallacher, D.; Hartmann, M. *Angew. Chem., Int. Ed.* **2009**, *48*, 4639.
- (291) Bae, Y. S.; Hauser, B. G.; Farha, O. K.; Hupp, J. T.; Snurr, R. Q. *Microporous Mesoporous Mater.* **2011**, *141*, 231.
- (292) Xu, Q.; Liu, D. H.; Yang, Q. Y.; Zhong, C. L.; Mi, J. G. *J. Mater. Chem.* **2010**, *20*, 706.
- (293) Mondloch, J. E.; Katz, M. J.; Isley, W. C.; Ghosh, P.; Liao, P.; Burry, W.; Wagner, G. W.; Hall, M. G.; DeCoste, J. B.; Peterson, G. W.; Snurr, R. Q.; Cramer, C. J.; Hupp, J. T.; Farha, O. K. *Nat. Mater.* **2015**, in press; doi:10.1038/nmat4238.
- (294) (a) Aijaz, A.; Xu, Q. *J. Phys. Chem. Lett.* **2014**, *5*, 1400. (b) Chen, B.; Xiang, S.; Qian, G. *Acc. Chem. Res.* **2010**, *43*, 1115. (c) Li, Q.; Ji, S.; Hao, Z. *Prog. Chem.* **2012**, *24*, 1506.
- (295) Dhakshinamoorthy, A.; Opanasenko, M.; Cejka, J.; Garcia, H. *Adv. Synth. Catal.* **2013**, *355*, 247.
- (296) Tuci, G.; Giambastiani, G.; Kwon, S.; Stair, P. C.; Snurr, R. Q.; Rossin, A. *ACS Catal.* **2014**, *4*, 1032.
- (297) Tonigold, M.; Lu, Y.; Mavrandonakis, A.; Puls, A.; Staudt, R.; Mollmer, J.; Sauer, J.; Volkmer, D. *Chem.—Eur. J.* **2011**, *17*, 8671.
- (298) Tonigold, M.; Lu, Y.; Bredenkotter, B.; Rieger, B.; Bahnmueller, S.; Hitzbleck, J.; Langstein, G.; Volkmer, D. *Angew. Chem., Int. Ed.* **2009**, *48*, 7546.
- (299) Jelic, J.; Denysenko, D.; Volkmer, D.; Reuter, K. *New J. Phys.* **2013**, *15*.
- (300) Tkatchenko, A.; Scheffler, M. *Phys. Rev. Lett.* **2009**, *102*, 073005.
- (301) Ryan, P.; Konstantinov, I.; Snurr, R. Q.; Broadbelt, L. J. *J. Catal.* **2012**, *286*, 95.
- (302) Chizallet, C.; Lazare, S.; Bazer-Bachi, D.; Bonnier, F.; Lecocq, V.; Soyer, E.; Quineaud, A. A.; Bats, N. *J. Am. Chem. Soc.* **2010**, *132*, 12365.
- (303) Luz, I.; Leon, A.; Boronat, M.; Xamena, F.; Corma, A. *Catal. Sci. Technol.* **2013**, *3*, 371.
- (304) Xiao, D. J.; Bloch, E. D.; Mason, J. A.; Queen, W. L.; Hudson, M. R.; Planas, N.; Borycz, J.; Dzubak, A. L.; Verma, P.; Lee, K.; Bonino, F.; Crocellà, V.; Yano, J.; Bordiga, S.; Truhlar, D. G.; Gagliardi, L.; Brown, C. M.; Long, J. R. *Nat. Chem.* **2014**, *6*, 590.
- (305) Hohenberger, J.; Ray, K.; Meyer, K. *Nat. Commun.* **2012**, *3*, 720.
- (306) Maihom, T.; Wannakao, S.; Boekfa, B.; Limtrakul, J. *J. Phys. Chem. C* **2013**, *117*, 17650.
- (307) Gascon, J.; Aktay, U.; Hernandez-Alonso, M. D.; van Klink, G. P. M.; Kapteijn, F. *J. Catal.* **2009**, *261*, 75.
- (308) Cortese, R.; Duca, D. *Phys. Chem. Chem. Phys.* **2011**, *13*, 15995.
- (309) (a) Cui, Q.; Karplus, M. *J. Chem. Phys.* **2000**, *112*, 1133. (b) Friesner, R. A.; Guallar, V. *Annu. Rev. Phys. Chem.*, **2005**, *56*, 389. (c) Lin, H.; Truhlar, D. G. *Theor. Chem. Acc.* **2007**, *117*, 185. (d) Senn, H. M.; Thiel, W. *Angew. Chem., Int. Ed.* **2009**, *48*, 1198.
- (310) Vermoortele, F.; Vandichel, M.; Van de Voorde, B.; Ameloot, R.; Waroquier, M.; Van Speybroeck, V.; De Vos, D. E. *Angew. Chem., Int. Ed.* **2012**, *51*, 4887.
- (311) Vandichel, M.; Biswas, S.; Leus, K.; Paier, J.; Sauer, J.; Verstraelen, T.; Van der Voort, P.; Waroquier, M.; Van Speybroeck, V. *ChemPlusChem* **2014**, *79*, 1183.
- (312) Fischer, M.; Hoffmann, F.; Froba, M. *Colloids Surf. A* **2010**, *357*, 35.
- (313) Mu, W.; Liu, D. H.; Yang, Q. Y.; Zhong, C. L. *Microporous Mesoporous Mater.* **2010**, *130*, 76.
- (314) Wu, H.; Zhou, W.; Yildirim, T. *J. Am. Chem. Soc.* **2007**, *129*, 5314.
- (315) Liu, Y.; Liu, J.; Chang, M.; Zheng, C. G. *J. Phys. Chem. C* **2012**, *116*, 16985.
- (316) Torrisi, A.; Mellot-Draznieks, C.; Bell, R. G. *J. Chem. Phys.* **2009**, *130*, 044705.
- (317) (a) Lim, D. W.; Yoon, J. W.; Ryu, K. Y.; Suh, M. P. *Angew. Chem., Int. Ed.* **2012**, *51*, 9814. (b) Vilhelmsen, L. B.; Sholl, D. S. *J. Phys. Chem. Lett.* **2012**, *3*, 3702. (c) Vilhelmsen, L. B.; Walton, K. S.; Sholl, D. S. *J. Am. Chem. Soc.* **2012**, *134*, 12807.
- (318) Guo, Z. Y.; Xiao, C. X.; Maligal-Ganesh, R. V.; Zhou, L.; Goh, T. W.; Li, X. L.; Tesfagaber, D.; Thiel, A.; Huang, W. Y. *ACS Catal.* **2014**, *4*, 1340.
- (319) Thanh Dang, T.; Chen, A.; Majeed Seayad, A. *RSC Adv.* **2014**, *4*, 30019.
- (320) (a) Henderson, G. S.; de Groot, F. M. F.; Moulton, B. J. A. In *Spectroscopic Methods in Mineralogy and Materials Sciences*; Henderson, G. S., Neuvill, D. R., Downs, R. T., Eds.; Mineralogical Society of America: Chantilly, VA, 2014; Vol. 78, pp 75-138. (b) Yano, J.; Yachandra, V. K. *Photosynth. Res.* **2009**, *102*, 241.
- (321) Lin, K. S.; Adhikari, A. K.; Su, Y. H.; Chiang, C. L.; Dehvari, K. *Chin. J. Phys.* **2012**, *50*, 322.
- (322) Goesten, M. G.; Juan-Alcaniz, J.; Ramos-Fernandez, E. V.; Gupta, K.; Stavitski, E.; van Bekkum, H.; Gascon, J.; Kapteijn, F. *J. Catal.* **2011**, *281*, 177.
- (323) Prendergast, D.; Galli, G. *Phys. Rev. Lett.* **2006**, *96*, 215502.
- (324) Borfecchia, E.; Maurelli, S.; Gianolio, D.; Groppo, E.; Chiesa, M.; Bonino, F.; Lamberti, C. *J. Phys. Chem. C* **2012**, *116*, 19839.
- (325) Rehr, J. J.; Kas, J. J.; Vila, F. D.; Prange, M. P.; Jorissen, K. *Phys. Chem. Chem. Phys.* **2010**, *12*, 5503.
- (326) (a) Ankudinov, A. L.; Rehr, J. J. *Phys. Rev. B* **2000**, *62*, 2437. (b) Zabinsky, S. I.; Rehr, J. J.; Ankudinov, A.; Albers, R. C.; Eller, M. J. *Phys. Rev. B* **1995**, *52*, 2995.
- (327) (a) Baroni, S.; de Gironcoli, S.; Dal Corso, A.; Giannozzi, P. *Rev. Mod. Phys.* **2001**, *73*, 515. (b) Gonze, X.; Lee, C. *Phys. Rev. B* **1997**, *55*, 10355.
- (328) Koch, W.; Holthausen, M. C. *A Chemist's Guide to Density Functional Theory*; Wiley-VCH: Weinheim, 2000.

- (329) Sun, G. Y.; Kurti, J.; Rajczy, P.; Kertesz, M.; Hafner, J.; Kresse, G. *J. Mol. Struct. THEOCHEM* **2003**, *624*, 37.
- (330) Civalieri, B.; Napoli, F.; Noel, Y.; Roetti, C.; Dovesi, R. *CrystEngComm* **2006**, *8*, 364.
- (331) Nijem, N.; Thissen, P.; Yao, Y.; Longo, R. C.; Roodenko, K.; Wu, H.; Zhao, Y.; Cho, K.; Li, J.; Langreth, D. C.; Chabal, Y. J. *J. Am. Chem. Soc.* **2011**, *133*, 12849.
- (332) Yao, Y.; Nijem, N.; Li, J.; Chabal, Y. J.; Langreth, D. C.; Thonhauser, T. *Phys. Rev. B* **2012**, *85*, 064302.
- (333) Valenzano, L.; Civalieri, B.; Chavan, S.; Palomino, G. T.; Arean, C. O.; Bordiga, S. *J. Phys. Chem. C* **2010**, *114*, 11185.
- (334) Noei, H.; Kozachuk, O.; Amirjalayer, S.; Bureekaew, S.; Kauer, M.; Schmid, R.; Marler, B.; Muhler, M.; Fischer, R. A.; Wang, Y. *J. Phys. Chem. C* **2013**, *117*, 5658.
- (335) Liu, D. H.; Zhong, C. L. *J. Phys. Chem. Lett.* **2010**, *1*, 97.
- (336) Benco, L.; Bucko, T.; Hafner, J.; Toulhoat, H. *J. Phys. Chem. B* **2004**, *108*, 13656.
- (337) Tan, K.; Canepa, P.; Gong, Q.; Liu, J.; Johnson, D. H.; Dyevoich, A.; Thallapally, P. K.; Thonhauser, T.; Li, J.; Chabal, Y. J. *Chem. Mater.* **2013**, *25*, 4653.
- (338) Kong, L. Z.; Cooper, V. R.; Nijem, N.; Li, K. H.; Li, J.; Chabal, Y. J.; Langreth, D. C. *Phys. Rev. B* **2009**, *79*, 4.
- (339) Feng, P. L.; Perry, J. J.; Nikodemski, S.; Jacobs, B. W.; Meek, S. T.; Allendorf, M. D. *J. Am. Chem. Soc.* **2010**, *132*, 15487.
- (340) Klan, P.; Wirz, J. *Photochemistry of organic compounds: From concepts to practice*; Wiley: Hoboken, NJ, 2009.
- (341) Chen, B.; Wang, L.; Zapata, F.; Qian, G.; Lobkovsky, E. B. *J. Am. Chem. Soc.* **2008**, *130*, 6718.
- (342) Sui, X.; Ji, M.; Lan, X.; Mi, W. H.; Hao, C.; Qiu, J. S. *Inorg. Chem.* **2013**, *52*, 5742.
- (343) Liu, Y. Y.; Leus, K.; Bogaerts, T.; Hemelsoet, K.; Bruneel, E.; Van Speybroeck, V.; Van Der Voort, P. *ChemCatChem* **2013**, *5*, 3657.
- (344) Bloch, E. D.; Britt, D.; Lee, C.; Doonan, C. J.; Uribe-Romo, F. J.; Furukawa, H.; Long, J. R.; Yaghi, O. M. *J. Am. Chem. Soc.* **2010**, *132*, 14382.
- (345) Liu, Y. Y.; Decadt, R.; Bogaerts, T.; Hemelsoet, K.; Kaczmarek, A. M.; Poelman, D.; Waroquier, M.; Van Speybroeck, V.; Van Deun, R.; Van Der Voort, P. *J. Phys. Chem. C* **2013**, *117*, 11302.
- (346) Boese, A. D.; Handy, N. C. *J. Chem. Phys.* **2001**, *114*, 5497.
- (347) Zhang, H.; Zhou, L.; Wei, J.; Li, Z.; Lin, P.; Du, S. *J. Mater. Chem.* **2012**, *22*, 21210.
- (348) Lu, Z.; Wen, L.; Ni, Z.; Li, Y.; Zhu, H.; Meng, Q. *Cryst. Growth Des.* **2007**, *7*, 268.
- (349) Hendon, C. H.; Tiana, D.; Fontecave, M.; Sanchez, C.; D'Arras, L.; Sassoie, C.; Rozes, L.; Mellot-Draznieks, C.; Walsh, A. J. *Am. Chem. Soc.* **2013**, *135*, 10942.
- (350) Lin, C.-K.; Zhao, D.; Gao, W.-Y.; Yang, Z.; Ye, J.; Xu, T.; Ge, Q.; Ma, S.; Liu, D.-J. *Inorg. Chem.* **2012**, *51*, 9039.
- (351) Kuc, A.; Enyashin, A.; Seifert, G. *J. Phys. Chem. B* **2007**, *111*, 8179.
- (352) Flage-Larsen, E.; Royset, A.; Cavka, J. H.; Thorshaug, K. J. *Phys. Chem. C* **2013**, *117*, 20610.
- (353) Flage-Larsen, E.; Thorshaug, K. *Inorg. Chem.* **2014**, *53*, 2569.
- (354) Pham, H. Q.; Mai, T.; Pham-Tran, N. N.; Kawazoe, Y.; Mizuseki, H.; Nguyen-Manh, D. *J. Phys. Chem. C* **2014**, *118*, 4567.
- (355) Gao, J.; Miao, J.; Li, P.-Z.; Teng, W. Y.; Yang, L.; Zhao, Y.; Liu, B.; Zhang, Q. *Chem. Commun.* **2014**, *50*, 3786.
- (356) Foster, M. E.; Azoulay, J. D.; Wong, B. M.; Allendorf, M. D. *Chem. Sci.* **2014**, *5*, 2081.
- (357) Yang, L. M.; Fang, G. Y.; Ma, J.; Ganz, E.; Han, S. S. *Cryst. Growth Des.* **2014**, *14*, 2532.
- (358) Choi, J. H.; Jeon, H. J.; Choi, K. M.; Kang, J. K. *J. Mater. Chem.* **2012**, *22*, 10144.
- (359) Choi, J. H.; Choi, Y. J.; Lee, J. W.; Shin, W. H.; Kang, J. K. *Phys. Chem. Chem. Phys.* **2009**, *11*, 628.
- (360) Botas, J. A.; Calleja, G.; Sanchez-Sanchez, M.; Orcajo, M. G. *Int. J. Hydrogen Energy* **2011**, *36*, 10834.
- (361) (a) Liu, Y. Y.; Grzywa, M.; Tonigold, M.; Sastre, G.; Schuttrigkeit, T.; Leeson, N. S.; Volkmer, D. *Dalton Trans.* **2011**, *40*, 5926. (b) Sippel, P.; Denysenko, D.; Loidl, A.; Lunkenheimer, P.; Sastre, G.; Volkmer, D. *Adv. Funct. Mater.* **2014**, *24*, 3885.
- (362) Truhlar, D. G. In *The Reaction Path in Chemistry: Current Approaches and Perspectives*; Heidrich, D., Ed.; Kluwer: Dordrecht, 1995, p 229.
- (363) Nicholson, D.; Parsonage, N. G. *Computer simulations and statistical mechanics of adsorption*; Academic Press: London, 1982.
- (364) Vangunsteren, W. F.; Berendsen, H. J. C. *Angew. Chem., Int. Ed.* **1990**, *29*, 992.
- (365) Perez-Pellitero, J.; Amrouche, H.; Siperstein, F. R.; Pirngruber, G.; Nieto-Draghi, C.; Chaplais, G.; Simon-Masseron, A.; Bazer-Bachi, D.; Peralta, D.; Bats, N. *Chem.—Eur. J.* **2010**, *16*, 1560.
- (366) (a) Chen, L. J.; Grajciar, L.; Nachtigall, P.; Duren, T. *J. Phys. Chem. C* **2011**, *115*, 23074. (b) Yazaydin, A. O.; Snurr, R. Q.; Park, T. H.; Koh, K.; Liu, J.; LeVan, M. D.; Benin, A. I.; Jakubczak, P.; Lanuza, M.; Galloway, D. B.; Low, J. J.; Willis, R. R. *J. Am. Chem. Soc.* **2009**, *131*, 18198. (c) Zang, J.; Nair, S.; Sholl, D. S. *J. Phys. Chem. C* **2013**, *117*, 7519.
- (367) Colon, Y. J.; Snurr, R. Q. *Chem. Soc. Rev.* **2014**, *43*, 5735.
- (368) Li, B.; Wen, H.-M.; Zhou, W.; Chen, B. *J. Phys. Chem. Lett.* **2014**, *5*, 3468.
- (369) Lee, S. J.; Bae, Y. S. *J. Phys. Chem. C* **2014**, *118*, 19833.
- (370) Rana, M. K.; Koh, H. S.; Zuberi, H.; Siegel, D. J. *J. Phys. Chem. C* **2014**, *118*, 2929.
- (371) Qiao, Z. W.; Zhou, J.; Lu, X. H. *Fluid Phase Equilib.* **2014**, *362*, 342.
- (372) Perry, J. J.; Teich-McGoldrick, S. L.; Meek, S. T.; Greathouse, J. A.; Haranczyk, M.; Allendorf, M. D. *J. Phys. Chem. C* **2014**, *118*, 11685.
- (373) Gurdal, Y.; Keskin, S. *J. Phys. Chem. C* **2013**, *117*, 5229.
- (374) Parkes, M. V.; Staiger, C. L.; Perry, J. J.; Allendorf, M. D.; Greathouse, J. A. *Phys. Chem. Chem. Phys.* **2013**, *15*, 9093.
- (375) Gomez, D. A.; Toda, J.; Sastre, G. *Phys. Chem. Chem. Phys.* **2014**, *16*, 19001.
- (376) (a) Pham, T.; Forrest, K. A.; McLaughlin, K.; Eckert, J.; Space, B. *J. Phys. Chem. C* **2014**, *118*, 22683. (b) Cirera, J.; Sung, J. C.; Howland, P. B.; Paesani, F. *J. Chem. Phys.* **2012**, *137*, 054704. (c) McDaniel, J. G.; Li, S.; Tylianakis, E.; Snurr, R. Q.; Schmidt, J. R. *J. Phys. Chem. C* **2015**, *119*, 3143. (d) McDaniel, J. G.; Schmidt, J. R. *J. Phys. Chem. A* **2013**, *117*, 2053. (e) Schmidt, J. R.; Yu, K.; McDaniel, J. G. *Acc. Chem. Res.* **2015**, *48*, 548.
- (377) Fu, J.; Liu, Y.; Tian, Y.; Wu, J. *J. Phys. Chem. C* **2015**, *119*, 5374.
- (378) Rao, D. W.; Lu, R. F.; Meng, Z. S.; Xu, G. J.; Kan, E. J.; Liu, Y. Z.; Xiao, C. Y.; Deng, K. M. *Mol. Simul.* **2013**, *39*, 968.
- (379) Wahiduzzaman, M.; Walther, C. F. J.; Heine, T. *J. Chem. Phys.* **2014**, *141*, 064708.
- (380) Zhao, Q.; Yuan, W.; Liang, J. M.; Li, J. P. *Int. J. Hydrogen Energy* **2013**, *38*, 13104.
- (381) Brand, S. K.; Colon, Y. J.; Getman, R. B.; Snurr, R. Q. *Microporous Mesoporous Mater.* **2013**, *171*, 103.
- (382) Deniz, E.; Karadas, F.; Patel, H. A.; Aparicio, S.; Yavuz, C. T.; Atilhan, M. *Microporous Mesoporous Mater.* **2013**, *175*, 34.
- (383) Gee, J. A.; Sholl, D. S. *J. Phys. Chem. C* **2013**, *117*, 20636.
- (384) Hou, X. J.; He, P.; Li, H. Q.; Wang, X. R. *J. Phys. Chem. C* **2013**, *117*, 2824.
- (385) Torrisi, A.; Bell, R. G.; Mellot-Draznieks, C. *Microporous Mesoporous Mater.* **2013**, *168*, 225.
- (386) Wang, B.; Huang, H.; Lv, X.-L.; Xie, Y.; Li, M.; Li, J.-R. *Inorg. Chem.* **2014**, *53*, 9254.
- (387) Peng, X.; Cao, D. P. *AIChE J.* **2013**, *59*, 2928.
- (388) Xiao, Y. L.; Yang, Q. Y.; Liu, D. H.; Zhong, C. L. *CrystEngComm* **2013**, *15*, 9588.
- (389) Siepmann, J. I.; Frenkel, D. *Mol. Phys.* **1992**, *75*, 59.
- (390) Torres-Knoop, A.; Krishna, R.; Dubbeldam, D. *Angew. Chem., Int. Ed.* **2014**, *53*, 7774.
- (391) Planchais, A.; Devautour-Vinot, S.; Giret, S.; Salles, F.; Trens, P.; Fateeva, A.; Devic, T.; Yot, P.; Serre, C.; Ramsahye, N.; Maurin, G. *J. Phys. Chem. C* **2013**, *117*, 19393.

- (392) Bernini, M. C.; Fairen-Jimenez, D.; Pasinetti, M.; Ramirez-Pastor, A. J.; Snurr, R. Q. *J. Mater. Chem. B* **2014**, *2*, 766.
- (393) Gutierrez-Sevillano, J. J.; Martin-Calvo, A.; Dubbeldam, D.; Calero, S.; Hamad, S. *RSC Adv.* **2013**, *3*, 14737.
- (394) Krishna, R.; van Baten, J. M. *Phys. Chem. Chem. Phys.* **2013**, *15*, 7994.
- (395) Song, X. D.; Wang, S.; Hao, C.; Qiu, J. S. *Inorg. Chem. Commun.* **2014**, *46*, 277.
- (396) Zwanzig, R. W. *J. Chem. Phys.* **1954**, *22*, 1420.
- (397) Annapureddy, H. V. R.; Motkuri, R. K.; Nguyen, P. T. M.; Truong, T. B.; Thallapally, P. K.; McGrail, B. P.; Dang, L. X. *Mol. Simul.* **2014**, *40*, 571.
- (398) Graham, A. J.; Banu, A. M.; Duren, T.; Greenaway, A.; McKellar, S. C.; Mowat, J. P. S.; Ward, K.; Wright, P. A.; Moggach, S. A. *J. Am. Chem. Soc.* **2014**, *136*, 8606.
- (399) Rudenko, A. N.; Bendt, S.; Keil, F. J. *J. Phys. Chem. C* **2014**, *118*, 16218.
- (400) Guillot, B. *J. Mol. Liq.* **2002**, *101*, 219.
- (401) Borycz, J.; Lin, L.-C.; Bloch, E. D.; Kim, J.; Dzubak, A. L.; Maurice, R.; Semrouni, D.; Lee, K.; Smit, B.; Gagliardi, L. *J. Phys. Chem. C* **2014**, *118*, 12230.
- (402) Lin, L.-C.; Lee, K.; Gagliardi, L.; Neaton, J. B.; Smit, B. *J. Chem. Theory Comput.* **2014**, *10*, 1477.
- (403) Yu, J.; Balbuena, P. B. *J. Phys. Chem. C* **2013**, *117*, 3383.
- (404) Kim, J.; Lin, L.-C.; Lee, K.; Neaton, J. B.; Smit, B. *J. Phys. Chem. C* **2014**, *118*, 2693.
- (405) Addicoat, M. A.; Vankova, N.; Akter, I. F.; Heine, T. *J. Chem. Theory Comput.* **2014**, *10*, 880.
- (406) Bristow, J. K.; Tiana, D.; Walsh, A. *J. Chem. Theory Comput.* **2014**, *10*, 4644.
- (407) (a) Cioce, C. R.; McLaughlin, K.; Belof, J. L.; Space, B. *J. Chem. Theory Comput.* **2013**, *9*, 5550. (b) Mullen, A. L.; Pham, T.; Forrest, K. A.; Cioce, C. R.; McLaughlin, K.; Space, B. *J. Chem. Theory Comput.* **2013**, *9*, 5421.
- (408) Han, S. S.; Jung, D. H.; Choi, S.-H.; Heo, J. *ChemPhysChem* **2013**, *14*, 2698.
- (409) (a) Chen, B. L.; Eddaoudi, M.; Hyde, S. T.; O'Keeffe, M.; Yaghi, O. M. *Science* **2001**, *291*, 1021. (b) Reineke, T. M.; Eddaoudi, M.; Moler, D.; O'Keeffe, M.; Yaghi, O. M. *J. Am. Chem. Soc.* **2000**, *122*, 4843. (c) Yaghi, O. M. *Nat. Mater.* **2007**, *6*, 92.
- (410) Han, S. S.; Jung, D.-H.; Heo, J. *J. Phys. Chem. C* **2012**, *117*, 71.
- (411) Mayo, S. L.; Olafson, B. D.; Goddard, W. A. *J. Phys. Chem.* **1990**, *94*, 8897.
- (412) Babarao, R.; Coghlan, C. J.; Rankine, D.; Bloch, W. M.; Gransbury, G. K.; Sato, H.; Kitagawa, S.; Sumby, C. J.; Hill, M. R.; Doonan, C. J. *Chem. Commun.* **2014**, *50*, 3238.
- (413) Yang, Q. Y.; Wiersum, A. D.; Llewellyn, P. L.; Guillerm, V.; Serred, C.; Maurin, G. *Chem. Commun.* **2011**, *47*, 9603.
- (414) Pham, T.; Forrest, K. A.; Eckert, J.; Georgiev, P. A.; Mullen, A.; Luebke, R.; Cairns, A. J.; Belmabkhout, Y.; Eubank, J. F.; McLaughlin, K.; Lohstroh, W.; Eddaoudi, M.; Space, B. *J. Phys. Chem. C* **2013**, *118*, 439.
- (415) (a) Eubank, J. F.; Nouar, F.; Luebke, R.; Cairns, A. J.; Wojtas, L.; Alkordi, M.; Bousquet, T.; Hight, M. R.; Eckert, J.; Embs, J. P.; Georgiev, P. A.; Eddaoudi, M. *Angew. Chem., Int. Ed.* **2012**, *51*, 10099. (b) Luebke, R.; Eubank, J. F.; Cairns, A. J.; Belmabkhout, Y.; Wojtas, L.; Eddaoudi, M. *Chem. Commun.* **2012**, *48*, 1455. (c) Nouar, F.; Eubank, J. F.; Bousquet, T.; Wojtas, L.; Zaworotko, M. J.; Eddaoudi, M. *J. Am. Chem. Soc.* **2008**, *130*, 1833.
- (416) (a) Martin, M. G.; Siepmann, J. I. *J. Phys. Chem. B* **1998**, *102*, 2569. (b) Potoff, J. J.; Siepmann, J. I. *AIChE J.* **2001**, *47*, 1676.
- (417) Jain, A.; Ong, S. P.; Hautier, G.; Chen, W.; Richards, W. D.; Dacek, S.; Cholia, S.; Gunter, D.; Skinner, D.; Ceder, G.; Persson, K. A. *Appl. Mater.* **2013**, *1*, 011002.
- (418) (a) <http://helios.princeton.edu/mofomics/>, 2015. (b) <http://hmofo.northwestern.edu/hc/crystals.php>, 2015.
- (419) Lin, L.-C.; Berger, A. H.; Martin, R. L.; Kim, J.; Swisher, J. A.; Jariwala, K.; Rycroft, C. H.; Bhowan, A. S.; Deem, M. W.; Haranczyk, M.; Smit, B. *Nat. Mater.* **2012**, *11*, 633.
- (420) Bao, Y.; Martin, R. L.; Simon, C. M.; Haranczyk, M.; Smit, B.; Deem, M. W. *J. Phys. Chem. C* **2014**, *119*, 186.
- (421) Ufimtsev, I. S.; Martinez, T. J. *Comput. Sci. Eng.* **2008**, *10*, 26.
- (422) <http://www.exascale.org/bdec/>.
- (423) (a) Goodpaster, J. D.; Barnes, T. A.; Miller, T. F. *J. Chem. Phys.* **2011**, *134*, 164108. (b) Manby, F. R.; Stella, M.; Goodpaster, J. D.; Miller, T. F. *J. Chem. Theory Comput.* **2012**, *8*, 2564. (c) Neugebauer, J.; Louwerse, M. J.; Baerends, E. J.; Wesolowski, T. A. *J. Chem. Phys.* **2005**, *122*, 094115. (d) Wesolowski, T. A.; Gourso, A.; Weber, J. *J. Chem. Phys.* **2001**, *115*, 4791. (e) Mayhall, N. J.; Raghavachari, K. *J. Chem. Theory Comput.* **2011**, *7*, 1336. (f) Wen, S.; Nanda, K.; Huang, Y.; Beran, G. J. O. *Phys. Chem. Chem. Phys.* **2012**, *14*, 7578. (g) Isegawa, M.; Wang, B.; Truhlar, D. G. *J. Chem. Theory Comput.* **2013**, *9*, 1381. (h) Richard, R. M.; Lao, K. U.; Herbert, J. M. *J. Chem. Phys.* **2014**, *141*, 014108. (i) Nakata, H.; Schmidt, M. W.; Fedorov, D. G.; Kitaura, K.; Nakamura, S.; Gordon, M. S. *J. Phys. Chem. A* **2014**, *118*, 9762.
- (424) (a) Nesbet, R. K. *Adv. Chem. Phys.* **1969**, *14*, 1. (b) Stoll, H. *J. Chem. Phys.* **1992**, *97*, 6090. (c) Friedrich, J.; Hanrath, M.; Dolg, M. *J. Chem. Phys.* **2007**, *126*, 154110.
- (425) Laio, A.; Gervasio, F. L. *Rep. Prog. Phys.* **2008**, *71*, 126601.
- (426) Kastner, J. *Wiley Interdiscip. Rev. Comput. Mol. Sci.* **2011**, *1*, 932.
- (427) (a) Tempkin, J. O. B.; Leverentz, H. R.; Wang, B.; Truhlar, D. G. *J. Phys. Chem. Lett.* **2011**, *2*, 2141. (b) Wang, B.; Truhlar, D. G. *J. Chem. Theory Comput.* **2012**, *8*, 1989. (c) Wang, B.; Truhlar, D. G. *J. Chem. Theory Comput.* **2014**, *10*, 4480.
- (428) Sillar, K.; Sauer, J. *J. Am. Chem. Soc.* **2012**, *134*, 18354.